Proton-Coupled Reduction of N_2 Facilitated by Molecular Fe Complexes

Thesis by
Jonathan Rittle

In Partial Fulfillment of the Requirements for the Degree
of
Doctor of Philosophy

CALIFORNIA INSTITUTE OF TECHNOLOGY
Pasadena, California
2016
(Defended November 9, 2015)

ACKNOWLEDGEMENTS

My epochal experience in graduate school has been marked by hard work, intellectual growth, and no shortage of deadlines. These facts leave little opportunity for an acknowledgement of those whose efforts were indispensable to my progress and perseverance, and are therefore disclosed here. First and foremost, I would like to thank my advisor, Jonas Peters, for his tireless efforts in molding me into the scientist that I am today. His scientific rigor has constantly challenged me to strive for excellence and I am grateful for the knowledge and guidance he has provided. Jonas has given me the freedom to pursue scientific research of my choosing and shown a remarkable degree of patience while dealing with my belligerent tendencies. Perhaps equally important, Jonas has built a research group that is perpetually filled with the best students and postdoctoral scholars. Their contributions to my graduate experience are immeasurable and I wish them all the best of luck in their future activities. In particular, John Anderson, Dan Suess, and Ayumi Takaoka were senior graduate students who took me under their wings when I joined the lab as a naïve first-year graduate student. I am grateful for the time and effort that they collectively spent in teaching me the art of chemical synthesis and for our unforgettable experiences outside of lab. Hill Harman and Marc-Etienne Moret were excellent postdocs that taught me a great deal about all aspects of science while providing comprehensive guidance. I joined the lab concurrent with Sid Creutz, who has been a truly great friend and one of the most brilliant people I have met. I have had the distinct pleasure of eating lunch with Charles McCrory over much of the past five years and I will sorely miss his humor and 'positive' attitude. My thesis committee has additionally consisted of Theo Agapie, Harry Gray, and Doug Rees, who have provided me with a wealth of feedback, criticism, and insight towards my research objectives that will undoubtedly shape many aspects of my future in science. The exceptional staff at Caltech have made my research possible, and I would like to thank all of them for their contributions. Larry Henling has spent an incredible amount of time teaching me aspects of X-ray crystallography and I am grateful for these efforts and his friendship. Michael T. Green has been a dedicated mentor and friend of mine during the past 8 years and I am grateful for everything he has done for me. I would like to thank my family and friends that I have met at Caltech or otherwise who have provided unwavering support during the past five years. Finally, I would like to thank my best friend, Liz Smith, whose sincerity and compassion during the past four years may have played the single largest role in my completion of these endeavors.

ABSTRACT

The activation of Fe-coordinated N_2 via the formal addition of hydrogen atom equivalents is explored in this thesis. These reactions may occur in nitrogenase enzymes during the biological conversion of N_2 to NH_3. To understand these reactions, the N_2 reactivity of a series of molecular Fe(N_2) platforms is investigated. A trigonal pyramidal, carbon-ligated Fe^I complex was prepared that displays a similar geometry to that of the resting state 'belt' Fe atoms of nitrogenase. Upon reduction, this species was shown to coordinate N_2, concomitant with significant weakening of the C-Fe interaction. This hemilability of the axial ligand may play a critical role in mediating the interconversion of Fe(N_xH_y) species during N_2 conversion to NH_3. In fact, a trigonal pyramidal borane-ligated Fe complex was shown to catalyze this transformation, generating up to 8.49 equivalents of NH_3. To shed light on the mechanistic details of this reaction, protonation of a borane-ligated Fe(N_2) complex was investigated and found to give rise to a mixture of species that contains an iron hydrazido(2-) [Fe(NNH_2)] complex. The identification of this species is suggestive of an early N-N bond cleavage event *en route* to NH_3 production, but the highly-reactive nature of this complex frustrated direct attempts to probe this possibility. A structurally-analogous silyl-ligated Fe(N_2) complex was found to react productively with hydrogen atom equivalents, giving rise to an isolable Fe(NNH_2) species. Spectroscopic and crystallographic studies benefitted from the enhanced stability of this complex relative to the borane analogue. One-electron reduction of this species initiates a spontaneous disproportionation reaction with an iron hydrazine [Fe(NH_2NH_2)] complex as the predominant reaction product. This transformation provides support for an Fe-mediated N_2 activation mechanism that proceeds via a late N-N bond cleavage. In hopes of gaining more fundamental insight into these reactions, a series of Fe(CN) complexes were prepared and reacted with hydrogen-atom equivalents. Significant quantities of CH_4 and NH_3 are generated in these reactions as a result of complete C-N bond activation. A series of Fe(CNH_x) were found to be exceptionally stable and may be intermediates in these reactions. The stability of these compounds permitted collection of thermodynamic parameters pertinent to the unique N-H bonds. This data is comparatively discussed with the theoretically-predicted data of the N_2-derived Fe(NNH_x) species. Exceptionally-weak N-H bond enthalpies are found for many of these compounds, and sheds light on their short-lived nature and tendency to evolve H_2. As a whole, these works both establish and provide a means to understand Fe-mediated N_2 activation via the addition of hydrogen atom equivalents.

TABLE OF CONTENTS

DETAILED TABLE OF CONTENTS

LIST OF FIGURES

LIST OF SCHEMES

LIST OF TABLES

LIST OF ABBREVIATIONS

A^X	Hyperfine coupling constant due to nucleus X
Ad	1-Adamantyl
Anal	Analysis
atm	Atmosphere
Avg	Average
BAr^F_{24}	$B(3,5\text{-}C_6H_3(CF_3)_2)_4^-$
br	broad
BDE	Bond Dissociation Enthalpy
Bu	n-Butyl
C	constant
ca	circa
calcd	Calculated
C_{alkyl}	C-atom of a sp^3-hybridized, anionic carbon ligand
CCD	Charge-coupled device
cm	centimeter
cm^{-1}	Wave number
CN	Cyanide
CNH_x	Generic CN-derived ligand with x H atoms
CO	Carbon monoxide
Cp	Cyclopentadienyl
Cp*	Pentamethylcyclopentadienyl
CPET	Concerted Proton Electron Transfer
CSD	Cambridge Structural Database
$C^{Si}P^{Ph}_3$	$(Ph_2PCH_2SiMe_2)_3CH$
CV	cyclic voltammogram
d	doublet or deuterium
dd	doublet of doublets
d_x	compound with x deuterium atoms
depe	1,2-Bis(diethylphosphino)ethane
DFT	Density Functional Theory
DME	1,2-dimethoxyethane
DMSO	Dimethylsulfoxide
dppe	1,2-Bis(diphenylphosphino)ethane
e	electron
ENDOR	Electron nuclear double resonance
EPR	Electron paramagnetic resonance
eq	Equivalents
equiv	Equivalents
EXAFS	Extended X-ray absorption fine structure
eV	Electron volt
E^0	Reduction or oxidation potential
F	Structure factor
Fc	Ferrocene

FID	Flame Ionization Detection
FeMoco	Iron-Molybdenum cofactor
GC	gas chromatography
G	Gauss
g	Gram
g	Electron g-factor
GC	Gas chromatography
GHz	Gigahertz
H	Enthalpy
HIPT	*h*exa-*i*so*p*ropyl-*t*erphenyl
HMQC	heteronuclear multiple quantum coherence
HOMO	Highest-Occupied Molecular Orbital
Hz	Hertz
I	Nuclear spin quantum number
iPr	isopropyl
IR	Infrared
${}^{x}J_{AB}$	NMR coupling constant between atoms A and B along X number of bonds
J	NMR coupling constant or magnetic coupling constant
K	Kelvin or equilibrium constant or 1s-orbital
L	Generic neutral dative ligand
LUMO	Lowes-Unoccupied Molecular Orbital
kcal	Kilocalorie
keV	Kiloelectron volt
m	multiplet
M	Concentration in molarity
max	Maximum
Me	Methyl
mg	Milligram
MHz	Megahertz
mL	Milliliter
mM	Millimolar
mm	Millimeter
mV	Millivolt
mmol	Millimole
MO	Molecular orbital
mol	Mole
M_s	Magnetic spin quantum number
MS	Mass spectrum
n	generic number
NBO	Natural Bond Orbital
nm	nanometer
NMR	Nuclear magnetic resonance
N_xH_y	Generic nitrogenous ligand with x N atoms and y H atoms
NNH_x	Generic nitrogenous ligand with 2 N atoms and x H atoms
NRVS	Nuclear Resonance Vibrational Spectroscopy
o	*ortho*

OTf	OSO_2CF_3
Ph	Phenyl
pK_a	Acid dissociation constant
q	quartet or charge of a specified atom
R	generic organic group or R-factor
RT	Room temperature
S	Entropy
S	Spin quantum number
s	Singlet or second
SiP_2O	$[(o\text{-}P(iPr)_2C_6H_4)_2Si]_2O^{2-}$
SiP_3	$(o\text{-}PR_2C_6H_4)_3Si^-$
$SiP^{iPr}{}_3$	$(o\text{-}P(iPr)_2C_6H_4)_3Si^-$
t	Triplet or time
TBA	Tetra-*n*-butyl ammonium
tBu	*tert*-Butyl
TEMPO	2,2,6,6-tetramethylpiperidine *N*-oxide
Tf	SO_2CF_3
THF	Tetrahydrofuran
TMS	Trimethylsilyl
TPB	$o\text{-}iPr_2P(C_6H_4))_3B$ or generically $o\text{-}R_2P(C_6H_4))_3B$
TPP	Tetraphenylporphyrin
UV	Ultraviolot
V	Volt
vbr	very broad
Vis	Visible
wR	Weighted R-factor
X	Generic anionic atom or molecule
XAS	X-ray absorption spectroscopy
XANES	X-ray Absorption Near Edge Spectroscopy
XRD	X-ray diffraction
$^{\alpha}N$	Proximal nitrogen atom of a bound N_2 ligand
$^{\beta}N$	Terminal nitrogen atom of a bound N_2 ligand
γ	High frequency electromagnetic radiation
ΔE_Q	Mössbauer quadrupole splitting
δ	chemical shift or Mössbauer isomer shift
°	Degree
°C	Degrees Celsius
ε	Extinction coefficient in units of $M^{-1}cm^{-1}$
η^x	Hapticity of order x
η	Mössbauer Asymmetry parameter
λ	Wavelength
λ_{max}	Wavelength of local maximum intensity
μ	Bridging
μA	Microamps
μ-X	Bridging X ligand
μ_B	Bohr magneton

μ_{eff}	Effective magnetic moment
μL	Microliter
ν_{xy}	Vibrational frequency between atoms x and y
Σ	Summation
σ	Sigma symmetry orbital or interaction
σ*	Sigma symmetry antibonding interaction
π	Pi symmetry orbital or interaction
π*	Pi symmetry antibonding interaction
$\tau_{(1/2)}$	Half-life
τ_4	Index of geometry between tetrahedral and trigonal pyramidal
τ_5	Index of geometry between square pyramidal and trigonal bipyramidal
χ_n	Electronegativity of n Element
Å	Angstrom
12-C-4	12-crown-4
^{1}H	Hydrogen-1
^{2}H	Hydrogen-2
^{11}B	Boron-11
^{13}C	Carbon-13
^{15}N	Nitrogen-15
^{31}P	Phosphorus-31
^{31}Si	Silicon-29
$\{^{1}H\}$	Proton-decoupled
2-MeTHF	2-Methyl-tetrahydrofuran
6-31G, etc.	Basis sets for DFT
BP86 etc.	DFT functional

PUBLISHED CONTENT AND CONTRIBUTIONS

1. Anderson, J. S.; Rittle, J.; Peters, J. C. *Nature.* **2013**. 501, 84-87.

http://dx.doi.org/10.1038/nature12435

In this manuscript, I analyzed the ability of synthetic Fe complexes to catalytically reduce atmosphere N_2 to NH_3, performed mechanistic investigations to determine how such complexes were degraded in these reaction mixtures and wrote portions of the manuscript.

2. Anderson, J. S.; Cutsail, G. E.; Rittle, J.; Connor, B. A.; Gunderson, W. A.; Zhang, L.; *et al.* *J. Amer. Chem. Soc.* **2015**. 137, 7803-7809. http://dx.doi.org/10.1021/jacs.5b03432

In this manuscript, I performed ^{57}Fe Mossbauer investigations of synthetic Fe complexes that are relevant to the catalytic reduction of N_2 to NH_3 and wrote portions of the manuscript.

3. Rittle, J.; Peters, J. C.; *Proc. Natl. Acad. Sci.* 2013, 110, 15898-15903.

http://dx.doi.org/10.1073/pnas.1310153110

I performed all of the experiments contained in, and wrote the manuscript for this work.

4. Rittle, J.; McCrory, C. C. L.; Peters, J. C.; *J. Amer. Chem. Soc.* **2014**. 136, 13853-13862.

http://dx.doi.org/10.1021/ja507217v

I performed all of the experiments contained in, and wrote the manuscript for this work.

Chapter 1. Introduction

1.1. Opening Remarks

Why would anyone want to study dinitrogen (N_2)? Most humans do not utilize N_2 in any part of their everyday lives or even know what it is. N_2 is a colorless, odorless gas that makes up 80% of the air we breathe. Despite its prevalence in the atmosphere, N_2 does not affect the size of the ozone layer or measurably contribute to Global Warming. Unlike the closely-related dioxygen (O_2), N_2 has no physiological role in human metabolism. It does not cause or cure cancer. Unlike helium, it does not alter the pitch of your voice. There is no interest in developing better methods for its production. In fact, N_2 is very cheap; one gallon of the gas costs only $0.003 US dollars. Unfortunately, it is not a source of renewable energy: it does not even combust. In his 1772 doctoral thesis, the discoverer of N_2, Daniel Rutherford, referred to it as 'mephitic' or poisonous air.[1] Following the publication of this work, Rutherford left the field of chemistry, never to return.[2] Why would anyone want to study N_2?

1.2. Transition Metal-mediated Dinitrogen Activation

As it turns out, N_2 is the ultimate source of nitrogen-containing molecules in biology, including the DNA and proteins that constitute the building blocks of Life.[3] Without N_2, we would simply cease to exist. However, in order to incorporate N_2-derived nitrogen into these molecules, it must be 'activated'. This task is by no means straightforward and many of the properties described above are due to the essentially *non*reactive nature of N_2. Given the abundance of N_2 on Earth, its activation would serve to generate an unlimited supply of nitrogen for the synthesis of the aforementioned biomolecules and many other commodity chemicals. In its free form, however, N_2 is not

easily protonated, reduced, or oxidized, a consequence of the three strong covalent bonds that bind the two nitrogen atoms of N_2.[4] The mystique of N_2 is therefore in understanding *how* it is converted into a form that can be utilized.

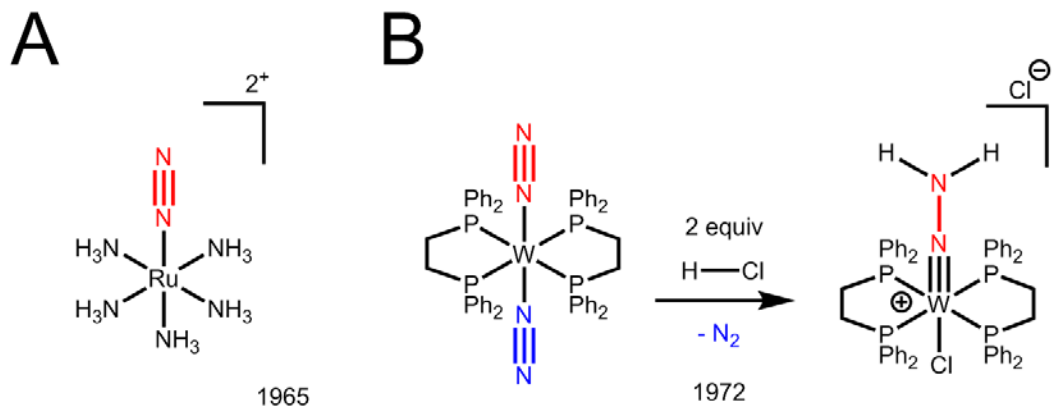

Figure 1.1. (A) The first example of a transition metal complex that contains coordinated N_2. (B) Protonation of a W(N_2) complex results in partial cleavage of the N≡N triple bond.

Only a few clever methods that have been devised to activate N_2 rely on the cleavage of its N-N triple bond.[5] These methods employ the use of transition metals which are uniquely capable of forming chemical bonds with N_2. As a first step in understanding these processes, the manner in which N_2 bonds, or coordinates, to transition metals must be established. The coordination of N_2 to a transition metal was first reported in 1965 (Figure 1.1A).[6] It was found that N_2 can coordinate to an atom of ruthenium (Ru) in a linear fashion, meaning that only one of the two N atoms are actually bonded to the Ru atom. This coordination process serves to polarize the N_2 molecule: the Ru-bound nitrogen atom develops a partial positive charge, and to compensate, the terminal nitrogen atom gains a partial negative charge.[4] This 'charging' of the N_2

molecule upon coordination to a transition metal sets the stage for chemical reactions to take place at one or both nitrogen atoms.

The extent of N_2 activation is intimately linked to the identity of the transition metal with which it binds. In the example above, the Ru atom does not sufficiently 'charge' the N_2 molecule and simple chemical reactions, such as protonation, do not occur at either nitrogen atom.[7] Other metals, such as molybdenum (Mo) or tungsten (W), offer a much greater degree of activation (Figure 1.1B).[4] In 1972, it was demonstrated that a W complex sufficiently activated N_2 to permit the addition of two hydrogen atoms onto the terminal nitrogen atom, via a protonation reaction with hydrochloric acid (HCl).[8] The W atom makes this reaction possible by transferring a large degree of negative charge onto the terminal nitrogen atom of N_2, and thus favoring its chemical reaction with the positively charged H-atom of HCl. By forming two strong N-H bonds the N-N bond of N_2 is significantly weakened. This weakening is judged by the distance that separates the two nitrogen atoms. In free N_2, this N-N distance is 1.10 Å, reflecting an N-N triple bond. In the W complex shown, this N-N distance is 1.37 Å and is close to that of a N-N single bond.[8b] These represent crucial first steps in cleaving the N-N triple bond entirely and therefore converting N_2 into a more useable form.[9]

These N_2 activation experiments are only possible because the compounds shown are *stable* molecules that can be rigorously studied and 'put into a bottle'. Transition metals of groups 8-11, for example, form comparatively weaker bonds with N_2 and these compounds are prone to decomposition.[10] The different transition metal complexes shown in Figure 1.1 are supported by a number of other coordinating groups that serve to stabilize these compounds. Furthermore, these 'ancillary ligands' can tune the physical

properties of the central transition metal in ways that directly influence its ability to activate the N_2 molecule.[4,10,11] For example, in Figure 1.1A, the Ru atom is bound to five ammonia (NH_3) groups, which are easily installed onto the Ru atom, but do not confer desirable N_2-activation properties. The large phosphine ligands that support the W atom in Figure 1.1B are much more difficult to synthesize and bind to the metal, but they provide the W atom with an ideal chemical environment that allows for the protonation reaction to proceed.[11] By employing the 'right' ancillary ligands, almost any transition metal can be properly equipped to activate N_2.

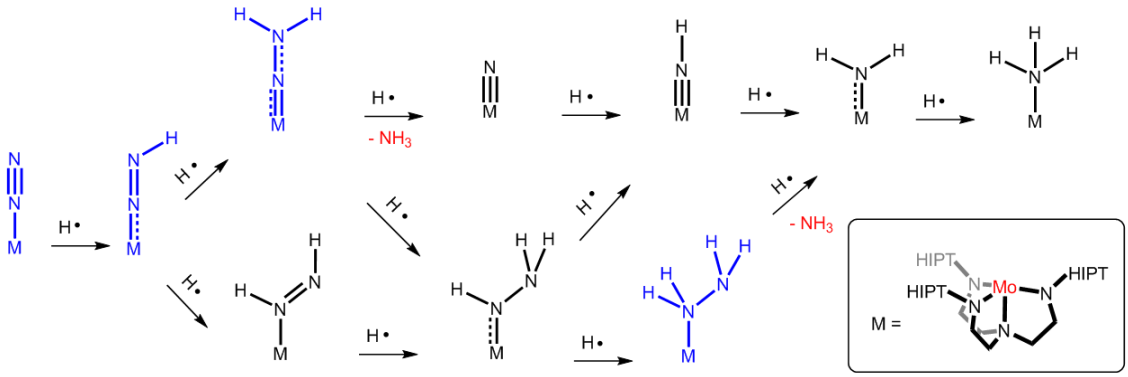

Figure 1.2. Sequential addition of H-atoms to an arbitrary N_2-bound transition metal (M) complex. Compounds highlighted in blue are of exceptional importance to this thesis. The inset shows one example of a transition metal complex that can mediate many of the shown steps. Molecular charges are not shown. HIPT = *h*exa-*iso*propyl-*t*erphenyl.

The mechanism(s) of N_2 activation can follow a number of different routes (Figure 1.2). In line with the protonation experiments described above, the most common means of activating N_2 involves the sequential addition of H-atoms to both of the nitrogen atoms.[4] In principle, the *order* and *site* of H-atom addition to N_2 is quite flexible, but the only

unequivocally-established reaction pathway follows the upper course in Figure 1.2. In 2002, Schrock and Yandulov disclosed a Mo-based system that featured a very large ancillary ligand (inset of Figure 1.2).[12] The massive "HIPT" substituents (which are too big to reasonably portray) enshroud the N_2-derived N_xH_y ligands (where x = 1, or 2 and y = 0 - 4). This design property engenders an increased stability to the various Mo(N_xH_y) species that represent intermediate stages of N_2 activation, allowing for detailed fundamental studies of their chemical properties and interconversion. This elegant system serves as the benchmark for studying N_2 activation with molecular transition metals.

1.3. Biological N_2 Activation

Despite the wealth of knowledge gained in these endeavors, the systems described above find little practical use in converting N_2 to more important nitrogen-containing molecules such as DNA. The molybdenum system described above is only capable of activating 4 molecules of N_2 before it simply falls apart.[12b] It is estimated that roughly $3x10^{36}$ molecules of N_2 must be activated each year to sustain human civilization;[3] an impossible assignment for these fragile compounds.

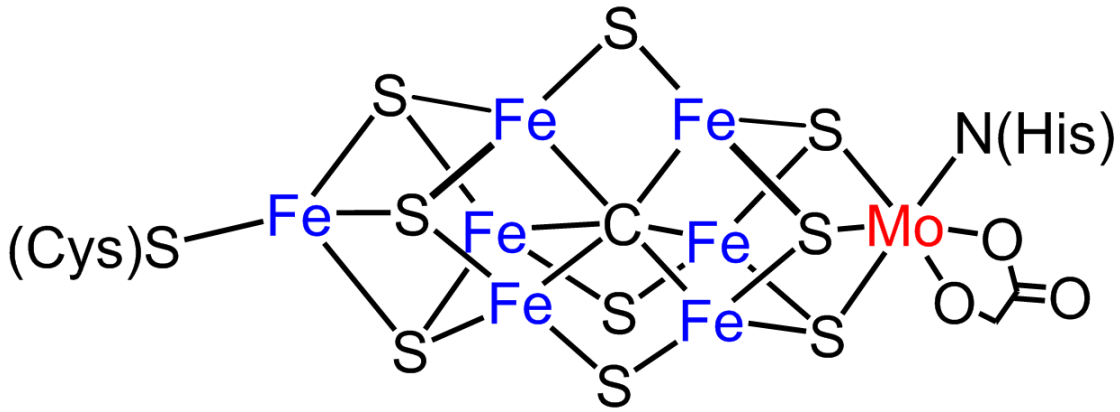

Figure 1.3. Simplified schematic of the FeMoco found in the nitrogenase protein.

Nitrogenase is a biological protein found in microorganisms throughout the world, and converts N_2 to ammonia (NH_3), the perfect building block for constructing nitrogen-containing biomolecules.[3] Nitrogenase is a catalytic protein, or enzyme, that is responsible for mediating half of the global N_2 activation.[3a] However, unlike the Schrock system described above, we have no idea how this system works! We know that N_2 interacts with a complex transition metal cluster buried in the center of the nitrogenase protein (Figure 1.3) and NH_3 is subsequently produced. This cluster, referred to as the "FeMoco", contains a *co*factor composed of iron (*Fe*) and *Mo* atoms that are stitched together by a web of sulfur and carbon atoms. We do not know where N_2 binds or how it is activated and these facts have prompted a great deal of ongoing scientific inquiry.[13]

At a very basic level, the Schrock system[12] described above *may* model the chemistry of the single Mo atom in FeMoco. If N_2 were to bind to this Mo atom, it might be activated by a similar mechanism as that shown in the top of Figure 1.2. But what if N_2 is bound and activated at one of the Fe sites? Most Fe complexes are similar to the Ru example (Figure 1.1a) and only weakly 'charge' the bound N_2.[10] This low degree of N_2 activation means that H-atoms are not efficiently transferred to the nitrogen atoms of an Fe-bound N_2 molecule, and therefore the production of NH_3 from such units is unlikely. Nonetheless, some circumstantial evidence suggests that one or more of the Fe atoms in FeMoco plays an integral, yet undefined, role in the conversion of N_2 to NH_3.[10,13]

1.4. N_2 Activation at Well-defined Fe Sites

Can we prepare and study well-defined Fe species that model the functional aspects of nitrogenase? This is a central question to the research endeavors described in these pages. In pursuit of an answer, strategies must be developed that enhance the ability of Fe

to activate a bound N_2 molecule, and prevent the decomposition of Fe(N_xH_y) species prepared by H-atom addition to these complexes. To this end, electron donating and sterically-encumbering ancillary ligands will be coordinated to Fe and the resulting compounds will be investigated (Figure 1.4).[14] The electron donation imparted by the electropositive[15] P, Si, and C atoms should enhance the ability of Fe to activate N_2. The size and shape of these ligands (Figure 1.4A) are ideally suited for the coordination of one (Figure 1.4A-B) or more (Figure 1.4C) diatomic ligands, such as N_2, CO, or CN. Moreover, the rather large nature of the ancillary ligands (Figure 1.4A) serves to protect the fragile (N_xH_y) ligands generated *en route* to the formation of NH_3.

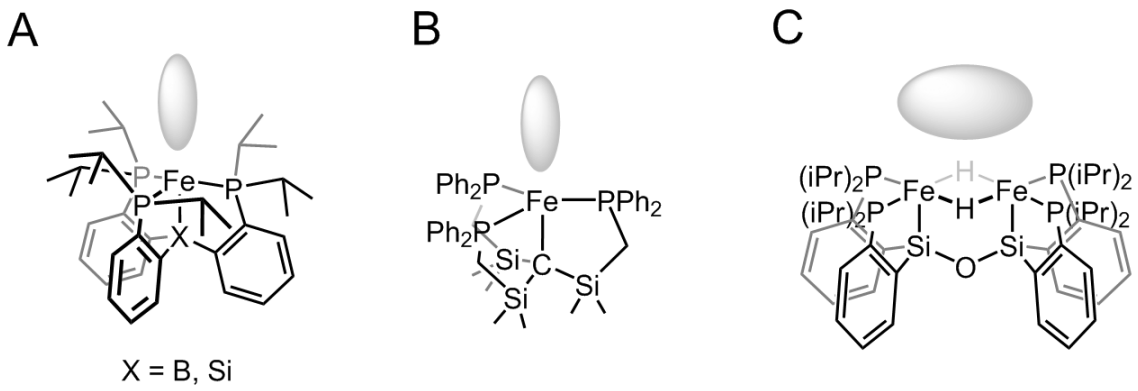

Figure 1.4. Fe platforms employed in this thesis to study Fe(N_2) species. (A) [SiP^{iPr}_3]Fe (X = Si) and (TPB)Fe (X = B) platforms with isopropyl (iPr) groups explicitly drawn. (B) [$C^{Si}P^{Ph}_3$]Fe platform with phenyl (Ph) groups abbreviated. (C) [SiP_2O]Fe_2 platform with isopropyl groups abbreviated. Gray spheres represent open coordination sites that permit the binding of diatomic substrates, such as N_2, CO, and CN.

Since Fe only poorly activates N_2, we reasoned that any resulting Fe(N_xH_y) species generated from such reactions might be unstable, and therefore the use of specialized

methods of preparation and characterization may be required. Prior to the work described in this thesis, very little was known about the details, or even possibility, of H-atom addition to Fe(N_2) units. Specifically, well-defined reactivity of Fe(N_2) species with proton sources, such as HCl (Figure 1.1) was essentially unreported.[10] As we discovered, the Fe(N_xH_y) complexes studied within are found to be *exceedingly* sensitive to air and moisture and decompose at low temperatures. In certain cases, these species rapidly decompose at temperatures of less than -100 ^oC! A suite of non-classical spectroscopic methods amenable to these extreme reaction conditions, such as Electron Paramagnetic Resonance (EPR) and ^{57}Fe Mössbauer spectroscopy, are extensively employed to characterize the Fe products. Through these and other techniques we establish that suitable Fe platforms can support the sequential addition of H-atom equivalents to bound N_2. These platforms generate significant quantities of NH_3, via a number of well-defined Fe(N_xH_y) intermediates.

1.5. Overview of Individual Chapters

In chapter two, a molecular Fe system is described that catalytically converts molecular N_2 into NH_3 at remarkably low temperatures (-78 ^oC). An intermediate Fe(N_xH_y) species was characterized that may be relevant to these catalytic mixtures, but was too reactive to isolate. These results highlight the importance of judicious ancillary ligand selection for high catalytic performance, as similar Fe-containing systems were found to be poor N_2 activation catalysts. We hypothesize that this system benefits from flexible interactions with its supporting ancillary ligand, allowing for facile interconversion of a variety of Fe(N_xH_y) species.

Chapter three details the synthesis and characterization of unique carbon-ligated Fe complexes that were found capable of binding and activating N_2. As shown in Figure 1.3, many of the Fe atoms of FeMoco are bound to an 'ancillary' carbon atom. Prior to the work described in this chapter, very few Fe compounds with both N_2 and an anionic carbon ligand in its immediate coordination sphere had been reported. Does the central C-atom of FeMoco play a more active role in facilitating N_2 binding and activation? The compounds discussed in this chapter indicate that anionic carbon ligands can play a hemi-labile role, serving to augment the electronic and geometric properties of an N_2-bound Fe atom.

In chapter four, we report the isolation and exhaustive characterization of an Fe(NNH_2) species derived from the protonation of an N_2-bound Fe complex. The stability of this molecule allowed for its crystallographic characterization and subsequent reactivity studies; both of which are unprecedented for molecules of this type. This compound displays unusual redox properties and upon one-electron reduction, significant radical character builds up on the Fe-bound nitrogen atom of the NNH_2 ligand. This property alludes to subsequent reactivity at this site and an Fe-bound hydrazine complex, Fe(NH_2NH_2), is obtained on warming solutions of this compound to ambient temperatures. This sequence of reactions defines a viable mechanism of proton-coupled N_2 reduction at a well-defined Fe site.

In chapter five, we report the proton coupled reduction of an Fe(CN) complex to methane (CH_4) and NH_3. This reaction is highly unusual and the only molecular systems that catalyze this reaction are nitrogenase and its isolated cofactor. Intermediate Fe(CNH_x) species, obtained upon stoichiometric protonation reactions, are remarkably stable, providing a means to study the intimate details of H-atom addition to these Fe(CN) species.

These results are broadly discussed in the context of H-atom addition to Fe(N_2) species, providing unparalleled insight into understanding the reactive nature of Fe(NNH_x) species. Furthermore, the comparative stability of Mo(NNH_x) complexes is explained by thermodynamic analyses.

The presence of multiple Fe atoms in FeMoco (Figure 1.3) may suggest that two or more metal centers may be required for efficient N_2 activation. In chapter six, we present a bimetallic, diiron (Fe_2) complex that was found capable of activating N_2 to produce significant amounts of NH_3. The Fe atoms of this complex are bridged by hydride ligands, which have been proposed to accumulate on the FeMoco during catalysis. In our system, these hydride ligands modulate the interaction of the two Fe sites leading to measurable differences in the ability of each site to bind N_2. These compounds were found to be redox-active, and upon one-electron reduction, their affinity for N_2 is increased a million-fold.

1.6. Cited References

1. Dobbin, L. *J. Chem. Ed.* **1935**. 12, 370-375
2. Weeks, M. E. *J. Chem. Ed.* **1932**. 9, 215-235.
3. (a) Howard, J. B.; Rees, D. C. *Chem. Rev.* **1996**. 96, 2965-2982. (b) Burgess, B. K.; Lowe, D. J. *Chem. Rev.* **1996**. 96, 2983-3011.
4. (a) Jia, H-P.; Quadrelli, A. *Chem. Soc. Rev.* **2014**. 43, 547-564. (b) Fryzuk, M. D.; Johnson, S. A. *Coord. Chem. Rev.* **2000**. 200, 379-409.
5. (a) Laplaza, C. E.; Cummins, C. C. *Science.* **1995**. 268, 861-863. (b) Pool, J. A.; Lobkovsky, E.; Chirik, P. J. *Nature*. **2004**. 527-530. (c) Rodrigues, M. M.; Bill, E.; Brennessel, W. W.; Holland, P. L. *Science*. **2011**. 334, 780-783.
6. (a) Allen, A. D.; Senoff, C. V. *J. Chem. Soc., Chem. Commun.* **1965**. 621-622. (b) Bottomley, F; Nyburg, S. C. *J. Chem. Soc., Chem. Commun.* **1966**. 897-898.
7. Chatt, J.; Richards, R. L.; Sanders, J. R.; Ferguson, J. E. *Nature*. **1969**. 221, 551-552.
8. (a) Chatt, J.; Heath, G. A.; Richards, R. L. *J. Chem. Soc., Chem. Commun.* **1972**. 1010-1011. (b) Heath, G. A.; Mason. R.; Thomas, K. M. *J. Amer. Chem. Soc.* **1974**. 96, 259-260.
9. (a) Chatt, J.; Pearman, A. J.; Richards, R. L. *Nature*. **1975**. 253, 39-40. (b) Anderson, S. N.; Fakley, M. E.; Richards, R. L.; Chatt, J. *J. Chem. Soc., Dalton Trans.* **1981**. 1973-1980.
10. Hazari, N. *Chem. Soc. Rev.* **2010**. 39, 4044-4056.
11. (a) Tolman, C. A. *J. Amer. Chem. Soc.* **1970**. 92, 2953-2956. (b) Tolman, C. A. *Chem. Rev.* **1977**. 77, 313-348.

12. (a) Yandulov, D. V.; Schrock, R. R. *J. Amer. Chem. Soc.* **2002**. 124, 6252-6253. (b) Yandulov, D. V.; Schrock, R. R. *Science*. **2003**. 301, 76-78. (c) Yandulov, D. V.; Schrock, R. R. *Inorg. Chem.* **2005**. 44, 1103-1117.

13. (a) Hu, Y.; Ribbe, M. W. *J.Biol. Inorg. Chem.* **2014**. 19, 731-736. (b) Seefeldt, L. C.; Hoffman, B. M.; Dean, D. R. *Annu. Rev. Biochem.* **2009**. *78*, 701-722. (c) Spatzal, T.; Perez, K. A.; Einsle, O.; Howard, J. B.; Rees, D.C. *Science.* **2014**. 345, 1620-1623. (d) Lancaster, K. M.; Roemelt, M.; Ettenhuber, P.; Hu, Y.; Ribbe, M. W.; Neese, F.; Bergmann, U.; DeBeer, S. *Science*. **2011**. 334, 974-977.

14. (a) Mankad, N. P.; Whited, M. T.; Peters, J. C. *Angew. Chem., Int. Ed.* **2007**. 46, 5768-5771. (b) Moret, M. E.; Peters, J. C. *Angew. Chem., Int. Ed.* **2011**. 50, 2063-2067. (c) Rittle, J.; McCrory, C. C. L.; Peters, J. C. *J. Amer. Chem. Soc.* **2014**. 136, 13853-13862.

15. Allred, A. L.; *J. Inorg. Nucl. Chem.* **1961**. 17, 215-221.

Chapter 2. Catalytic Conversion of Nitrogen to Ammonia by a Molecular Iron Model Complex

Reproduced in part with permission from:

Anderson, J. S.; Rittle, J.; Peters, J. C. *Nature.* **2013**. 501, 84-87.

and

Anderson, J. S.; Cutsail, G. E.; Rittle, J.; Connor, B. A.; Gunderson, W. A.; Zhang, L.; *et al. J. Amer. Chem. Soc.* **2015**. 137, 7803-7809.

2.1. Introduction

Nitrogen is fixed on a vast scale by the industrial Haber–Bosch process using a solid-state Fe catalyst at very high temperatures and pressures, and in nature by nitrogenase enzymes under ambient conditions.[1] These enzymes feature active-site cofactors rich in S and Fe (FeFe-cofactor), and can additionally contain a Mo (FeMo-cofactor; Fig. 2.1) or V (FeV-cofactor) site.[2,3]

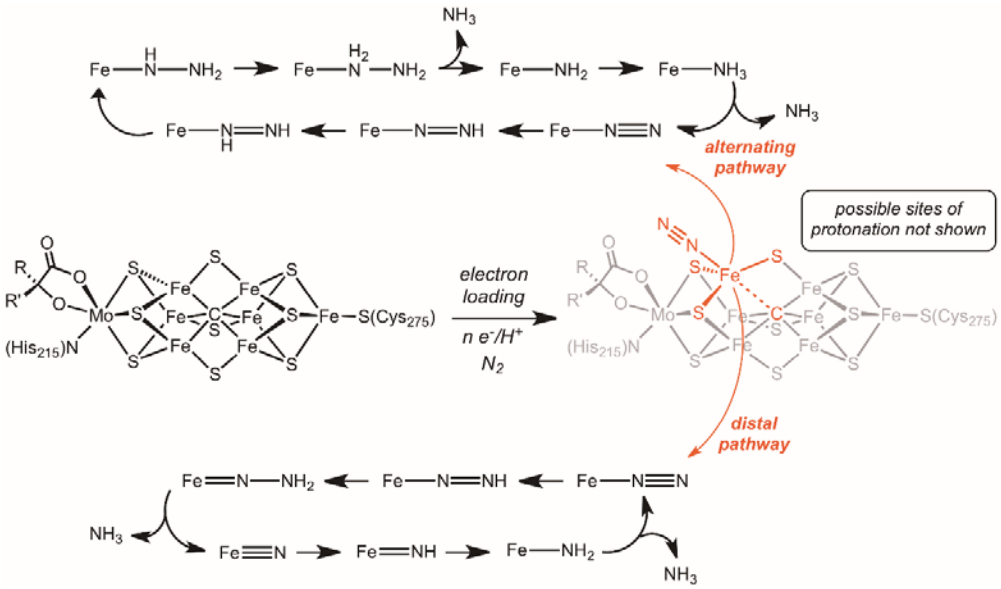

Figure 2.1. Chemical line representations of the FeMo-cofactor of nitrogenase. A schematic depiction of postulated N_2 binding and reduction at an Fe site by limiting alternating (top) and distal (bottom) mechanisms. The drawing emphasizes a possible hemilabile role for the interstitial C atom with respect to an Fe–N_2 binding site.

The intimate mechanism of biological nitrogen fixation is a topic that has fascinated chemists, biochemists, and biologists.[4–8] Synthetic chemists have searched for decades for well-defined complexes that can catalyze N_2 reduction to NH_3.[19–22]

Chatt's early work with low-valent Mo complexes provided a mechanistic outline for approaching this problem now commonly called the Chatt, or distal, mechanism, wherein a terminal nitride intermediate is generated on liberation of the first NH_3 equiv[9] (Fig. 2.1, bottom). Other mechanisms, including an 'alternating' scenario (Fig. 2.1, top), have also received attention.[6] So far, even modest catalysis of NH_3 production directly from N_2 by a well-defined model complex is still limited to the original tri(amido)amine Mo systems[10] and the more recently discovered phosphine-pincer Mo system.[11] Earlier work had established the electrochemical feasibility of an NH_3 production cycle with W.[19]

Synthetic efforts to establish whether one or more Fe sites can catalyze N_2 reduction to NH_3 in a well-defined model complex have progressed more slowly. For example, previous Fe–N_2 model complexes have not afforded more than ~10% of NH_3 per Fe equiv on treatment with proton sources.[7,23,24] Despite important advances,[24] which have most recently included reductive N_2 cleavage at Fe[22] and the catalytic reductive silylation of N_2 facilitated by unknown Fe species derived from Fe precursors such as ferrocene and iron pentacarbonyl,[25] the delivery of protons and electrons to N_2 to generate NH_3 catalytically at a synthetic Fe complex has remained an unsolved challenge. Here we show that a recently reported mononuclear Fe complex,[13,14] [(TPB)Fe(N_2)][Na(12-crown-4)$_2$] (TPB, tris(phosphine)borane; Fig. 2.2a), can catalyze the reduction of N_2 to NH_3 by protons and electrons in solution at −78 °C under one atmosphere of N_2.

2.2. Results

2.2.1. Stoichiometric NH_3 Generation from (TPB)Fe(N_2) Complexes

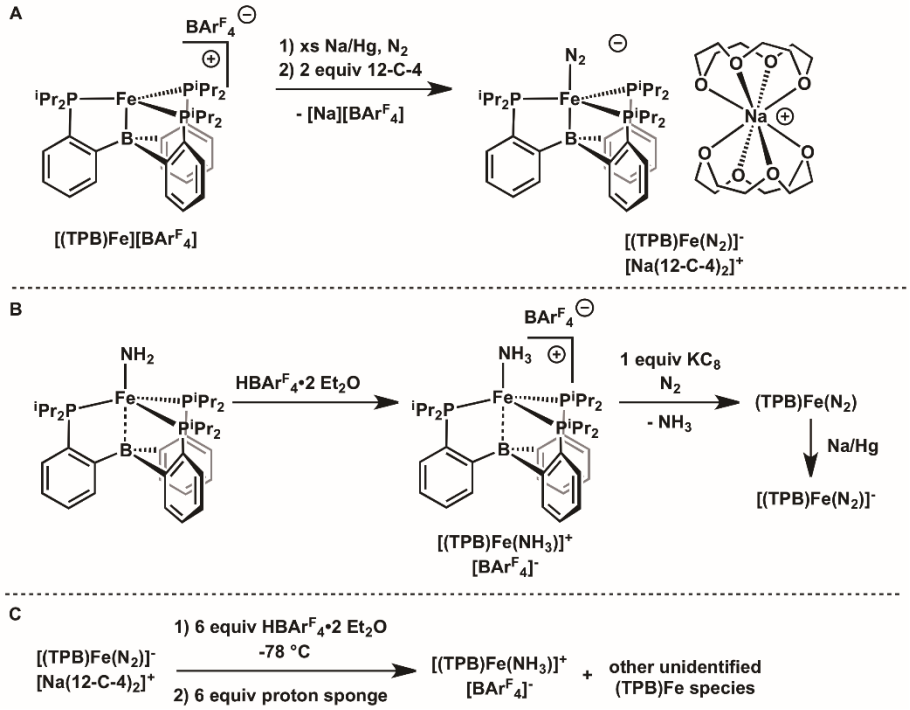

Figure 2.2. Stoichiometric (TPB)Fe–N_2 model reactions. (A) N_2 binding to [(TPB)Fe][BAr$^F_4$] under electron loading to generate [(TPB)Fe(N_2)][Na(12-crown-4)$_2$]. (B) Reductive protonolysis of (TPB)Fe(NH_2) to release NH_3 with concomitant N_2 uptake. (C) Generation of [(TPB)Fe(NH_3)][BAr$^F_4$] and other (TPB)Fe species on addition of acid to [(TPB)Fe(N_2)][Na(12-crown-4)$_2$] at low temperature, followed by warming and then addition of base.

The Fe center of the '(TPB)Fe' fragment readily binds N_2 as evidenced by the featured five-coordinate complex [(TPB)Fe(N_2)][Na(12-crown-4)$_2$] and the previously reported neutral N_2 adduct, (TPB)Fe(N_2).[14] The same scaffold also accommodates a variety of other nitrogenous ligands relevant to NH_3 generation,

including terminally bonded NH_2, NH_3, and N_2H_4 ligands.[15] Both the substrate-free complex, [(TPB)Fe][BAr^F_4] (where [BAr^F_4]$^-$ represents the weakly coordinating anion [B(3,5-$(CF_3)_2$-$C_6H_3)_4$]$^-$, and (TPB)Fe(N_2) may be reduced to [(TPB)Fe(N_2)][Na(12-crown-4)$_2$] by Na/Hg reduction under 1 atm N_2 followed by the addition of 2 equiv of 12-crown-4 to encapsulate the sodium cation (Fig. 2.2a).[15] Model reactions with silyl electrophiles have also shown that the Nβ of the coordinated N_2 ligand can be mono- or difunctionalized with concomitant lengthening of the Fe–B bond.13 Furthermore, starting from (TPB)Fe(NH_2), a reductive protonation sequence has been established (Fig. 2.2b) that liberates NH_3 and affords (TPB)Fe(N_2).[15] This reaction sequence demonstrates the synthetic viability of reductive release of NH_3 from an Fe–NH_2 intermediate with simultaneous uptake of N_2. In sum, the rich reaction chemistry of the (TPB)Fe scaffold with nitrogenous ligands motivated us to examine more closely the possibility that it might catalyze N_2 fixation.

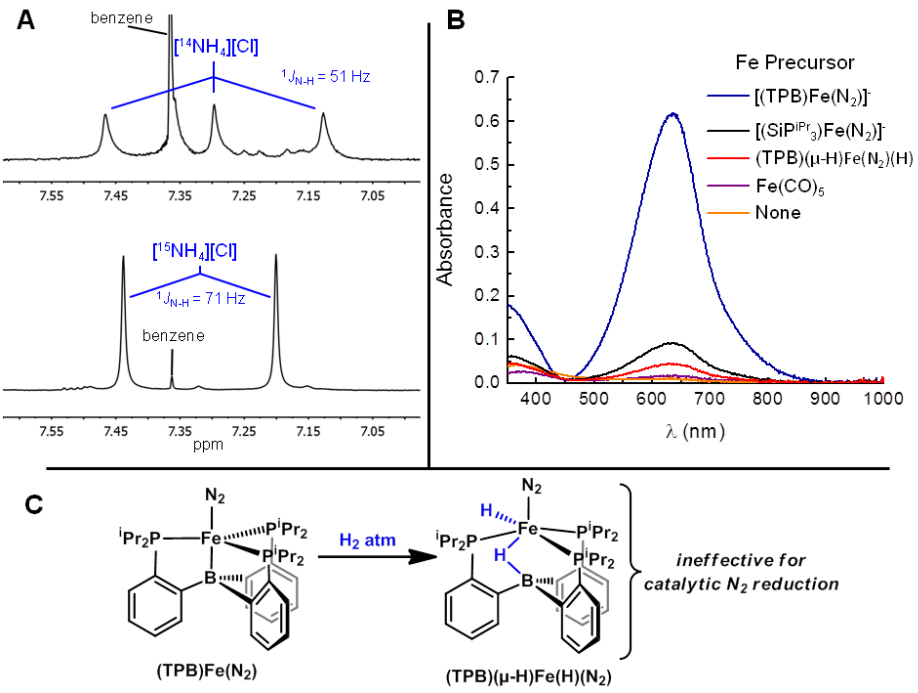

Figure 2.3. Spectral data for ammonia analysis, and catalyst poisoning. (A) ^{1}H NMR spectrum (300 MHz) of [^{14}NH$_4$][Cl] in DMSO-d_6 produced from a catalytic run under ^{14}N$_2$ (top) and of [^{15}NH$_4$][Cl] in DMSO-d_6 produced from an independent catalytic run under 1 atm ^{15}N$_2$. (B) Representative optical data for NH$_3$ product analysis using the indophenol method from catalytic runs using the standard conditions with the precursors indicated. (C) H$_2$ binds to (TPB)Fe(N$_2$) to generate (TPB)(μ-H)Fe(N$_2$)(H), which itself is ineffective for the catalytic generation of NH$_3$ from N$_2$ under the standard conditions.

To explore the possibility of N$_2$ reduction catalysis using this (TPB)Fe system, we tested several reductants (for example Na[naphthalenide], Mg(THF)$_3$(anthracene), Na/Hg and KC$_8$) and acids (for example HCl, trifluoromethanesulfonic acid and HBAr$^{F}_4$·2Et$_2$O) in a variety of solvents and solvent mixtures (for example THF,

dimethoxyethane, diethyl ether, and toluene). When carried out at −78 °C numerous reaction conditions showed unusually high yields of NH_3 relative to the number of Fe equivalents in the reaction vessel, and the combination of KC_8, $HBAr^F{}_4 \cdot 2Et_2O$ and Et_2O solvent enabled the catalytic generation of NH_3.

2.2.2. Catalytic NH_3 Generation from (TPB)Fe(N_2) Complexes

In a representative catalytic run, red [(TPB)Fe(N_2)][Na(12-crown-4)$_2$] was suspended in diethyl ether in a reaction vessel at −78 °C, followed by the sequential addition of excess acid and then excess reductant. Ammonia analysis followed the indophenol protocol and the independent identification of ammonium salts by ^{1}H NMR spectroscopy in DMSO by comparison with an authentic sample of [NH_4][Cl] (Fig. 2.3a). An experiment performed using the [(TPB)Fe($^{14}N_2$)][Na(12-crown-4)$_2$] catalyst under an $^{15}N_2$ atmosphere, followed by ^{1}H NMR analysis (Fig. 2.3a) of the

Table 2.1. Catalytic NH_3 Generation from N_2 Mediated by Fe Precursors.

Using standard catalytic conditions as described in the Chapter		
Entry	Fe precursor	NH_3 equiv./Fe†
1	[(TPB)Fe(N_2)][Na(12-Crown-4)$_2$]	7.0 ± 1‡
2	[(TPB)Fe][$BAr^F{}_4$]	6.2
3	[($SiP^{iPr}{}_3$)Fe(N_2)][Na(12-Crown-4)$_2$]	0.7
4	(TPB)(μ-H)Fe(N_2)(H)	0.5
5	$FeCl_2 \cdot 1.5THF$	<0.1
6	$FeCl_3$	<0.1
7	Cp_2Fe	<0.2
8	$Fe(CO)_5$	<0.1
9	None	<0.1
Variations on conditions using [(TPB)FeN_2][Na(12-Crown-4)$_2$]		
Entry	Variation	NH_3 equiv./Fe†
10	HOTf as acid	0.4
11	[Lutidinium][$BAr^F{}_4$] as acid	<0.1
12	HCl as acid	<0.1
13	$Cp^*{}_2Co$ as reductant	0.6
14	$Cp^*{}_2Cr$ as reductant	<0.2
15	K metal as reductant	0.4

† Unless noted otherwise, all yields are reported as an average of 4 runs.

‡Average of 16 runs.

volatile reaction products, confirmed the production of [$^{15}NH_4$][Cl], as expected, with only trace [$^{14}NH_4$][Cl]. This overall procedure has been repeated many times, and Table 2.1 includes data averaged from 16 independent runs (entry 1) in which yields were, on average, 7.0 equiv. NH_3 per Fe equiv. Using 7.0 equiv. NH_3 as the product stoichiometry, 44% of the added protons are reliably delivered to N_2 to produce NH_3. Our individual runs reached a maximum of 8.5 equiv. NH_3 per Fe equiv. under these standard conditions. [(TPB)Fe][BAr^F_4] is also an effective catalyst and afforded 6.2 ± 0.7 equiv. NH_3 per added Fe equiv. (Table 2.1, entry 2). For comparison, the Mo systems[10,11] have afforded between 7 and 12 equiv. NH_3 per Mo equiv. The current Fe system seems to be active at an unusually low temperature (−78 °C) but benefits from a strong reductant (KC_8). We do not yet know whether conditions can be found that will tolerate a milder reductant, for example by circumventing the need to generate the (TPB)Fe(N_2)$^-$ anion during catalysis.

Table 2.1 lists several sets of conditions (entries 10–15) other than the standard conditions described above that were studied. Several of these alternative conditions showed NH_3 generation, although not in catalytic or even in high yields. N_2H_4 was not detected as an additional product when using the standard catalytic protocol for NH_3 generation with [(TPB)Fe(N_2)][Na(12-crown-4)$_2$]. If 2 equiv. N_2H_4 (per Fe) are added to [(TPB)Fe(N_2)][Na(12-crown-4)$_2$] in diethyl ether and the mixture is then subjected to the standard catalytic conditions and work-up, only trace

N_2H_4 remains. This result suggests that if N_2H_4 is generated as an intermediate during catalysis, it would not likely be detectable on work-up and analysis. It is worth noting that $HBAr^F_4 \cdot 2Et_2O$ and KC_8 react in the absence of an Fe precursor, under the standard catalytic conditions at −78 °C, to generate H_2 but not NH_3 (>75% yield of H_2 after 40 min). That H_2 generation is kinetically feasible without the addition of an Fe precursor, and yet NH_3 can nonetheless be generated with the addition of [(TPB)Fe(N_2)][Na(12-crown-4)$_2$] or [(TPB)Fe][BAr^F_4], underscores the facility with which this Fe system mediates overall hydrogen-atom delivery to N_2.

2.2.3. NH_3 Production by Alternative Fe Pre-catalysts

To explore further whether a (TPB)Fe-containing precursor is needed to facilitate the overall catalysis, beyond the stoichiometric model reactions summarized above, we canvassed several Fe complexes under analogous conditions. Of most interest is the complex [(SiP^{iPr}_3)Fe(N_2)][Na(12-crown-4)$_2$], which is isostructural to [(TPB)Fe(N_2)][Na(12-crown-4)$_2$] but in which the B atom of TPB is replaced by a Si atom.[26] A central difference between (TPB)Fe and (SiP^{iPr}_3)Fe complexes is the far greater flexibility of the Fe–B bond by comparison with the Fe–Si bond that is positioned *trans* to the apical ligand.[13–15,26] Although some NH_3 generation was observed for [(SiP^{iPr}_3)Fe(N_2)][Na(12-crown-4)$_2$] when subjected to the standard catalytic reaction conditions described above, sub-stoichiometric yields of NH_3 relative to Fe were obtained (0.7 ± 0.5 equiv. NH_3 per Fe equiv.; Table 2.1, entry 3). We also conducted additional control experiments under the standard catalytic conditions with $FeCl_2 \cdot 1.5THF$, $FeCl_3$, Cp_2Fe[25] and $Fe(CO)_5$[25] (entries 5–8) and found that only trace amounts of NH_3 (<0.2 equiv. in all cases on average; four runs) were

produced by these Fe precursors.[27] The known phosphine-supported Fe(0)–N_2 complex Fe(depe)$_2$(N_2)[28] was also subjected to the standard conditions and afforded sub-stoichiometric yields of NH_3 per Fe equiv.

In separate work, the addition of an atmosphere of H_2 to (TPB)Fe(N_2) was shown to generate (TPB)(μ-H)Fe(N_2)(H) as a stable product[29] (Fig. 2.3c). We thus suspected that catalyst poisoning might occur in part through the formation of (TPB)(μ-H)Fe(N_2)(H) under the catalytic reaction conditions. In accord with this idea, when [(TPB)Fe(N_2)][Na(12-crown-4)$_2$] was exposed to 10 equiv. $HBAr^F{}_4 \cdot 2Et_2O$ and 12 equiv. KC_8 at low temperature, infrared and ^{31}P NMR analysis of the resulting mixture showed the presence of (TPB)(μ-H)Fe(N_2)(H) through its signature spectroscopic features[29] (30% of total Fe by ^{31}P NMR integration). (TPB)(μ-H)Fe(N_2)(H) is stable for short periods to both $HBAr^F{}_4 \cdot 2Et_2O$ and also KC_8 in Et_2O at room temperature, and when subjected to the standard catalytic conditions for NH_3 production liberates only 0.5 ± 0.1 equiv. NH_3 per Fe equiv. (Table 2.1, entry 4, Fig. 2.3b).

2.2.4. Characterization of an Fe=N=NH_2 Complex Relevant to NH_3 Production

Many mechanistic questions arise from the present Fe catalyst system. Although all of the model complexes relevant to the (TPB)Fe(N_xH_y) system are mononuclear, we cannot exclude the possibility of bimolecular reaction intermediates. More generally, we do not know whether the N_2 reduction catalysis proceeds along a distal pathway via a terminal nitride intermediate, such as (TPB)Fe(N) or (TPB)Fe(N)$^+$, via intermediates along an alternating pathway, such as (TPB)Fe–NH–NH_2 or (TPB)Fe–NH_2–NH_2^+, or via some hybrid pathway. We were

therefore interested in characterizing the Fe(N_xH_y) species derived from protonation of [(TPB)Fe(N_2)][Na(12-crown-4)$_2$].

The addition of acid at low temperature to [(TPB)Fe(N_2)][Na(12-crown-4)$_2$] results in a new S = 1/2 Fe species. EPR, ENDOR, Mössbauer, and EXAFS analysis unequivocally assign this new species as [(TPB)Fe≡N-NH_2][$BAr^F{}_{24}$], a doubly protonated hydrazido(2-) complex featuring an Fe-to-N triple bond. This unstable species offers strong evidence that the first steps in Fe-mediated nitrogen reduction by [(TPB)Fe(N_2)][Na(12-crown-4)$_2$] can proceed along a distal or 'Chatt-type' pathway.

Mixing of pre-catalyst [(TPB)Fe(N_2)][Na(12-crown-4)$_2$] and 10 equivalents of $HBAr^F{}_4 \cdot 2\ Et_2O$ in thawing 2-MeTHF solutions at -135 °C (Scheme 2.2) resulted in the disappearance of the dark red color characteristic of [(TPB)Fe(N_2)][Na(12-crown-4)$_2$] and the formation of a brown-yellow solution. Analysis by CW X-band EPR indicates complete consumption of [(TPB)Fe(N_2)][Na(12-crown-4)$_2$] and appearance of an intense and highly rhombic *S* = 1/2 signal at 77 K (Figure 2.4B) assigned to [(TPB)Fe≡N-NH_2][$BAr^F{}_{24}$] (vide infra). If stoichiometric acid is added to [(TPB)Fe(N_2)][Na(12-crown-4)$_2$] at low temperature, rapid oxidation to neutral *S* = 1 (TPB)Fe(N_2) with loss of 0.5 equiv H_2 occurs instead (Eqn 2.1) and no EPR signal is observed.

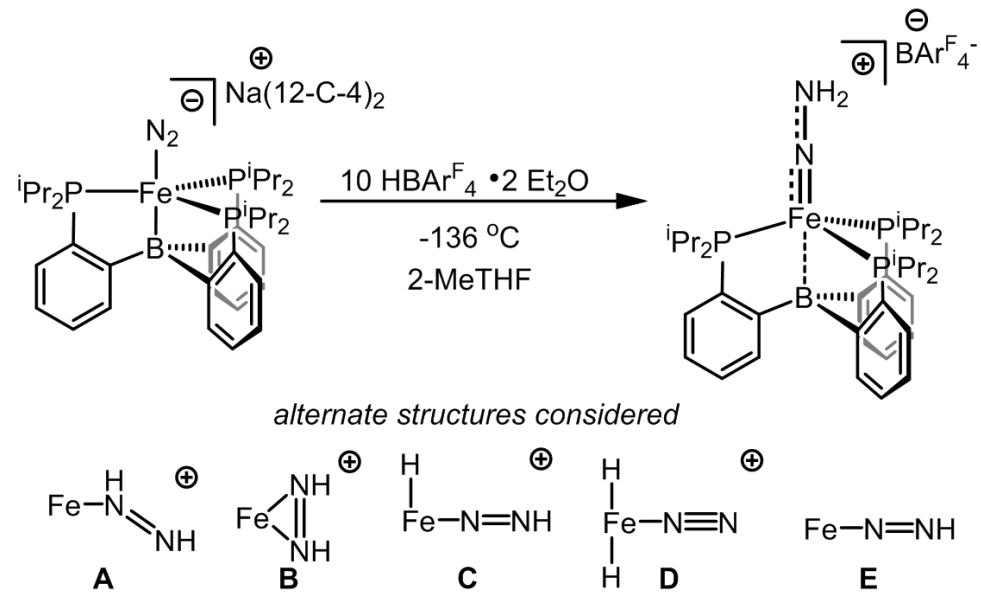

Scheme 2.2. Stoichiometric protonation of [(TPB)Fe(N_2)][Na(12-crown-4)$_2$].

The signal for [(TPB)Fe≡N-NH_2][$BAr^F{}_{24}$] can be generated, albeit at lower intensity, with as little as 2 equivalents of acid. EPR spectra collected at 10 K reveal weak, complicated signals at low field that are consistent with one or more S = 3/2 species, in addition to those stemming from [(TPB)Fe≡N-NH_2][$BAr^F{}_{24}$]. The EPR spectrum of [(TPB)Fe≡N-NH_2][$BAr^F{}_{24}$] is distinct from the more axial signature of [(TPB)Fe(N_2)][Na(12-crown-4)$_2$] (Figure 2.4A) and it is also distinct from the previously reported EPR spectrum for (TPB)Fe(N_2SiMe_3).[13] The fact that structurally characterized (TPB)Fe(N_2SiMe_3), a model complex of the as yet uncharacterized complex '(TPB)FeN_2H', displays a more axial EPR spectrum than that of [(TPB)Fe≡N-NH_2][$BAr^F{}_{24}$] suggests that [(TPB)Fe≡N-NH_2][$BAr^F{}_{24}$] is electronically distinct from (TPB)Fe(N_2SiMe_3), and by extension is unlikely to be the parent (TPB)FeN_2H diazenido species (candidate **E** in Scheme 2.2). Moreover, the

requirement of ≥ 2 equiv of acid strongly suggests an alternative structure to **E**. ENDOR and ESEEM analyses of these EPR signatures are consistent with this hypothesis, and these data collected on [(TPB)Fe≡N-NH_2][BAr^F_4] can be fit to a model that contains two protons on the beta-N-atom of the N_2-derived ligand.

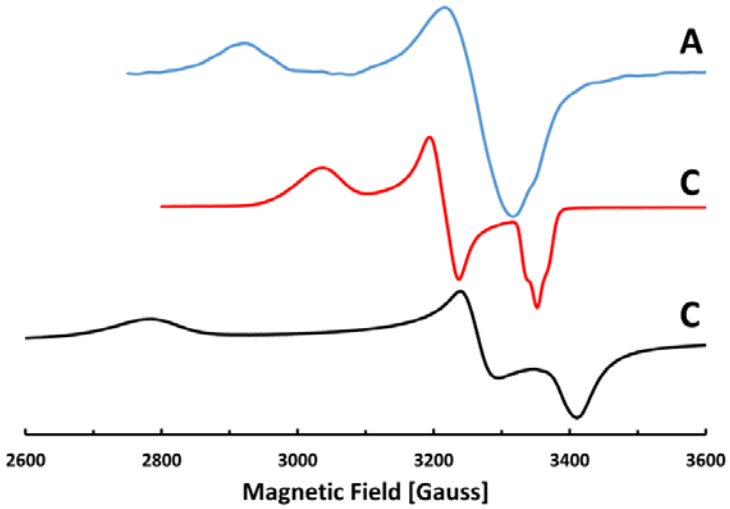

Figure 2.4. (A) 77 K X-Band EPR of [(TPB)Fe(N_2)][Na(12-crown-4)$_2$]. (B) 77 K X-Band EPR after addition of 10 equivalents of $HBAr^F_4 \cdot 2\ Et_2O$ to [(TPB)Fe(N_2)][Na(12-crown-4)$_2$] to generate [(TPB)Fe≡N-NH_2][BAr^F_4]. The fit to the spectrum is shown in red with the following parameters: g_1 = 2.221, g_2 = 2.090, g_3 = 2.006, A^{H1} = 56 MHz, A^{H2} = 38 MHz. (C) 77 K X-Band EPR of [(TPB)Fe≡N-Ad][BAr^F_4].

Metal hydrazido(2-) complexes typically display substantial M-N multiple bonding, and are thus electronically similar to metal imido complexes.[4,7,18] The cationic imido complex [(TPB)Fe≡N-Ad][BAr^F_4] is isoelectronic to [(TPB)Fe≡N-NH_2][BAr^F_4], but was found to be thermally stable. This imido complex

has been crystallographically characterized and also displays a rhombic EPR spectrum (Figure 2.4C). The rhombic EPR spectrum of [(TPB)Fe≡N-Ad][BAr^F_4] reflects a pseudotetrahedral iron center resulting from Fe-B elongation (Fe-B = 2.770 Å) as the iron center slips above the P_3 plane. This geometry should place an unpaired spin in a relatively nonbonding orbital arising from a $^2E_{dx}2_{-y}2_{,xy}$ state. This electronic structure is reminiscent of the ferrocenium cation and is also similar to various low spin L_3Fe^{III}≡NR imides that have been previously described.[7,18]

$$[(TPB)Fe(N_2)]^{(-)} + HBAr^F_4 \cdot 2\ Et_2O \rightarrow (TPB)Fe(N_2) + 0.5\ H_2 \qquad \textbf{Eqn 2.1}$$

Fe-N triply bonded species supported by the TPB scaffold include [(TPB)Fe≡N-Ad][BAr^F_4] (this work) and (TPB)Fe≡N(4-OMe-Ph)[14] and they have characteristically short Fe-N distances of 1.660 Å and 1.668 Å, respectively. Structural data was sought for [(TPB)Fe≡N-NH_2][BAr^F_4] to probe for an anticipated short *Fe*≡*N*-NH_2 triple bond. Iron K-edge X-ray extended X-ray absorption fine structure (EXAFS) data were collected and allowed for the observation of Fe-ligand distances in solution samples. These data were collected on frozen preparations of [(TPB)Fe≡N-NH_2][BAr^F_4] in 2-MeTHF and are shown in Figure 2.5. Three pronounced peaks are observed in the Fourier transform spectrum, including one peak much shorter than expected for a singly-bonded Fe-N pair. Indeed, the EXAFS and Fourier transform spectra can be best fit with a short Fe-N distance of 1.64 Å and two Fe-P distances of 2.28 Å and 2.42 Å in a 1:2 ratio. Additionally, an Fe-B scattering path may be included in the fit at a distance of 2.67 Å, although convolution from the Fe-P scatterers makes this assignment tentative.

The observation of two different Fe-P scatterers for a complex with three phosphorous ligands can arise from various scenarios. If one assumes the EXAFS sample contains a single species, the two distances observed could correspond to a distorted structure with two long Fe-P distances and one short distance. A similar, though substantially lessened, distortion is observed in [(TPB)Fe≡N-Ad][BAr^F_4]. Alternatively, these disparate distances could arise from the presence of more than one species in the sample, each with a narrow distribution of Fe-P distances, a scenario that seems more likely based on the observation that oxidation of [(TPB)Fe(N_2)][Na(12-crown-4)$_2$] by acid is a competing side reaction (Eqn 2.1). The apparently larger than expected Debye-Waller factor in the fitting for the Fe-N scatterer would thereby result from the presence of multiple species; the short and long Fe-P distances correspond closely to those observed in low-spin and high-spin iron complexes of the (TPB) ligand scaffold, which display variable Fe-N distances.[13,14,15]

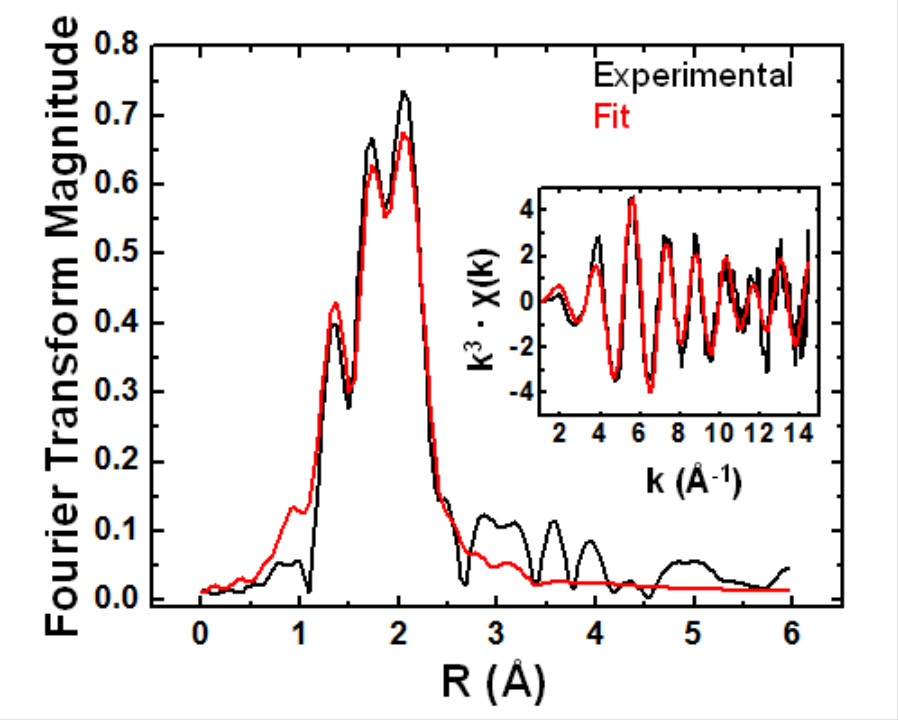

Figure 2.5. Fourier transform of the EXAFS data. Inset shows the EXAFS oscillations. Scatterer distances (Å) are Fe-P = 2.279(5), Fe-P = 2.422(3), Fe-N = 1.639(7), and Fe-B = 2.674(12).

2.2.5. ^{57}Fe Mössbauer Studies of Preparations Containing an Fe=N=NH$_2$

To further probe the possible presence of multiple iron species generated on addition of acid to [(TPB)Fe(N_2)][Na(12-crown-4)$_2$] at low temperature, ^{57}Fe Mössbauer analysis of in-situ generated solutions of [(TPB)^{57}Fe≡N-NH_2][$BAr^F{}_4$] was undertaken. In brief, an ethereal solution of ^{57}Fe-enriched [(TPB)^{57}Fe(N_2)][Na(Et_2O)$_x$] was frozen and then layered with excess $HBAr^F{}_4 \cdot 2$ Et_2O in Et_2O that was then also frozen. This sample was then allowed to thaw at -110 °C and then mechanically stirred. The sample was then transferred to a Mossbauer cup chilled at 80 K for analysis. The Mössbauer spectrum of a representative sample

is shown in Figure 2.6 and suggests the presence of three primary iron-containing species. Similarly prepared samples showed the same features but in variable ratios and hence caution must be exercised with respect to extrapolating the population of $[(TPB)Fe{\equiv}N\text{-}NH_2][BAr^F{}_4]$ in this specific Mössbauer sample relative to the population of $[(TPB)Fe{\equiv}N\text{-}NH_2][BAr^F{}_4]$ in independently prepared EXAFS and EPR samples. Nevertheless, the Mössbauer data confirm the presence of three (TPB)Fe-species generated under relatively comparable conditions. One of the three species present in the representative Mössbauer spectrum shown (~20% of total Fe present) can be definitively assigned as the neutral $S = 1$ Fe-N_2 adduct (TPB)Fe(N_2) by comparison with an authentic sample ($\delta = 0.56$ mm/s; $\Delta E_Q = 3.34$ mm/s). The two other species are present in approximately equal amounts (40% each of total Fe) and simulations suggest one of them to be the previously characterized $S = 3/2$ cation $[(TPB)Fe]^+$ ($\delta = 0.75$ mm/s; $\Delta E_Q = 2.55$ mm/s) or a similar related complex. The third species is presumed therefore to be the iron hydrazido(2-) cation $[(TPB)Fe{\equiv}N\text{-}NH_2][BAr^F{}_4]$ ($\delta = 0.35$ mm/s; $\Delta E_Q = 1.02$ mm/s).

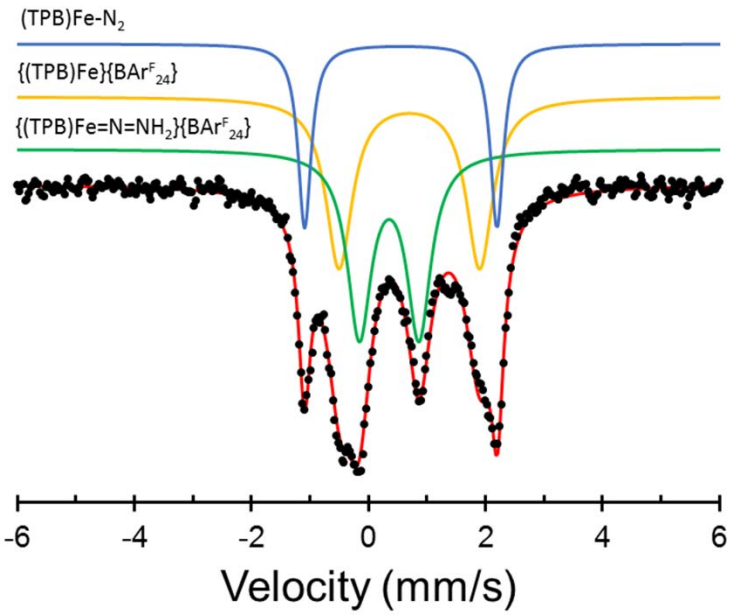

Figure 2.6. ^{57}Fe Mössbauer spectrum obtained by the reaction of ^{57}Fe-enriched [(TPB)^{57}Fe(N_2)][Na(Et_2O)$_x$] with 5 equiv $HBAr^F_4 \cdot 2\ Et_2O$ in Et_2O at -110 ^oC. Data is shown as black dots and the combined simulation is shown in red. The individual sub-spectra representing the different components are offset for clarity. The spectrum was collected at 77 K in the presence of a 50 mT applied magnetic field.

The presence of (TPB)Fe(N_2) and [(TPB)Fe]$^+$ in the sample is consistent with our previous finding that the addition of $HBAr^F_4 \cdot 2\ Et_2O$ to [(TPB)Fe(N_2)][Na(12-crown-4)$_2$] leads to net oxidation of the complex to generate (TPB)Fe(N_2) via loss of H_2 (*vide supra*). Likewise, (TPB)Fe(N_2) can be further oxidized to [(TPB)Fe]$^+$ via addition of $HBAr^F_4 \cdot 2\ Et_2O$. In sum, the available Mössbauer data predicts that variously prepared samples of [(TPB)Fe≡N-NH_2][BAr^F_4] may contain (TPB)Fe(N_2) and [(TPB)Fe]$^+$ and this fact helps explain the additional P scatterer in the EXAFS data, as well as the larger than expected Fe-N Debye-Waller factor. As (TPB)Fe(N_2) is

EPR-silent, and $[(TPB)Fe]^+$ does not display EPR signals at 77 K, this Fe speciation is fully consistent with the clean spectrum observed by CW X-band EPR (Figure 2.4B).

While $[(TPB)Fe{\equiv}N\text{-}NH_2][BAr^F{}_4]$ has been generated herein with excess acid at -135 °C in 2-MeTHF, N_2 reduction catalysis by $[(TPB)Fe(N_2)][Na(12\text{-crown-}4)_2]$ is carried out at -78 °C in Et_2O by addition of acid followed by addition of reductant. As such, we sought to determine whether $[(TPB)Fe{\equiv}N\text{-}NH_2][BAr^F{}_4]$ could be detected in mixtures more relevant to catalysis, prior to the addition of the reductant. X-band EPR spectra of solutions prepared from the addition of acid to $[(TPB)Fe(N_2)][Na(12\text{-crown-}4)_2]$ at either -136 °C in 2-MeTHF or at -78 °C in Et_2O indicate that $[(TPB)Fe{\equiv}N\text{-}NH_2][BAr^F{}_4]$ is present in both preparations. Furthermore, upon warming to -40 °C or to room temperature, both preparations show the growth of $S = 3/2$ signals concomitant with the decay of the signals of $[(TPB)Fe{\equiv}N\text{-}NH_2][BAr^F{}_4]$. The identity of these $S = 3/2$ species is hard to determine due to convolution of the quartet signals. One such $S = 3/2$ species, $[(TPB)Fe(NH_3)]^+$, has been definitively assigned by inspection of the ^1H NMR spectrum of a similarly-prepared mixture following warming to room temperature (vide supra). Therefore, $[(TPB)Fe{\equiv}N\text{-}NH_2][BAr^F{}_4]$ decays at least in part to $[(TPB)Fe(NH_3)]^+$ upon warming even without exogenous reductant.

2.3. Conclusion

The general absence of a functional, catalytic Fe model system over the past few decades has often led to an emphasis on Mo[30] as a plausible site of N_2 uptake and reduction at the most widely studied FeMo-cofactor. Although this may yet prove to be true, recent spectroscopic and biochemical evidence has sharpened the focus on an

Fe center as the N_2-binding site.[12] The results reported here establish that it is possible to catalyze the conversion of N_2 to NH_3 by protons and electrons using a well-defined mononuclear Fe–N_2 complex, and suggests the possibility that a single Fe-binding site of the cofactor could in principle mediate N_2 reduction catalysis.[18] To achieve this catalytic behaviour, geometric flexibility at the Fe–N_2 binding site would be beneficial as it would stabilize N_xH_y intermediates with different electronic structure requirements. Such geometric and redox flexibility, under the local three-fold symmetry presented by an Fe center, its three neighbouring sulfides, and the interstitial light atom of the FeMo-cofactor,[16,17] may at least in part be achieved by attributing a hemilabile role to the interstitial C atom (Fig. 2.1). Such a role could serve to expose an initial Fe–N_2 binding site by Fe–C elongation. Subsequent modulation of the Fe–C interaction and hence the local Fe geometry as a function of the N_2 reduction state would enable the Fe center to stabilize the various N_xH_y intermediates along a pathway to NH_3. Although it is inherently speculative, this hypothesis is rooted in the functional (TPB)Fe catalysis discussed here, along with the types of (TPB)Fe complex and stoichiometric transformation described previously for this scaffold.[13–15]

2.4. Experimental Section

General Considerations

[(TPB)Fe(N_2)][Na(12-crown-4)$_2$],[14] [(TPB)Fe][$BAr^F{}_{24}$],[15] (TPB)(μ-H)Fe(H)(N_2),[29] [Lutidinium][BArF4],[31] $HBAr^F4\cdot 2Et_2O$,[32] [($SiP^{iPr}{}_3$)Fe(N_2)][Na(12-crown-4)$_2$],[26] $FeCl_2\cdot(THF)_{1.5}$,[33] KC_8,[34],[(TPB)Fe(NH_3)][$BAr^F{}_{24}$],[15] [(TPB)Fe(N_2H_4)][$BAr^F{}_4$],[15] and Fe(depe)$_2N_2$[28] were prepared according to literature

procedures. Labelled $^{15}N_2$ (98% purity) was obtained from Cambridge Isotope Laboratories. Solvents used for catalytic runs were additionally stirred for more than 2 h over Na/K alloy and then filtered before use, as well as undergoing standard sparging (Ar gas) and passage through an activated alumina column.

Ammonia Quantification

A Schlenk tube was charged with HCl (3 ml of a 2.0 M solution in Et_2O, 6 mmol). Reaction mixtures were vacuum-transferred into this collection flask. Residual solid in the reaction vessel was treated with a solution of [Na][O-t-Bu] (40 mg, 0.4 mmol) in 1,2-dimethoxyethane (1 ml) and sealed. The resulting suspension was stirred for 10 min before all volatiles were again vacuum-transferred into the collection flask. After completion of the vacuum transfer, the flask was sealed and warmed to room temperature. Solvent was removed *in vacuo* and the remaining residue was dissolved in H_2O (1 ml). An aliquot of this solution (20 or 40 μL) was then analyzed for the presence of NH_3 (trapped as $[NH_4][Cl]$) by the indophenol method.[35] Quantification was performed with ultraviolet–visible spectroscopy by analyzing absorbance at 635 nm. Runs with small absorbance levels (<0.02 absorbance units) suffer from a large degree of error due to a small signal-to-noise ratio. Catalytic runs that used a 40 μL aliquot are denoted with an asterisk, accounting for larger relative absorbances.

Standard Catalytic Protocol

We suspended $[(TPB)Fe(N_2)][Na(12\text{-crown-}4)_2]$ (2 mg, 0.002 mmol) in Et_2O (0.5 ml) in a 20-ml scintillation vial equipped with a stir bar. This suspension was vigorously stirred and cooled to −78 °C in a cold well inside the glove box. A similarly

cooled solution of $HBAr^F_4 \cdot 2Et_2O$ (93 mg, 0.092 mmol) in Et_2O (1.5 ml) was added to the suspension in one portion with rapid stirring. Any remaining acid was dissolved in cold Et_2O (0.25 ml) and added subsequently. The reaction mixture turned light yellow-orange and became homogeneous upon addition of acid, and the resulting solution was stirred for 5 minutes before being transferred into a pre-cooled Schlenk tube equipped with a stir bar. The original reaction vial was washed with cold Et_2O (0.25 ml) and was subsequently transferred to the Schlenk tube. Solid KC_8 (15 mg, 0.100 mmol) was suspended in cold Et_2O (0.75 ml) and added drop by drop to the rapidly stirred solution in the Schlenk tube, which was then tightly sealed. The reaction was stirred for 40 minutes at −78 °C before being warmed to room temperature and stirred for a further 15 minutes.

EPR Spectroscopy

EPR X-band spectra were obtained on a Bruker EMX spectrometer with the aid of Bruker Win-EPR software suite version 3.0. The spectrometer was equipped with a rectangular cavity which operated in the TE_{102} mode. Temperature control was achieved with the use of an Oxford continuous-flow helium cryostat (temperature range 3.6 – 300 K). All spectra were recorded at 9.37 GHz with a microwave power of 20 mW, a modulation amplitude of 4 G, and a modulation frequency of 100 kHz. Simulations were performed with the EasySpin software suite.[36] EPR samples were thawed to -40 °C with a dry ice/acetonitrile slush bath for a time period of 5 minutes or alternately thawed to room temperature for a time period of 5 minutes.

XAS Measurements

XAS measurements were conducted at the Stanford Synchrotron Radiation Laboratory (SSRL) with the SPEAR 3 storage ring containing 500 mA at 3.0 GeV. Fe K-edge data were collected on the beamline 9-3 operating with a wiggler field of 2 T and employing a Si(220) double-crystal monochromator. Beamline 9-3 is equipped with a rhodium-coated vertical collimating mirror upstream of the monochromator and a bent-cylindrical focusing mirror (also rhodium-coated) downstream of the monochromator. Harmonic rejection was accomplished by setting the energy cutoff angle of the mirrors to 10 keV. The incident and transmitted X-ray intensities were monitored using Nitrogen-filled ionization chambers, and X-ray absorption was measured as the Fe Kα fluorescence excitation spectrum using an array of 100 Canberra germanium detectors. During data collection, samples were maintained at a temperature of approximately 10 K using an Oxford instruments liquid helium flow cryostat. The energy was calibrated by reference to the absorption of a standard iron metal foil measured simultaneously with each scan, assuming a lowest energy inflection point of the iron foil to be 7111.2 eV.

The extended x-ray absorption fine structure (EXAFS) oscillations $\chi(k)$ were quantitatively analyzed by curve-fitting using the EXAFSPAK suite of computer programs.[37] Ab-initio theoretical phase and amplitude functions were calculated using the program FEFF version 8.[38] No smoothing, filtering, or related operations were performed on the data.

2.5. Cited References

1. Smil, V. *Enriching the Earth*. **2001**. MIT Press.
2. Burgess, B. K.; Lowe, D. J. *Chem. Rev*. **1996**. 96, 2983–3012.
3. Eady, R. R. *Chem. Rev*. **1996**. 96, 3013–3030.</jrn>
4. Howard, J. B.; Rees, D. C. *Proc. Natl Acad. Sci.* **2006**. 103, 17088–17093.
5. Schwarz, G.; Mendel, R. R.; Ribbe, M. W. *Nature.* **2009**. 460, 839–847.
6. Seefeldt, L.; Hoffman, B. M.; Dean, D. R. *Annu. Rev. Biochem*. **2009**. 78, 701–722.
7. Peters, J. C.; Mehn, M. P. in *Bio-organometallic Approaches to Nitrogen Fixation Chemistry Activation of Small Molecules*. **2006**. Wiley-VCH. 81–119.
8. Shilov, A.; Denisov, N.; Efimov, O.; Shuvalov, N.; Shuvalova, N.; Shilova, A. *Nature*. **1971**. 231, 460–461.
9. Chatt, J.; Dilworth, J. R.; Richards, R. L. *Chem. Rev*. **1978**. 78, 589–625.
10. Yandulov, D. V.; Schrock, R. R. *Science*. **2003**. 301, 76–78.
11. Arashiba, A.; Miyake, Y.; Nishibayashi, Y. *Nature Chem*. **2011**. 3, 120–125.
12. Hoffman, B. M.; Dean, D. R.; Seefeldt, L. C. *Acc. Chem. Res*. **2009**. 42, 609–619.
13. Moret, M.-E.; Peters, J. C. *J. Am. Chem. Soc.* **2011**. 133, 18118–18121.
14. Moret, M.-E.; Peters, J. C. *Angew. Chem. Int. Ed.* **2011**. 50, 2063–2067.
15. Anderson, J. A.; Moret, M.-E.; Peters, J. C. *J. Am. Chem. Soc.* **2013**. 135, 534–537.
16. Lancaster, K. M.; Roemelt, M.; Ettenhuber, P.; Hu, Y.; Ribbe, M. W.; Neese, F.; Bergmann, U.; DeBeer, S. *Science.* **2011**. 334, 974–977.
17. Spatzal, T. M.; Aksoyoglu, M.; Zhang, L.; Andrade, S. L. A.; Schleicher, E.; Weber, S.; Rees, D. C.; Einsle, O. *Science.* **2011**. 334, 940.
18. Hendrich, M. P; Gunderson, W.; Behan, R. K.; Green, M. T.; Mehn, M. P.; Betley, T. A.; Lu, C. C.; Peters, J. C. *Proc. Natl Acad. Sci*. **2006**. 103, 17107–17112.

19. Pickett, C. J.; Talarmin, J. *Nature*. **1985**. 317, 652–653.

20. Fryzuk, M. D.; Love, J. B.; Rettig, S. J.; Young, V. G. *Science.* **1997**. 275, 1445–1447.

21. Pool, J. A.; Lobkovsky, E.; Chirik, P. J. *Nature*. **2004**. 427, 527–530.

22. Rodriguez, M. M.; Bill, E.; Brennessel, W. W.; Holland, P. L. *Science*. **2011**. 334, 780–783.

23. Hills, A.; Hughes, D. L.; Jimenez-Tenorio, M.; Leigh, J.; Rowley, A. T. *J. Chem. Soc. Dalton Trans*. **1993**. 25, 3041–3049.

24. Crossland, J. L.; Tyler, D. R. *Coord. Chem. Rev.* **2011**. 255, 949–974.

25. Yuki, M.; Tanaka, H.; Miyake, Y.; Yoshizawa, K.; Nishibayashi, Y. *Nature Commun.* **2012**. 3, 1254.

26. Lee, Y. H.; Mankad, N. P.; Peters, J. C. *Nature Chem*. **2010**. 2, 558–565.

27. Bell, L. G.; Brintzinger, H. H. *J. Am. Chem. Soc.* **1970**. 92, 4464–4465.

28. Hall, D. A.; Leigh, G. J. *J. Chem. Soc. Dalton Trans*. **1996**. 3539–3541.

29. Fong, H.; Moret, M.-E.; Lee, Y. H.; Peters, J. C. *Organometallics.* **2013.** 32, 3053–3062.

30. Schrock, R. R. *Nature Chem*. **2011.** 3, 95–96.

31. Yandulov, D. V.; Schrock, R. R. *J. Am. Chem. Soc*. **2002**. 124, 6252–6253.

32. Brookhart, M.; Grant, B.; Volpe, A. F., Jr. *Organometallics.* **1992**. 11, 3920–3922.

33. Kern, R. J. *J. Inorg. Nucl. Chem.* **1962**. 24, 1105–1109.

34. Weitz, I. S.; Rabinovitz, M. *J. Chem. Soc. Perkin Trans.* **1993**. 1, 117–120.

35. Weatherburn, M. W. *Anal. Chem.* **1967**. 39, 971-974.

36. Stoll, S.; Schweiger, A. *J. Magn. Reson.* **2006**, *178*, 42-55.

37. George, G.N., http://ssrl.slac.stanford.edu/exafspak.html.

38. Ankudinov, A. L.; Ravel, B.; Rehr, J. J.; Conradson, S. D. *Physical Review B.* **1998**, *58*, 7565-7576.

Chapter 3. Fe-N_2/CO Complexes that Model a Possible Role for the Interstitial C-atom of FeMoco.

3.1. Introduction

MoFe-nitrogenase catalyzes the fascinating but poorly understood conversion of nitrogen to ammonia at its iron-molybdenum cofactor, FeMoco.[1,2] The core of the FeMoco was originally thought to be vacant.[3] Later work on *Azotobacter vinelandii* indicated the presence of a light interstitial atom coordinated to six central, so-called "belt" Fe atoms.[4] Crystallographic and spectroscopic studies,[5,6] in addition to studies mapping the biosynthetic pathway of C-atom incorporation,[7,8] establish that carbon is the interstitial atom, as shown in Figure 3.1.

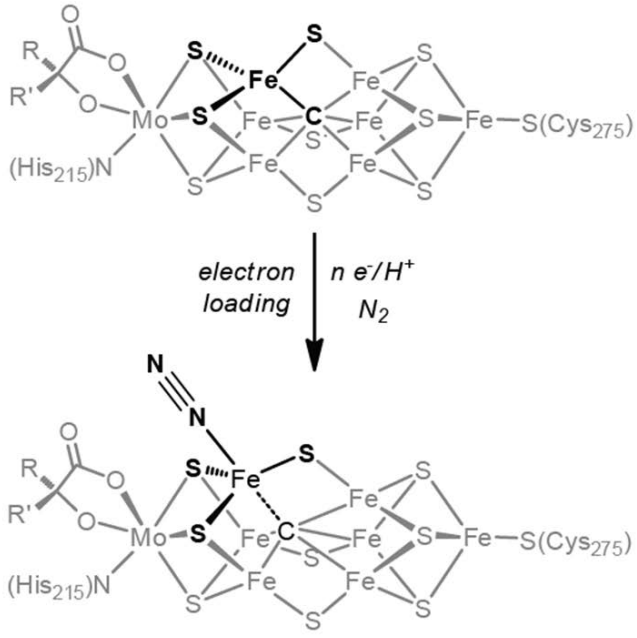

Figure 3.1. A hypothetical N_2-binding event at a belt iron in FeMoco illustrating a proposed Fe-C elongation. The degree and positions of protonation are unknown under electron loading but the inorganic sulfides are plausible candidate positions.

While the site(s) of N_2 reduction remain(s) uncertain, a body of evidence that includes biochemical, spectroscopic, and computational studies on FeMoco point to a

belt Fe center as a plausible candidate.[2,9,10,11,12,13] Under a scenario in which N_2 binds terminally to one of the belt Fe centers, the N_2 ligand would initially be coordinated *trans* to the interstitial C-atom (Figure 3.1).[10] This hypothesis calls for model complexes that depict such an arrangement to explore factors that might govern substrate coordination and subsequent reduction. Structurally faithful models of the FeMoco that include an Fe_6C unit stabilized by sulfide or other sulfur-based ligands present a formidable synthetic challenge.[14] Moreover, N_2 coordination to synthetic iron-sulfur clusters has yet to be established.[15] Model complexes featuring a single Fe site with a C-atom anchor positioned *trans* to an N_2 binding site are unknown, but would provide a useful tool to evaluate how an Fe-C interaction might respond to N_2 binding and the Fe redox state. Specifically, model compounds of this nature may facilitate the evaluation of theoretical[10] and spectroscopic studies[16] on FeMoco that suggest a single, flexible Fe-C interaction is observed under turnover conditions.

It is in this context that we have pursued mononuclear Fe complexes supported by tripodal, tetradentate ligands featuring three phosphine donor arms tethered to a tertiary alkyl anchor. Although a number of such ligands featuring a central C-atom have been described[17,18,19] we reasoned that an alkyl ligand featuring only electropositive substituents adjacent to the C-atom anchor would provide a crude model of the interstitial carbide of the FeMoco and permit a high degree of ionic bonding to a single Fe-N_2 binding site. To achieve this goal, the C-atom anchor of the auxiliary ligand described is surrounded by three electropositive Si centers, in addition to the Fe site. This model system successfully coordinates N_2 *trans* to the C-atom anchor and shows how the local Fe geometry and the Fe-C interaction respond as a function of

such binding. Using CO instead of N_2, this Fe system also presents an opportunity to study the Fe-C interaction as a function of the Fe redox state. As described below, unusually long Fe-C distances can be accessed that are consistent with a much higher degree of ionic character at the Fe-C interaction than would be anticipated for a prototypical Fe alkyl.

3.2. Results

3.2.1. Metalation of $[C^{Si}P^{Ph}_3]H$

A suitable ligand framework for the present study, whose lithium salt was previously reported by Avent and coworkers,[20] is $(Ph_2PCH_2SiMe_2)_3CH$. This ligand, denoted herein as $[C^{Si}P^{Ph}_3]$ (**3.1**) and depicted in Figure 3.2, features a tri(silyl)methyl core tethered to three soft phosphines. Given that the interstitial carbide in FeMoco is surrounded by six electropositive Fe centers, we speculated that an Fe_5C subunit would stabilize partial negative charge on the C-atom as the sixth Fe-C interaction elongates upon reduction/N_2 binding. Relative to methane, the three electropositive silyl substituents of the tri(silyl)methane subunit reduce the basicity of the central carbon ($pK_a[(Me_3Si)_3CH]$: 36.8 in THF) by approximately 20 orders of magnitude.[21,22] We anticipated that the tempered basicity of the tri(silyl)methyl subunit would translate to a flexible Fe-C interaction.

Benzyl potassium was found to effect rapid and quantitative deprotonation of **3.1** as evidenced by ^{31}P NMR spectroscopy. Subsequent salt metathesis with $FeCl_2$ (Scheme 3.1) afforded the Fe halide complex $[C^{Si}P^{Ph}_3]Fe(Cl)$ (**3.2**) as a pale-yellow powder. Complex **3.2** exhibits broad ^1H NMR signatures from δ = -1 to 30 ppm and a solution magnetic moment of 4.9 μ_B (CD_2Cl_2, 22 ^oC), consistent with an S = 2 species.

This high spin state is noteworthy given the strong ligand field strength that might be expected from a prototypical tris(phosphine)alkyl donor set and attests to the comparatively weak ligand field arising from the [$C^{Si}P^{Ph}_3$] ligand. The structurally similar and isoelectronic 5-coordinate Fe(II) chloride complexes supported by the tris(phosphine)silyl ligand [SiP^R_3][23,24] display an intermediate S = 1 spin state as a consequence of the strong and highly-covalent Fe-Si bond. Zero-field Mössbauer data collected on **3.2** is consistent with its S = 2 assignment (25).

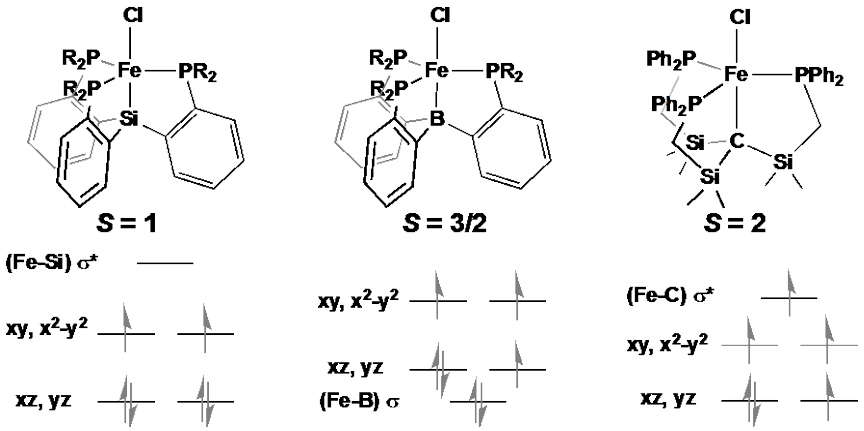

Figure 3.2. Qualitative d-orbital splitting diagrams reflective of experimentally measured ground spin states for Fe-Cl complexes of [SiP^R_3], [TP^RB], and [$C^{Si}P^{Ph}_3$].

The X-ray crystal structure of **3.2** exhibits a rigorously trigonal bipyramidal geometry about the Fe center as exemplified by a τ_5 value of 1.00, and confirms ligation of the tri(silyl)methyl carbon to Fe, albeit at a notably long distance (2.263(2) Å). Reported high-spin Fe(II)-C_{alkyl} distances range from 2.00 to 2.21 Å.[26] The Fe-P distances are also quite long (2.5696(3) Å) as a consequence of the high spin state. The Fe atom is displaced just 0.006 Å from the plane defined by the three crystallographically equivalent phosphine ligands. This structure contrasts the

geometric parameters imposed by phenylene- and ethylene-linked tetradentate tripodal phosphine ligands that force the metal center to protrude out of the equatorial phosphine plane away from the apical ligand.[27,28] The incorporation of Si and P atoms in each 5-membered chelate ring of [$C^{Si}P^{Ph}_3$] likely provides the flexibility required for the metal complex to adopt such a symmetric geometry.

3.2.2. Reduction and N_2 Coordination Chemistry

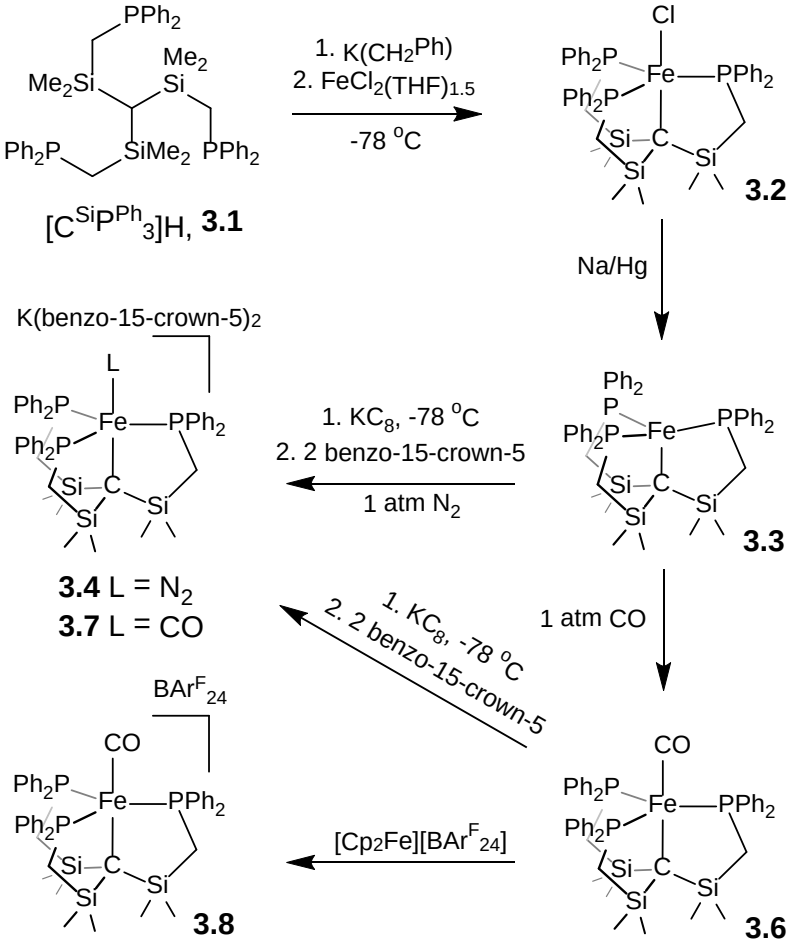

Scheme 3.1. Synthesis of iron complexes supported by a tris(phosphino)alkyl ([$C^{Si}P^{Ph}_3$]H, 1) tripod.

Na/Hg amalgam reduction of **3.2** under an N_2 atmosphere affords the Fe(I) complex **3.3** (Scheme 3.1) as a brick red powder. The absence of IR absorptions in the range of 2100 to 1700 cm^{-1} (KBr pellet) rules out terminal N_2 coordination to a mononuclear Fe center in the solid state. A solution magnetic moment of 3.8 μ_B (C_6D_6) is observed at room temperature, and EPR measurements of **3.3** recorded at 10 K display g values of 4.66, 3.77, and 2.02 arising from $M_s = 1/2$ transitions, in addition to a feature at g = 6.22 stemming from transitions within the $M_s = 3/2$ manifold, consistent with a quartet ground state.[29] The solid-state structure of **3.3** (Figure 3.3) reveals a four-coordinate Fe complex. The Fe center is positioned below the P_3-plane defined by the phosphine donors (d(Fe-P_{plane}): 0.322 Å), and displays a shortened Fe-C interaction (2.153(2) Å, Figure 3.3). The local Fe geometry is intermediate between tetrahedral and trigonal monopyramidal ($\tau_4 = 0.68$).[30] Its geometry is topologically similar, although more pyramidalized, to that of the belt Fe centers in the structurally-characterized resting state of FeMoco ($\tau_4 = 0.46$), where the Fe atoms are directed towards the interstitial C-atom and resting below the S_3-plane of the surrounding sulfides.[5]

In hopes of preparing an Fe-N_2 complex supported by this ligand scaffold, we investigated the chemical reduction of **3.3**. Compound **3.3** cleanly reacts with KC_8, and encapsulation of the potassium countercation of the resulting species with two equivalents of benzo-15-crown-5 affords a dark purple powder displaying an intense IR ν(NN) absorption at 1927 cm^{-1} for the terminal Fe-N_2 complex {K(benzo-15-crown-5)$_2$}{[$C^{Si}P^{Ph}_3$]FeN_2}, **3.4**. A Toepler pump analysis of **3.4** analyzed for 0.9 molar equivalents of N_2 upon oxidation with ferrocenium trifluoromethanesulfonate in THF. Complex **3.4** is diamagnetic in THF solution (^{31}P NMR, d_8-THF, δ = 43.6 ppm). Its

solid-state crystal structure (Figure 3.3) confirms axial coordination of N_2 *trans* to the Fe-C_{alkyl} donor and shows that, upon coordination, the Fe center slides back into the P_3-plane of the phosphines (d(Fe-P_{plane}): 0.012 Å) and away from the apical carbon (d(Fe-C) = 2.254(5) Å).

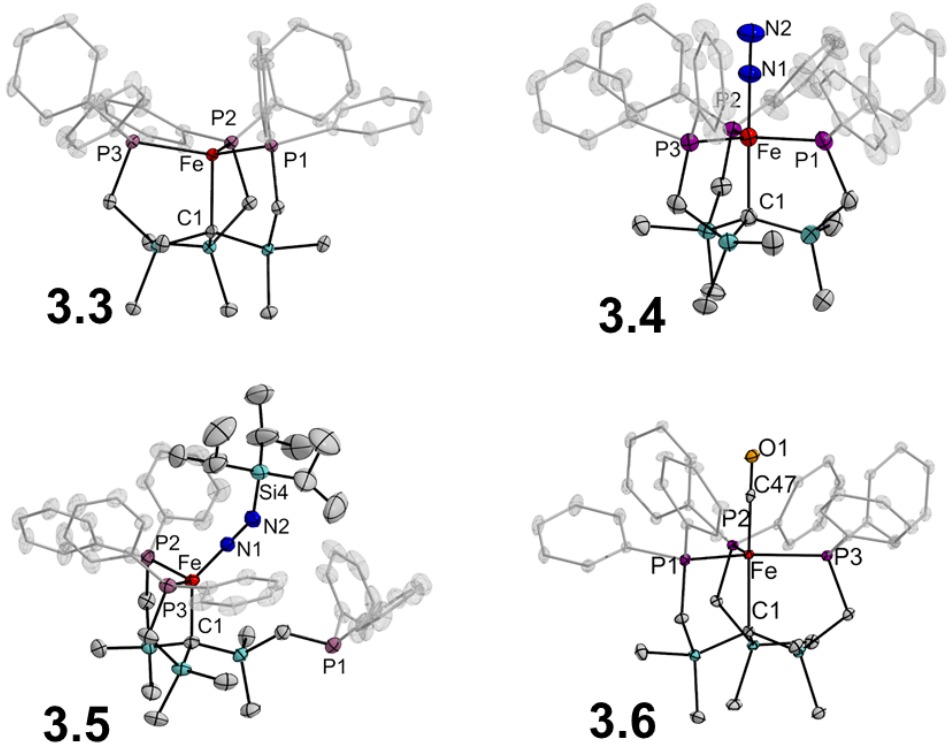

Figure 3.3. X-ray crystal structures of **3.3**, **3.4**, **3.5**, and **3.6** with thermal ellipsoids set at 50%. For clarity, hydrogen atoms and solvent molecules have been removed. The phenyl ring bonds and thermal ellipsoids have been rendered transparent to aid in visualization of the inner coordination sphere of iron. The {K(benzo-15-crown-5)2} countercation of **3.4** has been removed for clarity.

Silylation of M-N_2 complexes has been used to gauge the reactivity of the bound N_2 ligand towards electrophiles[31,32,33] and we canvassed related reactions with

the present system. Whereas trimethylsilyl chloride reacts productively with {[SiP^{iPr}_3]Fe(N_2)}$^-$ to afford [SiP^{iPr}_3]Fe(N_2SiMe_3),[24] the Fe-$N_2^{(-)}$, **3.4** required the use of a highly encumbered and electrophilic silylating agent, triisopropylsilyl trifluoromethanesulfonate, to furnish a tractable diazenido product **3.5**. Its characterization data include a ν(NN) vibration at 1719 cm^{-1}, a solution magnetic moment of 2.75 μ_B (C_6D_6, 23 °C), and a broad room temperature ^{1}H NMR spectrum. Upon cooling to -80 °C in d_8-toluene, the ^{1}H NMR signals of **3.5** resolve into 14 distinguishable resonances between δ = 32 and -10 ppm, suggestive of an unsymmetrical paramagnetic species. An XRD study of **3.5** (Figure 3.3) accounts for this asymmetry at low temperature by verifying silylation of the beta N-atom of the N_2 ligand and also establishing a dechelated phosphine donor arm. The Fe geometry of **3.5** in the solid state is thus four-coordinate with a short Fe-C_{alkyl} distance of 2.116(1) Å, an Fe-N(1) distance of 1.713(1) Å, and two Fe-P bonds with a Fe-P_{avg} of 2.332 Å. The diazenido ligand features an elongated N(1) – N(2) bond length of 1.203(2) Å, consistent with substantial activation of the N-N triple bond in free N_2 (1.098 Å). Notably, the diazenido ligand is severely bent at N(2) with a contracted N(1)-N(2)-Si(4) angle of 135.11°. Similar bond angles found in (TPB)Fe(N_2SiMe_3)[33] and [SiP^{iPr}_3]Fe(N_2SiMe_3)[24] of 166.64° and 165.55°, respectively, are far more obtuse. Dechelation of the phosphine donor arm in **3.5** can be attributed, at least in part, to the necessity of installing such a large silyl substituent.

3.2.3. Redox Series of Fe(CO) Complexes

To discern how the Fe-C_{alkyl} interaction changes as a function of Fe redox state, we pursued structurally related carbonyl complexes of the [$C^{Si}P^{Ph}_3$]Fe scaffold. The advantage of the {[$C^{Si}P^{Ph}_3$]Fe(CO)}^{n} (n = +1, 0, -1) series of complexes is that a five-coordinate, approximately trigonal bipyramidal geometry is conserved across the three redox states with the strong-field CO ligand remaining bound at the axial position. This is in contrast with the situation when N_2 is the terminally bonded ligand, where probing the Fe-C_{alkyl} interaction across redox states is not possible due to a variety of other geometric and electronic changes, most notably the loss of the N_2 ligand that occurs upon oxidation of **3.4** to **3.3**.

Table 3.1. Selected Bond Distances for [$C^{Si}P^{Ph}_3$]Fe- and [SiP^{iPr}_3]Fe-(CO) Compounds

	d(Fe-C_{alkyl}/Si)[a]	d(Fe-C_{CO})[a]	d(Fe-P_{avg})[a]
3.8	2.138(2)	1.786(2)	2.387
3.6	2.236[b]	1.734[b]	2.301[b]
3.7	2.303[c]	1.738[c]	2.177[c]
3.11[d]	2.3245(7)	1.842(3)	2.390
3.9[d]	2.2942(4)	1.769(2)	2.276
3.10[d]	2.2586(8)	1.732(3)	2.186

[a] Distance in Å. [b] Average from three molecules. [c] Average from two molecules. [d] Reference 34.

Preparation of this series (Scheme 3.1) begins with exposure of **3.3** to 1 atm of CO to afford the neutral and vacuum-stable carbonyl adduct [$C^{Si}P^{Ph}_3$]Fe(CO) **3.6**. Carbonyl **3.6** features a solid-state IR absorption at 1865 cm^{-1} and is obtained in near-quantitative yield as a red-orange powder. Its room temperature solution magnetic moment is 1.5 μ_B (C_6D_6) and it features a nearly axial signal in the frozen glass EPR spectrum (10 K, 2-MeTHF). An XRD study indicated the presence of three independent molecules of **3.6** in the unit cell and confirms coordination of CO to a distorted ($\tau_{5,\,avg}$ = 0.68) trigonal bipyramidal Fe center (Figure 4). The presence of nonlinear C_{alkyl}–Fe–$C_{carbonyl}$ angles (174.38° to 178.13°) and marked asymmetry of the three P-Fe-P angles in the pseudo-equatorial plane likely results from the orbitally-degenerate, Jahn-Teller active doublet ground state.

Reversible oxidation and reduction events at -0.62 and -1.85 V, respectively, are observed for **3.6**. Reduction of **3.6** with KC_8 in THF and subsequent encapsulation of the potassium ion with two equivalents of benzo-15-crown-5 furnishes **3.7** as a dark purple powder. An IR absorption at 1782 cm^{-1} (KBr pellet) is indicative of considerable π-backbonding from the formally Fe(0) center into the C-O π^* manifold, but to a lesser extent than in the isoelectronic complex {Na(12-crown-4)$_2$}{[SiP^{iPr}_3]Fe(CO)} (ν(CO) = 1757 cm^{-1}) in which isopropyl instead of phenyl substituents decorate the phosphines.[34] Compound **3.7** is diamagnetic in solution and gives rise to a single resonance in the ^{31}P NMR spectrum. Inspection of the XRD structure of **3.7** indicates a substantial lengthening of the Fe-C_{alkyl} distance upon reduction (Table 3.1, Figure 3.3) to greater than 2.30 Å. To the best of our knowledge, *this is the longest mononuclear Fe-C_{alkyl}*

distance yet reported. This fact highlights the effect of placing a flexible Fe-C subunit *trans* to a substrate binding site.

Oxidation of **3.6** with $[Cp_2Fe][B(3,5\text{-}(CF_3)_2\text{-}C_6H_3)_4]$ leads to a lightening of the solution and growth of an intense ν(CO) stretch at 1937 cm^{-1} arising from the cationic carbonyl complex $\{[C^{Si}P^{Ph}_3]Fe(CO)\}\{B(3,5\text{-}(CF_3)_2\text{-}C_6H_3)_4\}$, **3.8**. The solution magnetic moment for **3.8** (2.79 μ_B, CD_2Cl_2, 20 °C) is consistent with the expected $S = 1$ spin state. Attempts to obtain combustion analysis data on **3.8** were frustrated by its instability to vacuum. An XRD study confirms its structure and reveals a mildly-distorted ($\tau_5 = 0.85$) trigonal bipyramidal Fe center with an Fe-C_{alkyl} bond distance of 2.138(2) Å that is appreciably shortened by comparison to that in **3.6** and **3.7**. Cationic **3.8** displays the shortest Fe-C_{alkyl} bond of all of the five-coordinate compounds detailed herein.

Mössbauer measurements on compounds **3.6** – **3.8** were undertaken and indicate a decrease in the isomer shift (δ) upon reduction from **3.8** to **3.6** to **3.7**. This behavior is consistent with increasing back-donation into unfilled ligand orbitals upon reduction, and thus a higher degree of overall metal-ligand covalency and an increase in the s-electron density at Fe.[35] The δ range observed for compounds **3.6** – **3.8** (0.13 mm/s) is small and suggests that reduction occurs in diffuse orbitals, minimizing the electronic impact at the Fe nucleus. The trend (or lack thereof) in quadrupole splittings (ΔE_Q) is not readily explained.

3.2.4. Comparisons Between $[C^{Si}P^{Ph}_3]Fe$ and $[SiP^{iPr}_3]Fe$

The substantial reductive *elongation* of the Fe-C_{alkyl} bond that is observed across the $\{[C^{Si}P^{Ph}_3]Fe(CO)\}^n$ (n = +1, 0, -1) series from **3.8** to **3.6** to **3.7** differs

markedly from the corresponding and isoelectronic series $\{[SiP^{iPr}_3]Fe(CO)\}^n$ (n = +1, 0, -1), for which modest *shortening* of the Fe-Si distances is instead observed upon reduction.[34] On reduction, the Fe-Si bond in $\{[SiP^{iPr}_3]Fe(CO)\}\{B(3,5\text{-}(CF_3)_2\text{-}C_6H_3)_4\}$ (**3.11**) contracts from 2.3245(7) Å to 2.2942(4) Å in $[SiP^{iPr}_3]Fe(CO)$ (**3.9**), to 2.2586(8) Å in $[SiP^{iPr}_3]Fe(CO)\text{-}Na(THF)_3$ (**3.10**) (Table 1).

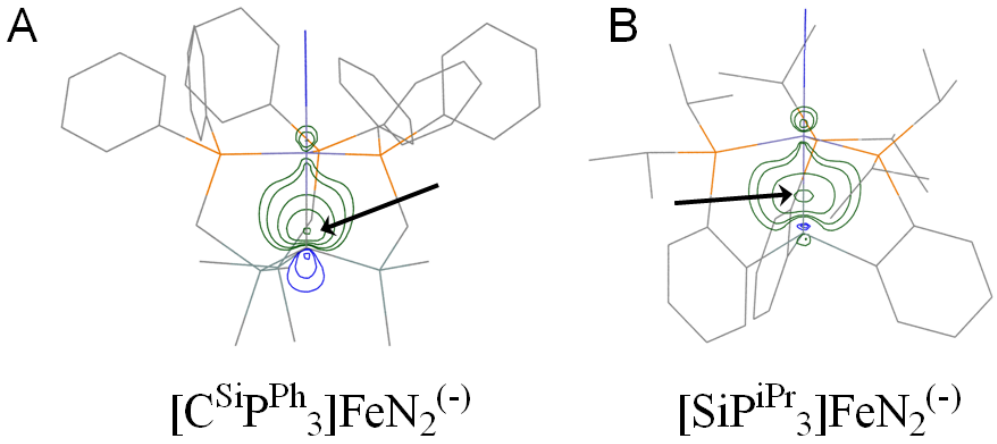

Figure 3.4. (A) Isocontour plot of the Fe-C_{alkyl} sigma bond of **3.7**, and (B) the Fe-Si sigma bond of $[SiP^{iPr}_3]FeN_2^{(-)}$ located from NBO analyses. Arrows indicate the location of highest electron density.

In compounds **6** – **8**, the Fe-$C_{carbonyl}$ and Fe-P bonds generally shorten on reduction just as they do in **9** – **11**. In contrast, the Fe-C_{alkyl} bond *lengthens* (Table 3.1), and in **7** the central C-atom forms three short Si-C_{alkyl} bonds (Table 3.2). The stability of tri(silyl)methyl carbanions has been attributed to the electropositive nature of Si and negative hyperconjugation into adjacent Si-C σ* orbitals,[36,37] resulting in shorter Si-C_{alkyl} bonds. Thus, the structural data suggests the formation of a partially dissociated tri(silyl)methyl carbanion subunit upon reduction.

The Fe-C_{alkyl} distances in anions **3.4** and **3.7** are remarkably long, especially given that they are diamagnetic species. To aid in explaining this observation, we undertook Natural Bond Orbital (NBO) analyses of these species as a means to compare the localized Fe-C bonding orbitals. NBO has been used previously to assess the differences in M-CH_3 and M-CF_3 bonding.[38] Single-point calculations were performed at the B3LYP/6-31++G** level of theory using the crystallographically determined coordinates of the heavy atoms in **3.4** and **3.7**. The calculations locate a highly polarized σ-interaction between the C_{alkyl} anchor of the [$C^{Si}P^{Ph}_3$] ligand and the coordinated Fe (Figure 5). The disparate contributions from Fe (22.7% **3.4**, 22.7% **3.7**) and C (77.3% **3.4**, 77.3% **3.7**) suggest a comparatively ionic σ bond (Figure 3.4, Table 3.2) that is atypical of a mid-to-late transition metal alkyl.[39] The dative Fe-P σ bonds display an average of 22.9 and 25.7% Fe-character in **3.4** and **3.7**, respectively. The degree of ionicity in the Fe-C_{alkyl} interaction contrasts that calculated for the Fe-Si bond in the isoelectronic [SiP^{iPr}_3]FeN_2^- complex, which displays a far more covalent σ bond between the Ar_3Si subunit and the Fe center (53.3 % Fe- and 46.7% Si-character).

3.2.5. NBO Computations on $(CO)_4Fe(X)^{(-)}$ (X = CH_3 , $C(SiH_3)_3$)

To better understand the unusually long bond lengths found in **3.4** and **3.7**, we turned to computations on simple alkyl- and tri(silyl)alkyl-ligated five-coordinate Fe complexes. The structure of the *S* = 0, trigonal bipyramidal Fe alkyl complex [$(Ph_3P)_2N$][$(CO)_4$Fe-(*n*-propyl)] has been previously determined and it features an *n*-propyl ligand in an axial site with a long Fe-C_{alkyl} distance of 2.20(2) Å. As such, it was of interest to us to compare the Fe-C_{alkyl} bonding of complexes of this framework to that in **3.4** and **3.7**. To this end, NBO analyses were performed on the hypothetical

model complexes $(CO)_4Fe\text{-}CH_3^{(-)}$ **3.12** and $(CO)_4Fe\text{-}C(SiH_3)_3^{(-)}$ **3.13**. The optimized geometries of **3.12** and **3.13** also display axial coordination of the alkyl substituent to Fe. Notable structural parameters and NBO-derived data for **3.12** and **3.13** are tabulated in Table 3.2. Collectively, the data suggest that the introduction of electropositive Si substituents on carbon in **3.13** markedly increases the $Fe\text{-}C_{alkyl}$ bond length relative to **3.12**. The uncorrected energy of the $Fe\text{-}C_{alkyl}$ interaction in **3.13** is substantially less than that of **3.12**.[38] In addition, the $Fe\text{-}C_{alkyl}$ σ-bond displays a decrease in covalency upon introduction of the electropositive Si substituents. As reflected in the natural charges (Table 3.2) and seen in the electrostatic potential maps of **3.12** and **3.13** (Figure 3.5), the polarizable Si substituents in **3.13** display a comparatively positive charge, leading to a compensatory increase in the natural negative charge on the C_{alkyl} carbon relative to **3.12**. As the Fe sites also display negative natural charges, an enhanced electrostatic repulsion between Fe and C_{alkyl} may explain the long $Fe\text{-}C_{alkyl}$ distances in **3.13**, as well as **3.4** and **3.7**, relative to **3.12**. Finally, an augmented electrostatic attraction between the electropositive Si atoms and the highly charged central carbon explains the short $Si\text{-}C_{alkyl}$ bonds in **3.13**, 3.**4**, and 3.**7** (the Si-C bond length in Me_4Si is 1.875(2) Å).[40,41]

Table 3.2. Selected Results from Natural Bond Orbital Analysis

Complex	d(Fe-C_{alkyl})[a]	d(C_{alkyl}-Si) (Å)[a,b]	Fe-C_{alkyl} Partition	q(C_{alkyl})[c]	q(Fe)[c]	q(Si)[c]	$N_C \rightarrow N^*_{Fe}$ [d]
$[C^{Si}P^{Ph}_3]FeN_2^-$ **3.4**	2.2537(48)[e]	1.845(5)[e]	22.67% Fe	-1.75865	-1.39055	1.79097	102.17
$[C^{Si}P^{Ph}_3]FeCO^-$ **3.7**	2.3050(24)[f]	1.840(3)[f]	22.74% Fe	-1.75936	-1.77544	1.78300	101.21
$(CO)_4FeCH_3$ **3.12**	2.14361[g]	[h]	39.69% Fe	-0.73672	-1.95907	[f]	190.79
$(CO)_4FeC(SiH_3)_3$ **3.13**	2.25063[g]	1.86559[g]	31.62% Fe	-1.51202	-1.87424	0.95679	114.11

[a]Computed natural charge, [b] Donor-acceptor interaction energies (kcal/mol) from the second-order perturbation analysis, n_C denotes a lone pair centered on C_{alkyl}, n^*_{Fe} denotes an unoccupied lone pair centered on Fe, [c]Distance obtained from XRD structure, [d]Distance obtained from one molecule in the asymmetric unit of the XRD structure, [e]Distance obtained from geometry optimization, [f]Not relevant.

3.3. Discussion

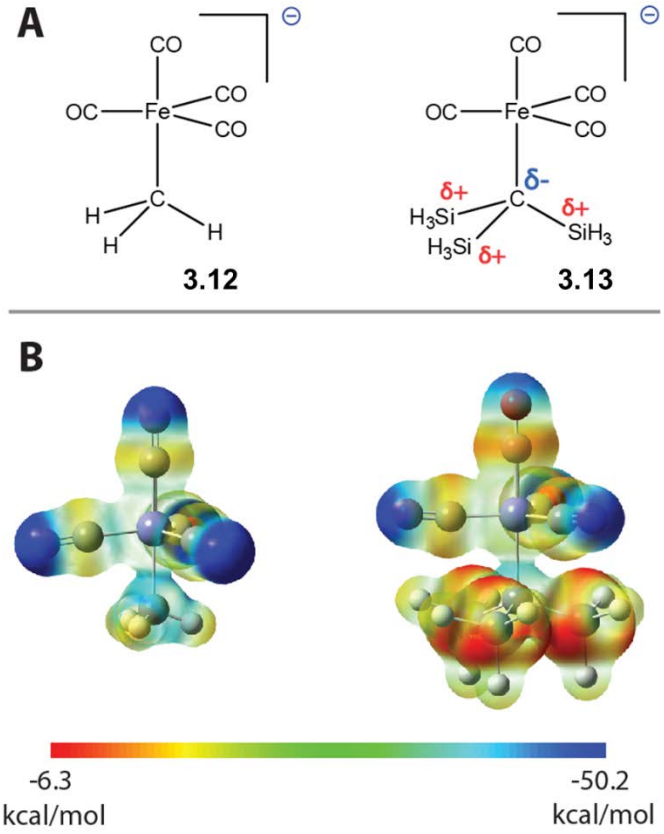

Figure 3.5. (A) Model compounds **3.12** and **3.13** used as *in silico* models of an Fe(0) site interacting with an alkyl ligand. Partial charges on the $C(SiH_3)_3$ ligand of **3.13** are illustrated to emphasize the enhanced negative charge found on C as a result of three electropositive Si substituents. (B) Electrostatic potential maps of **3.12** (left) and **3.13** (right). Blue and red colors represent areas of negative and more positive potentials, respectively.

With the above structural, spectroscopic and computational data in hand, it is of interest to return to the issue of the interstitial C-atom of the cofactor and to consider whether the data presented herein can be of use as a model. In the resting state of FeMoco, the six belt Fe-C bonds are all relatively short (d(Fe-C) ~2.0 Å),[5] imparting a

pseudotetrahedral geometry to each Fe center. Such a geometry is observed for complex **3.3**, albeit with an appreciably longer Fe-C distance (2.153(2) Å). Our hypothesis, as suggested previously and depicted in Figure 3.1,[11,42] is that under electron-loading conditions the interaction between a belt Fe center and the interstitial carbon atom is weakened, allowing the Fe center to slide into a position closer to, or within the plane of the three adjacent sulfide ligands (which may be protonated) concomitant with or prior to substrate coordination. This geometric change would serve to favor a terminal Fe-N_2 π-backbonding interaction, as observed for the transformation of **3.3** to **3.4**.

Further reduction of the substrate-bound cluster (and possibly substrate protonation) could additionally weaken and thereby elongate the Fe-$C_{interstitial}$ interaction. Such elongation is modeled by the carbonyl complexes **3.6** and **3.7**, where additional Fe-C_{alkyl} lengthening occurs on reduction. Upon reduction, the buildup of negative charge on C_{alkyl} is compensated by shorter Si-C_{alkyl} bonds observed in **3.4**, **3.7** and hypothetical **3.13** (Table 2). As the Pauling electronegativities of Fe (χ_{Fe} = 1.83) and Si (χ_{Si} =1.90) are quite similar,[43] the behavior of the Si atoms in [$C^{Si}P^{Ph}_3$] may crudely model that proposed for the remaining five Fe atoms within FeMoco. Specifically, these electropositive Fe atoms may stabilize an interstitial carbide bearing an increasing degree of negative charge as it moves away from the substrate-bound Fe site, while at the same time maintaining overall structural integrity of the cofactor. This hypothesis finds some theoretical support in computational studies performed by the groups of Dance,[44] Nørskov,[10] and Noodleman[45] on the FeMoco. Their studies, performed prior to[10,45] and after[44] the assignment of the light interstitial atom (X) as C, suggest that substrate coordination to Fe at a site *trans* to X is favorable, and induces an elongation of the Fe-X interaction. Likewise, these studies

suggest that an increase in charge density at X, caused by the singular elongated Fe-X interaction, is compensated by shorter Fe-X bonds to the five additional belt Fe atoms in what has been described as coordinative allosterism.[44] Interestingly, George and coworkers[16] have recently communicated NRVS/EXAFS results that suggest elongation of a single Fe-C bond in the FeMoco under catalytic conditions in the presence of propargyl alcohol.

3.4. Conclusions

In conclusion, we have prepared a series of Fe coordination complexes designed to explore a possible role of the interstitial C-atom recently assigned for the FeMoco. Specifically, we have shown that the [$C^{Si}P^{Ph}_3$] ligand can be installed on Fe to afford complexes featuring an unusually flexible Fe-C_{alkyl} interaction owing to a high degree of ionicity in the Fe-C_{alkyl} bond made possible by the three silyl substituents bonded to the C-atom. A trigonal pyramidal [$C^{Si}P^{Ph}_3$]Fe complex can be prepared that, upon reduction, exhibits Fe-C_{alkyl} bond lengthening concomitant with N_2 binding *trans* to the C-atom. The resulting five-coordinate trigonal-bipyramidal anion [$C^{Si}P^{Ph}_3$]Fe(N_2)$^-$ thus features an unusually long Fe-C_{alkyl} bond distance and, according to an NBO analysis, an electron pair between Fe and C_{alkyl} that is polarized towards the carbon atom (i.e., carbanion character). Silylation of the coordinated N_2 ligand at the beta N-atom furnishes a silyldiazenido product [$C^{Si}P^{Ph}_3$]Fe(N_2SiR_3) wherein one phosphine arm has dissociated from Fe in the solid state. To further explore how the Fe-C_{alkyl} interaction responds solely as a function of the formal Fe redox state, the series of geometrically similar trigonal bipyramidal carbonyl complexes {[$C^{Si}P^{Ph}_3$]Fe(CO)}^{n} (n = +1, 0, -1) was characterized. Combined Mössbauer, structural, and DFT data collectively suggest a decreasing degree of covalency in the Fe-

C_{alkyl} bond and a corresponding increase in the covalency of the Fe-P and Fe-C_{CO} bonds as the formal oxidation state at Fe is decreased from Fe(II) to Fe(I) to Fe(0). The presence of the three electropositive and polarizable silyl substituents allows the C_{alkyl} carbanion to partially dissociate from the Fe center as electrons are added to the complex. The collection of data described has been considered as an inorganic model to explore the hypothesis that a belt Fe-$C_{interstitial}$ bond in FeMoco might be modulated as a means of facilitating N_2 binding and reduction at a single Fe site.

3.5. Experimental Section

General Considerations

All manipulations were carried out using standard Schlenk or glovebox techniques under a N_2 atmosphere. Unless otherwise noted, solvents were deoxygenated and dried by thoroughly sparging with Ar gas followed by passage through an activated alumina column in the solvent purification system by SG Water, USA LLC. Non-halogenated solvents were tested with a standard purple solution of sodium benzophenone ketyl in tetrahydrofuran in order to confirm effective oxygen and moisture removal. All reagents were purchased from commercial vendors and used without further purification unless otherwise stated. $[C^{Si}P^{Ph}_3]H$ (**3.1**), benzyl potassium, KC_8, and $[Cp_2Fe][B(3,5\text{-}(CF_3)_2\text{-}C_6H_3)_4]$ were synthesized following literature procedures. Elemental analyses were performed by Midwest Microlab, LLC., Indianapolis, IN. Deuterated solvents were purchased from Cambridge Isotope Laboratories, Inc., degassed, and dried over activated 3 Å molecular sieves prior to use. Deuterated THF was dried over NaK alloy prior to use. ^1H chemical shifts are reported in ppm relative to tetramethylsilane, using residual solvent proton resonances as internal standards. ^{31}P chemical shifts are reported in ppm relative to 85%

aqueous H_3PO_4. Solution phase magnetic measurements were performed by the method of Evans. IR measurements were obtained on samples prepared as KBr pellets on a Bio-Rad Excalibur FTS 3000 spectrometer. X-band EPR spectra were obtained on a Bruker EMX spectrometer on 5mM solutions prepared as frozen glasses in 2-MeTHF. Optical spectroscopy measurements were taken on a Cary 50 UV-Vis spectrophotometer using a 1-cm two-window quartz cell.

X-Ray Crystallography

XRD studies were carried out at the Beckman Institute Crystallography Facility on a Brüker Kappa Apex II diffractometer and Brüker Smart 1000 CCD diffractometer (Mo Kα radiation). Structures were solved using SHELXS and refined against F^2 on all data by full-matrix least squares with SHELXL. The crystals were mounted on a glass fiber with Paratone N oil.

Electrochemistry

Electrochemical measurements were carried out in a glovebox under a N_2 atmosphere in a one-component cell using a CD instruments 600B electrochemical analyzer. A glassy carbon electrode was used as the working electrode and platinum wire was used as the auxiliary electrode. All reported potentials referenced to the ferrocene couple Cp_2Fe^+/Cp_2Fe. Solutions (THF) of electrolyte (0.3 M tetra-*n*-butylammonium hexafluorophosphate) and analyte were also prepared under an inert atmosphere.

Mössbauer Spectroscopy

Spectra were recorded on a spectrometer from SEE Co (Edina, MN) operating in the constant acceleration mode in a transmission-geometry. Spectra were recorded with the temperature of the sample maintained at 80 K. The sample was kept in an SVT-400 dewar

from Janis (Wilmington, MA), at zero field. Application of a magnetic field of 54 mT parallel to the γ-beam did not cause detectable changes in the spectra recorded at 80 K. The quoted isomer shifts are relative to the centroid of the spectrum of a metallic foil of α-Fe at room temperature. Samples were prepared by grinding polycrystalline material into a fine powder and then mounted in a cup fitted with a screw-cap as a boron nitride pellet. Data analysis was performed using the program WMOSS (www.wmoss.org) and quadrupole doublets were fit to Lorentzian lineshapes.

DFT Calculations

Single-point calculations and NBO analyses were performed using the Gaussian03 suite of programs with the RB3LYP level of theory and a 6-31++G** basis set for all atoms. The geometries of **3.12** and **3.13** were optimized with RB3LYP/6-31++G**. The geometries of **3.4** and **3.7** were obtained from the XRD coordinates. To obtain donor-acceptor interaction energies from the second order perturbation analysis portion of NBO for the Fe-C_{alkyl} sigma bonds, the occupancy threshold was manually adjusted. The total electron density described by these alternative Lewis structures is only slightly lower than that of the default options (percent electron densities for default/alternative Lewis structures: **3.4**, 97.7/94.8; **7**, 97.5/94.7; **3.12**, 97.0 /95.9; **3.13**, 97.7/97.1).

3.6. Cited References

1. Burgess, B. K.; Lowe, D. J. *Chem Rev.* **1996**. 96, 2983-3012.
2. Hoffman, D. M.; Dean, D. R.; Seefeldt, L. C. *Acc. Chem. Res.* **2009**. 42, 609-619.
3. Kim, J.; Rees, D. C. *Science.* **1992**. 257, 1677-1682.
4. Einsle, O.; Tezcan, F. A.; Andrade, S. L. A.; Schmid, B.; Yoshida, M.; Howard, J. B. Reese, D. C. *Science*. **2002**. 297, 1696-1700.
5. Spatzal, T.; Aksoyoglu, M.; Zhang, L.; Andrade, S. L. A.; Schleicher, E.; Weber, S.; Reese, D. C.; Einsle, O. *Science.* **2011**. 334, 940.
6. Lancaster, K. M.; Roemelt, M.; Ettenhuber, P.; Hu, Y.; Ribbe, M. W.; Neese, F.; Bergmann, U.; DeBeer, S. *Science.* **2011**. 334, 974-977.
7. Lancaster, K. M.; Bergmann, U.; Ribbe, M. W.; DeBeer, S. *J. Amer. Chem. Soc.* **2013**. 135, 610-612.
8. Wiig, J. A.; Hu, Y.; Lee, C. C.; Ribbe, M. W. *Science.* **2012**. 337, 1672-1675.
9. Kastner, J.; Blochl, P. E. *J. Amer. Chem. Soc.* **2004**. 129, 2998-3006.
10. Hinnemann, B.; Norskov, J. K. *J. Amer. Chem. Soc.* **2004**. 126, 3920-3927.
11. Peters, J. C.; Mehn, M. P. in *Activation of Small Molecules*, eds Tolman, W. B. (Wiley-VCH, Weinheim), 81-120.
12. Crossland, J. L.; Tyler, D. R.; *Coord. Chem. Rev.* **2010** 254, 1883-1894.
13. Holland, P. L. *Can. J. Chem.* **2005**. 83, 296-301.
14. Lee, S. C.; Holm, R. H. *Chem. Rev.* **2004**. 104, 1135-1157.
15. Takaoka, A.; Mankad, N. P.; Peters, J. C. *J. Amer. Chem. Soc.* **2011**. 133, 8440-8443.

16. George, S. J.; Barney, B. B.; Mitra, D.; Igarashi, R. Y.; Guo, Y, *et al. J. Inorg. Biochem.* **2012.** 112, 85-92.

17. Halder, P.; Dey, A.; Paine, T. K. *Inorg. Chem.* **2009**. 48, 11501-11503.

18. Allen, O. R.; Field, L. D.; Magill, A. M.; Voung, K. Q.; Bhadbhade, M. M.; Dalgarno, S. J. *Organometallics.* **2011.** 30, 6433-6440.

19. Ciclosi, M.; Lloret, J.; Estevan, F.; Lahuerta, P.; Sanau, M.; *et al. Angew. Chem., Int. Ed.* **2006**. 45, 6741-6744.

20. Avent, A. G.; Bonafoux, D.; Eaborn, C.; Hill, M. S.; Hitchcock, P. B.; Smith, J. D. *J. Chem. Soc., Dalton Trans.* **2000.** 2183-2190.

21. Bordwell, F. G. *Acc. Chem. Res.* **1988.** 21, 456-463.

22. Streitweiser, A.; Xie, L.; Wang, P.; Bachrach, S. M. *J. Org. Chem.* **1993**. 58, 1778-1784.

23. Mankad, N. P.; Whited, M. T.; Peters, J. C.; *Angew. Chem., Int. Ed.* **2007**. 46, 5768-5771.

24. Lee, Y.; Mankad, N. P.; Peters, J. C. *Nature Chem.* **2010**. 2, 558-565.

25. Nakajima, Y.; Nako, Y.; Sakaki, S.; Tamada, Y.; Ono, T.; Ozawa, F. *J. Amer. Chem. Soc.* **2010**. 132, 9934-9936.

26. Bart, S. C.; Hawrelak, E. J.; Schmisseur, A. K.; Lobkovsky, E.; Chirik, P. J. *Organometallics.* **2004**. 23, 237-246.

27. Mealli, C.; Ghilardi, C. A.; Orlandini, A. *Coord. Chem. Rev.* **1992**. 120, 361-387.

28. Dawsons, J. W.; Lane, B. C.; Mynott, R. J.; Venanzi, L. M.; *Inorg. Chim. Acta.* **1971**. 5, 25-29.

29. Kostka, K. L.; Fox, B. G.; Hendrich, M. P.; Collins, T. J.; Rickard, C. E. F. *J. Amer. Chem. Soc.* **1993**. 115, 6746-6757.

30. Vela, J.; Cirera, J.; Smith, J. M.; Lachicotte, R. J.; Flaschenriem, C. J.; Alvarez, S.; Holland, P. L. *Inorg Chem.* **2007**. 46, 60-71.

31. Hidai, M.; Kmori, K.; Kodama, T.; Jin, D-M.; Takahashi, T.; Suguira, S.; *et al*. *J. Organomet. Chem.* **1984**. 272, 155-167.

32. Kol, M.; Schrock, R. R.; Kempe, R.; Davis, W. M.; *J. Amer. Chem. Soc.* **1994**. 116, 4382-4390.

33. Moret, M-E.; Peters, J. C. *J. Amer. Chem. Soc.* **2011**. 133, 18118-18121.

34. Lee, Y.; Peters, J. C. *J. Amer. Chem. Soc.* **2011.** 133, 4438-4446.

35. Neese, F.; *Inorg. Chim. Acta.* **2002**. 337, 181-192.

36. Mo, Y.; Zhang, Y.; Gao, J. *J. Amer. Chem. Soc.* **1999**. 121, 5737-5742.

37. Brinkman, E. A.; Berger, S.; Brauman, J. I. *J. Amer. Chem. Soc.* **1994**. 116, 8304-8310.

38. Algarra, A. G.; Grushin, V. V.; Macgregor, S. A. *Organometallics.* **2012**. 31, 1467-1476.

39. Weinhold, F.; Landis, C. in *Valency and Bonding: A Natural Bond Orbital Donor-Acceptor Perspective*, (Cambridge University Press, Cambridge, UK), 387-399.

40. Almansour, A. I.; Eaborn, C.; Hawkes, S. A.; Hitchcock, P. B.; Smith, J. D. *Organometallics*. **1997**. 16, 6035-6037.

41. Beagley, B.; Monaghan, J. J.; Hewitt, T. G. *J. Mol. Struct.* **1971**. 8, 401-411.

42. MacBeth, C. E.; Harkins, S. B.; Peters, J. C.; *Can. J. Chem.* **2005**. 83, 332-340.

43. Allred, A. L. *J. Inorg Nucl. Chem.* **1961**. 17, 215-221.

44. Dance, I. *Dalton Trans.* **2012.** 41, 4859-4864.

45. Pelmenschikov, V.; Case, D. A.; Noodleman, L. *Inorg. Chem.* **2008**. 47, 6162-6172.

Chapter 4. Stepwise Conversion of Fe-N≡N to Fe-NH_2-NH_2 via a Redox-Active Fe=N=NH_2 Complex

4.1. Introduction

The ability of certain transition metals to catalyze the proton-coupled reduction of dinitrogen (N_2) to ammonia (NH_3) has sustained life on this planet for millennia and intrigued scientists for decades. The most efficient catalysts for this reaction are the Mo-containing nitrogenase enzymes which employ a cofactor composed of seven Fe atoms and one additional metal site (Mo, V or Fe).[1] Despite a suite of crystallographic, theoretical, and spectroscopic studies,[2] the mechanistic details of N_2 reduction and the metallic site(s) of N_2 coordination have yet to be elucidated.

The chemical plausibility of N_2 reduction at an Fe- or Mo-site may be tested with synthetic model complexes. Well-defined Mo-based systems have been reported to catalyze the direct reduction of N_2 to NH_3 in the presence of proton and electron equivalents.[3] Meanwhile our group has recently disclosed molecular Fe complexes that furnish comparable catalytic yields of NH_3 from N_2.[4] While studies of the Mo systems have revealed a number of isolable Mo(N_xH_y) intermediates that aid in delineating the mechanism of N_2 activation,[5,3c] similar studies on the Fe catalyzed systems are challenged by the high reactivity of the putative Fe(N_xH_y) intermediates.

Iron hydrazido(2-) [Fe(NNH_2)] complexes have been invoked as critical intermediates in the Fe-catalyzed reaction mixtures, although direct evidence for such species is lacking and their reactivity patterns are not well understood.[4] In Chapter 2, we described a transient Fe(NNH_2) complex, {[TPB]Fe(NNH_2)}{$BAr^F{}_{24}$}, which was identified within a complex mixture of Fe-containing species ([TPB] = tris(2-(di-*iso*-propylphosphino)phenyl)borane).[6] This compound decays rapidly at temperatures of -78 °C and higher, frustrating attempts at purification and detailed studies of its structure and

reactivity. Herein, we report the synthesis of an *isolable* $Fe(NNH_2)$ species derived from the direct protonation of an iron-dinitrogen complex $[Fe(N_2)]$ and demonstrate its intermediacy *en route* to NH_3 formation. A high-resolution crystal structure and accompanying spectroscopic data provides unequivocal evidence for this unusual $Fe(N_xH_y)$ species. One-electron reduction of this species at low temperatures reveals an S =1/2, neutral $Fe(NNH_2)$ species that displays significant radical character at the NNH_2 ligand. At higher temperatures this compound converts to an iron hydrazine complex $[Fe(N_2H_4)]$ via a spontaneous disproportionation reaction. Further reduction of this species has previously been reported[7a] to produce significant quantities of NH_3. This reaction sequence defines a viable pathway of N_2 activation mediated by a well-defined Fe platform.

4.2. Results

4.2.1. Protonation of $[SiP^{iPr}_3]Fe(N_2)^{(-)}$

Similar to our previous report,[6] cursory studies suggested that the successful protonation of $Fe(N_2)$ complexes supported by the $[SiP^{iPr}_3]$ ligand required very cold reaction temperatures ($[SiP^{iPr}_3]$ = tris(2-(di-*iso*-propylphosphino)phenyl)silyl$^{(-)}$).[7] For example, the addition of one or two equivalents of $\{H(OEt_2)_2\}\{BAr^F_{24}\}$ to $\{K(Et_2O)\}\{[SiP^{iPr}_3]Fe(N_2)\}$ (**4.1**) at modest temperatures of -78 ºC resulted in the undesirable formation of the one-electron oxidized $[SiP^{iPr}_3]Fe(N_2)$ (**4.2**) and two-electron oxidized $\{[SiP^{iPr}_3]Fe(N_2)\}\{BAr^F_{24}\}$ (**4.3**), respectively. We hypothesized that these proton-induced oxidation reactions may proceed via an unstable iron diazenido species, $[SiP^{iPr}_3]Fe(NNH)$ (**4.4**), analogous to the previously reported silyldiazenido complex, $[SiP^{iPr}_3]Fe(NNSiMe_3)$.[7a] At sufficiently low temperatures, where the lifetime of **4.4** is likely extended, it may be possible to trap **4.4** with another equivalent of $\{H(OEt_2)_2\}\{BAr^F_{24}\}$ as

{[SiP$^{iPr}_3$]Fe(NNH$_2$)}{BAr$^F_{24}$} (**4.5**). Indeed, the combination of **4.1** with 5 equivalents of {H(OEt$_2$)$_2$}{BAr$^F_{24}$} in thawing 2-MeTHF (-135 ^{o}C) produces a pale lavender solution (Figure 4.1a) with UV-visible features that are distinct from **4.2** and **4.3**. The *in situ* ^{57}Fe Mössbauer spectrum (Figure 4.1b) of similarly-prepared lavender solutions derived from ^{57}Fe-enriched **4.1** evidences a new integer-spin Fe complex (δ = 0.126 mm/s and ΔE_Q = 1.484 mm/s) assigned as **4.5**, that constitutes >90% of the Fe in solution, with the remainder identified as complex **4.3** derived from competitive oxidation (vide supra).

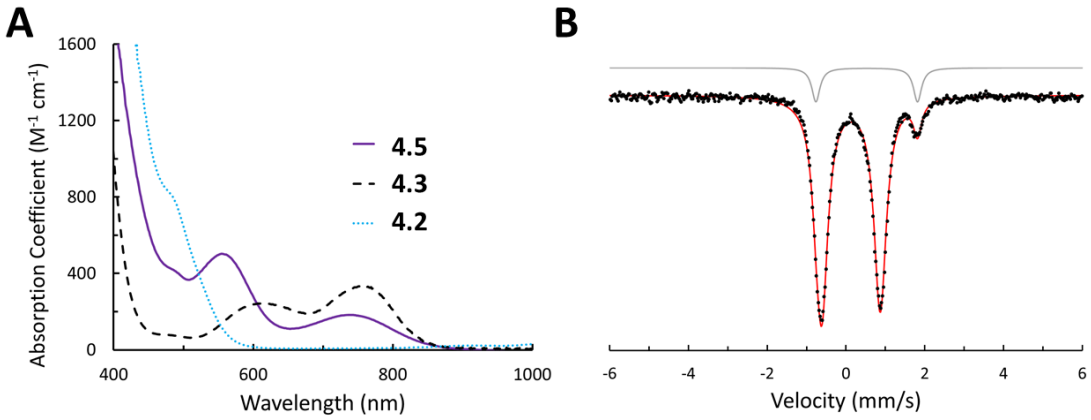

Figure 4.1. (A) UV-visible absorbance spectra of **4.3**, **4.2** and *in situ*-generated **4.5**. Spectra were collected in 2-MeTHF, at -80 ^{o}C. (B) Zero-field ^{57}Fe Mossbauer spectra of ^{57}Fe-enriched **4.5** as a 3 mM solution in 2-MeTHF prepared from **4.1** and collected at 80 K.

The isolation of **4.5** as a crystalline solid was facilitated by the substitution of the BAr$^F_{24}$ counteranion with a less-soluble analogue. Consequently, the reaction of **4.1** with 2.5 equivalents of trifluoromethanesulfonic acid (HOTf) proceeded similarly at -135 ^{o}C but this compound (**4.5'**) can be effectively precipitated out of solution in 49% yield by the addition of pentane at temperatures of -78 ^{o}C or lower. Solid **4.5'** displays intense features at 3207 and 3039 cm^{-1} that shift to 2380 and 2241 cm^{-1} in **4.5'-*d*$_2$** (prepared from the

reaction of **4.1** with HOTf-d_1) and can be assigned to N-H stretching frequencies engaged in strong hydrogen bonding interactions.[8,9] Notably, these features persist in solid samples of **4.5'** that have been stored for days at -30 °C in the absence of air and moisture.

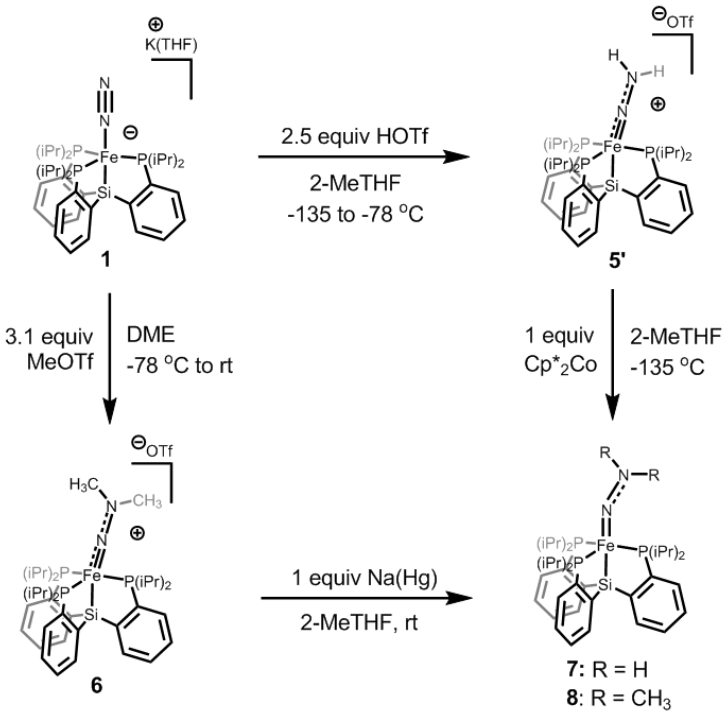

Scheme 4.1. Functionalization of Fe(N_2) complexes

4.2.2. Characterization of [SiP^{iPr}_3]Fe(NNH_2)$^{(+)}$

The stability of **4.5'** permitted growth of single crystals suitable for X-ray diffraction at -78 °C and its structure is depicted in Figure 4.2. Notably, a short Fe-N distance is found that reflects substantial multiple bond character (Table 4.1); a characteristic feature of most terminal metal hydrazido(2-) complexes.[5] The N-N distance is suggestive of a lengthened N-N double bond[10,11] and is markedly increased from that displayed by {Na(12-crown-4)$_2$}{[SiP^{iPr}_3]Fe(N_2)} (1.132(4) Å) and 4.**1** (Appendix 1).[7a] This distance corroborates a broad feature centered at 1443 cm^{-1} in the IR spectrum of solid

4.5' that shifts to 1401 cm^{-1} in **^{15}N-4.5'**, and is hence assigned to the υ(NN) stretching frequency. The $^{\alpha}$N-atom displays a linear geometry and the location of the nitrogen-bound protons in the Fourier difference map of **4.5'** divulge a trigonal-planar $^{\beta}$N-atom. Strong hydrogen bonding between the cation of **4.5'** and the OTf anion is observed (d(N···O): 2.830(3) Å, 2.817(3) Å. <(O···H-N): 165(3)^{o}, 167(3)^{o}) and these interactions form the basis of dimeric (**4.5'**)$_2$ units in the crystal lattice (Appendix 1). While a number of X-ray diffraction studies on mononuclear[12] and dinuclear[13] Fe complexes that support the isomeric diazene ligand (HN=NH) have been disclosed, **4.5'** is the first crystallographically characterized complex that contains a terminal Fe(NNH$_2$) unit.

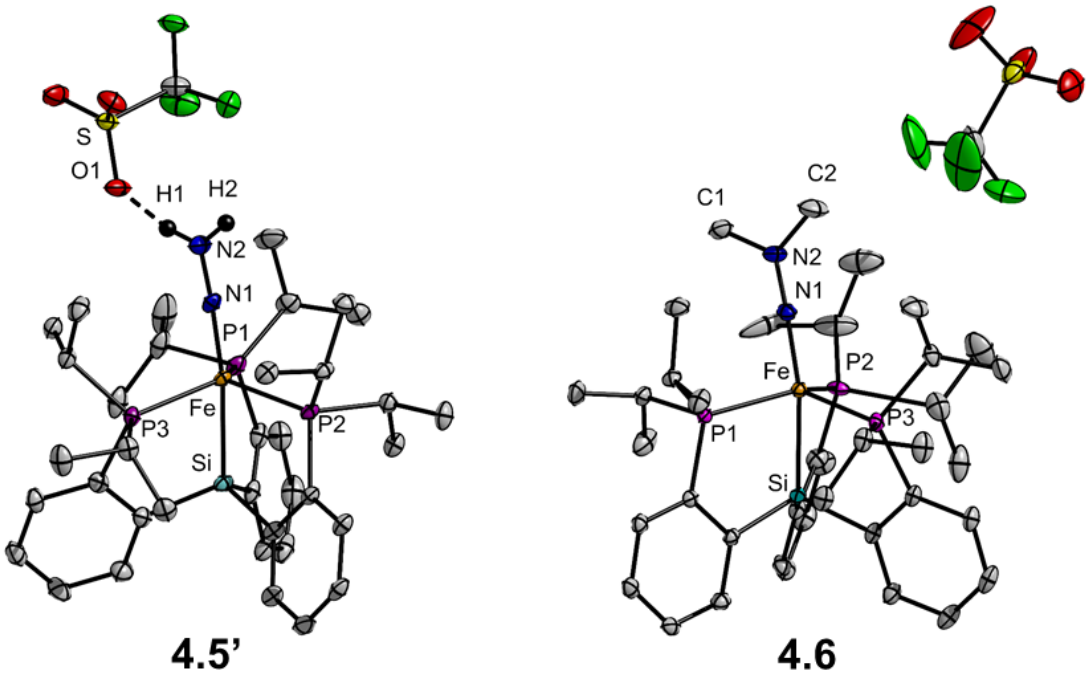

Figure 4.2. X-ray diffraction crystal structures of **4.5'** and **4.6** with thermal ellipsoids drawn at 50% probability. Hydrogen atoms (excepting the N-H's of **4.5'**), and co-crystallized solvent molecules have been removed for clarity.

While the Fe(NNH_2) **4.5'** can be prepared as a stable solid, solutions of **4.5'** readily decompose at temperatures of 0 ^oC and higher. Seeking to prepare a more stable analogue of **4.5'** on the [SiP^{iPr}_3] framework, we explored the direct alkylation of **4.1** with MeOTf. At -78 ^oC, the reaction of **4.1** with excess methyl trifluoromethanesulfonate (MeOTf) leads to a darkening of the reaction mixture and upon warming to room temperature, {[SiP^{iPr}_3]Fe($NNMe_2$)}{OTf} (**4.6**) precipitates out of solution as a purple solid. Unlike the Fe(NNH_2) **4.5'**, the isoelectronic Fe($NNMe_2$) **4.6** is indefinitely stable in the solid state and persists in solution at temperatures of 80 ^oC and lower. At least three features in the IR spectrum of **4.6** are sensitive to the isotopic composition of the N atoms as a result of strong mixing between the υ(NN), υ(NC) and υ(CH) modes of the $NNMe_2$ ligand. Consequently, these modes are decoupled in {[SiP^{iPr}_3]Fe[$NN(CD_3)_2$]}{OTf} (**4.6-*d*$_6$**), resulting in an intense υ(NN) feature at 1439 cm^{-1} that shifts to 1399 cm^{-1} in ^{15}**N-4.6-*d*$_6$**. The solid-state crystal structure of **4.6** (Figure 4.2) reveals similar features to that of **4.5'** (Table 4.1).

Table 4.1. Crystallographic Bond Metrics

	4.5'	**4.6**	**4.8**
Fe-N[a]	1.667(2)	1.691(2)	1.773(1)
N-N[a]	1.273(4)	1.271(2)	1.276(2)
Fe-N-N[b]	174.9(2)	174.7(2)	158.64(9)
Si-Fe-N[b]	170.81(8)	164.73(6)	174.20(4)

[a]Bond distances in Å. [b]Bond angle in degrees.

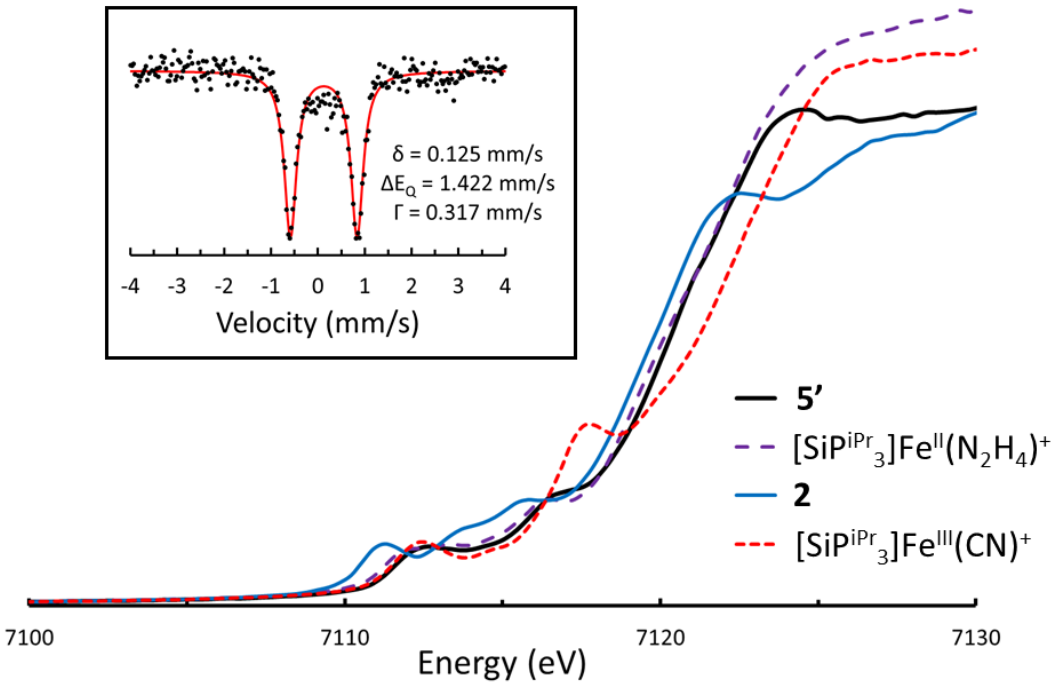

Figure 4.3. Normalized Fe K-Edge XANES spectra collected on solid **4.5'** (black, solid), {[SiP$^{iPr}_3$]Fe(N_2H_4)}{BAr$^F_{24}$} (purple, dashed), Compound **4.2** (blue, solid), and {[SiP$^{iPr}_3$]Fe^{III}(CN)}{BAr$^F_{24}$} (red, dotted). (Inset) Zero field ^{57}Fe Mössbauer spectra of solid **4.5'** collected at 80 K.

^{57}Fe Mössbauer and Fe K-Edge XANES studies were conducted (Figure 4.3) to gauge the electronic structure of the Fe center in these Fe(NNR_2) complexes. Fe(NNH_2) **4.5'** displays a sharp quadrupole doublet centered at 0.125 mm/s with a ΔE_Q = 1.422 mm/s in the 80 K zero field Mössbauer spectrum. Complex **4.6** displays similar parameters (δ = 0.135 mm/s, ΔE_Q = 1.493 mm/s). Isomer shift values reported for diamagnetic Fe(IV) compounds bearing nitrogenous ligands range from δ = -0.34 to -0.09 mm/s,[14] considerably shifted from that of **4.5'**. These δ values appear to be more consistent with that of other low-spin Fe(II) complexes.[15] The Fe K-edge XANES spectrum of **4.5'** presents a number

of weak pre-edge features (Appendix 1) and an edge energy of 7120.8 eV (Figure 4.3). Related compounds with formal oxidation states of Fe^{I}, Fe^{II}, and Fe^{III} supported by $[SiP^{iPr}_3]$ are shown for comparison. Notably, the edge energy of compound **4.5'** is identical to that of $\{[SiP^{iPr}_3]Fe^{II}(N_2H_4)\}\{BAr^{F}_{24}\}$[7a] (7120.8 eV) and markedly lower in energy than that of $\{[SiP^{iPr}_3]Fe^{III}(CN)\}\{BAr^{F}_{24}\}$[16] (7122.6 eV). Taken together, the structural and spectroscopic data appear to be most consistent with a physical oxidation state of Fe^{II} in **4.5'**.[17]

The bonding characteristics of the $Fe(NNR_2)$ units in these complexes are understood by considering the archetypal metal-hydrazido(2-) bonding interactions (Scheme 4.2).[18] The FeN π bond within the plane of the NNR_2 ligand (II) is characterized as a covalent, 2-center interaction, similar to that found in metal imido complexes.[19] A consistent feature of most terminal metal hydrazido(2-) complexes is the presence of a planar, sp^2-hybridized $^{\beta}N$ atom.[5,18] The lone pair of the $^{\beta}N$ atom is engaged in a 3-center 4-electron bond (III) that is conceptually related to the 3-center π interaction in diazomethane.[20] The polarization of this interaction dictates the formal Fe-N and N-N bond orders, and is dependent on the electron-releasing character of the metal and the identity of the $^{\beta}N$-atom substituents. In W- and $Mo(NNH_2)$ compounds, comparatively long N-N bond distances (crystallographic average of 1.33(3) Å)[5,11] reflect substantial N-N single-bond character arising from the increased π-basicity of these early transition metals. Disilylhydrazido(2-) complexes of Fe[21] also exhibit N-N single bond character (1.33(1) Å), due in part to the low energy of Si_2N lone pair.[22] Overall, the bond metrics and spectroscopic characteristics displayed by **4.5'** and **4.6** indicate a delocalized description which is intermediate between these two extremes.

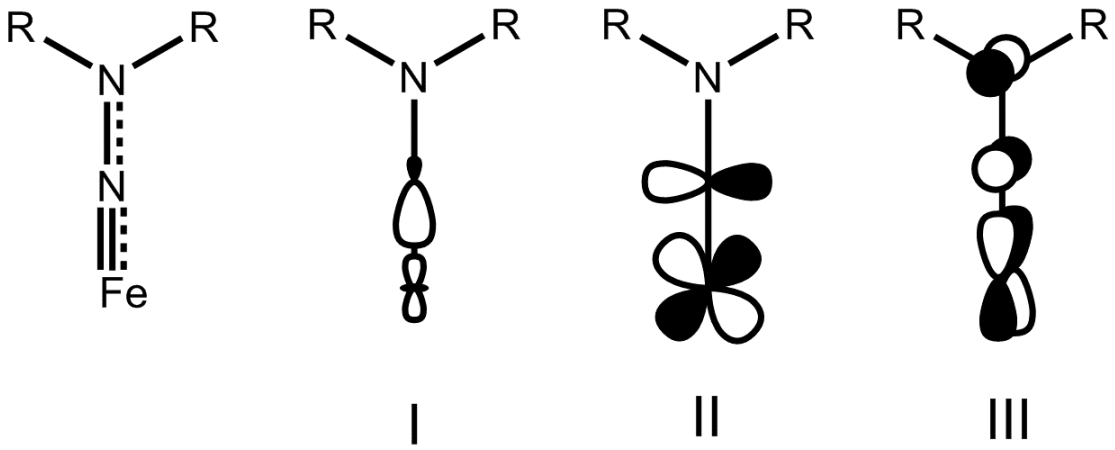

Scheme 4.2. $FeNNR_2$ Bonding Interactions

Compounds **4.5'** and **4.6** exhibit diamagnetic ground states, permitting incisive characterization by multinuclear NMR spectroscopies (Figure 4.4) at low temperatures. A single broad resonance is found in the $^{31}P\{^{1}H\}$ NMR spectrum of $Fe(NNH_2)$ **4.5'**, consistent with apparent 3-fold symmetry in solution. Compound **^{15}N-4.5'** exhibits two resonances in the ^{15}N NMR spectrum at 518 and 198 ppm, corresponding to $^{\alpha}N$- and $^{\beta}N$-atoms, respectively (Figure 4.4).[5b,24] The resonance at 198 ppm appears as a triplet of doublets ($^{1}J_{NH}$: 96 Hz, $^{1}J_{NN}$: 11 Hz) whereas the feature at 518 ppm is broadened due to unresolved coupling to the phosphine ligands. In the ^{1}H NMR spectrum, **^{15}N-4.5'** displays a broad doublet ($^{1}J_{NH}$: 97 Hz) at 9.5 ppm assigned to the NNH_2 protons. The magnitude of the $^{1}J_{NH}$ coupling constant in **4.5'** is consistent with sp^2 hybridization at the $^{\beta}N$-atom[25] and similar to that found in other terminal metal-hydrazido(2-) complexes.[5b,24] These data unequivocally confirm that the structure of **4.5'** found in the solid state is maintained in solution. NMR data collected on **4.6** at low temperatures reproduces the salient feature of **4.5'** (Appendix 1).

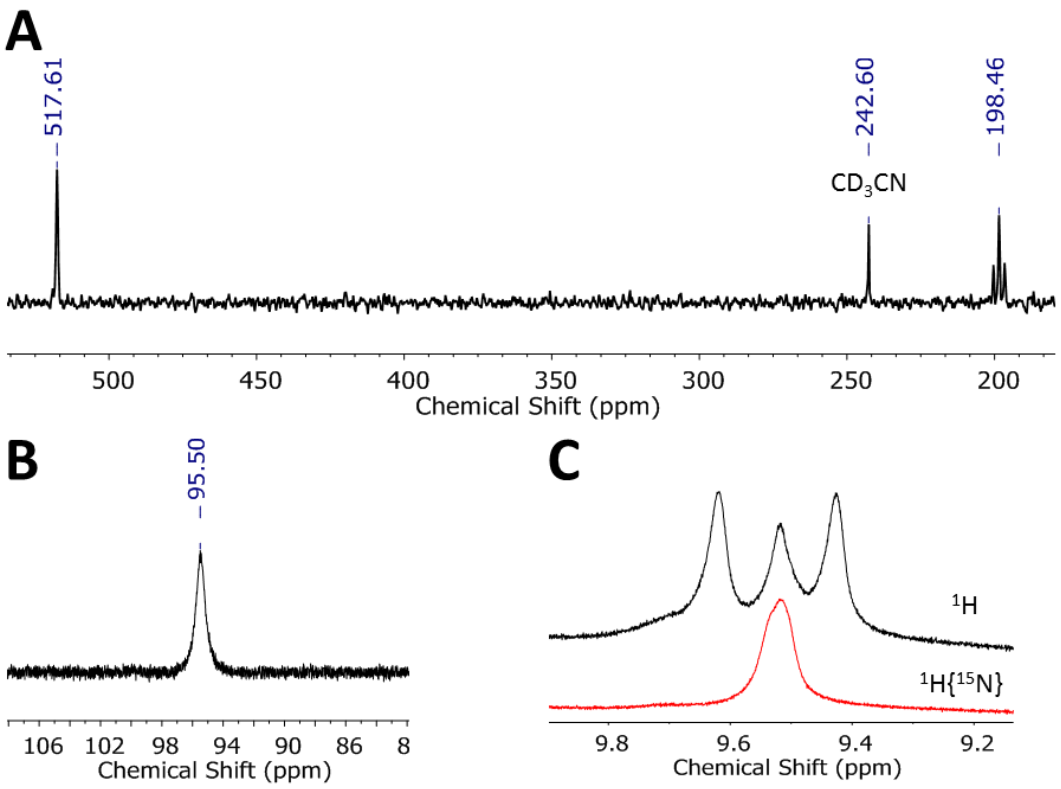

Figure 4.4. NMR spectra of **4.5'** recorded at -60 °C in 9:1 THF-d_8:CD_3CN. (A) ^{15}N NMR spectrum of **^{15}N-4.5'**. (B) $^{31}P\{^1H\}$ NMR spectrum of **4.5'**. (C) Overlaid ^1H and $^1H\{^{15}N\}$ spectra of **^{15}N-4.5'**. The central feature in the ^1H spectrum results from contamination of **^{15}N-4.5'** with the natural abundance **4.5'**.

At elevated temperatures, compound **4.6** displays temperature-dependent paramagnetism, consistent with the thermal population of an excited triplet state.[26] On warming CD_3CN solutions of **4.6**, the chemical shifts of resonances in the ^1H, ^{13}C, ^{15}N, ^{31}P, and ^{29}Si NMR spectra dramatically move in a non-linear and non-exponential fashion (Appendix 1). For example, the ^{29}Si resonance of **4.6** displays a chemical shift of +74.2 ppm at -40 °C that shifts to -9.7 ppm at +40 °C. The variable temperature behavior of the

^{31}P, ^{29}Si, and [NN(CH_3)$_2$]-^{1}H resonances can be simulated by an excited-state magnetization function (Appendix 1), indicating that **4.6** possesses a singlet-triplet gap of 6.7(3) kcal/mol. Comparison of the thermal energies of the gas-phase optimized geometries of the cation of **4.6** in S = 0 and S = 1 spin states corroborates this experimental value (4.28 kcal/mol, refer to Appendix 1 for calculation details). Similar spin-crossover behavior has been observed in related terminal iron-imido[26b] and -phosphiniminato[26c] complexes. While the instability of **4.5'** in solution precludes similar experimental studies, gas-phase DFT studies on the cation of **4.5'** optimized in S = 1 and S = 0 spin states reveal a similar thermal energy difference (6.18 kcal/mol) to that of **4.6**. Whether or not the instability of **4.5'** in solution is influenced by such spin-crossover behavior is presently unknown, but this hypothesis warrants future consideration.

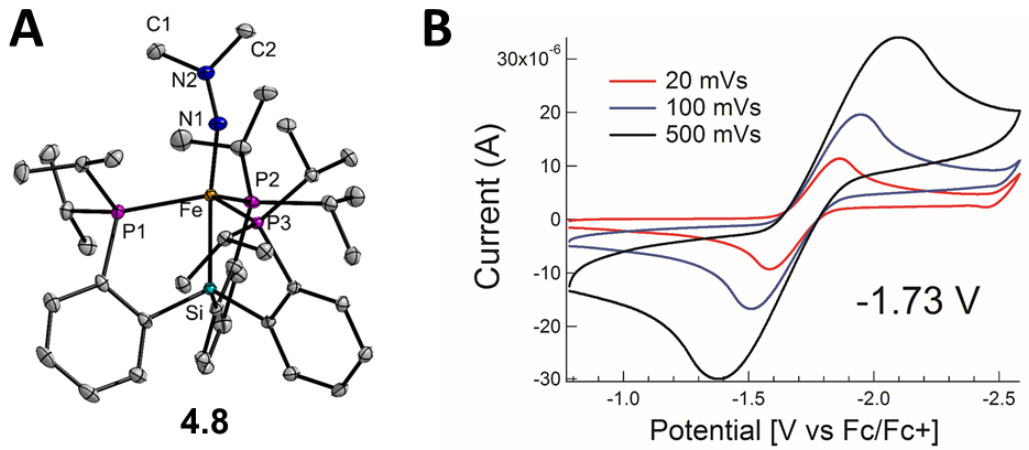

Figure 4.5. (A) X-ray diffraction crystal structure of **4.8** with thermal ellipsoids drawn at 50% probability. Hydrogen atoms have been removed for clarity. (B) Cyclic voltammograms obtained on THF solutions of 1 mM **4.6** (298 K, 0.1 M tetra-*n*-butylammonium hexafluorophosphate) at the listed scan rate.

4.2.3. Redox Chemistry of $[SiP^{iPr}_3]Fe(NNR_2)^{(+)}$

The intermediacy of $Fe(NNH_2)$ **4.5'** in the formation of NH_3 may rest on its ability to react with additional proton or electron equivalents. Both **4.5** and **4.5'** were found to be stable at -78 ^oC to the presence of additional proton equivalents, and we therefore explored the reduction chemistry of these compounds. The temperature-dependent paramagnetism exhibited by $Fe(NNMe_2)$ **4.6** emphasizes the presence of one or more low-lying unoccupied orbitals and underscores potential redox activity of these iron hydrazido complexes. Accordingly, we endeavored to prepare the neutral analogues, $[SiP^{iPr}_3]Fe(NNH_2)$ (**4.7**) and $[SiP^{iPr}_3]Fe(NNMe_2)$ (**4.8**). Cyclic voltammetry measurements on **4.6** reveal a reversible reduction event at -1.73 V (Figure 4.5B). The chemical reduction of **4.6** with one equivalent of Na(Hg) and subsequent workup furnishes neutral **4.8**, whose crystal structure (Figure 4.5A) reveals a lengthened Fe-N distance concomitant with substantial bending at the $^{\alpha}$N-atom (Table 4.1). The $^{\beta}$N-atom retains sp^2-hybridization and the N-N bond length is essentially unchanged from that of **4.6**. X-band EPR spectra indicate that **4.8** displays an $S = 1/2$ ground state (Figure 4.6, g_{avg}: 2.04)**,** consistent with the room temperature magnetic moment displayed by **4.8** in C_6D_6 (1.7 μ_B). Magnetically-perturbed ^{57}Fe Mössbauer studies of ^{57}Fe-enriched **4.8** (Figure 4.7) demonstrate strong ^{57}Fe hyperfine coupling, and much slower relaxation properties compared to **4.2** (Appendix 1), resulting in distinctive features that span a range of 5 mm/s at temperatures of 80 K and lower. Compound **4.8** is unstable in C_6D_6 solutions, decaying to a mixture of **4.2** and $[SiP^{iPr}_3]Fe(H)(N_2)$ over the course of hours at room temperature. The fate of the $NNMe_2$ ligand is presently unknown.

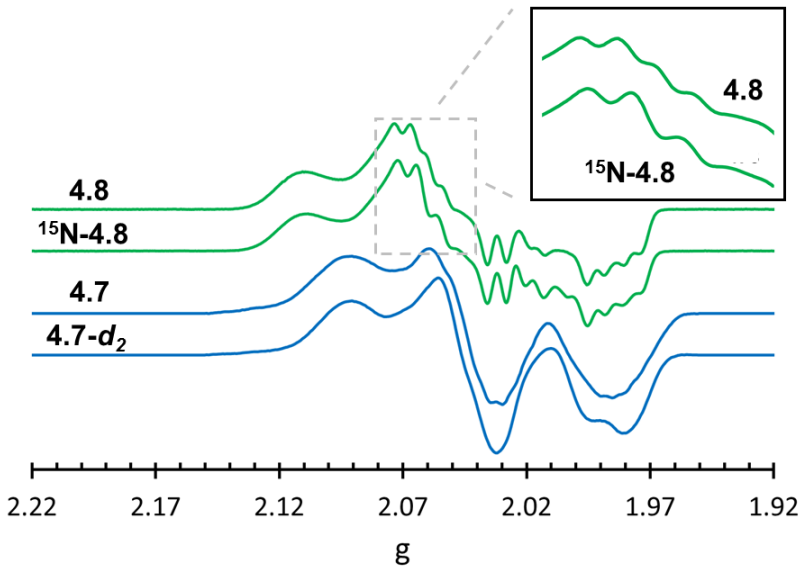

Figure 4.6. X-Band EPR spectra of **4.7** and **4.7-*d*$_2$**, derived from the *in situ* reduction of **4.5'** or **4.5'-*d*$_2$**, respectively, with Cp*$_2$Co; **4.8** and **^{15}N-4.8** collected at 77 K in 2-MeTHF glasses. Signals derived from **4.2** have been subtracted from the displayed spectra of **4.7** and **4.7-*d*$_2$** for clarity. (Inset) Prominent features of **4.8** that differ in **^{15}N-4.8**. These features arise from hyperfine coupling to ^{31}P and $^{14/15}$N nuclei of comparable magnitude. Refer to Appendix 1 for further details and discussion.

The preparation of the neutral Fe(NNH$_2$) **4.7** proved to be synthetically challenging, and this compound could only be characterized at cryogenic temperatures. Compound **4.5'** was found to react with Cp*$_2$Co in 2-MeTHF at -135 ^{o}C to produce dark brown solutions that rapidly bleach when warmed to -78 ^{o}C or higher temperatures (*vide infra*). EPR (Figure 4.6) and ^{57}Fe Mössbauer spectra (Figure 4.7) collected on similarly-prepared frozen reaction mixtures derived from ^{57}Fe-enriched **4.5'** evidence the generation of a new S = ½ species (g_{avg}: 2.04) as the major Fe-containing component.[27] Notably, the ^{57}Fe Mössbauer

spectra of this complex are nearly identical to that displayed by alkylated analogue **4.8**, facilitating the assignment of this species as the isoelectronic Fe(NNH_2) **4.7**. Indeed, the gas-phase optimized geometry and electronic structure of **4.7** are remarkably similar to that of **4.8** (Appendix 1). Compounds **4.7** and **4.8** display substantial radical character on the NNR_2 and phosphine ligands, as evidenced by the EPR data. Differences between the spectra of **^{15}N-4.8** and **4.8** establish strong hyperfine coupling (ca. 30 MHz) to a single N atom (Inset of Figure 4.6). In addition, marked differences in the EPR spectra of **4.7** and **4.7-*d*$_2$** demonstrate significant hyperfine coupling to one or both nitrogen-bound H-atom(s) and this value is estimated to be greater than 25 MHz through analysis of the 2nd derivative EPR spectrum (Appendix 1). Overall, the reduction of **4.5'** to **4.7** represents a rare demonstration of well-defined redox activity at a M(NNH_2) complex.[28]

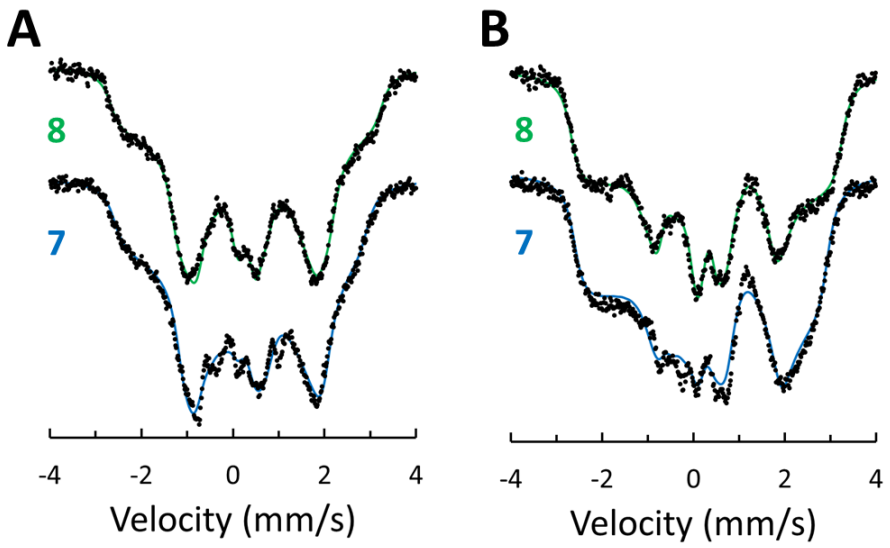

Figure 4.7. ^{57}Fe Mössbauer spectra of *in situ*-prepared **4.7** and **4.8** obtained by subtracting out quadrupole doublet impurities from the raw data. A 50 mT magnetic field was applied (A) perpendicular and (B) parallel to the propagation of γ–beam. The solid lines are theoretical fits to an S = 1/2 spin Hamiltonian operating in the slow relaxation regime.

Refer to the Appendix 1 for a more detailed discussion and the spin Hamiltonian parameters derived from the fit.

4.2.4. Conversion of $[SiP^{iPr}_3]Fe(NNH_2)^{(+)}$ to $[SiP^{iPr}_3]Fe(NH_2NH_2)^{(+)}$

At higher temperatures, the reaction of **4.5'** with Cp^*_2Co results in a spontaneous disproportionation to a mixture of Fe species that include the iron hydrazine complex, $\{[SiP^{iPr}_3]Fe(N_2H_4)\}\{OTf\}$ (**4.9**), as a major component. Thawing THF solutions (-110 °C) of **4.5'** were combined with Cp^*_2Co and allowed to warm slowly to room temperature over 20 min, causing a color change to orange. After minimal workup, room temperature NMR analyses of the resulting mixtures (Appendix 1) reveal the formation of roughly equivalent molar quantities of **4.9** and **4.2** as major products, alongside small amounts of $[SiP^{iPr}_3]Fe(OTf)$ (**4.10**) and $\{[SiP^{iPr}_3]Fe(NH_3)\}\{OTf\}$ (**4.11**).[7] Compound **4.9** is also detected when these reactions are performed with 0.5 equiv of Cp^*_2Co relative to **4.5'**. Exposure of **4.5'** to >2 equiv of Cp^*_2Co under these conditions result in increased yields of **4.2** and very little detectable **4.9**. The identification of **4.9** as a consistent product of these reactions was further confirmed by comparison of features present in the IR and UV-visible spectra of these mixtures with those of independently prepared **4.9**.[7a] Furthermore, single crystals of **4.9** (cocrystallized with **4.11**) suitable for X-ray diffraction can be grown from these reaction mixtures (Appendix 1).

The formation of these Fe-containing products can be understood by the reactions shown in Scheme 4.3. As discussed above, ^{57}Fe Mössbauer and EPR studies indicate that **4.5'** is effectively reduced by Cp^*_2Co to generate **4.7** at temperatures as low as -135 °C. At higher temperatures, we speculate that *in situ* generated **4.7** engages in a bimolecular

reaction with the remaining **4.5'** in solution. Effective transfer of H^+ and e^- equivalents between these two compounds, possibly via concerted proton-electron transfer (CPET),[29] results in the formation of the Fe(N_2) **4.2** and the Fe(N_2H_4)$^{(+)}$ **4.9** as the immediate reaction products. Whereas **4.2** is stable to the presence of Cp^*_2Co, **4.9** is slowly reduced by Cp^*_2Co at room temperature to afford detectable quantities of NH_3 and a mixture of **4.2** and **4.10**. These considerations account for all of the reaction products observed in the NMR spectrum. Furthermore, DFT studies predict that the conversion of **4.5'** + **4.7** → **4.2** + **4.9** is highly exergonic (-45 kcal/mol), lending support for the viability of the proposed reaction stoichiometry (Appendix 1).

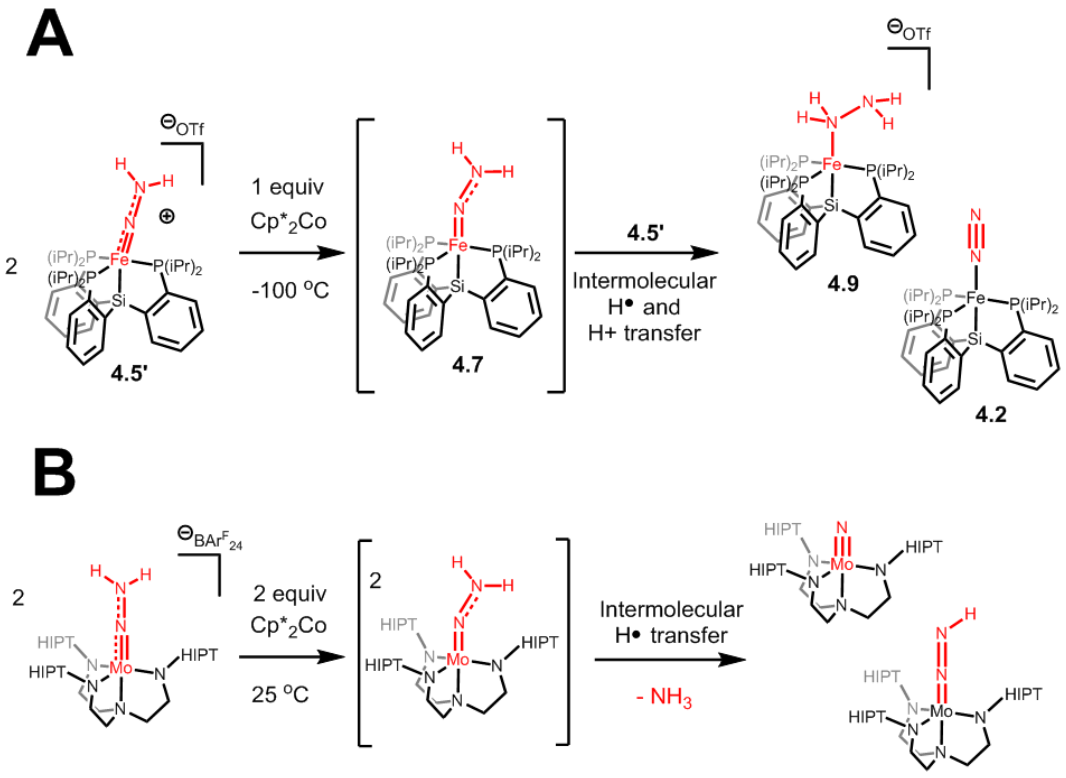

Scheme 4.3. Comparison of the reaction products observed in the reduction of (A) Fe(NNH_2) complexes supported by the [SiP^{iPr}_3]$^{(-)}$ ligand framework and (B) Mo(NNH_2) complexes supported by the [$HIPTN_3N$]$^{(3-)}$ ligand framework.[28,30]

Disproportionation reactions that are conceptually-related to the conversion of **4.5'** to **4.9** have been previously invoked in the reactions of molecular W- and Mo(NNH_2) species to afford NH_3 and N_2H_4.[5c,28,30,31] In certain cases, W- and Mo complexes bearing hydrazido(1-) ($N_2H_3^{(-)}$) ligands have been proposed as intermediates in the formation of N_2H_4,[5c,31a] although direct evidence for such species is absent.[31b] In a contrasting pathway, Schrock has reported the reductive disproportionation of a Mo(NNH_2) complex supported by the bulky [$HIPTN_3N$] ligand to form a molybdenum nitride [Mo(N)] species and a Mo(NNH) complex ($HIPTN_3N$= $[(\{3,5\text{-}(2,4,6\text{-}i\text{-}Pr_3C_6H_2)_2C_6H_3\}NCH_2CH_2)_3N]^{3-}$) (Scheme 4.3B).[28,30] In this example H^+ and e^- equivalents are transferred in an intermolecular fashion between the $^{\beta}$N-atoms of the Mo(NNH_2) species, resulting in an early N-N bond cleavage with concomitant formation of NH_3. The reaction conditions reported for this transformation are markedly similar to that observed in the partial reduction of **4.5'**, but in this case H^+ and e^- equivalents are transferred to the $^{\alpha}$N-atom, resulting in the formation of Fe(N_2H_4) **4.9**. Subsequently, any NH_3 formed from this species would be the result of a late N-N bond cleavage event, representing a marked contrast in the mechanism of N_2 activation by these two systems.

In general, Fe-mediated examples of the transformation N_2 to NH_3 in a well-defined manner are rare.[4,32] While the intimate mechanistic details of the conversion of **4.5'** to **4.9** are presently unknown, the direct formation of an iron-bound hydrazine complex from a terminal iron hydrazido(2-) species establishes a novel reaction pathway in the activation of N_2 by an Fe complex. This key transformation completes a synthetic cycle for the proton-coupled reduction of N_2 to NH_3 mediated by the [SiP^{iPr}_3]Fe platform. As discussed above,

an $Fe(N_2)$ species (**4.1**) is sequentially-protonated at the $^{\beta}$N-atom to afford the cationic $Fe(NNH_2)$ compound **4.5'**. The partial reduction of this species initiates an intermolecular transfer of proton and electron equivalents to form the $Fe(N_2H_4)$ complex **4.9**. Mild reduction of this species results in the expulsion of NH_3 and reuptake of the N_2 substrate to form **4.2**.[7a] Finally, further reduction of **4.2** to **4.1** primes the $^{\beta}$N-atom towards protic attack and completes the synthetic cycle.

Given the stoichiometric reactions presented in this chapter and elsewhere,[7a] it is interesting that $\{Na(12\text{-crown-}4)_2\}\{[SiP^{iPr}_3]Fe(N_2)\}$ is not an effective pre-catalyst for the *catalytic* generation of NH_3, as is the case with the related $\{Na(12\text{-crown-}4)_2\}\{[TPB]Fe(N_2)\}$ and C-anchored analogue.[4] Upon exposure of $\{Na(12\text{-crown-}4)_2\}\{[SiP^{iPr}_3]Fe(N_2)\}$ to 48 equivalents of $\{H(OEt_2)_2\}\{BAr^F_{24}\}$ and KC_8, no N_2H_4 was observed and only 0.7(1) equiv of NH_3 were detected. While any comparative discussion of the intermediate $Fe(N_xH_y)$ species that are relevant to these catalytic reactions is likely to be tenuous, the comparative behavior of the $\{[TPB]Fe(NNH_2)\}\{BAr^F_{24}\}$ complex discussed in Chapter 2 and **4.5** warrant some discussion. The $[TPB]Fe(NNH_2)^{(+)}$ species rapidly decomposes at -78 ^{o}C, even in the absence of additional H^+ and e^- equivalents, to afford appreciable quantities of NH_3. In contrast, compounds **4.5** and **4.5'** prepared in otherwise identical reaction conditions are stable at -78^{o}C for hours, if not longer. The competing formation of H_2 from the background reaction of $\{H(OEt_2)_2\}\{BAr^F_{24}\}$ and KC_8 at these temperatures rapidly consumes the H^+ and e^- equivalents necessary for the regeneration of $\{[TPB]Fe(NNH_2)\}\{BAr^F_{24}\}$ and **4.5**, which are plausible reaction intermediates.[4] We therefore speculate that the enhanced stability of $Fe(N_xH_y)$ intermediates supported by $[SiP^{iPr}_3]$ platform, such as **4.5,** may lead to comparatively

sluggish reaction kinetics and lower NH_3 turnover numbers, relative to those of the [TPB]Fe system. Nonetheless, the rapid conversion of **4.5'** to **4.7** at cryogenic temperatures sheds some doubt on this hypothesis. Further mechanistic investigations of these systems are needed to reveal the key properties required for catalytic NH_3 formation. Very little is known regarding the viable Fe(N_xH_y) intermediates supported by the C-atom anchored scaffold or their interconversion.[4b]

4.3. Conclusions

We have presented the structural and spectroscopic characterization of isolable Fe(NNH_2) and Fe($NNMe_2$) species derived from the direct functionalization of a terminally-bound Fe(N_2) complex. Upon one-electron reduction, neutral iron hydrazido complexes display markedly increased Fe-N distances, and their EPR spectra reflect the accumulation of significant radical character on the hydrazido ligands. These features allude to further reactivity at the NNR_2 ligand and warming of these solutions result in the formation of an Fe(N_2H_4) complex derived from the addition of proton and electron equivalents to the $^{\alpha}$N-atom. This unprecedented sequence of reactions forms the basis of a viable scheme for proton-coupled reduction of N_2 mediated by a well-defined Fe site.[32]

While the stability of the presented Fe(NNH_2) complexes is noteworthy, their *in*stability relative to previously characterized Mo(NNH_2) complexes[3,5] is remarkable. The facile interconversion of Fe(N_xH_y) species at very low reaction temperatures suggests that Fe may possess a significant kinetic advantage over Mo in mediating H-atom delivery to bound N_xH_y ligands *en route* to NH_3 formation. Side-by-side kinetic comparisons of the NH_3 production rates by molecular Fe and Mo systems would allow these hypotheses to be

tested. Nonetheless, the factors governing the stability of these and other N_2-derived $Fe(N_xH_y)$ species are not presently understood and are the subject of Chapter 5.[16]

4.4. Cited References

1. Howard, J. B.; Rees, D. C. *Chem. Rev.* **1996**. 96, 2965-2982.
2. (a) Lancaster, K. M.; Roemelt, M.; Ettenhuber, P.; Hu, Y.; Ribbe, M. W.; Neese, F.; Bergmann, U.; DeBeer, S. *Science*. **2011**. 334, 974-977. (b) Seefeldt, L. C.; Hoffman, B. M.; Dean, D. R. *Annu. Rev. Biochem.* **2009**. 78, 701-722. (c) Spatzal, T.; Perez, K. A.; Einsle, O.; Howard, J. B.; Rees, D. C. *Science*. **2014**. 345, 1620-1623. (d) Hinnemann, B.; Norskov, J. K. *Topics in Cat.* **2006**. 37, 55-70.
3. (a) Yandulov, D. V.; Schrock, R. R.; *Science*. **2003**. 301, 76-78. (b) Arashiba, K.; Kinoshita, E.; Kuriyama, S.; Eizawa, A.; Nakajima, K.; Tanaka, H.; Yoshizawa, K.; Nishibayashi, Y. *J. Amer. Chem. Soc.* **2015**. 137, 5666-5669. (c) Arashiba, K.; Miyake, Y.; Nishibayashi, Y. *Nat. Chem.* **2010**. 3, 120-125.
4. (a) Anderson, J. S.; Rittle, J.; Peters, J. C. *Nature*. **2013**. 501, 84-87. (b) Creutz, S. E.; Peters, J. C. *J. Amer. Chem. Soc.* **2014**. 136, 1105-1115. (c). Ung, G.; Peters, J. C. *Angew. Chem., Int. Ed.* **2015**. 54, 532-535.
5. (a) Chatt, J.; Dilworth, J. R.; Richards, R. L. *Chem. Rev.* **1978**. 78, 589-625. (b) Yandulov, D. V.; Schrock, R. R. *J. Amer. Chem. Soc.* **2002**. 124, 6252-6253. (c) Hidai, M.; Mizobe, Y. *Chem. Rev.* **1995**. 95, 1115-1133.
6. Anderson, J. S.; Cutsail, G. E.; Rittle, J.; Connor, B. A.; Gunderson, W. A.; Zhang, L.; Hoffman, B. M.; Peters, J. C. *J. Amer. Chem. Soc.* **2015**. 137, 7803-7809.

7. (a) Lee, Y.; Mankad, N. P.; Peters, J. C. *Nat. Chem.* **2010**. 2, 558-565. (b) Mankad, N. P.; Muller, P.; Peters, J. C. *J. Amer. Chem. Soc.* **2010**. 132, 4083-4085. (c) Lee, Y.; Peters, J. C. *J. Amer. Chem. Soc.* **2011**. 133, 4438-4446.

8. Lehnert, N.; Tuczek, F. *Inorg. Chem.* **1999**. 38, 1659-1670.

9. Steiner, T. *Angew. Chem., Int. Ed*. **2002**. 41, 48-76.

10. Crystallographically characterized examples of aliphatic N=N bonds display bond distances of 1.24(2) Å (11).

11. Allen, F. H. *Acta Cryst. Sect. B: Struct. Sci*. **2002**. 58, 380-388.

12. Field, L. D.; Li, H. L.; Dalgarno, S. J.; Turner, P. *Chem. Commun.* **2008**. 1680-1682.

13. (a) Sellmann, D.; Soglowek, W.; Knoch, F.; Moll, M. *Angew. Chem., Int. Ed*. **1989**. 28, 1271-1272. (b) Saouma, C. T.; Muller, P.; Peters, J. C. *J. Amer. Chem. Soc.* **2009**. 131, 10358-10359. (c) Li, Y.; Li, Y.; Wang, B.; Luo, Y.; Yang, D.; Tong, P.; Zhao, J.; Luo, L.; Zhou, Y.; Chen, S.; Cheng, F.; Qu, J. *Nat. Chem.* **2013**. 5, 320-326.

14. Bancroft, G. M.; Mays, M. J.; Prater, B. E. *J. Chem. Soc. A-Inorg. Phys. Theor.* **1970**. 6, 956-968.

15. (a) Hendrich, M. P.; Gunderson, W.; Behan, R. K.; Green, M. T.; Mehn, M. P.; Betley, T. A.; Lu, C. C.; Peters, J. C. *Proc. Natl. Acad. Sci*. **2006**. 103, 17107-17112. (b) Scepaniak, J. J.; Vogel, C. S.; Khusniyarov, M. M.; Heinemann, F. W.; Meyer, K.; Smith, J. M. *Science*. **2011**. 331, 1049-1052. (c) Lewis, R. A.; Smiles, D. E.; Darmon, J. M.; Stieber, S. C. E.; Wu, G.; Hayton, T. *Inorg. Chem.* **2013.** 52, 8218-8227. (d) Searles, K.; Fortier, S.; Khusniyarov, M. M.; Carroll, P. J.; Sutter, J.; Meyer, K.; Mindiola, D. J.; Caulton, K. G. *Angew. Chem., Int. Ed*. **2014.** 53, 14139-14143.

16. Rittle, J.; and Peters, J. C. *Manuscript in preparation*.

17. Chaudhuri, P.; Verani, C. N.; Bill, E.; Bothe, E.; Weyhermuller, T.; Wieghardt, K. *J. Amer. Chem. Soc.* **2001**. 123, 2213-2223.

18. (a) Kahlal, S.; Saillard, J-Y.; Hamon, J-R.; Manzur, C.; Carrillo, D. *J. Chem. Soc., Dalton Trans.* **1998**. 1229-1240. (b) Tonks, I. A.; Durrell, A. C.; Gray, H. B.; Bercaw, J. E. *J. Amer. Chem. Soc.* **2012**. 134, 7301-7304.

19. Cundari, T. R. *J. Amer. Chem. Soc.* **1992**. 114, 7879-7888.

20. Pimentel, G. C. *J. Chem. Phys.* **1951**. 19, 446-448.

21. (a) Moret, M-E.; Peters, J. C.; *J. Amer. Chem. Soc.* **2011**. 133, 18118-18121. (b) Suess, D. L. M.; Peters, J. C. *J. Amer. Chem. Soc.* 135, 4938-4941.

22. Mo, Y.; Zhang, Y.; Gao, J. *J Amer. Chem Soc.* **1999**. 121, 5737-5742.

23. Green, M. L. H. *J. Organomet. Chem.* **1995**. 500, 127-148.

24. Donovan-Mtunzi, S.; Richars, R. L.; Mason, J. *J. Chem Soc., Dalton. Trans.* **1984**. 1329-1332.

25. Binsch, G.; Lambert, J. B.; Roberts, B. W.; Roberts, J. D. *J. Amer. Chem. Soc.* **1964**. 86, 5564-5570.

26. (a) Pfirrmann, S.; Limberg, C.; Herwig, C.; Knispel, C.; Braun, B.; Bill, E.; Stosser, R. *J. Amer. Chem. Soc.* **2010**. 132, 13684-13691. (b) Bowman, A. C.; Milsmann, C.; Bill, E.; Turner, Z. R.; Lobkovsky, E.; DeBeer, S.; Wieghardt, K.; Chirik, P. J. *J. Amer. Chem. Soc.* **2011**. 133, 17353-17369. (c) Lin, H-J.; Siretanu, D.; Dickie, D. A.; Subedi, D.; Scepaniak, J. J.; Mitcov, D.; Clerac, R.; Smith, J. M. *J. Amer. Chem. Soc.* **2014**. 136, 13326-13332.

27. Preparations of complex **4.7** are invariably contaminated with **4.2** and other species which are evident in the EPR and ^{57}Fe Mössbauer spectra. However, the

spectroscopic signatures of **4.7** are fortuitously well-isolated from the impurities in these spectra. Refer to Appendix 1 for further discussion.

28. (a) Yandulov, D. V.; Schrock, R. R. *Inorg. Chem.* **2005**. 44, 1103-1117. (b) Munisamy, T.; Schrock, R. R. *Dalton Trans.* **2012**. 41, 130-137.
29. Mayer, J. M. *Annu. Rev. Phys. Chem.* **2004**. 55. 363-390.
30. (a) Schrock, R. R. *Angew. Chem., Int. Ed*. **2008**. 47, 5512-5522. (b) Schenk, S.; Le Guennic, B.; Kirchner, B.; Reiher, M. *Inorg. Chem.* **2008**. 47, 3634-3650.
31. (a) Takahashi, T.; Mizobe, Y.; Sato, M.; Uchida, Y.; Hidai, M. *J. Amer. Chem. Soc.* **1979**. 101, 3405-3407. (b) Chatt, J.; Fakley, M. E.; Hitchcock, P. B.; Richards, R. L.; Luong-Thi, N. T. *J. Chem. Soc., Dalton Trans.* **1982**. 345-352.
32. Rodrigues, M. M.; Bill, E.; Brennessel, W. W.; Holland, P. L. *Science*. **2011**. 334, 780-783.

Chapter 5. Proton Coupled Reduction of Fe-CN to CH_4 and NH_3

5.1. Introduction

The proton-coupled reduction of $CN^{(-)}$ to CH_4 and NH_3 is conceptually related to the reduction of N_2 to two equivalents of NH_3.[1] In this regard, nitrogenase enzymes, as well as the isolated cofactors, catalyze the transformation of $CN^{(-)}$ to CH_4 and NH_3 alongside small quantities of methylamine and C-C coupled alkanes and alkenes.[2] Synthetic chemists have attempted to understand these reactions through the preparation of well-defined mono- and polynuclear complexes that support partially-reduced and protonated cyanide (CNH_x) ligands.[3,4] Yet the complete conversion of a CN ligand to CH_4 and NH_3 in synthetic systems has little precedence. In general, well-defined transition metal systems that cleave the triple bond of $CN^{(-)}$ in any fashion are exceedingly rare.[5] The only abiological examples of $CN^{(-)}$ reduction to CH_4 are that catalyzed by the isolated nitrogenase cofactors and an electrochemical example at Ni electrodes.[2b,6]

To complement our efforts in understanding the proton-coupled reduction of $Fe(N_2)$ species to NH_3,[7] we report here that Fe(CN) complexes supported by the $[SiP^{iPr}_3]$ ligand framework release substantial quantities of NH_3 and CH_4 on exposure to proton and electron equivalents ($[SiP^{iPr}_3]$ = tris(2-(di-*iso*-propylphosphino)phenyl)silyl$^{(-)}$). Stoichiometric protonation reactions of these Fe(CN) complexes occur at the N-atom to furnish unusual Fe(CNH) and $Fe(CNH_2)$ species which are the subject of a suite of spectroscopic and crystallographic studies. These and related compounds are remarkably stable in solution, especially in comparison to the N_2-derived $Fe(N_xH_y)$ species we have recently disclosed. Nonetheless, the N-H bonds of these $Fe(CNH_x)$ species are susceptible to H-atom abstraction, and thermochemical measurements are used to provide quantitative estimates of the corresponding homolytic bond enthalpies. These thermodynamic analyses

provide unprecedented insight into the reactivity patterns of the Fe(CNH_x) and Fe(N_xH_y) species that may be relevant to the cleavage of N_2 and CN to NH_3 (and CH_4) in synthetic and biological systems.

5.2. Results

5.2.1. Synthesis and Interconversion of Fe(CNH_x) Species

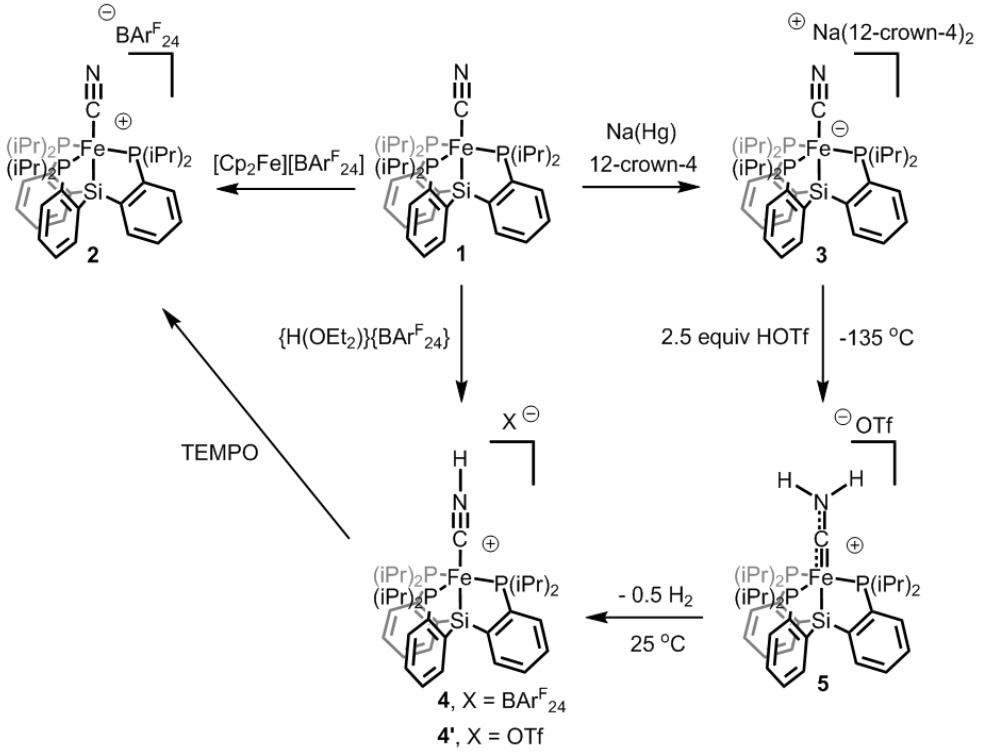

Scheme 5.1. Synthesis of [SiP$^{iPr}_3$]Fe(CNH_x) compounds

The synthetic entry into this work was made by the reaction of [SiP$^{iPr}_3$]Fe(Cl)[7b] with either NaCN, K^{13}CN, or KC^{15}N, furnishing the various isotopomers of [SiP$^{iPr}_3$]Fe(CN) (**5.1**) as pink solids. Compound **5.1** was found to display rich redox behavior and its reaction with [Cp_2Fe][BAr$^F_{24}$] yields the one-electron oxidized {[SiP$^{iPr}_3$]Fe(CN)}{BAr$^F_{24}$} (**5.2**) as a microcrystalline green solid (BAr$^F_{24}$ = (3,5-$(CF_3)_2$-$C_6H_3)_4B^{(-)}$) (Scheme 5.1, Figure 5.1). Likewise, the reduction of **5.1** with Na(Hg) in the presence of 12-crown-4

furnishes one-electron reduced {Na(12-crown-4)$_2$}{[SiP$^{iPr}_3$]Fe(CN)} (**5.3**) as a dark brown solid. The solid-state structures of complexes **5.1**-**5.3** were determined and reveal a trigonal-bipyramidal Fe center in **5.1**, **5.2**, and **5.3** (τ_5 = 1.02, 0.85, 1.03, respectively)[8] with the CN ligand positioned *trans* to the apical Si atom. Notably, these Fe-CN complexes are nearly isostructural with the Fe-N_2 complexes supported by the [SiP$^{iPr}_3$] platform.[7b] Complexes **5.1**-**5.3** were characterized by a suite of spectroscopic and analytical techniques: the pertinent results are tabulated in Table 5.1, and spectra can be found in Appendix 2.

While the reduction of **5.1** to **5.3** may represent a first step in CN activation, an initial protonation event is equally plausible. Compound **5.1** was found to react instantly with the strong acid {H(OEt$_2$)$_2$}{BAr$^F_{24}$} to afford the cationic hydrogen-isocyanide complex, {[SiP$^{iPr}_3$]Fe(CNH)}{BAr$^F_{24}$} (**5.4**) (Scheme 5.1). This reaction is reversible and **5.1** is reformed upon exposure of THF solutions of **5.4** to NEt$_3$. The solid-state structure of **5.4** reveals a linear C-N-H linkage (176(3)^o) (Figure 5.1) as the N-H proton could be located in the Fourier difference map. The CNH ligand is engaged in a strong hydrogen bonding interaction with a molecule of diethyl ether (d(N···O): 2.639(3) Å. <(O···H-N): 173(4)^o). The KBr IR spectrum of **5.4** displays very broad absorbances that span from 3100 to 1900 cm^{-1}, a feature that may arise from the coupling of N-H and C≡N vibrational modes and a continuum of hydrogen bonding interactions in this non-crystalline state.[3]

Compound	**5.1**	**5.2**	**5.3**	**5.4**	**5.5**	**5.6**	**5.7**	**5.8**	**5.9**	**5.10**
d(Fe-C)[a]	1.973(1)	2.024(2)	1.949(2)	1.913(3)	1.800(4)[j]	1.708(1)	1.737(2)	1.821(2)	1.732(3)	1.913(3)
d(C-N)[a]	1.168(1)	1.130(3)	1.170(3)	1.144(4)	1.216(5)[j]	1.326(1)	1.310(2)	1.186(2)	1.338(5)	1.156(4)
<(Si-Fe-C)[b]	179.06(5)	179.55(6)	178.84(6)	178.32(8)	176.0(1)[j]	170.06(4)	169.70(6)	176.50(5)	168.0(1)	175.93(9)
τ_5[c]	1.02	1.03	0.85	1.00	0.80[j]	0.75	0.84	0.89	0.81	0.92
ν(C≡N)[d]	2076	1944	2014	~2029	1615	1520	1559	1970,1912[k]	1536	2128
δ[e]	0.44	0.42	0.31	0.43	0.13	0.06	0.19	0.25	0.16	0.41
ΔE_Q[e]	1.68	2.54	1.44	3.31	1.50	1.12	1.51	1.47	1.51	3.14
Spin State[f]	1	3/2	1/2	1	1/2	0	1/2	1/2	1/2	1
Fe K-Edge Energy[g]	7120.5	7122.6	n.d.[i]	7120.5	7120.9	7119.8	7121.6	n.d.[i]	n.d.[i]	n.d.[i]
E^{o} [h]	-2.06	-0.38	-3.05	-1.27	n.d.[i]	n.d.[i]	-1.27	-2.32	-1.27	-1.27

Table 5.1. Physical parameters for compounds **5.1-5.10**. [a]Bond distance in Å. [b]Bond angle in degrees (^{o}). [c]Reference 8. [d]KBr or Solid-state IR. [e]Mössbauer parameters in mm/s collected at 80 K at zero field. [f]As judged by the room temperature solution-state magnetic moment and/or EPR spectroscopy at 20 K. [g]Referenced to Fe foil at 7111.3 eV. [h]Observed reduction potential in 0.1 M [TBA][PF_6] THF electrolyte. [i]Not determined. [j]Values from one of two independent molecules in the unit cell. [k]Two features assigned to the ν(C≡N) are consistently observed for **5.8** in the solid state.

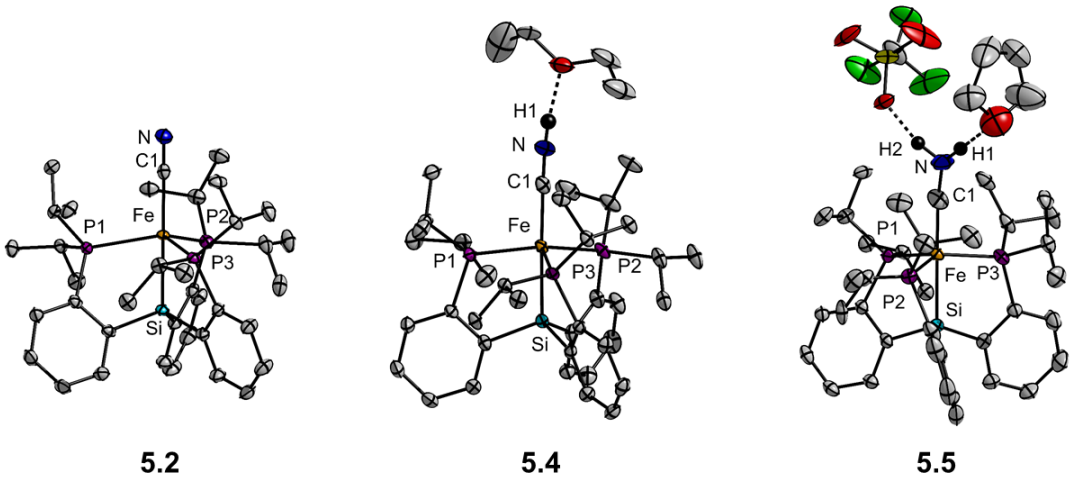

5.2 **5.4** **5.5**

Figure 5.1. X-ray diffraction crystal structures of **5.2**, **5.4**, and **5.5** with thermal ellipsoids drawn at 50% probability. Hydrogen atoms (excepting the N-H's of **5.4** and **5.5**), the BAr^{F}_{24} counteranions of **5.2** and **5.4** and co-crystallized solvent molecules have been removed for clarity. Two independent molecules of **5.5** are found in the unit cell and only one is shown.

Further activation of the CN ligand was achieved by protonation of the anionic FeCN complex **5.3**. Combining **5.3** with 2.5 equivalents of trifluoromethanesulfonic acid (HOTf) in thawing 2-MeTHF affords the cationic iron aminocarbyne complex, $\{[SiP^{iPr}_3]Fe(CNH_2)\}\{OTf\}$ (**5.5**) (Scheme 5.1). Solid IR spectra of **5.5** reveal strong absorptions centered at 3232 and 3031 cm^{-1} that shift to 2408 and 2247 cm^{-1} in **5.5-*d*$_2$** (prepared from **5.3** and HOTf-d_1) and can be assigned to N-H stretching frequencies engaged in strong hydrogen bonding interactions.[9] Crystals of **5.5** suitable for X-ray diffraction studies could be grown from a THF/pentane mixture at -35 ^{o}C and the resultant X-ray diffraction structure is shown in Figure 5.1. A shortened Fe-C bond in **5.5** relative to **5.1**-**5.4** is indicative of some degree of multiple bond character (Table 5.1). The CNH_2

hydrogen atoms were not directly located but their presence is inferred by close contacts with the triflate counteranion and a molecule of THF. An average C-N bond length of 1.223(5) Å is consistent with a double bond and indicates a large contribution of form B in the two canonical resonance forms of terminal aminocarbyne complexes (Scheme 5.2).[1,3] Only a handful of mononuclear CNH_2 complexes have been reported but compound **5.5** is the first example of a terminal $Fe(CNH_2)$ complex.[3b, 10]

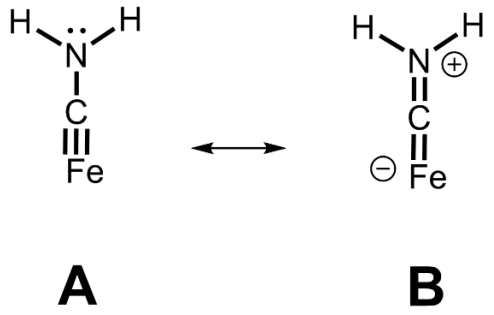

Scheme 5.2. Canonical resonance structures of the $Fe(CNH_2)$ unit in **5.5**

5.2.2. Reduction of $[SiP^{iPr}_3]Fe(CN)$ to CH_4 and NH_3

Having demonstrated the ability of the $[SiP^{iPr}_3]Fe$ fragment in stabilizing partially-reduced (CNH_x) ligands, we explored the possibility of cleaving the CN ligand in **5.1** with additional proton and electron equivalents. In this context, ethereal solutions of **5.1** were found to react with 20 equivalents of Cp^*_2Co and $[2,5\text{-}Cl_2\text{-}PhNH_3][OTf]$ at -78 °C to furnish appreciable quantities of NH_3 on warming to room temperature overnight.[11] An average of 0.33(4) equiv of $[NH_4][Cl]$ was detected by the Indophenol method over 4 runs. To ascertain the full complement of nitrogenous products, **^{15}N-5.1** was subjected to these conditions and volatiles were vacuum-transferred onto anhydrous HCl and subsequently dissolved in DMSO-d_6.^{15}N-enriched $[NH_4][Cl]$ was the sole nitrogen-containing product detected by ^{1}H NMR spectroscopy under these conditions (Appendix 2). Control reactions that replace **5.1** with [TBA][CN] as a source of $CN^{(-)}$ do not furnish detectable quantities of

NH_3, implicating a necessary role [SiP^{iPr}_3]Fe in the activation of bound CN towards proton-coupled reduction.

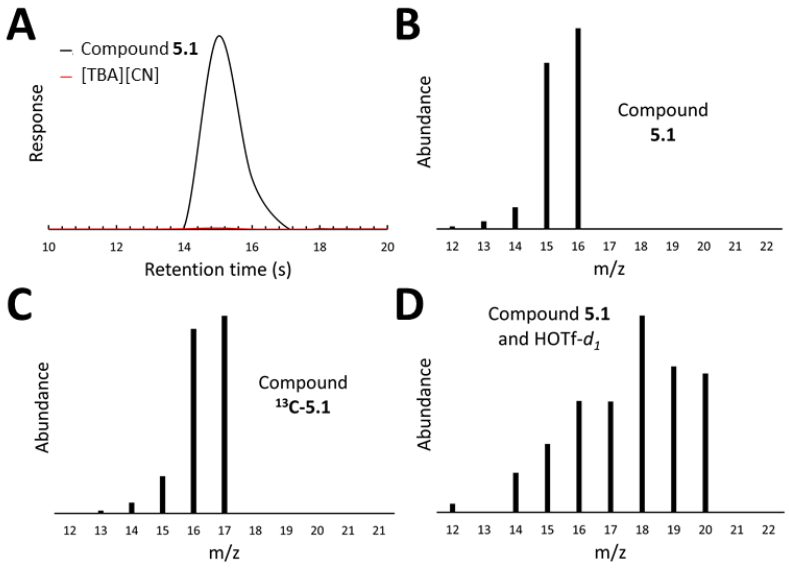

Figure 5.2. (A) GC-FID chromatograms of sampled reaction headspaces in the reaction of (black) **5.1** or (red) [TBA][CN] with 20 equiv Cp^*_2Co and 20 equiv HOTf in Et_2O. (B) Mass spectrum of $^{12}CH_4$ produced from compound **5.1**. (C) Mass spectrum of $^{13}CH_4$ produced from compound **^{13}C-5.1**. (D) Mass spectrum of CH_xD_{4-x} produced from compound **5.1** and HOTf-d_1.

To ascertain the C-containing product(s) of these reactions, the headspaces of these reactions were analyzed by gas chromatography (Figure 5.2). An average 0.41(8) equivalents of CH_4 was detected as the primary reduction product. Small amounts (<0.03 equiv) of other C-containing products were also observed but their identity is presently unknown. Exposure of **^{13}C-5.1** to these reaction conditions furnishes $^{13}CH_4$ as the dominant isotopomer detected by GC-MS (Figure 5.2C). Finally, replacing [2,5-Cl_2-$PhNH_3$][OTf] with HOTf-d_1 as the proton source furnishes a mixture of partially deuterated methane

products with masses up to and including 20 (Figure 5.2D). Very little CH_4 is detected (0.007 equiv) when [TBA][CN] replaces **5.1** in these reactions Figure 5.2A).

To gain insight into these reactions, the intermediacy of **5.5** in NH_3 production was tested. In the absence of additional proton and electron equivalents, compound **5.5** is unstable in solution at room temperature, and analysis of the CN-derived reaction products reveals small but detectable quantities of NH_3 (0.09 equiv NH_3). H_2 is a significant byproduct of this decomposition (0.24 equiv H_2, quantified by gas chromatography) and Fe-containing products identified by ^{1}H NMR spectroscopy are {[SiP$^{iPr}_3$]Fe(CNH)}{OTf} (**5.4'**) and [SiP$^{iPr}_3$]Fe(OTf).[12] Independently prepared **5.4'**, derived from the reaction of **5.1** and HOTf, slowly converts to [SiP$^{iPr}_3$]Fe(OTf) in THF solution, presumably with the loss of the intact CNH ligand upon coordination of the OTf anion. The dissociation of a (CNH_x) ligand is therefore a likely competing process during the proton-coupled reduction of **5.1** and may in part account for the moderate yields (<41 %) of CH_4 and NH_3 formed under the conditions described above.

5.2.3. C-N Bond Cleavage of an Fe(CNMe$_2$) Complex

The Fe(CNH$_2$)$^{(+)}$ complex **5.5** is a 17 electron complex and therefore its neutral analogue, [SiP$^{iPr}_3$]Fe(CNH$_2$) may be accessible and relevant in the reductive conditions described above. Attempts to prepare this complex from **5.5** have been futile, however, and we sought a model complex for this species in order to independently probe its reactivity. The neutral di*alkyl*aminocarbyne complex, [SiP$^{iPr}_3$]Fe(CNMe$_2$) (**5.6**) can be prepared in a one pot reaction via sequential addition of Na(Hg) and MeOTf to **5.1** (82 % yield) (Table 5.1). Furthermore, **5.6** is readily oxidized by [Cp$_2$Fe][BAr$^F_{24}$] to afford

{[SiP$^{iPr}_3$]Fe(CNMe$_2$)}{BAr$^F_{24}$} (**5.7**). The salient spectroscopic properties of **5.7** closely match those of the isoelectronic Fe(CNH$_2$)$^{(+)}$ **5.5**.

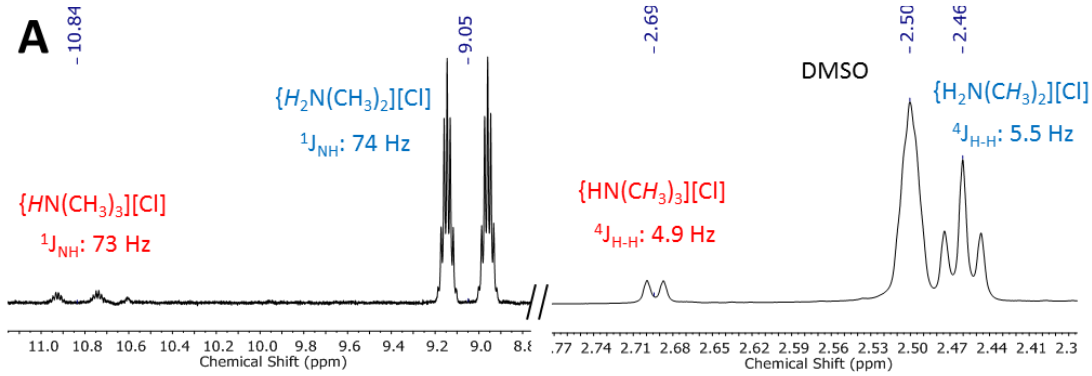

Figure 5.3. Truncated ^{1}H NMR spectrum (500 MHz) of [H$_2$^{15}NMe$_2$][Cl] and [H^{15}NMe$_3$][Cl] produced from the reductive cleavage of **^{15}N-5.6** in DMSO-*d*$_6$. The vertical scale of the downfield region has been increased to emphasize the features associated with the NH protons.

The Fe(CNMe$_2$) **5.6** was found to react with proton and electron equivalents to afford a mixture of CH$_4$, Me$_2$NH and small amounts of Me$_3$N, albeit under more forcing conditions. Whereas **5.1** is selectively reduced to CH$_4$ and NH$_3$ with Cp*$_2$Co and [2,5-Cl$_2$-PhNH3][OTf], exposure of Et$_2$O solutions of **5.6** to these reagents does not furnish appreciable quantities of CH$_4$. Stronger proton and electron equivalents were required to induce C-N bond scission in this case, and 0.47 equiv of CH$_4$ is detected when **5.6** is exposed to 10 equiv of KC$_8$ and HOTf. GC-MS analysis of the CH$_4$ produced from **^{13}C-5.6** confirm that the CH$_4$ is derived from the carbyne carbon. Multinuclear NMR spectroscopy was used to characterize the ^{15}N-containing product of these reaction mixtures (Figure 5.3, Appendix 2). Volatile products were vacuum-transferred onto anhydrous HCl as described above, and features assigned to the N-H protons of [H^{15}NMe$_3$][Cl] and [H$_2$^{15}NMe$_2$][Cl] are

observed at δ = 10.84 and 9.05 ppm, respectively, in the ^{1}H NMR spectrum (Figure 5.3). These features display well-resolved coupling to the ^{15}N nucleus and CH_3-derived protons, and heteronuclear multiple quantum coherence (HMQC) experiments allow for the detection of the ^{15}N and ^{13}C nuclei of these products. Finally, comparison of the ^{1}H and ^{13}C NMR chemical shifts to authentic samples of these ammonium salts confirms their assignment. Dimethylamine is the dominant product, accounting for 90% of the ^{15}N-containing products, and its formation is consistent with a mechanism whereby an early cleavage of the Fe(CN)-derived C-N bond occurs and is proceeded by the formation of CH_4 (Scheme 5.3, top). Although only a minor product, the generation of NMe_3 from **5.6** is interesting, and this product may be generated if H-atom equivalents are delivered to the carbyne carbon of **5.6** while the C-N bond remains intact (Scheme 5.3, bottom). The fact that different reaction conditions are required for the activation of the C-N bond in Fe($CNMe_2$) **5.6** clouds any extension of these mechanistic results to those of proton-coupled reduction of Fe(CN) **5.1**. Nonetheless, a mechanism analogous to that shown in the bottom of Scheme 5.3 does not appear to be operative in the proton-coupled reduction of Fe(CN) **5.1** since methylamine is not observed as a product of those reactions (vide supra).

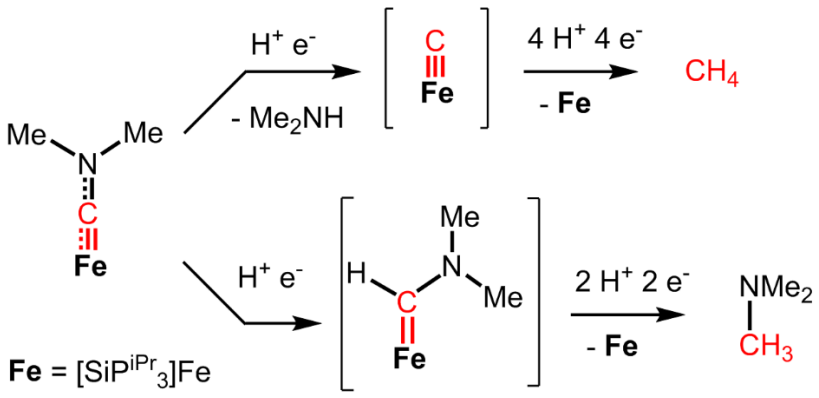

Scheme 5.3. Possible routes to the formation of $HNMe_2$ and CH_4 (top) and NMe_3 from compound **5.6**.

5.2.4. H-atom Transfer Reactivity of an Fe(CNH) Complex

Compounds **5.2**, **5.4,** and **5.5** form an unusual series of complexes wherein the cations differ solely by a single H-atom (Figure 5.1). In principle, the activation of the CN ligand could be mediated by the concerted delivery of H-atoms to the Fe(CN) **5.2** to form **5.4** or **5.5**. However this reactivity is not observed: 9,10-dihydroanthracene is unreactive with **5.2** after 24 hours, and **5.2** is only slowly decomposed by TEMPOH to unidentified Fe species over the course of hours in THF solution. In fact, **5.4** is highly susceptible to H-atom *abstraction*, and reacts instantly with 1 equivalent of TEMPO to form **5.2** (Scheme 5.1). These reactions indicate that the homolytic bond dissociation enthalpy (BDE) of the N-H bond of **5.4** is significantly lower than that of the BDE_{OH} in TEMPOH (71 kcal/mol in MeCN).[13]

The prolonged stability of the Fe(CN) **5.1**, $Fe(CN)^{(+)}$ **5.2** and $Fe(CNH)^{(+)}$ **5.4** in solution permits the collection of reliable thermochemical data that may be used to provide a quantitative estimate of the BDE_{NH} of **5.4**. The BDE_{NH} is proportional to the sum of its acidity (pKa) and the oxidation potential (E^0) of the corresponding conjugate base (N^-), and may be estimated by the application of equation 5.1,[13]

$$BDE(N-H) = 23.06 * E^o(N^-) + 1.37 * pK_a(N-H) + C \qquad \textbf{Eqn 5.1}$$

where C is a solvent-dependent constant reported as 66 kcal/mol in THF.[14] The cyclic voltammograms of **5.2** and **5.4** in a THF electrolyte (0.1 M [TBA][PF_6]) reveal reversible one-electron oxidation potentials of -0.38 and -1.27 V vs Fc/Fc^+, respectively (Figure 5.4A, Appendix 2). To determine the acidity of **5.4** in THF solution, compound **5.1** was titrated with a series of acids and these reaction mixtures were probed with UV-Visible spectroscopy. [$HNEt_3$][OTf] (pKa: 13.7) or [LutH][OTf] (pKa: 9.5) were not effective in

protonating **5.1** but the stoichiometric addition of chlorinated anilinium salts caused the formation of equilibrium mixtures of **5.1** and **5.4** that persist for hours at room temperature (Figure 5.4B).[15] Spectrophotometric titrations performed with [2-Cl-PhNH$_3$][OTf] (pKa = 6.0 in THF) or [2,5-Cl$_2$-PhNH$_3$][OTf] (pKa = 4.5 in THF) and **5.1** furnish an average pKa(FeCN-H) value for **5.4** of 5.6(1).[15]

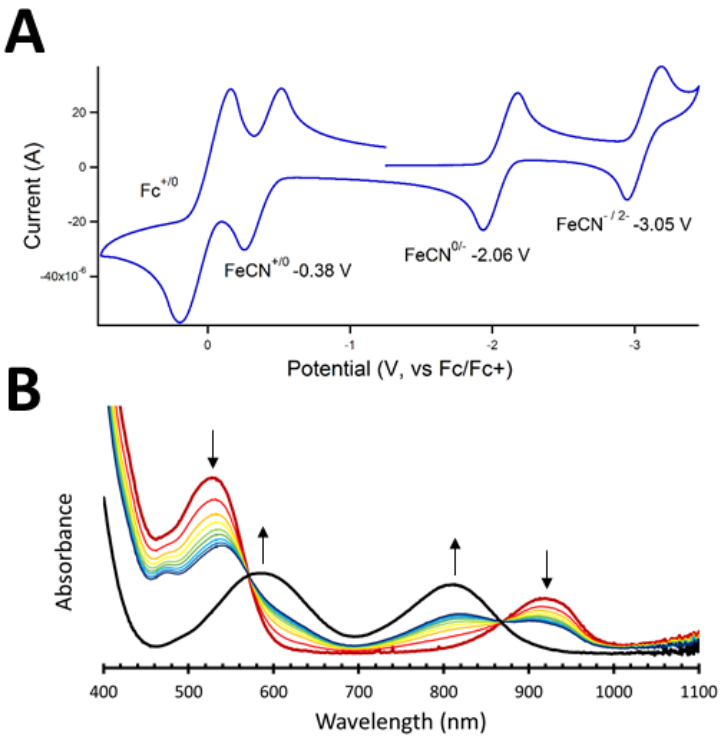

Figure 5.4. (A) Cyclic voltammogram obtained on a 1 mM solution of **5.1** in THF electrolyte (0.1 M [TBA][PF$_6$]) in the presence of ferrocene (Fc) to serve as an internal reference (scan rate 100 mV/s). (B) UV-visible absorption spectra of **5.1** (dark Red) and **5.4'** (Black) in THF at 25 ^{o}C. The other traces were obtained following the sequential addition of 0.33 molar equivalents of [2-Cl-PhNH$_3$][OTf] to **5.1** with the blue trace derived from the net addition of 2.66 equiv [2-Cl-PhNH$_3$][OTf] to **5.1** and showing an equilibrium mixture of **5.1** and **5.4'**. Arrows indicate features that increase or decrease during this experiment.

With the relevant thermodynamic parameters in hand, the BDE_{NH} of compound **5.4** can be estimated with Equation 5.1 and is found to be 65(1) kcal/mol. The magnitude of this value is consistent with the complete and irreversible nature of the hydrogen atom abstraction reaction of **5.4** with TEMPO. Moreover, comparative gas-phase DFT calculations on the cations of **5.2** and **5.4** suggest a BDE_{NH} of 66 kcal/mol, in excellent agreement with the experimental value. The BDE_{NH} found for **5.4** is low, especially when compared to that of NH_3 (BDE_{NH}: 107.6, gas phase) and N_2H_4 (BDE_{NH}: 80.8, gas phase).[13] N-H bond strengths of comparable magnitude to those presented here were recently reported for NH_3-bound Ti^{III} and Zr^{III} complexes[16] and can be rationalized by the very negative reduction potentials displayed by these early transition metals.[17] In the present case, the Fe(CN) **5.1** is not highly-reducing (E^0(**5.1**): -0.38 V, vs Fc/Fc^+) but the $Fe(CNH)^{(+)}$ **5.4** bears an acidic proton (pKa 5.6), which, in part, contributes to the low BDE_{NH} value. As shown below, Fe-aminocarbyne complexes related to $Fe(CNH_2)^{(+)}$ **5.5** are significantly more reducing *and* carry acidic protons, resulting in remarkably low BDE_{NH} values.

5.2.5. Synthesis of Stable Fe(CNMe) Derivatives

Attempts to determine the BDE_{NH} of the $Fe(CNH_2)$ **5.5** by the methods described above are hampered by the tendency of this compound to spontaneously decay with the loss of H_2 (vide supra). Under equilibrium conditions, the instability of compound **5.5** with respect to the loss of H_2 implies the presence of an N-H bond with a BDE_{NH} that is less than, or equal to *half* of the BDE_{HH} of H_2 (106 kcal/mol in MeCN).[13] This instability in solution complicates the reliable measurement of redox and acidity data for **5.5**. Moreover,

attempts to synthesize the conjugate base of **5.5**, namely the neutral [SiP$^{iPr}_3$]Fe(CNH), result only in intractable mixtures of Fe species. We therefore prepared a series of stable methylisocyanide complexes (Scheme 5.4) to probe the BDE_{NH} of the related Fe[CN(Me)-H] species, which proved more amenable to such studies. The synthesis of these compounds closely follow that of the Fe(CNH_x) derivatives. Salient spectroscopic and structural data are tabulated in Table 5.1.

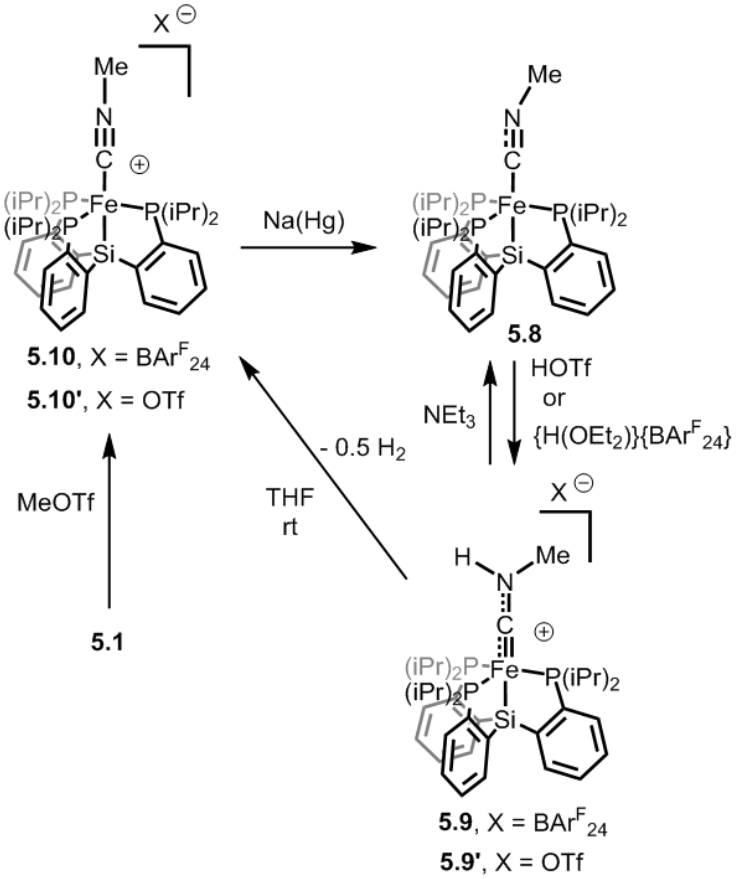

Scheme 5.4. Synthesis of Fe(CNMe) and Fe[CN(Me)H] complexes.

The neutral methylisocyanide complex, [SiP$^{iPr}_3$]Fe(CNMe) (**5.8**) (Scheme 5.4), is indefinitely stable in THF solutions at room temperature. The cyclic voltammogram collected on THF electrolyte solutions of **5.8** displays a reversible one-electron reduction

event at -2.32 V and a one-electron oxidation event at -1.27 V (Figure 5.5). Exposure of **5.8** to one equivalent of $\{H(OEt_2)_2\}\{BAr^F{}_{24}\}$ in Et_2O and subsequent workup furnishes the secondary aminocarbyne complex, $\{[SiP^{iPr}{}_3]Fe[CN(Me)H]\}\{BAr^F{}_{24}\}$ (**5.9**), as a purple solid that slowly converts to $\{[SiP^{iPr}{}_3]Fe(CNMe)\}\{BAr^F{}_{24}\}$ (**5.10**) in THF solution overnight with the concomitant loss of H_2 (Scheme 5.4) (0.4 equiv H_2 per Fe). The aminocarbyne complex **5.9** displays a sharp feature at 3337 cm^{-1} in its solid IR spectrum that shifts to 2478 cm^{-1} in **5.9-*d*$_1$** (prepared from **5.8** and $\{D(OEt_2)_2\}\{BAr^F{}_{24}\}$) and may be assigned to the N-H and N-D stretching frequencies, respectively. The cyclic voltammogram of freshly-prepared **5.9** in THF displays a reversible one-electron reduction event at -1.27 V (Figure 5.5). Compound **5.9** is readily deprotonated on exposure to a slight excess of NEt_3 in THF solution, reforming **5.8** and establishing reversible proton transfer under these conditions.

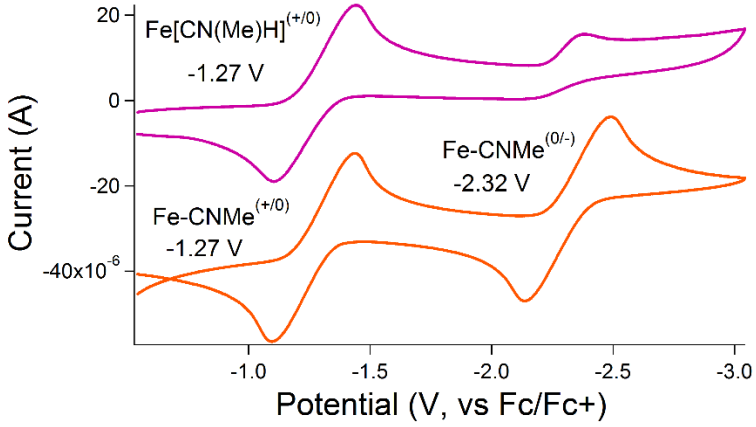

Figure 5.5. (A) Cyclic voltammograms obtained on 1 mM solutions of **5.9** (top) and **5.8** (bottom) in THF electrolyte (0.1 M $[TBA][PF_6]$). The traces were obtained at a scan rate of 100 mV/s.

5.2.6. Thermoneutral Proton and Electron Transfer Equilibria

Unlike the acid titration experiments with Fe(CN) **5.1**, the titration of Fe(CNMe) **5.8** with proton equivalents is complicated by competing electron transfer equilibria that are observed at intermediate stages of the titration (Figure 5.6). The complete conversion of **5.8** to {[SiP^{iPr}_3]Fe[CN(Me)H]}{OTf} (**5.9'**) is observed on exposure of 4 equiv of [2-Cl-$PhNH_3$][OTf] to THF solutions of **5.8**. At lower acid equivalents, features ascribable to **5.8** in the UV-visible spectrum initially decrease in intensity, and features assigned to those of the one-electron oxidized iron isocyanide complex {[SiP^{iPr}_3]Fe(CNMe)}{OTf} (**5.10'**) and the neutral iron aminocarbyne [SiP^{iPr}_3]Fe[CN(Me)H] (**5.11**) (vide infra) are apparent (Figure 5.6A). In a second phase, the expected features of the cationic Fe aminocarbyne **5.9'** grow in with the concomitant loss of features assigned to **5.11** (Figure 5.6B). Finally, at high concentrations of acid, the features assigned to **5.10'** decrease in intensity and reveal a clean spectrum of **5.9'**. This series of spectral changes has been repeatedly observed with a variety of chlorinated anilinium salts and with substoichiometric amounts of {$H(OEt_2)_2$}{BAr^F_{24}}. Inspection of the cyclic voltammetry data (vide supra) collected on the cationic Fe[CN(Me)H] **5.9** and its conjugate base **5.8** indicate that the *oxidation* of **5.8** (-1.27 V) occurs at the same potential as the *reduction* of **5.9** (Figure 5.5). During the acid titration experiment, solutions that contain both **5.8** and **5.9'** are generated and these species spontaneously disproportionate to an equilibrium mixture of **5.8**, **5.9'**, **5.10'**, and **5.11**.

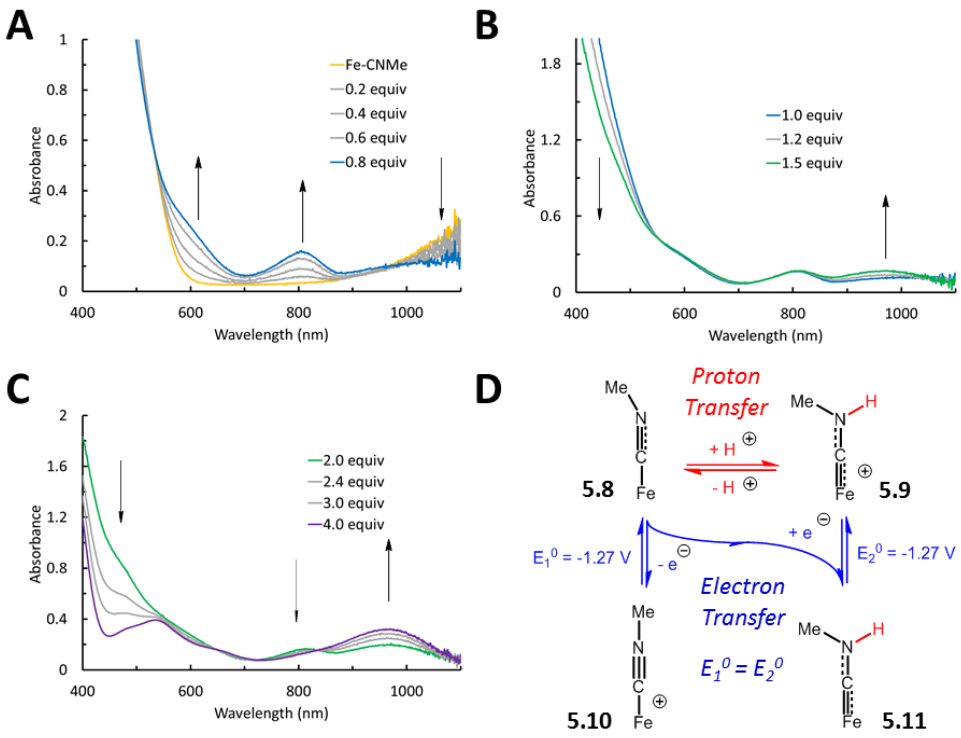

Figure 5.6. Representative UV-visible absorption spectra obtained following the sequential addition of the listed equivalents of [2-Cl-PhNH$_3$][OTf] to a THF solution of **5.8** at 25 ºC. Distinct phases of this addition are shown for clarity in tiles A, B, and C. (D) Tabulated reduction potential data for the relevant species. Arrows indicate features that increase or decrease during this experiment.

Direct evidence for the competing electron- and proton transfer processes observed in solutions containing **5.8** and **5.9** was obtained by NMR spectroscopy. The presented model predicts that diamagnetic Fe[CN(Me)H] **5.11** should accumulate in these solutions, and the generation of this species requires an intermolecular electron (or H-atom) transfer event between **5.8** and **5.9**. Therefore, diagnostic resonances in the ^{13}C and ^{15}N NMR spectra that can be assigned to the [CN(Me)H] ligand in **5.11** should be detectable. To test

this hypothesis and emulate the conditions at the midpoint of the acidity titrations described above, a 1:1:1 molar ratio of the Fe(CNMe) isotopomers **^{13}C-5.8**, **^{15}N-5.8**, and $\{H(OEt_2)_2\}\{BAr^F{}_{24}\}$ was dissolved in THF-d_8 at 193 K and analyzed by NMR spectroscopy. At this temperature, a sharp doublet ($^1J_{NH}$: 94 Hz) in the ^{15}N NMR spectrum appears at δ = 135.2 ppm that can be attributed to **^{15}N-5.11**. The chemical shift of this resonance compares well to that of the ^{15}N nucleus in the $Fe(CNMe_2)$ **^{15}N-5.6** (129.1 ppm, 293 K) and the magnitude of J_{NH} unambiguously confirms the presence of an N-H unit.[17] Two intense features are observed in the $^{13}C\{^1H\}$ NMR spectrum of the mixture containing **^{13}C-5.11**, at δ = 279.7 and 282.7 ppm that are assigned to aminocarbyne carbons.[19] The presence of two resonances likely arises from slightly different geometric isomers of **5.11** at low temperatures since **5.6** displays a similar pattern in its $^{13}C\{^1H\}$ NMR spectrum at this temperature (280.8 and 277.2 ppm) but only one feature is observed at 293 K (279.1 ppm) (Appendix 2). These NMR data unequivocally confirm the generation of **5.11** in these solutions, indicating that compounds **5.8** and **5.9** are subject to thermoneutral electron (or H-atom) transfer in THF solutions.

5.2.7. Estimation of the N-H bond Enthalpy of Iron Aminocarbyne Complexes

Having established that the proton- and electron transfer equilibria in THF are rapid and reversible, the acidity value for Fe[CN(Me)H] **5.9'** can be determined by simulation of the spectral data at a known acid concentration to define the relative proportions of the individual Fe species (refer to Appendix 2 for a detailed discussion of this procedure). However, the pure spectrum of **5.11** is unknown as attempts to prepare this compound in pure form have been unsuccessful ($\tau_{(1/2)}$ ~ 1 hour in THF at 20 ^{o}C). The neutral dialkylaminocarbyne complex **5.6** is likely to bear a similar electronic structure to **5.11**,

providing a model UV-Visible spectrum of this species. Indeed, the spectra shown in Figure 5.6 are well-simulated by a linear combination of the pure spectra of **5.8**, **5.9'**, **5.10'**, and **5.6** (as a surrogate for **5.11**) (Appendix 2). Using this procedure and analyzing the spectral data obtained by titrating **5.8** with [$PhNH_3$][OTf] (pKa = 7.97), [4-Cl-$PhNH_3$][OTf] (pKa = 6.97), and [2-Cl-$PhNH_3$][OTf] (pKa = 5.98), reveals an average pKa of 7.1(3) for the acidic proton of Fe[CN(Me)H] **5.9'** in THF.

Having established the redox potential and acidity values for **5.8** and **5.9'**, the relevant BDE_{NH} of **5.9'** may be estimated with Equation 5.1 and found to be 46(1) kcal/mol. A BDE_{NH} of this magnitude is very low but consistent with the tendency of **5.9'** to spontaneously evolve H_2, which requires a $BDE_{NH} \leq 53$ kcal/mol under equilibrium conditions. The parent $Fe(CNH_2)^{(+)}$ **5.5** also evolves H_2 (vide supra) and by extension must therefore display a BDE_{NH} of comparable magnitude to **5.9'**. Indeed, comparative gas-phase DFT calculations on the cations of **5.5** and **5.4** predict a BDE_{NH} of 47 kcal/mol in **5.5**, remarkably similar to that found experimentally for **5.9'** (Appendix 2). The loss of H_2 from these species is unusual but may in part account for the low efficiency of CH_4 and NH_3 production. H_2 evolution reactions mediated by transition metal complexes are generally thought to proceed via metal-bound hydride (M-H) intermediates[20], and the corresponding BDE_{MH} values for these species are similar in magnitude to that of the BDE_{NH} of **5.9'**.[13,21] In the present case, the enthalpy for this balanced reaction (Equation 5.2),

$$2\,[\mathbf{5.9'}] \rightarrow 2\,[\mathbf{5.10'}] + H_2 \qquad \textbf{Eqn 5.2}$$

can be estimated as -14 kcal/mol, employing the BDE_{HH} of H_2 in MeCN (106 kcal/mol). This analysis can be extended to the $Fe(CNH)^{(+)}$ **5.4**, which is *stable* with respect to the loss of H_2 and formation of **5.2**.

$$2\,[\mathbf{5.4}] \rightarrow 2\,[\mathbf{5.2}] + H_2 \qquad \textbf{Eqn 5.3}$$

The enthalpy of Equation 5.3 is estimated to be highly unfavorable (+26 kcal/mol), consistent with the prolonged stability of **5.4** in solution at ambient temperatures.

5.2.8. Attempts to Protonate $[SiP^{iPr}_3]Fe(N_2)$

The activation of the CN ligand in compound **5.1** to form CH_4 and NH_3 is conceptually related to the proton-coupled reductive cleavage of Fe-bound N_2 to form two equivalents of NH_3. While comparatively mild reagents (Cp^*_2Co and [2,5-Cl_2-PhNH][OTf]) effect the cleavage of the CN ligand in **5.1**, the successful conversion of $[SiP^{iPr}_3]Fe(N_2)$ (**5.11**) to NH_3 apparently requires proton equivalents of higher acidity and electron equivalents that are more reducing, namely $\{H(OEt_2)_2\}\{BAr^F_{24}\}$ and KC_8.[7a] This discrepancy implies an inherent difficulty (kinetic, thermodynamic, or both) in delivering H-atom equivalents to an $Fe(N_2)$ unit, relative to similar reactions with analogous Fe(CN) species. Put another way, the BDE_{NH} values for one or more intermediate $Fe(NNH_x)$ species formed on the protonation of $Fe(N_2)$ species may be lower than those of the corresponding $Fe(CNH_x)$ species (Equation 5.1). The determination of a BDE_{NH} of an $Fe(NNH_x)$ species is therefore of great interest.

A few observations suggest that the BDE_{NH} of the neutral $[SiP^{iPr}_3]Fe(NNH)$ is extraordinarily weak. As described in Chapter 4, the addition of stoichiometric proton equivalents to $[SiP^{iPr}_3]Fe(N_2)^{(-)}$ in hopes of preparing the neutral $[SiP^{iPr}_3]Fe(NNH)$ results in immediate oxidation at ambient temperatures, with concomitant formation of H_2. If these

reactions are performed at cryogenic temperatures, $[SiP^{iPr}_3]Fe(NNH_2)$ and $[SiP^{iPr}_3]Fe(N_2)$ are detectable by EPR and ^{57}Fe Mössbauer methods (Appendix 1). Similar mixtures are obtained upon the reaction of $[SiP^{iPr}_3]Fe(NNH_2)^{(+)}$ with the weak base NEt_3 at similar temperatures. The formation of these compounds may be explained by a disproportionation reaction of the formed $[SiP^{iPr}_3]Fe(NNH)$, via intermolecular H-atom transfer, and suggests that the BDE_{NH} of the neutral $Fe(NNH_2)$ is *stronger* than that of the neutral Fe(NNH). DFT calculations support this argument (vide infra).

Since the cationic Fe(CNH) **5.4** displays remarkable stability, we were curious whether the *cationic* $[SiP^{iPr}_3]Fe(NNH)$ could be accessed. The oxidation potential of $[SiP^{iPr}_3]Fe(N_2)$ (E^0: -1.0 V) has been previously reported[7b]. The direct estimation of the BDE_{NH} of the hypothetical $[SiP^{iPr}_3]Fe(NNH)^{(+)}$ proved impossible, however, due to the weakly basic properties of the neutral $[SiP^{iPr}_3]Fe(N_2)$. Addition of stoichiometric quantities of chlorinated anilinium salts or $\{H(OEt_2)_2\}\{BAr^F_{24}\}$ to $[SiP^{iPr}_3]Fe(N_2)$ in THF at 25 ^{o}C resulted in immediate oxidation to form $[SiP^{iPr}_3]Fe(OTf)$ and $\{[SiP^{iPr}_3]Fe(N_2)\}\{BAr^F_{24}\}$, respectively, prohibiting any further investigations at this temperature.[7b] Combining solutions of $[SiP^{iPr}_3]Fe(N_2)$ with 1-5 equivalents of $\{H(OEt_2)_2\}\{BAr^F_{24}\}$ ($pKa_{THF} \sim 0$)[22] at -100 ^{o}C does not cause a detectable change in the EPR signatures of the $[SiP^{iPr}_3]Fe(N_2)$ present in these frozen reaction mixtures, and upon warming these signals are lost entirely, presumably due to the generation of EPR-silent $\{[SiP^{iPr}_3]Fe(N_2)\}\{BAr^F_{24}\}$. These experiments indicate that $[SiP^{iPr}_3]Fe(N_2)$ is not protonated by $\{H(OEt_2)_2\}\{BAr^F_{24}\}$ (at the N-atom or otherwise) at -100 ^{o}C and therefore that the pKa of the putative $[SiP^{iPr}_3]Fe(NNH)^{(+)}$ must be ≤ 0 in THF solution.[23,24] According to Equation 5.1, the BDE_{NH} found for the hypothetical $[SiP^{iPr}_3]Fe(NNH)^{(+)}$ species is ≤ 43 kcal/mol,

significantly less than that displayed by the cationic Fe(CNH) **5.4** (65(1) kcal/mol). In fact, gas phase DFT studies predict a BDE_{NH} of 30 kcal/mol! Given the remarkable agreement between the experimental- and theoretically-obtained BDE_{NH} values of the Fe(CNH_x) species (vide supra), this value carries considerable merit. Such a low BDE_{NH} is consistent with the observed H_2 evolution on combining proton equivalents with [SiP^{iPr}_3]Fe(N_2) and would readily explain the transient nature of this hypothetical species.[7]

5.3. Discussion: Understanding N_2 and CN Activation at Molecular Fe Sites

The greater stability displayed by some of the Fe(CNH_x) species in comparison to the related N_2-derived Fe(NNH_x) species supported by the [SiP^{iPr}_3] platform is striking. As these two series of compounds are derived from the formal addition of H-atom equivalents to the terminal N-atom of structurally analogous Fe(N_2) or Fe(CN) derivatives, such disparate thermal stability was not expected. For example, the [SiP^{iPr}_3]Fe(NNH_2)$^{(0/+)}$ complexes discussed in Chapter 4 decay rapidly in solution at temperatures of 0 ^oC and higher. The stability of the cationic Fe(NNH_2) at lower temperatures permits the routine characterization of this compound, but attempts to probe its thermodynamic properties, such as acidity and redox potential, have been unsuccessful. These failures may in part be attributed to the apparently reactive nature of the conjugate base, [SiP^{iPr}_3]Fe(NNH), and the neutral Fe(NNH_2) compound. Despite considerable effort, the preparation of an Fe(NNH) complex, either via the protonation of Fe(N_2) species, or deprotonation of Fe(NNH_2) species, has not yet been possible in our hands. The neutral [SiP^{iPr}_3]Fe(NNH_2) is highly reactive, and can only be characterized when samples are prepared and handled at -135 ^oC. In contrast, the preparations of Fe(CNH) and Fe[CN(Me)H] species, in certain oxidation states, are straightforward and proceed at or near ambient temperatures.

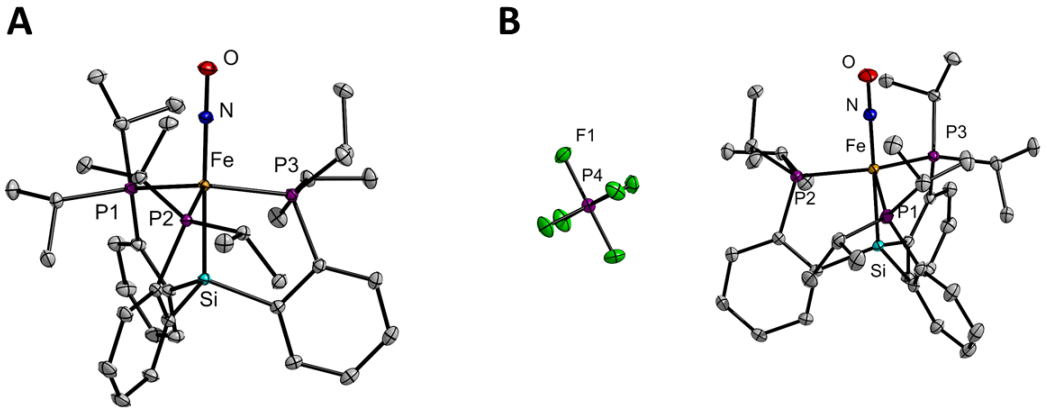

Figure 5.7. X-ray diffraction crystal structures of (A) [SiP$^{iPr}_3$]Fe(NO) and (B) {[SiP$^{iPr}_3$]Fe(NO)}{PF_6} with thermal ellipsoids drawn at 50%. Hydrogen atoms and a cocrystallized molecule of MeCN in B has been removed for clarity.

Why are the putative Fe(NNH) species so reactive? Stable W- and Mo(NNH) species have been previously reported and subject to spectroscopic and crystallographic characterization[25] indicating that, in principle, an Fe(NNH) is chemically feasible. The apparent instability of [SiP$^{iPr}_3$]Fe(NNH)$^{(+)}$ and [SiP$^{iPr}_3$]Fe(NNH) must be intimately linked to the NH unit as the isoelectronic Fe(NO) complexes are readily prepared and thermally robust (Figure 5.7).

To a first approximation, the addition of a single H-atom to a bound N_2 ligand requires the partial cleavage of the first N-N π bond. If this is not compensated by the simultaneous formation of an Fe-N π bond of comparable strength, the resulting N-H bond will be weak. As molecular Fe compounds are inherently less π-basic than Mo or W, for example, Fe-N π bonds should be weak, and we hypothesize that the BDE_{NH} of an Fe(NNH) species may be considerably weakened relative to that found in the W- or Mo(NNH) species, as well as more common N-H bonds.[13] The EPR experiments described

above lend support to this hypothesis and place an upper limit on the BDE_{NH} of the putative $[SiP^{iPr}_3]Fe(NNH)^{(+)}$ at ≤ 43 kcal/mol, a low value that alludes to the propensity of these and related compounds to eject H-atom equivalents in the form of H_2.[7,24,26] The low apparent pKa(N-H) value (≤ 0 in THF) directly reflects the inability of Fe to efficiently backbond into the N-N π^*-manifold in $[SiP^{iPr}_3]Fe(N_2)$, leaving a terminal N-atom with little basicity or nucleophilic properties.

Admitting experimental defeat, we turned to DFT calculations to ascertain the gas phase bond enthalpies of relevant $Fe(NNH_x)$ species supported by the $[SiP^{iPr}_3]$ platform (refer to Appendix 2 for calculation details). These and other thermodynamic values are collected and shown in Figure 5.8B alongside those of the $Fe(CNH_x)$ species (Figure 5.8A). It is immediately obvious that the BDE_{NH} values representative of the $Fe(CNH_x)$ manifold far exceed those of the $Fe(NNH_x)$, reflecting the greater stability of these compounds. All of the $Fe(NNH_x)$ species are predicted to be unstable with respect to H_2 loss by a considerable margin. The cationic $Fe(NNH_2)$ is the only isolable $Fe(NNH_x)$ species and interestingly its BDE_{NH} value is the greatest of this series. The *neutral* $Fe(NNH_2)$, whose marginal stability allowed for spectroscopic detection at low temperatures, displays a calculated BDE_{NH} of 35 kcal/mol. This value exceeds that of the neutral Fe(NNH) by a fair margin, and may in part explain the rapid consumption of Fe(NNH) in solution via disproportionation. Taken together, these low BDE_{NH} values directly reflect the higher acidity of $Fe(NNH_x)$ species and greater reducing power of their conjugate bases, relative to those of $Fe(CNH_x)$ compounds (equation 5.1).

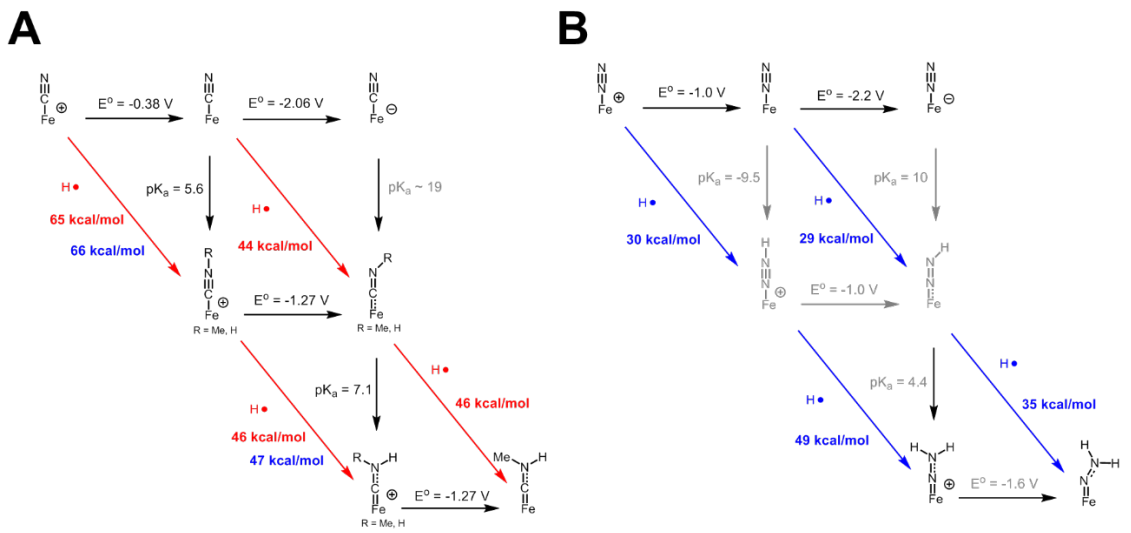

Figure 5.8. Tabulated thermodynamic parameters for (A) [SiP$^{iPr}_3$]Fe(CNH$_x$) and (B) [SiP$^{iPr}_3$]Fe(NNH$_x$) species. Arrows and molecules drawn in black represent experimentally-observed transformations and characterized compounds, respectively. Arrows and text drawn in red represent BDE$_{NH}$ values which have been estimated by the application of equation 5.1 on experimental data. Blue arrows and text represent gas-phase values predicted by DFT methods. Gray text represent values which were determined by the application of Hess' law. Gray molecules and arrows represent unobserved compounds and transformations, respectively.

To put these values into broader context, the BDE$_{NH}$ of the Mo(NNH) complex supported by the [HIPTN$_3$N]$^{(3-)}$ scaffold was estimated. Schrock and Yandulov have reported that the reaction of [HIPTN$_3$N]Mo(NNH) with stoichiometric DBU (pKa$_{THF}$: 16.6) forms equilibrium mixtures with [HIPTN$_3$N]Mo(N$_2$)$^{(-)}$, providing a crude estimate of this pKa(N-H) in THF.[27] As the redox couple for [HIPTN$_3$N]Mo(N$_2$)$^{(0/-)}$ is reported at -1.81 V in THF,[27] a BDE$_{NH}$ value of 47 kcal/mol is estimated for this neutral Mo(NNH) species. *The BDE$_{NH}$ of this Mo(NNH) species is 17 kcal/mol stronger than that of*

[SiP$^{iPr}_3$](Fe(NNH)$^{(0/+)}$. This difference underscores the greater observed thermal stability of Mo(NNH_x) species in general and speaks to the highly reactive nature of Fe(NNH_x) species.[24,25] Clearly, the high reactivity of Fe(NNH_x) units stabilized by the tripodal phosphine ligands [SiP$^{iPr}_3$] and (TPB) are a direct result of low BDE_{NH} values which favor the loss of H-atom equivalents in the form H_2, prior to the productive formation of NH_3 from bound N_2.

One additional factor that clearly distinguishes these systems is the steric profile exerted by the ancillary [SiP$^{iPr}_3$] and [$HIPTN_3N$] platforms. The [$HIPTN_3N$] ligand effectively shields the Mo-bound N_xH_y ligands from the surrounding medium, whereas [SiP$^{iPr}_3$] does not provide the analogous 'vertical' protection of the bound diatomic ligand.[7,25] The NH units of the NNH_x and CNH_x complexes of the [SiP$^{iPr}_3$]Fe platform are therefore readily accessible to the surrounding solvent and this fact may contribute to their rapid decomposition. Future efforts to increase the steric protection surrounding the labile Fe(NNH_x) species may allow for more detailed studies of these interesting fragments through kinetic stabilization. Alternatively, ancillary ligand platforms that incorporate hydrogen-bonding moieties may serve to stabilize the NNH_x fragments.[28] Either way, the preparation of new and *isolable* Fe(N_xH_y) species will likely require novel strategies that serve to stabilize fragile N-H bonds.

While the observed H_2 evolution from the aminocarbyne complexes **5.5** and **5.9'** as well as the Fe(NNH_x) species can be rationalized on thermodynamic grounds, little is known regarding the mechanism by which these reactions proceed. While we cannot rule out the intermediacy of a reactive Fe(H) as a critical intermediate in these H_2 evolution reactions, the possibility that H_2 is generated by the direct intermolecular coupling of H-

atoms on the aminocarbyne ligands in **5.5** and **5.9'** is worth considering. In this vein, reactivity that is conceptually related to these H_2 evolution reactions was reported by Pickett during the study of a tungsten aminocarbyne complex, $(dppe)_2(Cl)W(CNH_2)$.[10a] This complex delivers H-atom equivalents to azobenzene and aldehydes with concomitant formation of $(dppe)_2(Cl)W(CN)$ and these reactions were thought to proceed via direct H-atom transfer from the CNH_2 ligand. The combination of these $W(CNH_2)$-derived H-atom equivalents to form H_2 was not reported, and given the preceding discussion this observation may indicate the presence of greater BDE_{NH} values than those borne by the iron aminocarbynes **5.5** and **5.9'**.

5.4. Conclusions

To conclude, we have disclosed the proton-coupled reductive cleavage of the C-N triple of an iron-bound cyanide complex to CH_4 and NH_3. $Fe(CNH_x)$ intermediates, presumably formed *en route* to these products, and their alkylated analogues were readily prepared and characterized by a suite of structural and spectroscopic techniques. The remarkable stability of Fe(CNH) and Fe[CN(R)H] compounds allowed for the experimental determination of the N-H bond enthalpies of the CN-derived ligands. These low BDE_{NH} values aid in understanding the propensity of these, and related $Fe(N_2)$ compounds, to eject H-atom equivalents in the form of H_2 under conditions that otherwise permit the complete activation of CN or N_2 to NH_3. Finally, we have provided comparative estimates of N-H bond enthalpy of Mo- and Fe(NNH) species which reconcile the ephemeral nature of $Fe(NNH_x)$ species at ambient temperatures.

5.5. Cited References

1. Pombeiro, A. J. L.; Richards, R. L. *Coord. Chem. Rev.* **1990**. 104, 13-38.
2. (a) Li, J.; Burgess, B. K.; Corbin, J. L. *Biochemistry*, **1982**, 21, 4393-4402. (b) Lee, C. C.; Hu, Y.; Ribbe, M. W.; *Angew. Chem. Int. Ed.* **2015**. 54, 1219-1222.
3. (a) Fehlhammer, W. P.; Fritz, M. *Chem. Rev.* **1993**. 93, 1243-1280. (b) Pombeiro, A. J. L.; Fatima, M.; de Silva, C. G. *J. Organomet. Chem.* **2001**. 617, 65-69. (c) Pombeiro, A. J. L. *Inorg. Chem. Commun.* **2001**. 4, 585-597.
4. Fehlhammer, W. P.; Schoder, F.; Beck, G.; Schrolkamp, S. *Z. Anorg. Allg. Chem.* **1993**. 619, 1171-1176.
5. (a) Fehlhammer, W. P.; Schroder, A.; Fuchs, J.; Wurthwein, E-U. *Angew. Chem. Int. Ed.* **1992**. 31, 590-592. (b) Peters, J. C.; Baraldo, L. M.; Baker, T. A.; Johnson, A. R.; Cummins, C. C. *J. Organomet. Chem.* **1999**. 591, 24-35. (c) Cavigliasso, G.; Christian, G. J.; Stranger, R.; Yates, B. F. *Dalton Trans.* 2011. 40, 7327-7339.
6. (a) Fedurco, M.; Sartoretti, C. J.; Augustynski, J. *J. Amer. Chem. Soc.* **1999**. 121, 888-889. (b) Fedurco, M.; Sartoretti, C. J.; Augustynski, J. *J. Electrochem. Soc.* **2001**. 148, D19-D23.
7. (a) Anderson, J. S.; Rittle, J.; Peters, J. C. *Nature.* **2013**. 501, 84-87. (b) Lee, Y.; Mankad, N. P.; Peters, J. C. *Nature Chem.* **2010**. 2, 558-564.
8. Addison, A. W.; Rao, T. N.; Reedijk, J.; van Rijn, J.; Verschoor, G. C. *J. Chem. Soc. Dalton Trans.* **1984**. 1349-1356.
9. Steiner, T. *Angew. Chem. Int. Ed.* **2002**. 41, 48-76.

10. (a) Hughes, D. L.; Ibrahim, S. K.; Ali, H. M.; Pickett, C. J. *J. Chem. Soc., Chem. Commun.* **1994**. 425-427. (b) Pombeiro, A. J. L.; Hughes, D. L.; Pickett, C. J.; Richards, R. L. *J. Chem. Soc., Chem. Commun.* **1986**. 246-247.
11. While these reductions were performed under an atmosphere of N_2, compound **5.1** or [SiP^{iPr}_3]Fe(N_2) do not generate significant quantities of NH_3 under identical conditions, as judged by Indophenolic assays.[7]
12. Mankad, N. P.; Muller, P.; Peters, J. C. *J. Amer. Chem. Soc.* **2010**. 132, 4083-4085.
13. Warren, J. J.; Tronic, T. A.; Mayer, J. M. *Chem. Rev.* **2010**. 110, 6961-7001.
14. (a) Tilset, M. In *Electron Transfer in Chemistry;* Balzani, V., Ed.; Wiley-VCH: Weinheim, Germany, 2001; pp 677-713. (b) Dhar, D.; Tolman, W. B. *J. Amer. Chem. Soc.* **2015**. 137, 1322-1329.
15. Garrido, G.; Roses, M.; Rafols, C.; Bosch, E. *J. Solution Chem.* **2008**. 37, 689-700.
16. Pappas, I.; Chirik, P. J. *J. Amer. Chem. Soc.* **2015**. 137, 3498-3501.
17. Bard, A. J.; Parsons, R.; Jordan, J. *Standard Potentials in Aqueous Solutions.* **1985**. (Marcel Dekker, New York)
18. Binsch, G.; Lambert, J. B.; Roberts, B. W.; Roberts, J. D. *J. Amer. Chem. Soc.* **1964**. 86, 5564-5570.
19. Kim, H. P.; Angelici, R. J.; *Adv. In Organomet. Chem.* **1987**. 27., 51-111.
20. (a) Evans, D. J.; Pickett, C. J. *Chem. Soc. Rev.* **2003**. 32, 268-275. (b) McKone, J. R.; Marinescu, S. C.; Brunschwig, B. S.; Winkler, J. R.; Gray, H. B. *Chem. Sci.* **2014**. 5, 865-878.

21. (a) Eisenberg, D. C.; Lawrie, C. J. C.; Moody, A. E.; Norton, J. R. *J. Amer. Chem. Soc.* **1991**. 113, 4888-4895. (b) Tilset, M.; Parker, V. D. *J. Amer. Chem. Soc.* **1989**. 111, 6711-6717.

22. Ding, F.; Smith, J. M.; Wang, H. *J. Org. Chem.* **2009**. 74, 2679-2691.

23. As discussed in Chapter 4, rapid proton transfer occurs in ethereal solvents at temperatures as low as -135 ^{o}C. Therefore, any protonation of [SiP$^{iPr}_3$]Fe(N_2) at the discussed conditions should be observable and give rise to distinct features in the EPR spectrum.[24]

24. Anderson, J. S.; Cutsail, G. E.; Rittle, J.; Connor, B. A.; Gunderson, W. A.; Zhang, L.; Hoffman, B. M.; Peters, J. C. *J. Amer. Chem. Soc.* **2015**. 137, 7803-7809.

25. (a) Yandulov, D. V.; Schrock, R. R. *J. Amer. Chem. Soc.* **2002**. 124, 6252-6253. (b) Yandulov, D. V.; Schrock, R. R.; *Can. J. Chem.* **2005**. 83, 341-357.

26. (a) Lee, Y.; Peters, J. C. *J. Amer. Chem. Soc.* **2011**. 133, 4438-4446. (b) Creutz, S. E.; Peters, J. C. *J. Amer. Chem. Soc.* **2015**. 137, 7310-7313. (c) Del Castillo, T. J.; Thompson, N. B.; Suess, D. L. M.; Ung, G.; Peters, J. C. *Inorg. Chem.* **2015**. 54, 9256-9262.

27. Yandulov, D. V.; Schrock, R. R. *Inorg. Chem.* **2005**. 44, 1103-1117.

28. Back, R. A.; Willis, C. *Can. J. Chem.* **1974**. 74, 2513-2515.

Chapter 6. A 10^6-Fold Enhancement in N_2-Binding Affinity of an $Fe_2(\mu\text{-}H)_2$ Core Upon Reduction to a Mixed-Valence $Fe^{II}Fe^{I}$ State

Reproduced in part with permission from:

Rittle, J.; McCrory, C. C. L.; Peters, J. C.; *J. Amer. Chem. Soc.* **2014**. 136, 13853-13862.

6.1. Introduction

The intimate mechanism of biological nitrogen fixation at the FeMo-cofactor (FeMoco) of nitrogenase enzymes is a fascinating, unsolved problem. One or two of the central iron atoms of the FeMoco have been highlighted as plausible N_2 binding sites.[1] Yet, despite a supporting body of biochemical and spectroscopic data,[2,3] in addition to synthetic Fe-N_2 model chemistry establishing that N_2 reduction to NH_3 is possible at an iron center,[4-6] there remains the question as to how an iron site (or sites) that resides within a sulfide-rich environment would facilitate N_2 binding. To date, there is little synthetic precedent for Fe-N_2 complexes that feature sulfur within the immediate iron coordination sphere,[7,8] and there are no synthetic Fe-N_2 species where only sulfur ligates the iron center.

An interesting possibility to consider is whether iron-hydrides, either terminal or bridging, might facilitate better N_2 binding at an iron site of FeMoco by increasing its π-basicity, owing to the relatively strong ligand field exerted by a hydride.[9] Hydride ligands could be installed under the electron-loading phase, prior to N_2 uptake, a phase that is presumably leveled by the concomitant delivery of protons to iron and/or sulfur sites. It is noteworthy in this context that a bridging hydride form of the FeMoco (i.e., Fe(μ-H)Fe) has been proposed based on spectroscopic data under turnover conditions.[10] While elimination of H_2 upon N_2 binding has been suggested as a way to rationalize presumed obligatory H_2 elimination during N_2 reduction to two equiv NH_3,[11,12] an additional possibility to consider is that cofactor bound hydrides afford a sufficiently covalent Fe-N_2 interaction to render N_2 binding and reduction at an iron site (or sites) favorable.

Because bridging rather than terminal hydrides have been implicated as observable intermediates, we sought to prepare Fe(μ-H)Fe model complexes that have an affinity for N_2. Terminal Fe-H complexes are now well established to bind N_2,[13,14] even with sulfur in the immediate iron coordination sphere,[7] but to our knowledge there are no synthetic Fe-N_2 complexes featuring hydrides bridging another Fe center. This situation exists despite the fact that there are hundreds of crystallographically characterized complexes featuring bridging hydride Fe(μ-H)Fe subunits.[15]

Herein we present a new binucleating scaffold that installs two bridging hydrides to afford a Fe(μ-H)$_2$Fe subunit. This structural motif is shown to be compatible with N_2 binding and reductive protonation to release a substoichiometric but nevertheless substantial amount of NH_3. In addition, reversible coordination of N_2 to the second iron site is observed, and the N_2 binding affinity is shown to increase by six orders of magnitude upon further reduction of the N_2-Fe(μ-H)$_2$Fe subunit by one electron (Scheme 6.1). The S = ½ form, $\{N_2\text{-Fe}(\mu\text{-H})_2\text{Fe-}N_2\}^+$, shows strong hyperfine coupling through the bridging hydride ligands.

6.2. Results

6.2.1. Synthesis and Structure of 3-N_2

To support an unsaturated Fe(μ-H)Fe unit, we synthesized the bulky hexadentate ligand, $[SiP_2O]H_2$ (**6.2**). Compound **6.2** is synthesized by the controlled hydrolysis of previously-reported bis-(*o*-diisopropylphosphino-phenyl)-chlorosilane (**6.1**) (Scheme 6.1).[7] The ligand exhibits a singlet in the $^{31}P\{^1H\}$ NMR spectrum (δ = -0.5 ppm) and a

triplet in the $^{29}Si\{^{1}H\}$ spectrum (δ = -30.4 ppm, J_{Si-P} = 27 Hz). Two Si-H vibrations are observed in the solid state (2199 and 2166 cm^{-1}, KBr).

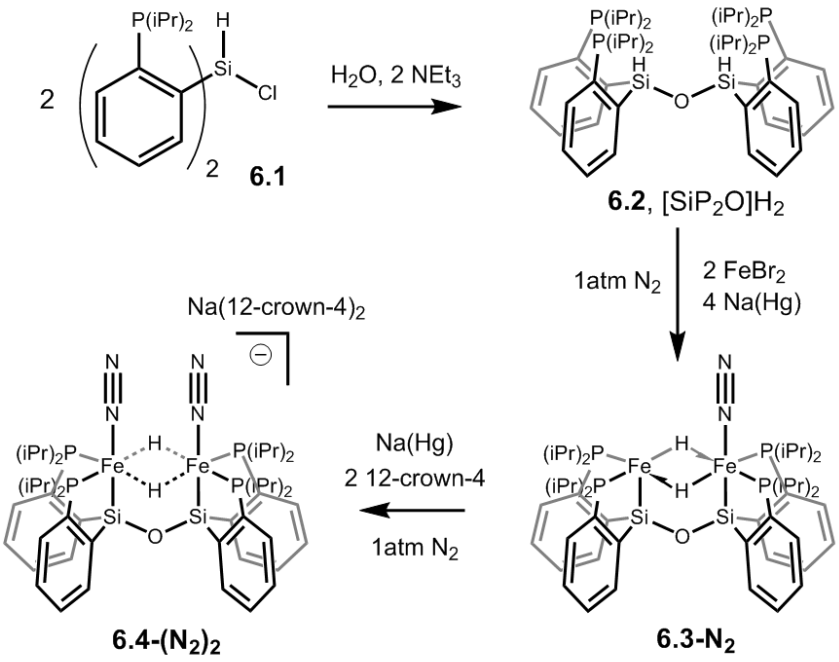

Scheme 6.1. Synthesis of $[SiP_2O]H_2$ (**6.2**) and supported diiron complexes.

Complexation of $[SiP_2O]H_2$ with two equivalents of $FeBr_2$, followed by reduction with Na(Hg) under 1 atm of N_2 (Scheme 6.1) furnishes **6.3-N_2** in 70% yields on gram scales. ^{57}Fe-enriched **6.3-N_2** can be obtained by substituting one equivalent of $FeBr_2$ with $^{57}FeCl_2$ (44% yield). The solid-state structure of **6.3-N_2** is shown in Figure 6.1 and confirms the presence of two Fe atoms supported by the ligand framework. Two bridging hydride ligands, presumably arising from in situ activation of the Si-H units in **6.2**, are located in the Fourier difference map ca. 1.64 Å from Fe2 and ca. 1.69 Å from Fe1. The long H50•••H51 distance (2.21(2) Å) confirms their assignment as hydrides and not a stretched-dihydrogen ligand. Furthermore, no interaction is observed between the Si and H atoms as reflected by long H•••Si distances (3.08(2) to 2.53(2) Å). N_2 coordinates

selectively to Fe2 in a terminal fashion with a Fe2-N1 distance of 1.8474(9) Å and a N1-N2 distance of 1.114(1) Å, reflecting a minimal degree of activation (the N-N distance in free N_2 is 1.0976 Å). The shortest methyl group Fe-C distance is 3.719(1) Å (to Fe1), ruling out the presence of agostic interactions in the solid state. While the Fe-P distances are similar for both sites, the Fe1-Si1 bond distance (2.1644(4) Å) is markedly shorter than that of Fe2-Si2 (2.2594(4) Å).

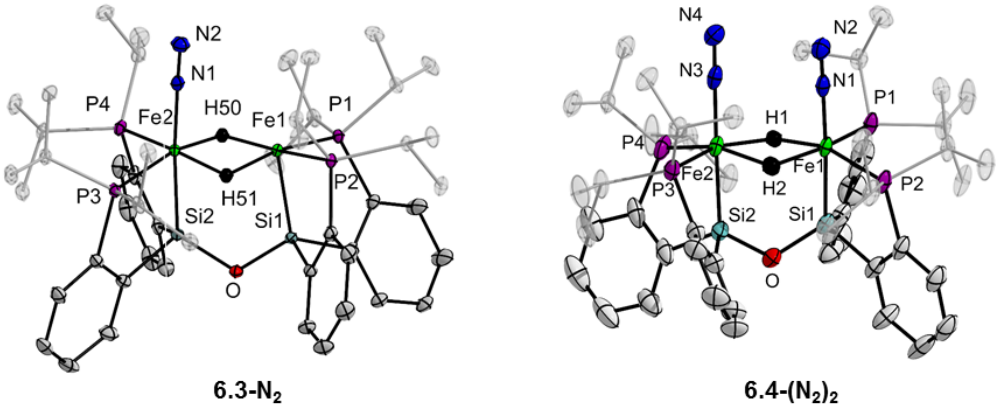

6.3-N_2 **6.4-$(N_2)_2$**

Figure 6.1. X-ray diffraction crystal structures of **6.3-N_2** and **6.4-$(N_2)_2$** with thermal ellipsoids drawn at 50% probability. Hydrogen atoms (excepting the iron hydrides), the Na(12-crown-4)$_2$ cation of **6.4-$(N_2)_2$** and co-crystallized solvent molecules have been removed for clarity. The isopropyl substituents have been rendered transparent to aid in visualization of the inner coordination sphere around the diiron unit.

The structure of **6.3-N_2** is maintained in solution in the absence of additional N_2. The room temperature ^{1}H NMR spectrum of **6.3-N_2** is unchanged following multiple freeze-pump-thaw cycles, indicating that the N_2 ligand is not labile. NMR spectra collected on **6.3-N_2** indicate an asymmetric molecule at low temperatures (Figure 6.2).

Four resonances are observed in the ^{31}P NMR spectrum of **6.3-N$_2$** at 213K and the hydride ligands are non-equivalent at temperatures below 273 K (*vide infra*).[16] The observed asymmetry can be explained in part by exclusive N_2 coordination to one Fe site.[17]

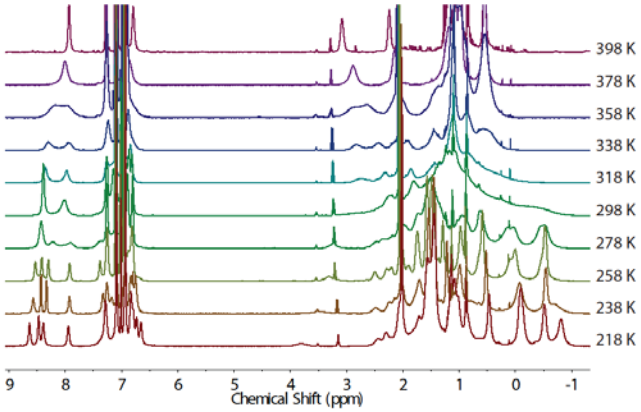

Figure 6.2. Variable temperature 500 MHz ^{1}H NMR spectra of **6.3-N$_2$** in toluene-d_8. To exclude additional N_2, NMR samples were subjected to three freeze-pump-thaw cycles in a J Young tube before backfilling with Ar gas prior to data collection. Spectra were obtained following equilibration at the listed temperature for at least 10 minutes. The hydride resonances are not shown.

At 373 K, the Fe sites were found to be equivalent on the NMR timescale. Eleven resonances are observed in the ^{1}H NMR spectrum (toluene-d_8, 1 atm Ar) including a single hydride resonance (*vide infra*). We speculate that this apparent equivalence results from N_2 ligand exchange between the two Fe sites. While slow decomposition of **6.3-N$_2$** is observed at 373 K, the Fe site equivalence was found to be reversible as cooling the sample back to 293 K restored the spectrum of the remaining **6.3-N$_2$**. The product(s) of

the thermal decomposition of **6.3-N$_2$** have not been ascertained despite our attempts to isolate and characterize them.

6.2.2. N$_2$-binding Equilibria of 3-N$_2$

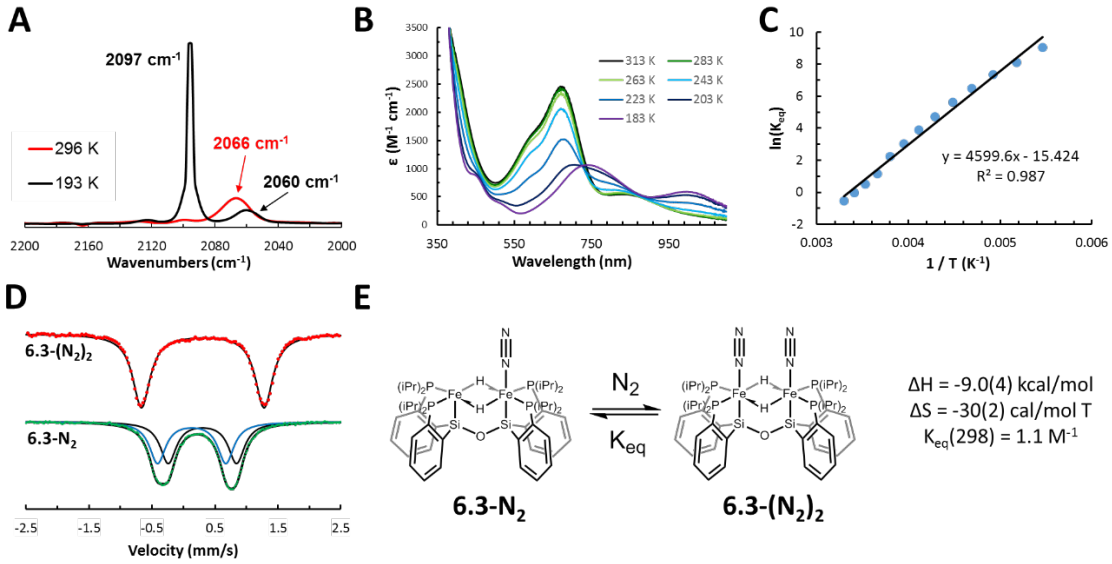

Figure 6.3. Spectroscopic observation of **6.3-(N$_2$)$_2$** at low temperatures. (A) Solution IR absorption spectra of **6.3-N$_2$** at 296 K (red) and **6.3-(N$_2$)$_2$** at 193 K (black) dissolved in N$_2$-saturated toluene. (B) UV-visible spectra of an N$_2$-saturated hexane solution of **6.3-N$_2$/6.3-(N$_2$)$_2$** at the listed temperatures. (C) Van't Hoff plot derived from the UV-visible spectral changes recorded at 675 nm and the published N$_2$ solubility values in cryogenic hexane.[18] (D) ^{57}Fe Mössbauer spectra (zero field, 80K) of polycrystalline **6.3-N$_2$** (bottom, green dots) and **6.3-(N$_2$)$_2$** in 2-MeTHF (top, red dots). The two subspectra of **6.3-N$_2$** shown are only one possible fit to the data (E) Chemical equilibrium and thermodynamic parameters derived from the Van't Hoff analysis of the equilibrium N$_2$-binding process.

IR spectroscopy indicates that an additional N_2 molecule coordinates to **6.3-N_2** at low temperatures in N_2-saturated solutions. At 298 K in toluene solution, a single υ(N-N) vibration is observed at 2066 cm^{-1} (Figure 6.3A) (KBr, 2062 cm^{-1}). Cooling this solution to 193 K results in the appearance of two features at 2097 and 2060 cm^{-1}. Warming the solution back to 298 K results in the loss of these bands and reappearance of the 2066 cm^{-1} vibration assigned to **6.3-N_2**. These data suggest that two N_2 molecules are bound at low temperatures forming a species denoted as **6.3-$(N_2)_2$**. The two vibrations observed at 193 K can be understood as symmetric and antisymmetric stretching modes derived from two coupled υ(N-N) vibrations of similar energy. Frequency calculations on the optimized geometry of **6.3-$(N_2)_2$** (*vide infra*) bolster these assignments and closely match the intensity pattern observed.

UV/visible spectroscopy was found to be a convenient tool for determining the thermodynamic parameters of N_2 binding to the five-coordinate Fe site of **6.3-N_2**. Room temperature solutions of dilute **6.3-N_2** in N_2-saturated hexane display absorption bands centered at 600, 680, and 864 nm (Figure 6.3B) in the visible spectrum. On cooling, these bands decrease in intensity, concomitant with the appearance of prominent absorption bands at 750 and 1006 nm ascribable to **6.3-$(N_2)_2$**. Argon-saturated solutions of **6.3-N_2** do not display these features on cooling. The temperature-dependent spectral changes observed in N_2–saturated hexane solutions can be fit to provide the thermodynamic binding constant, K_{eq}, for N_2 binding in equation 6.1.[18] A Van't Hoff analysis of the resulting data (Figure 6.3C) furnishes the pertinent thermodynamic parameters of this process. The large, negative entropy of bonding (-30(2) cal/mol•T) is consistent with the

coordination of a gas molecule[19] and the rather small enthalpy of binding (-9.0(4) kcal/mol) is in line with the exclusive observation of **6.3-$(N_2)_2$** at low temperatures.

$$\textbf{6.3-}N_2 + N_2 \underset{}{\overset{K_{eq}}{\rightleftharpoons}} \textbf{6.3-}(N_2)_2 \qquad \textbf{Eq 6.1}$$

Zero-field ^{57}Fe Mössbauer data (Figure 6.3D) corroborate the temperature-dependent nature of **6.3-N_2**. Solid **6.3-N_2** displays two broad features that can be fit with two quadrupole doublets in a 1:1 ratio, suggesting the presence of two distinct Fe environments. This is in accord with the solid-state structure of **3-N_2** and the NMR data in solution. The spectrum of **6.3-$(N_2)_2$**, prepared by dissolving ^{57}Fe-enriched **6.3-N_2** in N_2-saturated 2-MeTHF at 173 K followed by freezing at 77 K, reveals sharper features at different positions than that of **6.3-N_2**. This spectrum is well fit by a single Lorentzian quadrupole doublet, suggesting two equivalent Fe environments.

Fe K-edge Extended X-ray Absorption Fine Structure (EXAFS) measurements coupled to DFT calculations provide structural information on **6.3-$(N_2)_2$**. EXAFS data collected on **6.3-$(N_2)_2$** dissolved in a 2-MeTHF glass indicate an increased Fe•••Fe distance (2.75(2) Å) relative to that found for solid **6.3-N_2** by EXAFS (2.47(2) Å) and XRD (2.4797(3) Å). The DFT-optimized geometry of **6.3-N_2** and **6.3-$(N_2)_2$** (BP86/6-31G(d)) are in agreement with the experimental data and reveal Fe•••Fe distances of 2.494 Å and 2.729 Å, respectively. The calculated and experimental Fe-N and average Fe-P/Si distances were found to be similar in **6.3-N_2** and **6.3-$(N_2)_2$**.

6.2.3. Observation of a Low-lying Excited State in 3-N_2

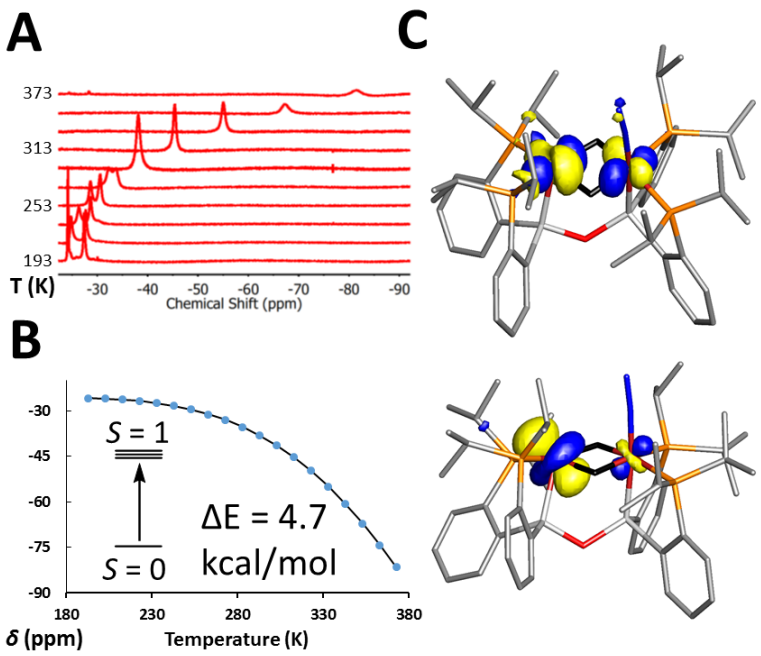

Figure 6.4. The temperature dependence of the Fe-(μ-H)-Fe chemical shift in **6.3-N_2** arises from thermal population of an excited triplet state. (A) ^{1}H NMR spectra of **6.3-N_2** collected at the listed temperatures. (B) Fit of the ^{1}H chemical shift of **6.3-N_2** to the magnetization equation. (C) Orbital surfaces of the two singly-occupied (occupancy = 1.00) Natural Orbitals. All other orbitals had occupancies of >1.90 or < 0.10 electrons.

In addition to the dynamic N_2-coordination behavior of **6.3-N_2** at low temperatures, NMR measurements suggest that this species has a thermally-accessible paramagnetic excited state. At 293 K an unusually-upfield hydride resonance is observed for **6.3-N_2** at a chemical shift of δ = -38.2 ppm (Figure 6.4). Previously reported Fe(μ-H)Fe complexes display hydride resonances in the region around -22 ppm.[20-22] On cooling, this resonance resolves into two signals in a 1 : 1 ratio centered at δ = -26.3 ppm at 193 K. With increasing temperature, the average position of the hydride resonances

smoothly decreases in a nonlinear fashion to δ = -81.5 ppm at 373 K. The temperature dependence of the average hydride chemical shift of **6.3-N_2** is not associated with N_2 coordination to form **6.3-$(N_2)_2$**: the hydride chemical shift is the same in N_2- and Ar-saturated solvents (at a given temperature), and the greatest changes in chemical shift are observed at temperatures where **6.3-N_2** predominates (K_{eq} << 1, Equation 6.1). Such a dramatic temperature dependence of a metal-hydride chemical shift has been previously observed on K_2[LNi(μ-H)$_2$Ni(μ-H)$_2$NiL] (L = [HC(CMeNC$_6$H$_3$(iPr)$_2$)$_2$]$^-$) and attributed to partial thermal population of a paramagnetic excited state.[23] The hydride chemical shift of **6.3-N_2** is well fit to a magnetization function suggesting the presence of an excited state lying 4.7 kcal/mol above the ground state.

Single-point calculations (BP86/6-31G(d)) on the optimized geometries of **6.3-N_2** in singlet, triplet, and quintet spin states correctly locate a diamagnetic ground state with triplet and quintet states lying 4.4 and 21.1 kcal/mol higher in energy, respectively. We therefore attribute the temperature-dependent hydride chemical shift to partial thermal population of a triplet excited state. The singly-occupied Natural Orbitals[24] of **6.3-N_2** optimized in a triplet spin state (Figure 6.4) illustrate that the unpaired spin density is delocalized over both Fe sites. However, the five-coordinate Fe site (spin density +1.96) bears more unpaired spin than the N_2-bound Fe site (spin density +0.43).

6.2.4. Formation of a Mixed-Valent $Fe_2(\mu\text{-}H)_2$ Species

Open-shell iron hydride species have been proposed as catalytically-relevant in nitrogenase and other metalloenzymes.[10,25-27] As such we explored the possibility of accessing paramagnetic Fe(μ-H)Fe species in this system. Briefly stirring **6.3-N_2** over an excess of Na(Hg) in the presence of 12-crown-4 in N_2-saturated THF and subsequent

workup affords {Na(12-crown-4)$_2$}{[SiP$_2$O]Fe$_2$(μ-H)$_2$(N$_2$)$_2$} (**6.4-(N$_2$)$_2$**).[28] The room temperature solution magnetic moment identifies **6.4-(N$_2$)$_2$** as an S = 1/2 species (μ_{eff} = 1.7 μ_B). The solid-state structure of **6.4-(N$_2$)$_2$** is shown in Figure 6.1. One N$_2$ ligand is bound to each of the Fe sites in a terminal fashion and the bridging hydrides can be located. Upon reduction the Fe•••Fe distance has increased to 2.8722(5) Å in **6.4-(N$_2$)$_2$**. In addition, the average Fe-H distances have slightly increased from 1.67(2) Å to 1.73(3) Å. Insignificant changes are observed in the average Fe-P, Fe-N, and N-N distances from **6.3-N$_2$** to **6.4-(N$_2$)$_2$**. IR measurements on solid **6.4-(N$_2$)$_2$** reveal two coupled υ(N-N) vibrations (2023 and 1979 cm^{-1}). The intensity pattern and spacing of these modes are similar to that observed for **6.3-(N$_2$)$_2$** in solution but display an average bathochromic shift of 78 cm^{-1}.

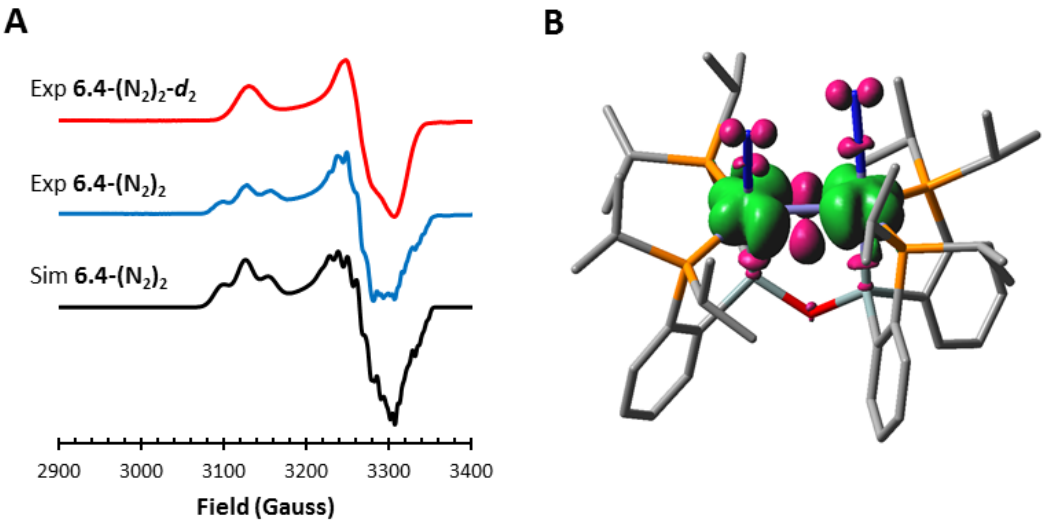

Figure 6.5. (A) X-band EPR spectra of **6.4-(N$_2$)$_2$-*d*$_2$** (red), **6.4-(N$_2$)$_2$** (blue) and the simulated EPR spectrum of **6.4-(N$_2$)$_2$**. Simulation parameters are listed in Table 6.1. Spectra were collected a 77 K in a 2-MeTHF glass at υ = 9.395 GHz at 2 mW power and modulation amplitude of 2 Gauss. (B) Spin density plot of **6.4-(N$_2$)$_2$** shown with an isovalue of 0.0015.

The EPR spectrum of **6.4-$(N_2)_2$**, collected at 77 K in a 2-MeTHF glass (Figure 6.5) is slightly rhombic and dominated by features arising from hyperfine coupling. The spectrum can be simulated by considering three sets of two $I = ½$ nuclei. The EPR spectrum of **6.4-$(N_2)_2$-*d*$_2$** does not display resolved hyperfine couplings, allowing the unambiguous assignment of the largest hyperfine coupling tensor to that arising from two equivalent bridging hydrides. The smaller values are therefore ascribed to two slightly different sets of ^{31}P nuclei (Table 6.1). The spin density plot of **6.4-$(N_2)_2$** (Figure 6.5) shows a symmetric distribution of unpaired spin density between the two Fe atoms. There is a notably high degree of spin polarization observed on the bridging hydride ligands and this likely contributes to the large hyperfine coupling values observed in the EPR spectrum.

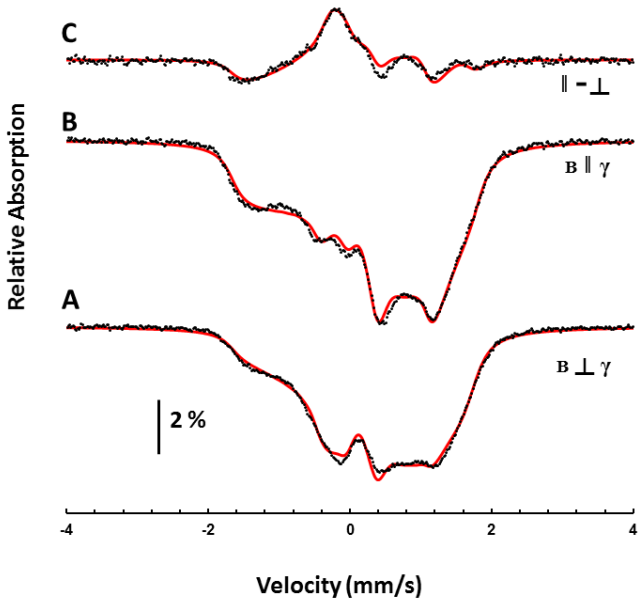

Figure 6.6. ^{57}Fe Mössbauer spectra recorded at 5K on frozen 2-MeTHF solutions of 5 mM **6.4-$(N_2)_2$** with a 50 mT magnetic field applied (A) perpendicular and (B) parallel to the propagation of the gamma beam. The difference spectra is shown in (C). The experimental traces are in black and the simulated traces are shown in red. δ = 0.35 mm/s , ΔE_Q = 0.69 mm/s, and η = 0.86 for **6.4-$(N_2)_2$**.

$$\mathcal{H} = \mathbf{S} \bullet \mathbf{A} \bullet \mathbf{I} + \beta \mathbf{S} \bullet \mathbf{g} \bullet \mathbf{B} + \mathcal{H}_Q \qquad \textbf{Eqn 6.2}$$

Mössbauer spectra of ^{57}Fe-enriched **6.4-$(N_2)_2$** (5 K, 5 mM 2-MeTHF glass) collected in the presence of a small magnetic field display multiple broad features (Figure 6.6). The intensity of these features are dependent on the orientation of the magnetic field relative to that of the γ-beam, indicative of a slowly-relaxing Kramers system.[29] The two spectra are well-simulated by an *S* = 1/2 spin Hamiltonian, including a magnetic hyperfine interaction, electronic Zeeman interaction and the quadrupole interaction of the ^{57}Fe nucleus, respectively. The inclusion of an unidentified quadrupole doublet impurity accounting for 6% of the total Fe content resulted in the fit shown in Figure 6.6. Good agreement between the experimental and simulated difference spectra validates the fit parameters listed in Table 6.1. Importantly, the simulation of **6.4-$(N_2)_2$** shown is obtained by assuming that the spin Hamiltonian parameters for each Fe atom are identical, allowing the classification of **6.4-$(N_2)_2$** as a Class III mixed-valence ion.[30]

Table 6.1. Select spectroscopic values found for 6.4-$(N_2)_2$

Axis	g	A(^{1}H)[a]	A($^{31}P_a$)[a]	A($^{31}P_b$)[a]	A(^{57}Fe)[b]
x	2.148	84	N.D.[c]	N.D[c]	4.1

y	2.057	66	29	29	21
z	2.030	69	30	16	4.5

[a] Hyperfine tensor derived from the EPR spectrum, units in MHz. [b] Hyperfine tensor derived from the Mössbauer spectra, units in Tesla. [c] Not determined; coupling was not resolved due to line broadening.

6.2.5. Electrochemical Studies

The chemical reduction of **6.3-N_2** at room temperature is coupled to the coordination of an additional tightly-bound N_2 ligand to form **6.4-$(N_2)_2$**. In **6.4-$(N_2)_2$**, the bound N_2 ligands are stable to multiple freeze-pump-thaw cycles, suggesting very strong binding to the two Fe sites. This is in contrast to that observed for **6.3-N_2** where formation of **6.3-$(N_2)_2$** is only observed at low temperatures. The inability to isolate **6.4-N_2** and measure its N_2 binding affinity directly prompted electrochemical experiments to quantify the binding affinity of **6.4-N_2**.

Cyclic voltammetry measurements on N_2-saturated THF solutions of **6.3-$(N_2)_2$** in THF electrolyte (Figure 6.7) recorded at 198 K reveal a reversible reduction event centered at -2.04 V at all recorded scan rates (Figure 6.7A; features a and a'). Comparison of the UV/Visible spectra collected at low temperature in hexane and THF confirm that **6.3-$(N_2)_2$** is the predominant (>95%) species in THF solution at 198 K. This reversible electrochemical event can thus be assigned to the reduction of **6.3-$(N_2)_2$** to **6.4-$(N_2)_2$** (Figure 6.7D, equation 6.4). The large peak to peak splitting (~1 V at 2000 mV/s scan rate) results from the large solution resistance due to the low temperature and the weakly polar electrolyte solution employed.

The cyclic voltammograms obtained on **6.3-N_2** at room temperature suggest dynamic N_2 coordination behavior. UV/visible spectra collected in N_2-saturated THF suggest that **6.3-N_2** is the predominant (>98%) neutral species at 298 K. Cyclic voltammograms recorded at slow scan rates at 298 K reveal an apparently reversible reduction event centered at -2.15 V, slightly shifted from that observed at 198 K (features b and b'). At faster scan rates, new cathodic (denoted with c in Figure 6.7B) and anodic features (denoted with c' in Figure 6.7B) appear at more negative potentials.

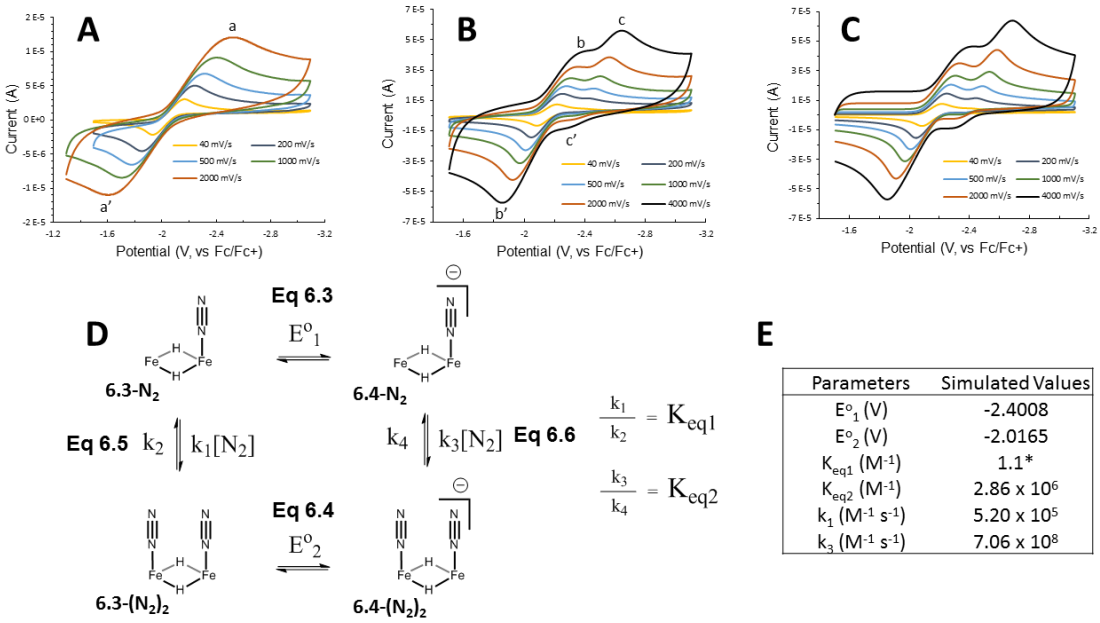

Figure 6.7. (A) Cyclic voltammetry measurements on N_2-saturated THF electrolyte solutions of **6.3-$(N_2)_2$** at 198K. (B) Cyclic voltammograms obtained on solutions of **6.3-N_2** at 298K. (C) Simulation of the voltammograms obtained at 298 K. (D) Square scheme model considered in the simulation traces shown in (C). Equations 6.3 and 6.4 represent the electrochemical reduction equilibria of **6.3-N_2** and **6.3-$(N_2)_2$**. Equations 6.5 and 6.6 represent the N_2-binding equilibria for **6.3-N_2** and **6.4-N_2**. The charges shown are representative of the full molecule. (E) Table listing critical parameters defined in the

model and the resulting values found upon simulation. An asterisk denotes values that were held constant during the simulation.

A mechanistic model consistent with the available temperature- and scan-rate-dependent cyclic voltammetry data suggests two competing pathways by which **6.3-N_2** is converted to **6.4-$(N_2)_2$**. The dominant pathway at slow scan rates appears to proceed through **6.3-$(N_2)_2$**: this is manifest in a pseudo-reversible wave observed at -2.15 V (40 mV/s; 298 K). We infer that this wave reflects the 1-electron reduction of **6.3-$(N_2)_2$** to **6.4-$(N_2)_2$** (C-E mechanism).[31] Direct one-electron reduction of **6.3-N_2** to **6.4-N_2** requires more driving force and can be observed at faster scan rates. For instance, at 4000 mV/s the waveform shows two features (b and c) that reflect **6.3-N_2** to **6.4-N_2** (c) and **6.3-N_2** to **6.4-$(N_2)_2$** (b) redox events. Rapid binding of N_2 to **6.4-N_2** to produce **6.4-$(N_2)_2$** constitutes the second path by which **6.3-N_2** funnels to **6.4-$(N_2)_2$** (E-C mechanism).

These N_2-binding and redox processes are collectively depicted in the square scheme shown in Figure 6.7D. Simultaneously fitting the various scan rates obtained at 298 K furnishes the simulated waveforms (Figure 6.7C) and parameters (Figure 6.7E). The individual rate constants were allowed to freely float but the equilibrium N_2-binding constant for **6.3-N_2** was constrained to that found in hexane via UV/visible spectroscopy (K_{eq1} = 1.1 M^{-1}). Reduction potentials derived from the simulation for the two electrochemical processes agree well with those obtained by visual inspection of the voltammograms. The individual N_2-binding rate constants are reasonable and their magnitudes are within the range found for CO and O_2 binding to Fe(porphyrin) complexes.[32]

6.2.6. Reduction of N_2 to NH_3 with H^+/e^- Equivalents

While the catalytic conversion of N_2 to NH_3 by protons and electrons has now been established in mononuclear Fe and Mo systems,[4,5,33,34] this transformation in nitrogenase may be most efficiently catalyzed by the combined action of multiple metal sites. As such, **6.3-N_2** or **6.4-$(N_2)_2$** may serve as a platform to study the cooperative activation and reduction of N_2 to NH_3. Analyses for the production of NH_3 from N_2 reveal the generation of 1.4 +/- 0.5 molar equivalents of NH_3 upon exposure of **6.3-N_2** to 48 equivalents of KC_8 and $\{(Et_2O)_2H\}\{(3,5\text{-}(CF_3)_2\text{-}C_6H_3)_4B\}$ at -78 ^oC in diethyl ether. Lowering the H^+/e^- equivalents to 10 results in a diminished yield (0.51(9) equiv NH_3). Very little NH_3 (0.2(1) equiv) is detected when this experiment is repeated at 0 ^oC. Use of **6.4-$(N_2)_2$** as a pre-catalyst also furnishes an appreciable yield of NH_3 (1.1(2) equiv). The yields of NH_3 produced *per Fe atom* in **6.3-N_2** are similar to that found for $\{Na(12\text{-crown-}4)_2\}\{[SiP^{iPr}_3]Fe(N_2)\}$ (**6.5**) ($[SiP^{iPr}_3]$ = (*o*-$C_6H_4P(iPr)_2)_3Si$ (-)) (0.7 equiv NH_3/Fe). With respect to the individual Fe sites, the formal replacement of a phosphine ligand in **6.5** with a $[Fe(\mu\text{-}H)_2]$ unit (**6.3-N_2)** has little effect on the overall reaction efficiency. It is not clear whether the two Fe sites in **6.3-N_2** act cooperatively to effect N_2 reduction or if the two sites act independently.

6.3. Discussion

In nitrogenase, mounting spectroscopic, enzymatic and theoretical data suggest that one or more Fe centers are intimately involved in N_2 reduction at FeMoco.[1,35] While molybdenum greatly enhances the efficiency of nitrogenase relative to FeVco and FeFeco congeners, its role in catalysis is unclear. Under a scenario where N_2 coordinates to an Fe site of FeMoco, it is noteworthy that isolable terminal Fe-N_2 species exclusively exhibit intermediate- or low-spin states and these species are further supported by strong-field

ancillary ligands.[7,36] In this regard, the weak-field, sulfur-rich environment of FeMoco would seem unfit for the stabilization of locally low- or intermediate spin Fe sites. Indeed, the FeMoco exhibits no affinity for N_2 (or even CO) in the crystallographically-characterized resting state of FeMoco, wherein the Fe sites are exclusively ligated to sulfide, thiolate, and carbide ligands.[37-39] At present, terminal Fe-N_2 complexes supported by ligands of these types are unknown.[15,40]

Transient bridging hydride ligands purportedly accumulate in FeMoco under turnover conditions.[1] These hydride ligands have been proposed to store reducing equivalents on the cluster.[41] We are considering the possibility that accumulated hydride ligands may also play a critical role in adjusting the electronic properties of the cluster to support the coordination of N_2 to an Fe center. The transient bridging hydrides on FeMoco may favor the formation of locally low- or intermediate spin Fe ions, apt for N_2 coordination and efficient nitrogenase activity. This hypothesis is rooted in the strong-field, electron-donating nature of *terminal* hydride ligands,[9] and the ability of these ligands to support the coordination of N_2 to Fe.[7,14] Prior to this work, the coordination and subsequent functionalization of N_2 at an Fe(μ-H)Fe unit was without literature precedent. It is thus worthwhile to consider the spectroscopic, geometric, and thermodynamic properties of the compounds presented herein as model complexes for a bridging hydride-bound state of FeMoco.

The diiron compounds studied in this work are supported by strong-field phosphine, silyl, and hydride ligands. The observation of low-spin ground states in **6.3-N_2** and **6.4-$(N_2)_2$** is thus unsurprising and favors the terminal coordination of N_2, allowing for the complete characterization of these model complexes. Unexpectedly, variable-

temperature NMR experiments are consistent with a low-lying triplet excited state of **6.3-N_2** that is observed to lie 4.7 kcal/mol above the ground $S = 0$ state. The five-coordinate geometry of Fe1 and the electron-deficient nature of the $Fe_2(\mu\text{-}H)_2$ core likely allow access to this state. This result underscores the propensity of coordinatively-unsaturated Fe centers to populate higher spin configurations, even in strong-field, tetragonal ligand environments.[42-44]

Since an N_2-bound form of FeMoco has yet to be characterized, it is important to delineate the thermodynamic factors of N_2-coordination to synthetic, multimetallic platforms.[45] As the two Fe sites in **6.3-$(N_2)_2$** are identical, it is curious that one N_2 ligand is lost on warming to room temperature. The accommodation of two N_2 molecules in the substrate pocket of [SiP_2O] likely results in increased steric repulsion, rendering one N_2 ligand labile. In addition, EXAFS data indicate that the formation of **6.3-$(N_2)_2$** from **6.3-N_2** is accompanied by a separation of the two Fe centers by *ca*. 0.3 Å. DFT-optimized geometries suggest that this elongation distorts the $Fe_2(\mu\text{-}H)_2$ rhomb and increases the average Fe-H distances by 0.04 Å. Combined with the aforementioned steric effects, the energetic penalty of reorganizing the $Fe_2(\mu\text{-}H)_2$ core manifests itself in the small overall enthalpy of N_2 binding.

The chemical reduction of **6.3-N_2** is coupled to the coordination of N_2 to form **6.4-$(N_2)_2$**, indicating much stronger binding of N_2 to the reduced $Fe_2(\mu\text{-}H)_2$ core. The large equilibrium binding constant found for the coordination of N_2 to the vacant site of **6.4-N_2** via electrochemical analysis supports this observation. Assuming that the entropy of N_2 coordination to **6.3-N_2** and **6.4-N_2** is similar,[46] this dictates a much more negative enthalpy of N_2 binding to **6.4-N_2** (ΔH = -18 kcal/mol) than to **6.3-N_2** (ΔH = -9 kcal/mol).

The experimental difference in N_2 binding enthalpy ($\Delta\Delta H_{exp}$= 9 kcal/mol) between **6.3-N_2** and **6.4-N_2** agrees well with that predicted by DFT in the gas phase ($\Delta\Delta H_{DFT}$ = 8 kcal/mol).

The ability to reduce **6.3-$(N_2)_2$** without a large geometric distortion is remarkable as 36 valence electrons are present and reduction thus requires the occupation of an antibonding orbital. The electrochemical data collected on **6.3-N_2** suggest that at room temperature, electron transfer is preceded by the coordination of N_2 to produce **6.4-$(N_2)_2$**, necessitating the intermediacy of **6.3-$(N_2)_2$**. The SOMO's of **6.4-N_2** and **6.4-$(N_2)_2$** are spatially very similar and are formally described as Fe-Fe π-antibonding. This orbital is *less* antibonding in **6.4-$(N_2)_2$** than in **6.4-N_2** as a result of the larger separation between the Fe sites (2.839 Å in **6.4-$(N_2)_2$**, 2.632 Å in **6.4-N_2**, DFT-optimized geometries). This analysis helps to rationalize why the reduction of **6.3-$(N_2)_2$** to **6.4-$(N_2)_2$** is accessed at much more positive potentials than for **6.3-N_2** to **6.4-N_2**: the $Fe_2(\mu\text{-}H)_2$ core in **6.3-$(N_2)_2$** is preorganized for electron transfer as the LUMO is nearly non-bonding with respect to the two Fe centers.

The electrochemical data obtained for this system suggests that the mixed-valent **6.4-N_2** displays a 10^6-fold enhancement of N_2-binding affinity over **6.3-N_2**. The SOMO of **6.4-$(N_2)_2$** and also **6.4-N_2** is mostly-centered on the two Fe atoms and non-bonding with respect to the N_2 ligands. Population of this orbital serves to raise the energy of the occupied d-orbitals, enhancing the pi-backbonding interaction with the bound N_2 ligands. We suspect that the reason for the increased N_2 binding affinity of **6.4-N_2** compared to **6.3-N_2** results from (i) the formal reduction of the Fe centers, increasing their ability to pi-backbond into the N-N pi-manifold, and (ii) the concomitant increase in Fe-Fe

separation upon reduction, which relaxes some steric pressure for the binding of the second N_2 equivalent. These two factors are difficult to distinguish from one another. We note that the presence of a low-spin, formally-d^7 metal center in a pseudo-octahedral ligand environment is unusual, but is made possible by bridging hydride ligands.[47] The bridging hydride ligands in the present system render the LUMO of **6.3-$(N_2)_2$** nonbonding with respect to the Fe-H bonds, and thus chemically-accessible.

Open-shell Fe(μ-H)Fe species have been proposed in a number of metalloenzymes, and well-characterized synthetic examples are rare.[47-50] Moreover, the precise location of the transient hydrides found on FeMoco are unknown.[10] The hydride-bound intermediate displays hyperfine coupling (A_{iso} ~ 23 MHz) to two chemically-equivalent hydrogen atoms that were assigned as hydride ligands bridging unspecified Fe atoms.[51] One possible structure considered by the authors was that of a $Fe_2(\mu\text{-}H)_2$ unit. The isolation of **6.4-$(N_2)_2$** allows for the spectroscopic parameters of a structurally well-defined $Fe^{II}(\mu\text{-}H)_2Fe^{I}$ core to be defined and tested against those of the cluster. X-band EPR data on **6.4-$(N_2)_2$** reveal large hyperfine coupling ($^{H}A_{iso}$ = 73 MHz) to the bridging hydride ligands. The large $^{H}A_{iso}$ value for **6.4-$(N_2)_2$** relative to the hydride-bound intermediate is expected since in **6.4-$(N_2)_2$** the total unpaired spin density is spread out over fewer atoms than in the large, spin-coupled FeMoco cluster. The spin-dipolar term, ^{H}T = [11, -7, -4] (MHz) in **6.4-$(N_2)_2$** is nearly axial, and distinct from the rhombic term found for the hydride-bound FeMoco intermediate [-13.3, 0.7, 12.7].[10] Definitive conclusions correlating **6.4-$(N_2)_2$** as a model of the hydride-bound intermediate are premature and require comparative ENDOR experiments and analyses.[45]

6.4. Concluding Remarks

Transient hydride ligands bridging two or more iron centers purportedly accumulate on the iron-molybdenum cofactor (FeMoco) of nitrogenase, and their role/s in the reduction of N_2 to NH_3 remains unknown. We have suggested herein that one role these hydrides may serve is to facilitate N_2 coordination at an iron site of FeMoco. We have considered this hypothesis in the context of a diiron model system supported by two bridging hydride ligands. Most noteworthy, these compounds bind either one or two molecules of N_2 depending on the redox state of the $Fe_2(\mu\text{-}H)_2$ unit. A highly unusual example of a mixed-valent $Fe^{II}(\mu\text{-}H)_2Fe^{I}$ has been described that displays a 10^6-fold enhancement of N_2 binding affinity over its oxidized congener, estimated by spectroscopic and electrochemical techniques. This result underscores the dramatic impact a single electron-transfer (ET) step can play in terms of substrate binding. Moreover, the model system points to the possibility that binding one molecule of substrate (N_2) can serve to facilitate an ET step and concomitant binding of a second equivalent of substrate. We have not yet considered further such a scenario for biological systems that reduce N_2, but it is a possibility we wish to note. Finally, the compounds described here show promise as functional models of nitrogenase as substantial amounts of NH_3 are produced upon exposure to proton and electron equivalents.

6.5. Experimental Section

General Considerations

All manipulations were carried out using standard Schlenk or glovebox techniques under an N_2 or Ar atmosphere where noted. Unless otherwise noted, solvents were deoxygenated and dried by thoroughly sparging with N_2 gas followed by passage through an activated alumina column in the solvent purification system by SG Water, USA LLC. Non-halogenated solvents were tested with a standard purple solution of sodium benzophenone ketyl in tetrahydrofuran in order to confirm effective oxygen and moisture removal. All reagents were purchased from commercial vendors and used without further purification unless otherwise stated. Bis-(2-diisopropylphosphinophenyl)-chlorosilane (**6.1**),[7] $[H(Et_2O)_2][(3,5\text{-}(CF_3)_2C_6H_3)_4B]$,[52] KC_8,[53] $[Cp_2Fe][PF_6]$,[54] and anhydrous $^{57}FeCl_2$[55] were synthesized following literature procedures. Deuterated solvents were purchased from Cambridge Isotope Laboratories, Inc., degassed and dried over NaK alloy then vacuum-transferred onto activated 3 Å molecular sieves prior to use. D_2 was freed of residual H_2O and O_2 by passage through a coiled trap maintained at 77K prior to use. Elemental analyses were performed by Robertson Microlit Laboratories, Ledgewood, N.J. ^1H, ^{13}C and ^{29}Si chemical shifts are reported in ppm relative to tetramethylsilane, using residual solvent resonances as internal standards. ^{31}P chemical shifts are reported in ppm relative to 85% aqueous H_3PO_4. Solution phase magnetic measurements were performed by the method of Evans.[56] Near-Infrared spectra were obtained on a Nicolet FT-NIR spectrometer using quartz cuvettes capped with a Teflon screw cap. X-band EPR spectra were obtained on a Bruker EMX spectrometer on 5mM solutions prepared as frozen glasses in 2-MeTHF. EPR spectra were simulated using the EasySpin suite of programs with Matlab 2014.[57]

IR Spectroscopy

KBr-IR measurements were obtained on a Bio-Rad Excalibur FTS 3000 spectrometer. Thin-film and room temperature solution-phase IR were obtained on a Bruker Alpha spectrometer equipped with a diamond ATR probe. Variable-temperature solution IR spectra were acquired with the use of a SpecAc cryostat mounted within the Bio-Rad spectrometer.

Optical Spectroscopy

Measurements were taken on a Cary 50 UV-Vis spectrophotometer using a 1-cm quartz cell connected to a round-bottom flask and sealed with a Teflon stopcock. Variable temperature measurements were collected with a Unisoku CoolSpek cryostat mounted within the Cary spectrophotometer. N_2-binding equilibrium data were collected after the temperature of the cryostat was maintained at the desired temperature for at least five minutes.

X-Ray Crystallography

XRD studies were carried out at the Beckman Institute Crystallography Facility on a Brüker Kappa Apex II diffractometer (Mo Kα radiation). Structures were solved using SHELXS and refined against F^2 on all data by full-matrix least squares with SHELXL. The crystals were mounted on a glass fiber under Paratone N oil.

Electrochemistry

Electrochemical measurements were carried out in a thick-walled single-compartment electrochemical cell fitted with a Teflon stopcock and tungsten leads protruding from the top of apparatus. A CH Instruments 600B electrochemical analyzer was used for data collection. A freshly-polished 0.071 cm^2 diameter glassy carbon

electrode (CH Instruments) was used as the working electrode, and platinum wire was used as the auxiliary electrode. The reference electrode was a $Ag/AgNO_3$(1_mM)/THF nonaqueous reference electrode (also contained 0.1 M tetra-*n*-butylammonium hexafluorophosphate) separated from the solution by a Vycor frit (Bioanalytical Systems, Inc.) Solutions (THF) of electrolyte (0.1 M tetra-*n*-butylammonium hexafluorophosphate) contained ferrocene (1 mM), to serve as an internal reference, and analyte (1 mM). All reported potentials are referenced to the ferrocene couple, Cp_2Fe^+/Cp_2Fe. All solutions were prepared under an N_2 atmosphere. Cyclic voltammograms were simulated with the DigiElch 7.0 software package.

^{57}Fe Mössbauer Spectroscopy

Spectra were recorded on a spectrometer from SEE Co (Edina, MN) operating in the constant acceleration mode in a transmission geometry. The sample was kept in an SVT-400 cryostat from Janis (Wilmington, MA). The quoted isomer shifts are relative to the centroid of the spectrum of a metallic foil of α-Fe at room temperature. Solid samples were prepared by grinding polycrystalline material into a fine powder and then mounted in a Delrin cup fitted with a screw-cap as a boron nitride pellet. Solution samples were transferred to a sample cup chilled to 77K inside of the glovebox. Upon freezing of the solution, the cup was quickly removed from the glovebox and immersed in liquid N_2 until being mounted in the cryostat. Data analysis was performed using the program WMOSS (www.wmoss.org) and quadrupole doublets were fit to Lorentzian lineshapes.

EXAFS

XAS data were collected in fluorescence mode at ~10K with a 30-element germanium detector (SSRL, BL7-3) using a Si(220) $\Phi = 90^o$ double monochromator with

a 9.5 keV cutoff for harmonic rejection. Photoreduction of the samples was not observed on subsequent scans (exposure time ~20 min per scan). Background removal and curve fitting were performed with EXAFSPAK (available at www-ssrl.slac.stanford.edu/exafspak.html). Data sets were fit over the range k = 2 – 12 $Å^{-1}$. A cobalt impurity in the slits prevented accurate fits over a wider range. All distances, R, and Debye-Waller factors, σ^2, were treated as adjustable parameters, and all threshold energy shifts, E_o, were linked but allowed to vary. The passive electron reduction factor, S_o, was fixed at 0.9.

DFT Calculations

Geometry optimizations, single-point calculations, frequency calculations and NO analyses were performed using the Gaussian03 suite of programs with the BP86 level of theory and a 6-31G(d) basis set for all atoms.

Synthesis of Compounds

$[SiP_2O]H_2$ (6.2). In the glovebox, a 100 mL Schlenk flask equipped with a Teflon stopper was charged with compound **6.1** (14.8 g, 32.8 mmol), triethylamine (3.5 g, 34.6 mmol), toluene (20 mL), and a magnetic stir bar. The flask was sealed and brought out of the glovebox. The clear solution was stirred and water (300 μL, 16.65 mmol) was added via micropipette in one portion under a backflow of N_2. A white solid immediately precipitated. The flask was sealed and heated to 100 ^oC for 3 days. The solution was subsequently cooled to rt and filtered through a coarse frit in the glovebox, leaving $[HNEt_3][Cl]$ (4.40 g, 32.0 mmol, 97%). The filtrate was concentrated to dryness *in vacuo* and triturated with hexamethyldisiloxane (2 x 2 mL) and concentrated yielding an off-white oily solid. This solid was suspended in 10 mL hexamethyldisiloxane and the

resulting suspension was stirred for 5 minutes and then cooled to -78 ^{o}C and filtered through a coarse frit leaving compound **6.2** as a white solid (9.44 g, 11.1 mmol, 68%). The mother liquor was concentrated to 2 mL and stored at -35 ^{o}C resulting in the slow formation of crystalline **6.2** (1.26 g, 1.5 mmol, 77% total yield). ^{1}H NMR (500 MHz, C_6D_6, 25^{o}C, ppm): 7.93 (d, 4H, Ar-H), 7.34 (d, 4H, Ar-H), 7.16 (t, 4H, Ar-H), 7.11 (m, 6H, Ar-H + Si-H), 2.03 (m, 4H, methine C-H), 1.92 (m, 4H, methine C-H), 1.08 (m, 24H, methyl C-H), 0.85 (m, 24H methyl C-H). ^{31}P{^{1}H} NMR (202.4 MHz, C_6D_6, 25 ^{o}C, ppm): -0.50 (s). ^{29}Si{^{1}H} NMR (99.3 MHz, C_6D_6, 25 ^{o}C, ppm): -30.42 (t, J_{Si-P} = 27.7 Hz). ^{13}C{^{1}H} NMR (125.7 MHz, C_6D_6, 25 ^{o}C, ppm): 146.98 (dd, J = 43.0 Hz, J = 2.6 Hz), 143.78 (d, J = 16.75 Hz), 137.48 (d, J = 16.0 Hz), 131.64 (d, J = 1.8 Hz), 128.99 (s), 128.35 (s), 25.21 (t, 14.5 Hz), 20.85 (d, J = 14.4 Hz), 20.63 (J = 18.7 Hz), 20.21 (t, J = 11.2 Hz). IR (KBr): ν(Si-H) = 2199, 2166 cm^{-1}.

[SiP$_2$O]Fe$_2$(μ-H)$_2$(N$_2$) (6.3-N$_2$). In the glovebox, a 100 mL Schlenk flask was charged with compound **6.2** (2.00 g, 2.36 mmol), $FeBr_2$ (1.02 g, 4.72 mmol), THF (50 mL) and a magnetic stir bar. The solution was stirred vigorously at room temperature for 3 hours resulting in a clear pale orange solution. Solvent was evaporated to dryness *in vacuo*, and Et_2O (50 mL) was added to the resulting residue. The Schlenk tube was sealed and the suspension was vigorously stirred for 2 hours at rt producing a fine powder. Solvent was evaporated *in vacuo* and the beige powder was subsequently dried under dynamic vacuum for 1 hour. Freshly prepared Na(Hg) amalgam (0.217 g Na, 9.44 mmol, 20 g Hg) and a 1:1 mixture of pentane:Et_2O (75 mL) was added to the flask and vigorous stirring was commenced. The suspension was stirred overnight at room temperature, resulting in the deposition of ample gray precipitate and a solution color change to dark green. The

mixture was filtered through Celite and the solids were washed with Et_2O (2 x 25 mL). The filtrate was evaporated *in vacuo* and pentane (10 mL) was added subsequently, resulting in the slow precipitation of green solid. The solution was decanted and the solid was washed with additional pentane (2 x 5 mL) furnishing 1.40 g of **6.3-N_2** (60% yield). ^{1}H NMR (500 MHz, C_6D_6, 25^{o}C, 1 atm N_2, ppm): 8.44 (bs, 4H, Ar-H), 8.11 (bs, 4H, Ar-H), 7.26 (bs, 4H, Ar-H), 6.90 (bs, 4H, Ar-H), 2.79 (bs, 2H, methine C-H), 2.41 (bs, 2H, methine C-H), 2.12 (bs, 2H, methine C-H), 1.95 (bs, 2H, methine C-H), 1.45 (bs, 12H, methyl C-H) , 1.07 (bs, 24H methyl C-H) , 0.56 (bs, 12H methyl C-H), -39.9 (bs, 2H Fe(μ-H)Fe). ^{31}P{^{1}H} NMR (202.4 MHz, C_6D_6, 25^{o}C, ppm): 112.6, 90.2, 80.7. UV-Vis (Hexane, 298K, nm {$cm^{-1}\,M^{-1}$}): 400 {2900}, 600 {1600}, 680 {2450}. Anal: calc. for $C_{48}H_{74}Fe_2OP_4Si_3$: C 58.42, H 7.56, N 2.84; found: C 58.16, H 7.42, N 2.68. IR (KBr): ν(N-N) = 2062 cm^{-1}.

[SiP$_2$O]Fe$_2$(μ-D)$_2$(N$_2$) (6.3-N$_2$-*d$_2$*). A 100 mL Schlenk flask was charged with **6.3-N_2** (78 mg, 79 μmol), pentane (20 mL) and a magnetic stirbar. The flask was sealed, chilled to 77K, and the head space was evacuated for five minutes and then resealed and allowed to warm to room temperature. This process was repeated two more times. The flask was subsequently backfilled with 1 atm of D_2, sealed and stirred at room temperature for 1 hour, causing no detectable color change. The volatiles were then removed *in vacuo* and the remaining residue was redissolved in toluene (5 mL) under an N_2 atmosphere, filtered into a 20 mL scintillation vial and then concentrated to dryness *in vacuo*. Minimal pentane (1 mL) was subsequently added to dissolve the green residue and this solution was allowed to stand overnight, depositing green crystals of **6.3-N_2-*d_2*** (43 mg, 43 μmol, 55%). Except for the hydride resonance, the ^{1}H NMR of **6.3-N_2-*d_2*** looked identical to

6.3-N_2. The residual hydride signal was integrated to verify that >95% of **6.3-N_2** was converted to **6.3-N_2-*d_2***.

[SiP_2O]$^{57}Fe_2(\mu\text{-}H)_2(N_2)$. In the glovebox, a 20 mL scintillation vial was charged with compound **6.2** (104 mg, 123 μmol), $FeBr_2$ (26.7 mg, 124 μmol), $^{57}FeCl_2$ (15.8 mg, 125 μmol), THF (10 mL) and a magnetic stir bar. The solution was stirred vigorously at room temperature for 3 hours resulting in a clear pale orange solution. Solvent was evaporated to dryness *in vacuo*, and Et_2O (10 mL) was added to the resulting residue. The scintillation vial was capped and the suspension was vigorously stirred for 1 hour at rt producing a fine powder. Solvent was evaporated *in vacuo* and the beige powder was subsequently dried under dynamic vacuum for 1 hour. Freshly prepared Na(Hg) amalgam (11.5 mg Na, 500 μmol, 2.3 g Hg) suspended in a 1:1 mixture of pentane : Et_2O (10 mL) was added to the flask and vigorous stirring was commenced. The suspension was stirred for 4 hours at room temperature, resulting in the deposition of ample gray precipitate and a solution color change to dark green. The mixture was filtered through Celite and the solids were washed with Et_2O (2 x 5 mL). The filtrate was evaporated *in vacuo* and pentane (2 mL) was added subsequently, resulting in the slow precipitation of green solid. The solution was decanted and the solid was washed with additional pentane (3 x 2 mL). The green solid was dissolved in toluene (2 mL), filtered and evaporated to dryness *in vacuo*. The residue was dissolved in pentane (2 mL) and allowed to stand overnight, resulting in the precipitation of crystalline ^{57}Fe enriched **6.3-N_2** (53.2 mg, 44% yield). The ^{1}H NMR looked identical to **6.3-N_2**. The level of ^{57}Fe incorporation was not explicitly determined.

{Na(12-crown-4)$_2$}{[SiP$_2$O]Fe$_2$(μ-H)$_2$(N$_2$)$_2$} (6.4-(N$_2$)$_2$). In a glovebox, a 20 mL scintillation vial was charged with sodium (4.5 mg, 196 μmol), mercury (2.45g), a solution of 12-crown-4 (50 mg, 284 μmol) in THF (5 mL) and a magnetic stir bar. The vial was capped and stirred vigorously for 5 minutes, resulting in a finely-divided Na(Hg) suspension. The vial was uncapped and complex **6.3-N$_2$** (104.1 mg, 105 μmol) was added in one portion. The vial was vigorously stirred for 3 minutes, resulting in a color change to a very dark amber. This solution was filtered and evaporated to dryness *in vacuo*. The residue was thoroughly digested with pentane (5mL) which was subsequently decanted. The resulting dark brown microcrystals were additionally washed with 2:1 pentane:Et$_2$O (5 mL) and then pentane (2 mL). Residual solvent was evaporated *in vacuo* leaving 141 mg of **6.4-(N$_2$)$_2$** (98% yield). ^{1}H NMR (300 MHz, THF-*d*$_8$, 25^{o}C, 1 atm N$_2$, ppm): 7.38, 3.78, -2.12. UV-Vis-NIR (2-MeTHF, 298K, nm {cm^{-1} M^{-1}}): 645 {1800}, 960 {600}, 1075 {300}, 1410 {150}. IR (KBr): ν(N-N) = 2023 cm^{-1}, 1979 cm^{-1}. μ_{eff} (THF-*d*$_8$, Evans method, 20 ^{o}C): 1.7 μ_B.

Typical NH$_3$ Generation Protocol

6.3-N$_2$ (2 mg, 0.002 mmol) was dissolved in Et$_2$O (0.5 mL) in a 50 mL Schlenk tube equipped with a stir bar. This suspension was vigorously stirred and cooled to -78 °C in a cold well inside of the glove box. A similarly cooled solution of [H(Et$_2$O)$_2$][(3,5-(CF$_3$)$_2$C$_6$H$_3$)$_4$B], (93 mg, 0.092 mmol) in Et$_2$O (1.0 mL) was added to the suspension in one portion with rapid stirring. Any remaining acid was dissolved in cold Et2O (0.5 mL) and added subsequently. The reaction mixture turned orange upon addition of acid. Solid KC$_8$ (15 mg, 0.100 mmol) was suspended in cold Et$_2$O (0.75 mL) and added in one portion to the rapidly stirred solution in the Schlenk tube which was then tightly sealed.

The reaction was allowed to stir for 40 minutes at -78 °C before being warmed to room temperature and stirred for 15 minutes.

Ammonia Quantification

A Schlenk tube was charged with HCl (3 mL of a 2.0 M solution in Et_2O, 6 mmol). Reaction mixtures were vacuum transferred into this collection flask. Residual solid in the reaction vessel was treated with a solution of [Na][O-t-Bu] (40 mg, 0.4 mmol) in 1,2-dimethoxyethane (1 mL) and sealed. The resulting suspension was allowed to stir for 10 minutes before all volatiles were again vacuum transferred into the collection flask. After completion of the vacuum transfer, the flask was sealed and warmed to room temperature. Solvent was removed in vacuo and the remaining residue was dissolved in H_2O (1 mL). An aliquot of this solution (40 µL) was then analyzed for the presence of NH_3 (trapped as $[NH_4][Cl]$) via the indophenol method.[58] Quantification was performed with UV-Visible spectroscopy by analyzing the absorbance at 635 nm.

6.6. Cited References

1. Hoffman, B. M.; Lukoyanov, D.; Dean, D. R.; Seefeldt, L. C. *Acc. Chem. Res.* **2013**, *46*, 587.
2. Lee, H. I.; Igarashi, R. Y.; Laryukhin, M.; Doan, P. E.; Dos Santos, P. C.; Dean, D. R.; Seefeldt, L. C.; Hoffman, B. M. *J. Am. Chem. Soc.* **2004**, *126*, 9563.
3. George, S. J.; Barney, B. M.; Mitra, D.; Igarashi, R. Y.; Guo, Y. S.; Dean, D. R.; Cramer, S. P.; Seefeldt, L. C. *J. Inorg. Biochem.* **2012**, *112*, 85.
4. Anderson, J. S.; Rittle, J.; Peters, J. C. *Nature* **2013**, *501*, 84.
5. Creutz, S. E.; Peters, J. C. *J. Am. Chem. Soc.* **2014**, *136*, 1105.
6. Rodriguez, M. M.; Bill, E.; Brennessel, W. W.; Holland, P. L. *Science* **2011**, *334*, 780.
7. Takaoka, A.; Mankad, N. P.; Peters, J. C. *J. Am. Chem. Soc.* **2011**, *133*, 8440.
8. Bart, S. C.; Lobkovsky, E.; Bill, E.; Wieghardt, K.; Chirik, P. J. *Inorg. Chem.* **2007**, *46*, 7055.
9. Chatt, J.; Hayter, R. G. *J. Chem. Soc.* **1961**, 772.
10. Igarashi, R. Y.; Laryukhin, M.; Dos Santos, P. C.; Lee, H. I.; Dean, D. R.; Seefeldt, L. C.; Hoffman, B. M. *J. Am. Chem. Soc.* **2005**, *127*, 6231.
11. Lowe, D. J.; Thorneley, R. N. F. *Biochem. J.* **1984**, *224*, 877.
12. Yang, Z. Y.; Khadka, N.; Lukoyanov, D.; Hoffman, B. M.; Dean, D. R.; Seefeldt, L. C. *Proc. Natl. Acad. Sci. U. S. A.* **2013**, *110*, 16327.
13. Ghilardi, C. A.; Midollini, S.; Sacconi, L.; Stoppioni, P. *J. Organomet. Chem.* **1981**, *205*, 193.

14. Vandersluys, L. S.; Eckert, J.; Eisenstein, O.; Hall, J. H.; Huffman, J. C.; Jackson, S. A.; Koetzle, T. F.; Kubas, G. J.; Vergamini, P. J.; Caulton, K. G. *J. Am. Chem. Soc.* **1990**, *112*, 4831.

15. Allen, F. H. *Acta Cryst. Sect. B-Struct. Sci.* **2002**, *58*, 380.

16. A single, broad resonance is observable in the ^{29}Si NMR spectrum of **6.3-N$_2$** at 223K but discrete coupling to ^{31}P or ^{1}H nuclei was not discerned.

17. Curiously, the presence of three ^{1}H resonances (relative integral 6 : 3 : 3) observed upfield of δ = 0 ppm can be attributed to isopropyl C-H bonds that are engaged in agostic interactions with an Fe center (Figure 2). On warming to 293 K, the upfield isopropyl ^{1}H resonances broaden and shift back to lower fields, concomitant with a coalescence of the hydride resonances into a single broad feature, suggesting that the agostic interactions are only observed at low temperatures in the absence of additional N_2.

18. Katayama, T.; Nitta, T. *J. Chem. Eng. Data* **1976**, *21*, 194.

19. Suess, D. L. M.; Tsay, C.; Peters, J. C. *J. Am. Chem. Soc.* **2012**, *134*, 14158.

20. Boncella, J. M.; Green, M. L. H.; Ohare, D. *J. Chem. Soc.-Chem. Commun.* **1986**, 618.

21. Brown, S. D.; Mehn, M. P.; Peters, J. C. *J. Am. Chem. Soc.* **2005**, *127*, 13146.

22. Walter, M. D.; Grunenberg, J.; White, P. S. *Chem. Sci.* **2011**, *2*, 2120.

23. Pfirrmann, S.; Limberg, C.; Herwig, C.; Knispel, C.; Braun, B.; Bill, E.; Stosser, R. *J. Am. Chem. Soc.* **2010**, *132*, 13684.

24. Lowdin, P. O. *Phys. Rev.* **1955**, *97*, 1474.

25. Lubitz, W.; Reijerse, E.; van Gastel, M. *Chem. Rev.* **2007**, *107*, 4331.

26. Amara, P.; Mouesca, J. M.; Volbeda, A.; Fontecilla-Camps, J. C. *Inorg. Chem.* **2011**, *50*, 1868.

27. Harmer, J.; Finazzo, C.; Piskorski, R.; Ebner, S.; Duin, E. C.; Goenrich, M.; Thauer, R. K.; Reiher, M.; Schweiger, A.; Hinderberger, D.; Jaun, B. *J. Am. Chem. Soc.* **2008**, *130*, 10907.

28. Treatment of freshly-prepared solutions of **6.4-$(N_2)_2$** with one equivalent of ferrocenium hexafluorophosphate in THF solution regenerates **6.3-N_2** in >90% yield (^{1}H NMR integration).While solid **6.4-$(N_2)_2$** is stable for extended periods, **6.4-$(N_2)_2$** decomposes in solution ($t_{1/2}$(298 K) ~ 60 min). Repeating the ferrocenium oxidation on solutions of **6.4-$(N_2)_2$** after standing for 12 hours does not recover **6.3-N_2** but instead furnishes a mixture of unidentified paramagnetic and diamagnetic species.

29. Münck, E. *Aspects of ^{57}Fe Mössbauer Spectroscopy*; University Science Books: Sausalito, CA, 2000.

30. Robin, M. B.; Day, P. In *Advances in Inorganic Chemistry and Radiochemistry*; Emeléus, H. J., Sharpe, A. G., Eds.; Academic Press: 1968; Vol. Volume 10, p 247.

31. Allen J. Bard, L. R. F. *Electrochemical Methods: Fundamentals and Applications*; 2nd ed.; John Wiley and Sons, Inc: New York, 2000.

32. Collman, J. P.; Brauman, J. I.; Iverson, B. L.; Sessler, J. L.; Morris, R. M.; Gibson, Q. H. *J. Am. Chem. Soc.* **1983**, *105*, 3052.

33. Yandulov, D. V.; Schrock, R. R. *Science* **2003**, *301*, 76.

34. Arashiba, K.; Miyake, Y.; Nishibayashi, Y. *Nat. Chem.* **2011**, *3*, 120.

35. Hinnemann, B.; Norskov, J. K. *Top. Catal.* **2006**, *37*, 55.

36. Tondreau, A. M.; Stieber, S. C. E.; Milsmann, C.; Lobkovsky, E.; Weyhermuller, T.; Semproni, S. P.; Chirik, P. J. *Inorg. Chem.* **2013**, *52*, 635.

37. Pickett, C. J.; Vincent, K. A.; Ibrahim, S. K.; Gormal, C. A.; Smith, B. E.; Best, S. P. *Chem-Eur. J.* **2003**, *9*, 76.

38. Spatzal, T.; Aksoyoglu, M.; Zhang, L. M.; Andrade, S. L. A.; Schleicher, E.; Weber, S.; Rees, D. C.; Einsle, O. *Science* **2011**, *334*, 940.

39. Lancaster, K. M.; Roemelt, M.; Ettenhuber, P.; Hu, Y. L.; Ribbe, M. W.; Neese, F.; Bergmann, U.; DeBeer, S. *Science* **2011**, *334*, 974.

40. Lee, S. C.; Holm, R. H. *Chem. Rev.* **2004**, *104*, 1135.

41. Doan, P. E.; Telser, J.; Barney, B. M.; Igarashi, R. Y.; Dean, D. R.; Seefeldt, L. C.; Hoffman, B. M. *J. Am. Chem. Soc.* **2011**, *133*, 17329.

42. Zhang, J.; Gandelman, M.; Herrman, D.; Leitus, G.; Shimon, L. J. W.; Ben-David, Y.; Milstein, D. *Inorg. Chim. Acta* **2006**, *359*, 1955.

43. Rittle, J.; Peters, J. C. *Proc. Natl. Acad. Sci. U. S. A.* **2013**, *110*, 15898.

44. Bouwkamp, M. W.; Lobkovsky, E.; Chirik, P. J. *J. Am. Chem. Soc.* **2005**, *127*, 9660.

45. Chiang, K. P.; Bellows, S. M.; Brennessel, W. W.; Holland, P. L. *Chem. Sci.* **2014**, *5*, 267.

46. Thermodynamic measurements of N_2 binding in synthetic systems invariably display large negative entropies. See reference 19 and references therein.

47. Wang, W. G.; Nilges, M. J.; Rauchfuss, T. B.; Stein, M. *J. Am. Chem. Soc.* **2013**, *135*, 3633.

48. Kinney, R. A.; Saouma, C. T.; Peters, J. C.; Hoffman, B. M. *J. Am. Chem. Soc.* **2012**, *134*, 12637.

49. Smith, J. M.; Lachicotte, R. J.; Holland, P. L. *J. Am. Chem. Soc.* **2003**, *125*, 15752.

50. Jablonskyte, A.; Wright, J. A.; Fairhurst, S. A.; Peck, J. N. T.; Ibrahim, S. K.; Oganesyan, V. S.; Pickett, C. J. *J. Am. Chem. Soc.* **2011**, *133*, 18606.

51. Lukoyanov, D.; Yang, Z. Y.; Dean, D. R.; Seefeldt, L. C.; Hoffman, B. M. *J. Am. Chem. Soc.* **2010**, *132*, 2526.

52. Brookhart, M.; Grant, B.; Volpe, A. F. *Organometallics* **1992**, *11*, 3920.

53. Weitz, I. S.; Rabinovitz, M. *J. Chem. Soc.-Perkin Trans. 1* **1993**, 117.

54. Barlow, S.; Murphy, V. J.; Evans, J. S. O.; Ohare, D. *Organometallics* **1995**, *14*, 3461.

55. Berto, T. C.; Hoffman, M. B.; Murata, Y.; Landenberger, K. B.; Alp, E. E.; Zhao, J. Y.; Lehnert, N. *J. Am. Chem. Soc.* **2011**, *133*, 16714.

56. Evans, D. F. *J. Chem. Soc.* **1959**, 2003.

57. Stoll, S.; Schweiger, A. *J. Magn. Reson.* **2006**, *178*, 42.

58. Weatherburn, M. W. *Anal. Chem.* **1967**, *39*, 971.

Appendix 1: Supplementary Data for Chapter 4

Experimental Part

General Considerations. All manipulations were carried out using standard Schlenk or glovebox techniques under an N_2 atmosphere. Unless otherwise noted, solvents were deoxygenated and dried by thoroughly sparging with N_2 gas followed by passage through an activated alumina column in the solvent purification system by SG Water, USA LLC. Non-halogenated solvents were tested with a standard purple solution of sodium benzophenone ketyl in tetrahydrofuran in order to confirm effective oxygen and moisture removal. All reagents were purchased from commercial vendors and used without further purification unless otherwise stated. $\{K(Et_2O)\}\{[SiP^{iPr}_3]Fe(N_2)\}$ (**4.1**),[1] $\{[SiP^{iPr}_3]Fe(N_2H_4)\}\{BAr^F_{24}\}$,[1] $\{H(OEt_2)_2\}\{BAr^F_{24}\}$,[2] and anhydrous $^{57}FeCl_2$[3] were synthesized following literature procedures with slight modifications. ^{57}Fe-enriched **4.1** was obtained via $[SiP^{iPr}_3]^{57}Fe(Cl)$ by replacing $FeCl_2$ with $^{57}FeCl_2$.[1] The synthesis and characterization of $\{[SiP^{iPr}_3]Fe(CN)\}\{BAr^F_{24}\}$ will be reported in a full paper. Deuterated solvents were purchased from Cambridge Isotope Laboratories, Inc., degassed and stored over activated 3 Å molecular sieves prior to use. Elemental analyses were performed by Midwest Microlab, LLC, Indianapolis, IN. ^{1}H, ^{13}C and ^{29}Si chemical shifts are reported in ppm relative to tetramethylsilane, using residual solvent resonances as internal standards. ^{31}P chemical shifts are reported in ppm relative to 85% aqueous H_3PO_4. ^{15}N chemical shifts are reported in ppm relative to liquid NH_3 at 0 ppm and internally referenced to $CD_3C^{15}N$ at 242.6 ppm. Solution phase magnetic measurements were performed by the method of Evans.[4] Solid IR measurements were obtained on a Bruker Alpha spectrometer equipped with a diamond ATR probe.

EPR Spectroscopy. X-band EPR spectra were obtained on a Bruker EMX spectrometer on 2-5 mM solutions prepared as frozen glasses in 2-MeTHF. Samples were collected at powers ranging from 20 μW to 15 mW and modulation amplitudes of 1 – 5 Gauss. Spectra were simulated using the EasySpin[5] suite of programs with Matlab 2013.

Optical Spectroscopy. Measurements were taken on a Cary 50 UV-Visible spectrophotometer using a 1-cm quartz cell connected to a round-bottom flask and sealed with a Teflon stopcock. Variable temperature measurements were collected with a Unisoku CoolSpek cryostat mounted within the Cary spectrophotometer. Spectra of **4.5'** were obtained by charging the cuvette with solid **4.5'** and a flea stir bar, followed by evacuation of the headspace and sealing the Teflon stopcock. The adjacent compartment was charged with THF and sealed after application of mild vacuum. The cuvette was then mounted within the Unisoku cryostat and chilled to the desired temperature. Stirring was commenced and the stopcock separating the two compartments was opened allowing the THF to transfer *in vacuo* and dissolve **4.5'** at the desired temperature.

X-Ray Crystallography. XRD studies were carried out at the Beckman Institute Crystallography Facility on a Brüker Kappa Apex II diffractometer (Mo Kα radiation). Structures were solved using SHELXS or SHELXT and refined against F^2 on all data by full-matrix least squares with SHELXL. The crystals were mounted on a glass fiber under Paratone N oil.

Electrochemistry. Electrochemical measurements were carried out in a thick-walled one-component electrochemical cell fitted with a Teflon stopcock and tungsten leads protruding from the top of apparatus. A CD instruments 600B electrochemical analyzer was used for data collection. A freshly-polished glassy carbon electrode was used as the

working electrode and platinum wire was used as the auxiliary electrode. Solutions (THF) of electrolyte (0.1 M tetra-*n*-butylammonium hexafluorophosphate) contained ferrocene (1 mM), to serve as an internal reference, and analyte (1 mM). All reported potentials are referenced to the ferrocene couple, Cp_2Fe^+/Cp_2Fe.

^{57}Fe Mössbauer Spectroscopy. Spectra were recorded on a spectrometer from SEE Co (Edina, MN) operating in the constant acceleration mode in a transmission geometry. The sample was kept in an SVT-400 cryostat from Janis (Wilmington, MA). The quoted isomer shifts are relative to the centroid of the spectrum of a metallic foil of α-Fe at room temperature. Solid samples were prepared by grinding polycrystalline material into a fine powder and then mounted in a Delrin cup fitted with a screw-cap as a boron nitride pellet. Solution samples were transferred to a sample cup chilled to 77K inside of the glovebox. Upon freezing of the solution, the cup was quickly removed from the glovebox and immersed in liquid N_2 until being mounted in the cryostat. Data analysis was performed using the program WMOSS (www.wmoss.org) and quadrupole doublets were fit to Lorentzian lineshapes.

Features undergoing slow electronic relaxation in the magnetically-perturbed Mossbauer data were fit in the $S = 1/2$ representation. The Hamiltonian in this representation is given by,

$$\mathcal{H} = \beta\vec{S} \cdot \mathbf{g} \cdot \vec{B} + \vec{S} \cdot \mathbf{A} \cdot \vec{I} + \mathcal{H}_Q \qquad \textbf{Eqn A1.1}$$

$$\mathcal{H}_Q = \left(\frac{eQV_{zz}}{12}\right)\left[3\mathrm{I}_z^2 - \frac{15}{4} + \eta\left(\mathrm{I}_x^2 - \mathrm{I}_y^2\right)\right] \qquad \textbf{Eqn A1.2}$$

Where **g** is the g tensor obtained by EPR simulation, **A** is the ^{57}Fe hyperfine tensor, H_Q is the nuclear quadrupole interaction of the $I = 3/2$ excited state, and $\eta = (V_{xx} - V_{yy}) / V_{zz}$ is the asymmetry parameter.[6]

Fe K-edge X-ray Absorption Spectra. Samples were prepared by grinding polycrystalline material into a fine powder and then mounted in a Delrin cup. XAS data were collected in fluorescence mode at ~20K with a 30-element germanium detector (SSRL, BL 4-1) using a Si(220) $\Phi = 90^o$ double monochromator with a 9.5 keV cutoff for harmonic rejection. Photoreduction of the samples was not observed on subsequent scans (exposure time ~20 min per scan). Data averaging, background removal and curve fitting were performed with the SIXPACK[7] and Demeter[8] suites of programs. Edge energies were calibrated using α-Fe metal foil (7111.3 eV).

DFT Calculations. Geometry optimizations, single-point calculations and frequency calculations were performed using the Gaussian 09 (Rev B.01) suite of programs with the BP86 functional, the 6-31G(d) basis set for C and H atoms, and the def2TZVPP basis set for Fe, P, Si and N atoms.[9] Frequency calculations were performed on optimized geometries to ensure true minima. TD-DFT calculations were performed with ORCA 2.9[10] with the BP86 functional and def2TZVP functional.

Synthetic Procedures

{[SiP$^{iPr}_3$]Fe(NNH$_2$)}{OTf} (4.5'). In the glovebox, complex **4.1** (0.125 g, 150 μmol) was dissolved in 2-MeTHF (2 mL) and this solutions was filtered into a 20-mL scintillation vial that was subsequently frozen in a coldwell chilled externally with liquid nitrogen. A

second scintillation vial was charged with HOTf (0.053 g, 353 μmol) and 2-MeTHF (2 mL) and similarly frozen in the cold well. The acid solution was briefly thawed and layered on top of the frozen Fe-containing solution followed by refreezing the solutions. To combine the two layers, the vial was elevated off of the floor of the coldwell with forceps, and a pre-chilled spatula was used to mechanically stir the two layers until homogenous. (NOTE: It is critical to combine the layers as soon as the solvent glass melts and while the solution remains rather viscous.) The resulting solution was layered with pre-chilled pentane (15 mL) and allowed to stand at -78 ^{o}C for 1 hr, at which point the layers were combined, causing the formation of a purple precipitate. This solid was separated via gravity filtration through a medium frit at -78 ^{o}C and subsequently washed with additional, chilled pentane (2 x 20 mL), toluene (10 mL), and then pentane (2 x 5 mL). 63.7 mg of **4.5'** was obtained as a purple solid (<49 % yield) after drying *in vacuo*. **4.5'** prepared in this manner was found to be free of Fe-containing impurities, as judged by ^{57}Fe Mössbauer spectroscopy, but contains variable amounts of KOTf that is evident in the solid IR spectra. Attempts to free **4.5'** from this salt have been unsuccessful. Single crystals of **4.5'** suitable for X-ray diffraction were obtained by layering a concentrated 2-MeTHF solution of **4.5'** with pentane at -78 ^{o} C and allowing the mixture to stand for 16 hours. ^{1}H NMR (500 MHz, 9:1 THF-d_8: CD_3CN, 233 K, ppm): 9.50 (bs, 2H, NNH_2). ^{31}P{^{1}H} NMR (202.4 MHz, 9:1 THF-d_8: CD_3CN, 193 K, ppm): 95.5 (bs). ^{29}Si{^{1}H} NMR (99.3 MHz, 9:1 THF-d_8: CD_3CN, 193 K, ppm): 81.4 (m, FWHM = 100 Hz). UV-Visible (THF, 193 K, nm {$cm^{-1}\,M^{-1}$}): 528 {1480}, 742 {536}. IR (Solid, 298 K, cm^{-1}): 3207, 3039, 1627, 1443, 826.

{[SiP$^{iPr}_3$]Fe(^{15}N^{15}NH$_2$)}{OTf} (^{15}N-4.5'). Prepared in an analogous fashion to **4.5'** but employing **^{15}N-4.1.** ^{1}H NMR (500 MHz, 9:1 THF-d$_8$: CD$_3$CN, 233 K, ppm): 9.50 (d, $^1J_{NH}$: 97 Hz, 2H, NN*H*$_2$). ^{15}N NMR (50.6 MHz, 9:1 THF-d$_8$: CD$_3$CN, 213 K, ppm): 517.54 (bs, FWHM = 36 Hz), 198.45 (td, $^1J_{NH}$: 96 Hz, $^1J_{NN}$: 11 Hz). IR (Solid, 298 K, cm^{-1}): 1623, 1401, 803.

{[SiP$^{iPr}_3$]Fe(NND$_2$)}{OTf} (4.5'-*d*$_2$). Prepared in an analogous fashion to **4.5'** but employing DOTf. IR (Solid, cm^{-1}): 2380, 2241.

{[SiP$^{iPr}_3$]Fe(NNMe$_2$)}{OTf} (4.6). In the glovebox, complex **4.1** (0.235 g, 293 μmol), a magnetic stir bar, and 1,2-dimethoxyethane (6 mL) were charged into a 20 mL scintillation vial and chilled to -78 ºC in the coldwell. Stirring was commenced and methyl trifluoromethanesulfonate (100 μL, 911 μmol) was added in one portion via syringe. The solution was allowed to stir at this temperature for 90 minutes, resulting in a dark-amber solution. The vial was subsequently evacuated and slowly warmed to 298 K while solvent was concentrated *in vacuo*. Purple solids deposit during this process. The solids were transferred to a medium frit and washed at room temperature with benzene (3 x 10 mL), 1,2-dimethoxyethane (3 x 5 mL), and Et$_2$O (5 mL), followed by extraction into CH$_3$CN (10 mL) and concentration *in vacuo*. The resulting film was triturated with Et$_2$O and dried *in vacuo* to afford 116 mg of **4.6** (45 % yield) as an analytically-pure, free-flowing purple powder. Single crystals suitable for X-ray diffraction were obtained by slow diffusion of Et$_2$O into a concentrated CH$_3$CN solution of **4.6** at 298 K. ^{1}H NMR (500 MHz, CD$_3$CN, 293 K, ppm): 8.08 (3H, d, 7.3 Hz), 7.70 (3H, d, 7.6 Hz), 7.50 (3H, t, 7.3 Hz), 7.39 (3H, t, 7.6 Hz), 2.95 (6H, s), 2.46 (6H, hept, 6.7 Hz), 1.21 (18H, bs), 0.67 (18H, bs). ^{13}C NMR (125.7 MHz, CD$_3$CN, 293 K, ppm): 156.18, 143.19, 132.22, 130.78,

130.54, 128.58, 53.93, 31.79, 19.94. $^{29}Si\{^{1}H\}$ NMR (99.3 MHz, CD_3CN, 233 K, ppm): 74.2 (bq, $^{2}J_{SiP}$ = 33 Hz). $^{31}P\{^{1}H\}$ NMR (202.4 MHz, CD_3CN, 233 K, ppm): 94.9 (bs). UV-Visible (THF, 298K, nm {$cm^{-1}\,M^{-1}$}): 543 {1340}, 745 {430}. IR (Solid, cm^{-1}): 1498, 1373, 858. Anal: calc. for $C_{39}H_{60}F_3FeN_2O_3P_3SSi$: C 53.79, H 6.95, N 3.22; found: C 53.96, H 6.84, N 3.27.

{[SiP$^{iPr}_3$]Fe(^{15}N^{15}NMe$_2$)}{OTf} (^{15}N-4.6). Prepared in an analogous fashion to **4.6** but employing **^{15}N-1**. ^{15}N NMR (50.6 MHz, CD_3CN, 298 K, ppm): 530.4 (m, FWHM= 24 Hz), 184.7 (d, $^{1}J_{NN}$: 11.5 Hz). IR (Solid, cm^{-1}): 1474, 1354, 847.

{[SiP$^{iPr}_3$]Fe(NN(CD$_3$)$_2$)}{OTf} (4.6-*d*$_6$). Prepared in an analogous fashion to **4.6** but employing MeOTf-d_3. IR (Solid, cm^{-1}): 1439.

{[SiP$^{iPr}_3$]Fe(^{15}N^{15}N(CD$_3$)$_2$)}{OTf} (^{15}N-4.6-*d*$_6$). Prepared in an analogous fashion to **4.6** but employing MeOTf-d_3 and **1-^{15}N**. IR (Solid, cm^{-1}): 1399.

[SiP$^{iPr}_3$]Fe(NNH$_2$) (4.7). *Preparation of EPR samples.* In the glovebox, a quartz EPR tube pre-chilled in a cold well by an external liquid nitrogen bath was charged with a thawing 5 mM solution of **4.5'** in 2-MeTHF (150 μL). This solution was frozen and a thawing 5 mM solution of Cp*$_2$Co in 2-MeTHF (150 μL) was layered on top of the frozen solution of **4.5'**. A pre-chilled steel cannula was inserted into the EPR tube. The tube was elevated off of the floor of the cold well, partially melting the solutions. While still viscous, the solutions were agitated with the cannula for 3 minutes or until the mixture appeared homogeneous. The cannula was removed and the solution was refrozen in the cold well. EPR tubes were quickly removed from the glovebox and stored in liquid nitrogen prior to the collection of EPR data.

[SiP$^{iPr}_3$]Fe(NND$_2$) (4.7-*d*$_2$). EPR samples were obtained in an identical fashion to **4.7** but employ **4.7-*d*$_2$** as a reagent.

[SiP$^{iPr}_3$]^{57}Fe(NNH$_2$) (^{57}Fe-4.7). *Preparation of ^{57}Fe Mössbauer samples.* In the glovebox, a 1 mL Delrin cup, pre-chilled to 77K in a cold well by an external liquid nitrogen bath, was charged with a thawing 5 mM solution of **^{57}Fe-4.5'** in 2-MeTHF (300 μL). This solution was frozen and a thawing 5 mM solution of Cp*$_2$Co in 2-MeTHF (300 μL) was layered on top of the frozen solution of **^{57}Fe-4.5'** and similarly frozen. A pre-chilled steel spatula was inserted into the cup. Using pre-chilled forceps, the cup was elevated off of the floor of the cold well, partially melting the solutions. While still viscous, the solutions were gently agitated with the spatula for 10 minutes or until the mixture appeared homogeneous. The solutions were periodically refrozen by lowering the cup back on to the cold well floor to prevent thermal decomposition of **^{57}Fe-4.7**. The spatula was finally removed and the solution was refrozen in the cold well. The cup was quickly removed from the glovebox and stored in liquid nitrogen prior to the collection of Mössbauer data.

[SiP$^{iPr}_3$]Fe(NNMe$_2$) (4.8). In the glovebox, **4.6** (45 mg, 51.7 μmol) was suspended in 2-MeTHF (2 mL) and stirred at rt. A portion of 0.5 % Na(Hg) (2.0 mg Na, 87.0 μmol) was added, causing an immediate darkening of the solution. The reaction mixture was concentrated to dryness *in vacuo* after 5 minutes of stirring and the dark brown residue was extracted with pentane (2 x 5 mL). The solution was concentrated to dryness *in vacuo* affording 18 mg of **4.6** (48% yield). Complex **4.6** decays to a mixture of **4.2** and [SiP$^{iPr}_3$]Fe(H)N$_2$ overnight at room temperature as judged by ^{1}H NMR spectroscopy. Therefore, combustion analysis was not obtained. Single crystals suitable for X-ray diffraction were obtained by storing a saturated pentane solution of **4.8** at -35 ^{o}C overnight.

^{1}H NMR (500 MHz, C_6D_6, 298 K, ppm): 7.69, 6.36, 4.76. UV-Visible (THF, 298K, nm {$cm^{-1}\,M^{-1}$}): 320 {7700}, 428 {3380}, 536 (sh) {2040}, 985 {170}. IR (Solid, cm^{-1}): 1331, 1125, 838. μ_{eff} (C_6D_6, 298 K): 1.7 μ_B.

{[SiP$^{iPr}_3$]Fe(NN(H)Me)}{OTf}. In the glovebox, complex **4.1** (0.100 g, 120 μmol), a magnetic stir bar, and 1,2-dimethoxyethane (5 mL) were charged into a 20 mL scintillation vial and chilled to -78 ºC in the coldwell. Stirring was commenced and methyl trifluoromethanesulfonate (15 μL, 132 μmol) was added in one portion via syringe. The solution was allowed to stir at this temperature for 3 hours, resulting in a dark-amber solution. Trifluoromethanesulfonic acid (10 μL, 113 μmol) was added via syringe in one portion, causing an immediate lightening of the solution. Pre-chilled pentane (10 mL) was added portion-wise and stirring was continued at -78 ºC until a finely-dispersed pink solid had formed. This solid was separated via gravity filtration through a medium frit at -78 ºC and subsequently washed with additional, chilled pentane (2 x 20 mL). The solid was finally washed with room temperature toluene (2 x 5 mL) and pentane (2 x 5 mL), furnishing 30 mg of product as a purple solid (28 % yield) after drying *in vacuo*. Single crystals suitable for X-ray diffraction were obtained by layering a concentrated THF solution with pentane at -78 ºC and allowing the mixture to stand for 16 hours.

Reduction of 4.5' at Elevated Temperatures. Formation of 4.9 and 4.2. In the glovebox, complex **4.5'** (10.0 mg, 12 μmol) and a magnetic stir bar were charged into a 20 mL scintillation vial and cooled to -78 ºC in the coldwell. Similarly-chilled THF (2 mL) was added and the mixture was stirred for 20 minutes or until all of the solids had dissolved. The solution was subsequently frozen at liquid nitrogen temperatures, and a suspension of finely-ground Cp*$_2$Co (3.8 mg, 11 μmol) in THF (2 mL) was layered on top and similarly

frozen. The external liquid nitrogen bath was subsequently removed, and the mixture was allowed to slowly warm to room temperature with vigorous stirring over 20 minutes. At this point, the solution was filtered and concentrated to dryness *in vacuo*. The remaining orange residue was dissolved in C_6D_6 (500 μL), filtered and analyzed by ^{1}H NMR spectroscopy.

NMR Spectra

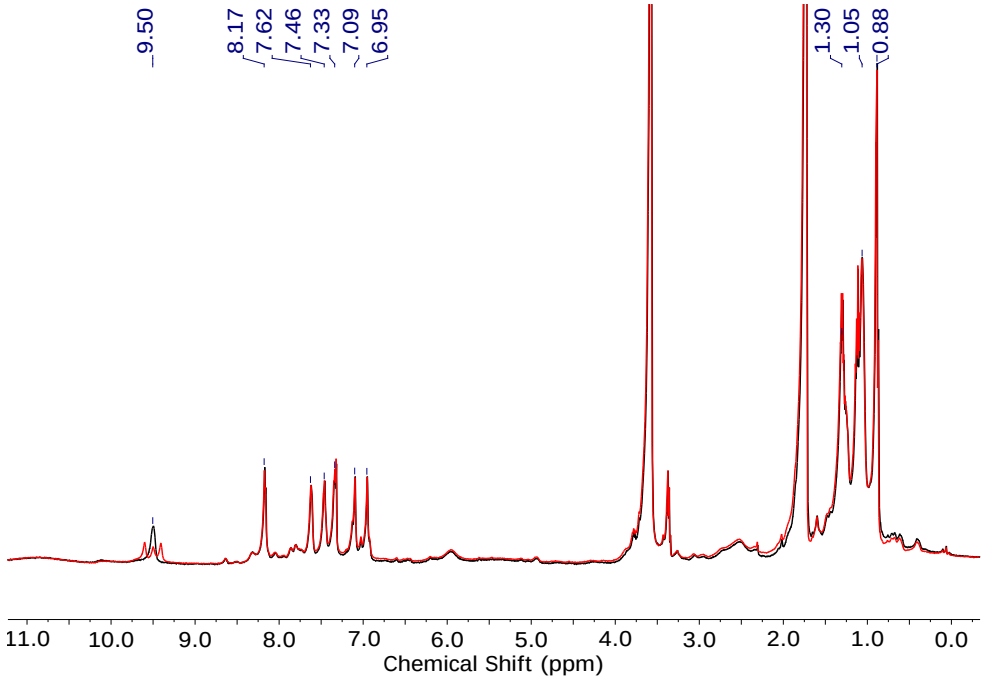

Figure A1.1. Overlaid ^{1}H NMR spectrum (500 MHz, 233K, Red) and {^{15}N}^{1}H NMR spectrum (Black) of **^{15}N-4.5'** recorded in THF-d_8. The ^{15}N decoupler window was centered at a chemical shift of 200 ppm. The broad, paramagnetically-shifted peaks scattered throughout the spectrum belong to one or more unidentified impurities that result from the partial warming of **4.5'** during the sample transfer into the NMR probe.

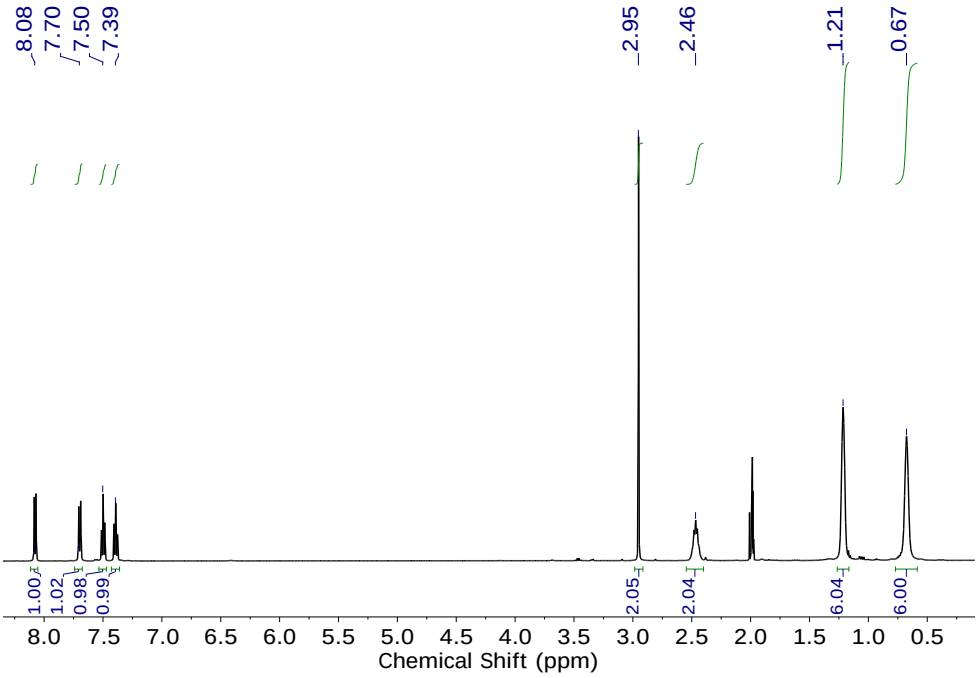

Figure A1.2. ^{1}H NMR spectrum (500 MHz, 293K) of **4.6** recorded in CD_3CN.

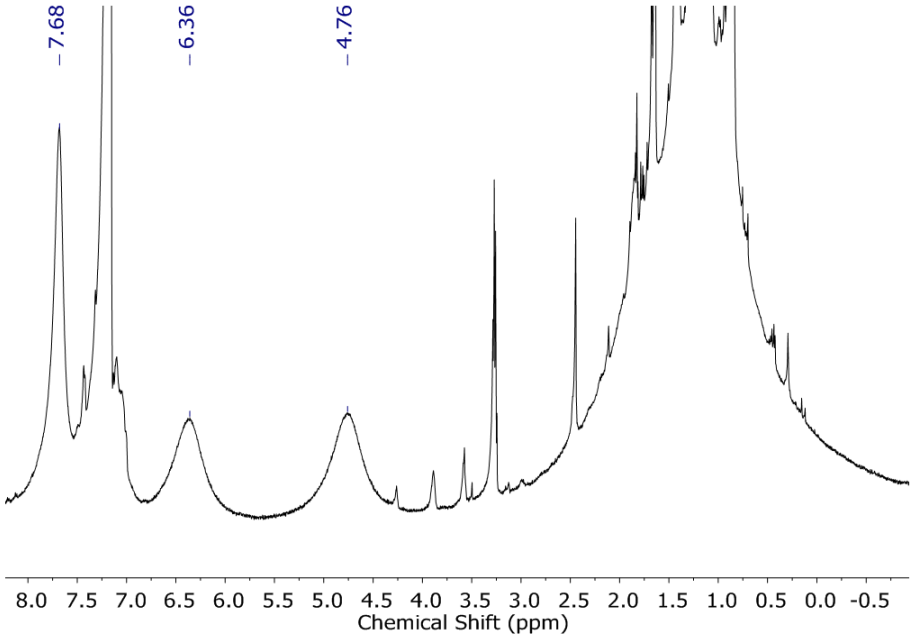

Figure A1.3. ^{1}H NMR spectrum (500 MHz, 298K) of **4.8** recorded in C_6D_6.

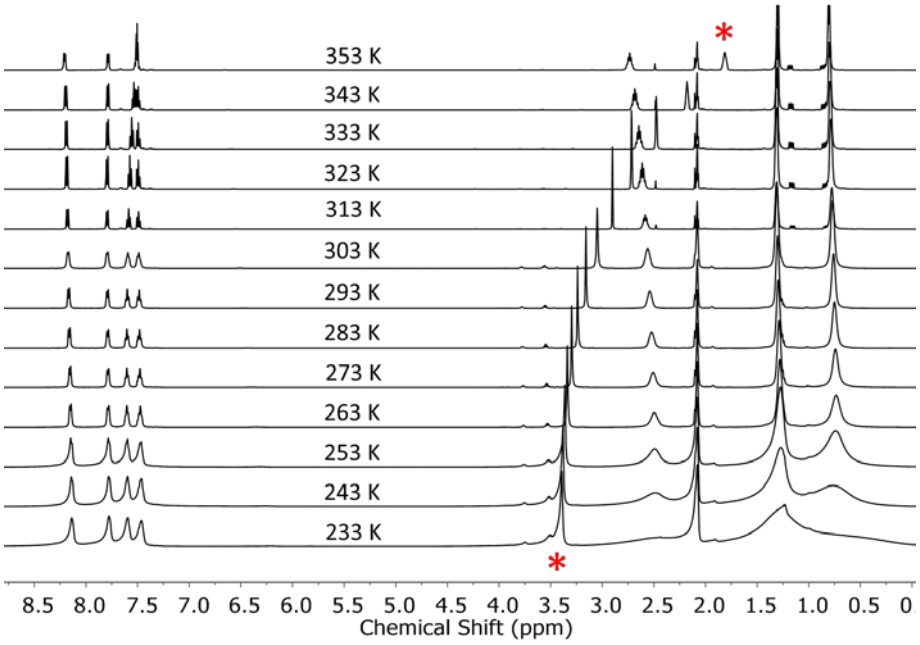

Figure A1.4. ^{1}H NMR spectra (500 MHz, listed temperatures) of **4.6** recorded in CD_3CN. The asterisk denotes the resonance assigned to the $NN(CH_3)_2$ protons.

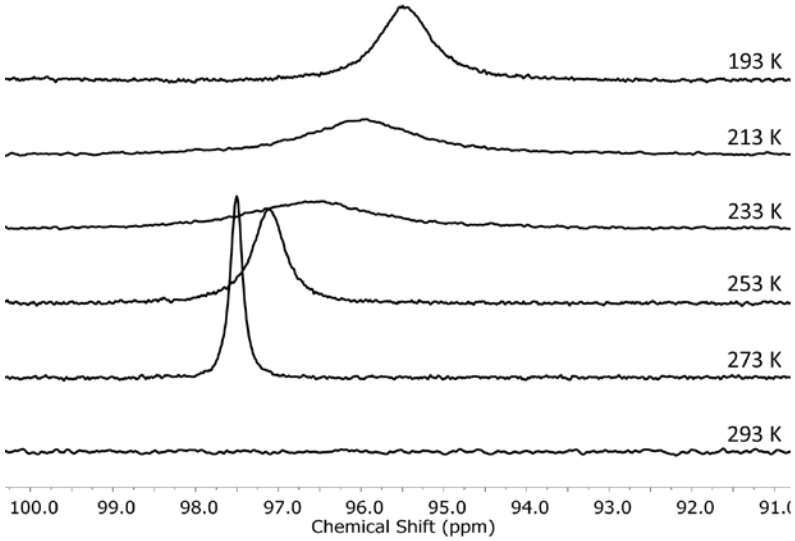

Figure A1.5. ^{31}P NMR spectra (202.4 MHz, listed temperatures) of **4.5'** recorded in 9:1 THF-d_8: CD_3CN. The absolute intensity of each spectra is arbitrary. Upon warming to 293 K, the signals of **4.5'** had completely vanished.

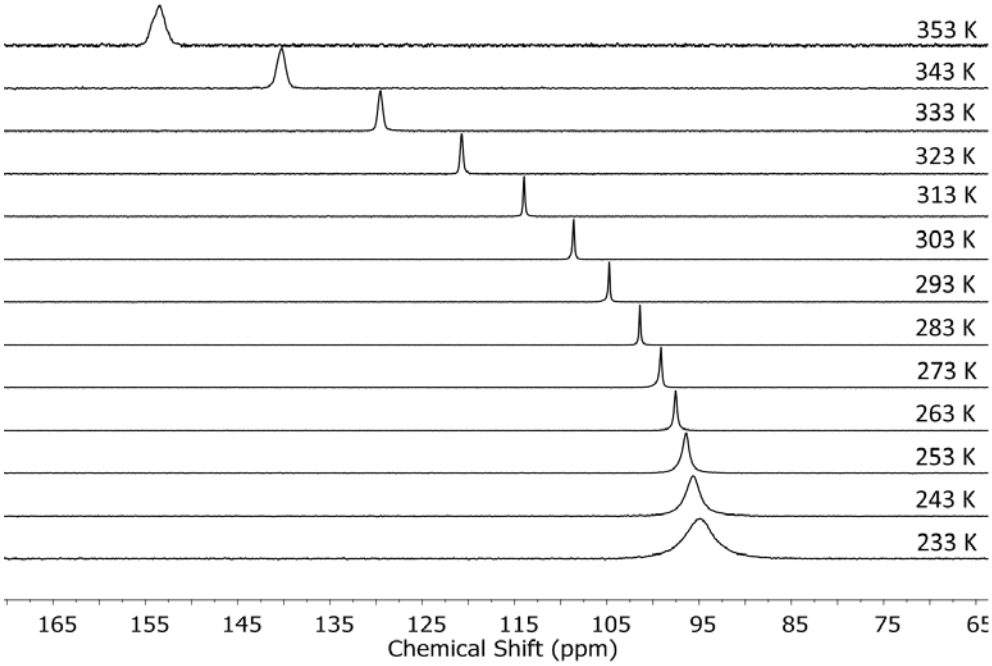

Figure A1.6. ^{31}P NMR spectra (202.4 MHz, listed temperatures) of **4.6** recorded in CD_3CN.

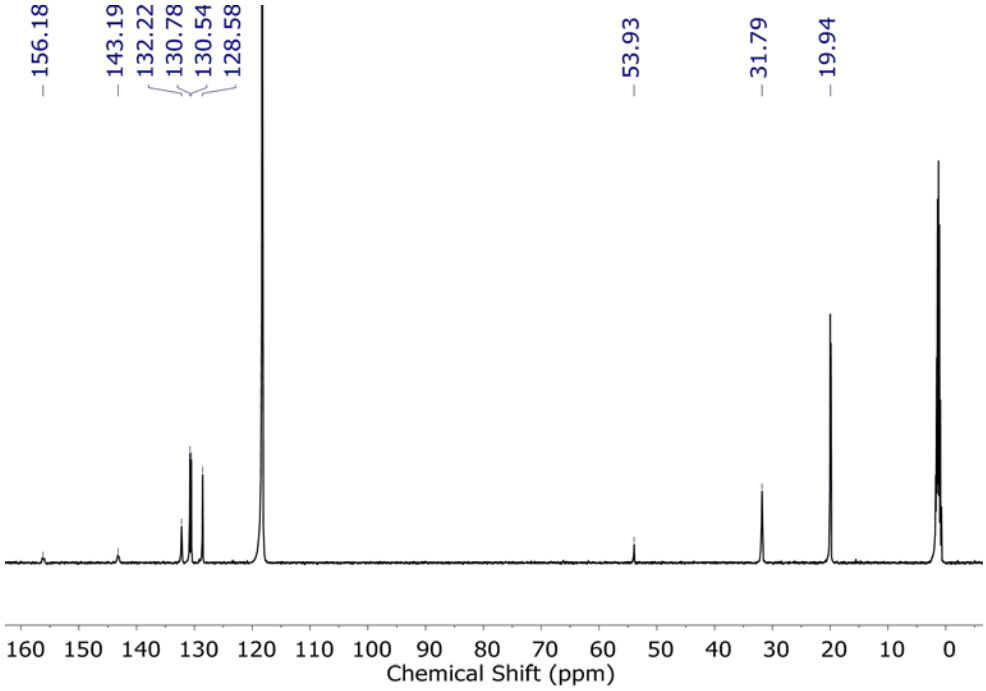

Figure A1.7. ^{13}C NMR spectrum (125.7 MHz, 293 K) of **4.6** recorded in CD_3CN.

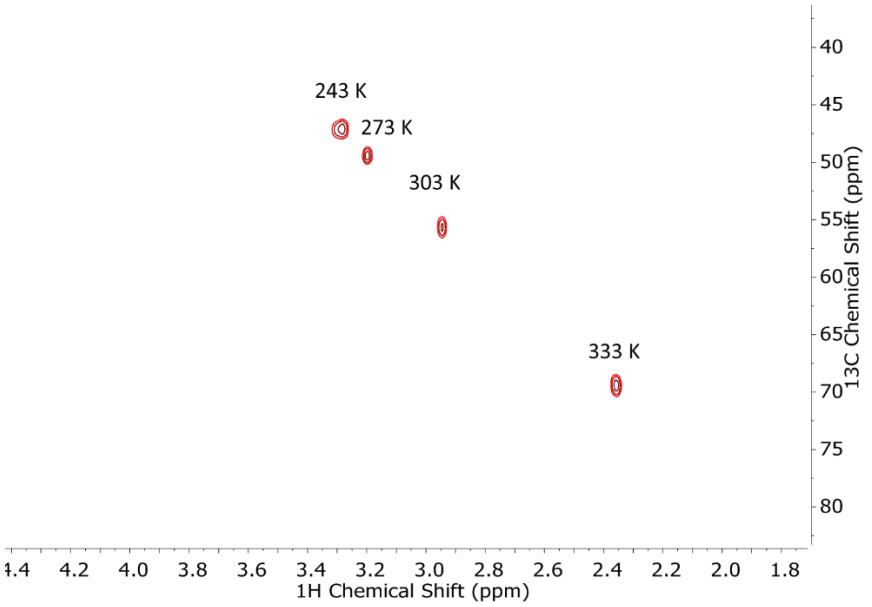

Figure A1.8. Stacked ^{1}H-^{13}C HMQC NMR spectra (125.7 MHz, listed temperatures) of **4.6** recorded in CD_3CN.

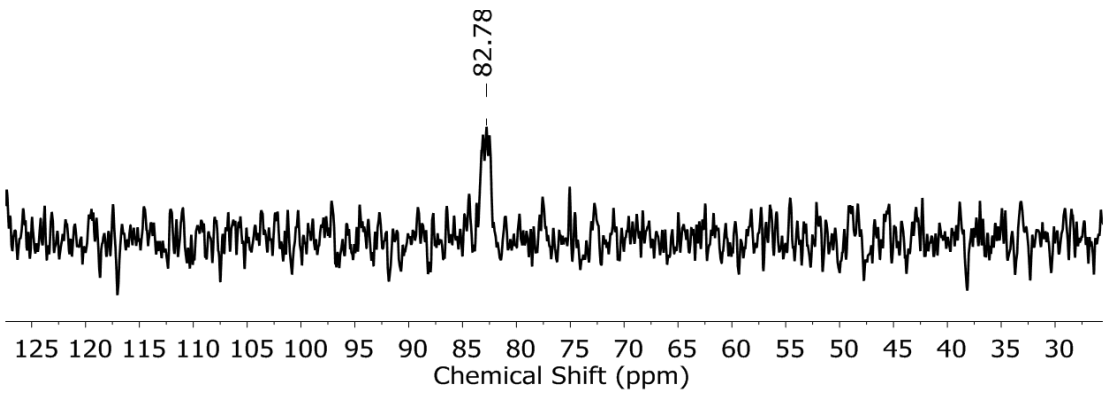

Figure A1.9. ^{29}Si NMR spectrum (99.3 MHz, 193 K) of **4.5'** recorded in 9:1 THF:CD_3CN.

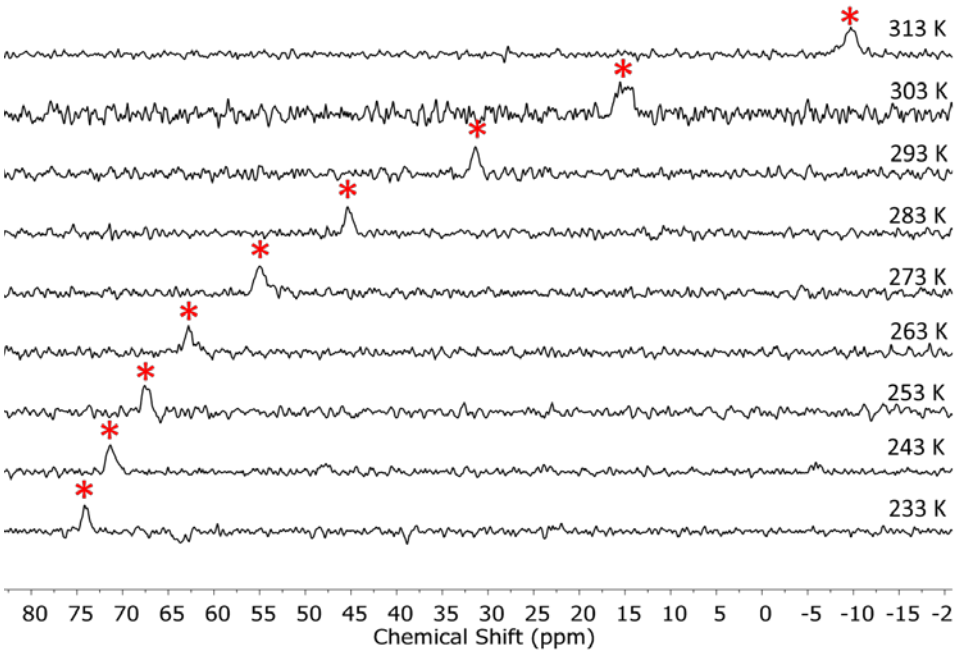

Figure A1.10. ^{29}Si NMR spectra (99.3 MHz, 193 K) of **4.6** recorded in CD_3CN.

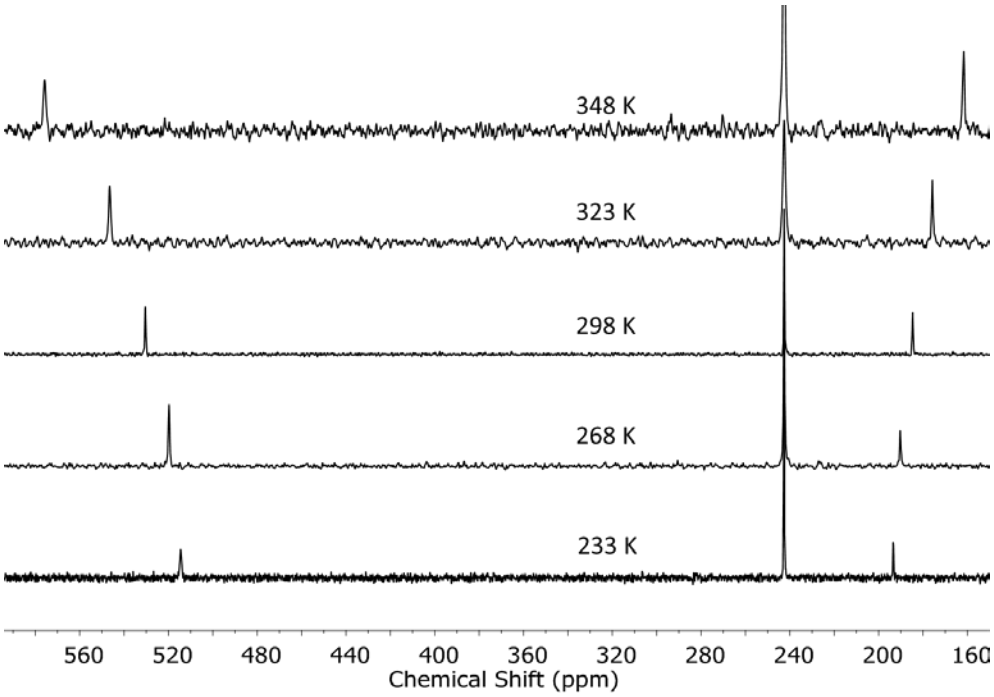

Figure A1.11. ^{15}N NMR spectra (50.6 MHz, listed temperatures) of **^{15}N-4.6** recorded in CD_3CN ($CD_3C^{15}N$ located at 242.6 ppm).

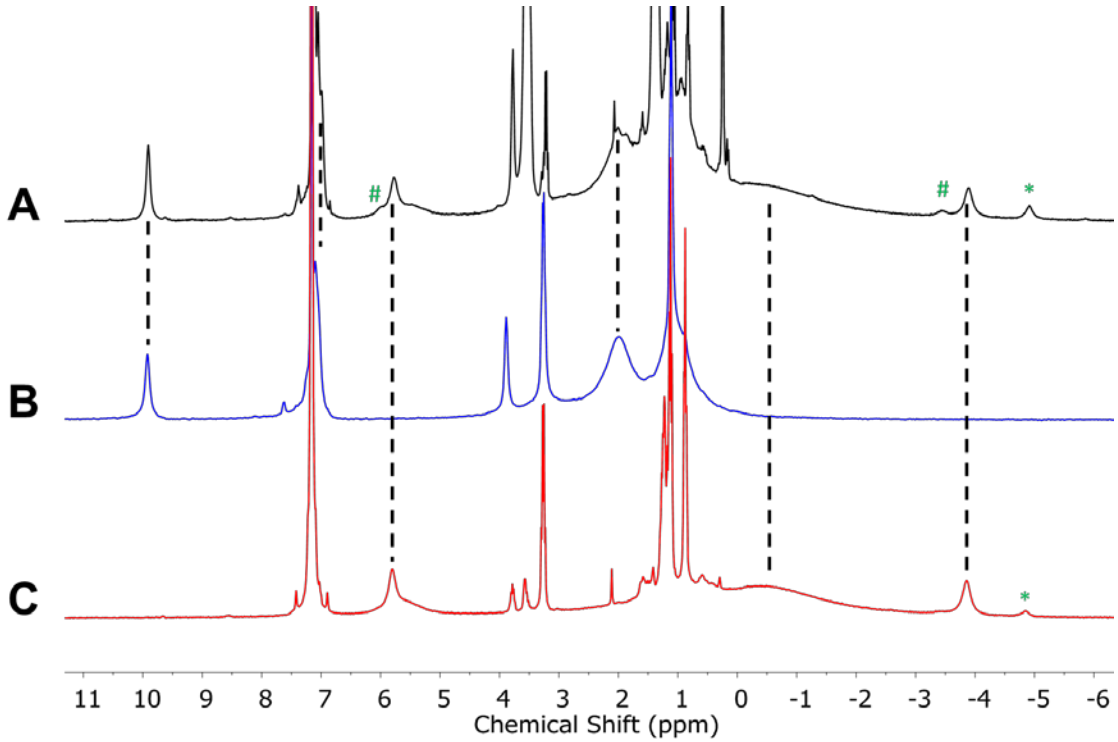

Figure A1.12. ^{1}H NMR spectra (300 MHz, 293 K, C_6D_6) of (A) the crude reaction mixture obtained by the reaction of **4.5'** with Cp^*_2Co in THF followed by warming to r.t. Trace (B) corresponds to the spectrum of **4.2** collected under identical conditions. Trace (C) corresponds to the spectrum of **4.9** collected under identical conditions. Features marked with an "#" arise from **4.11** and features marked with "*" arise from **4.10**. Compound **4.9** spontaneously decomposes to **4.10** in C_6D_6.[1]

Infrared Spectra

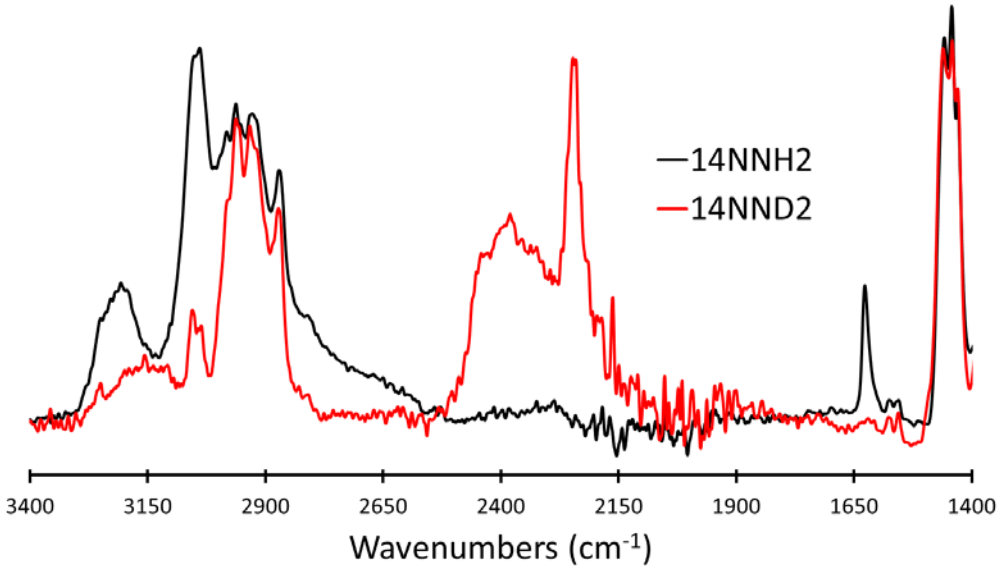

Figure A1.13. Overlaid IR absorption spectra of solid **4.5'** (Black), and **4.5'-*d*$_2$** (Red).

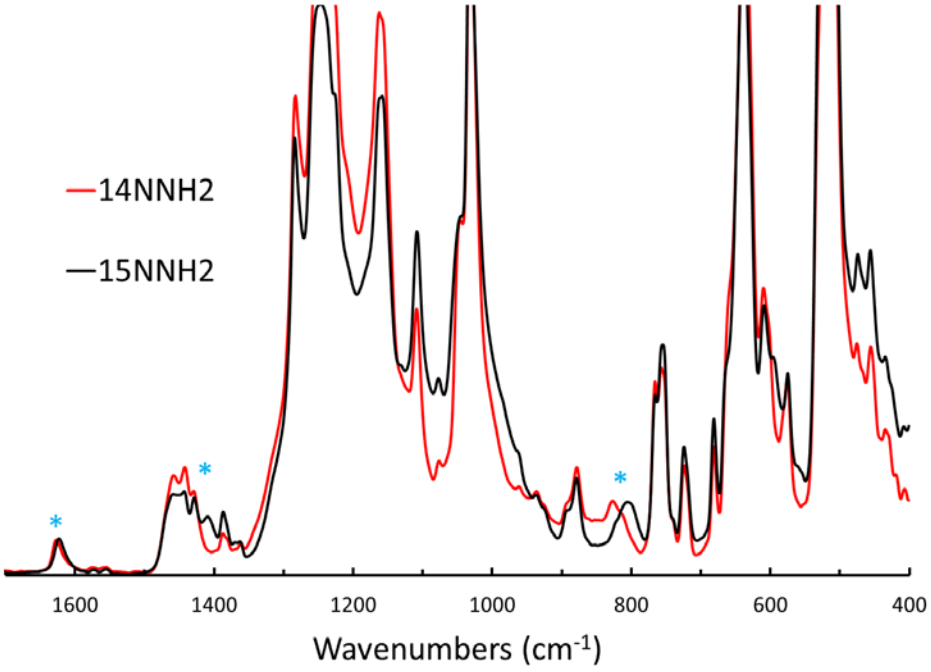

Figure A1.14. Overlaid IR absorption spectra of solid **4.5'** (Red), and **^{15}N-4.5'** (Black).

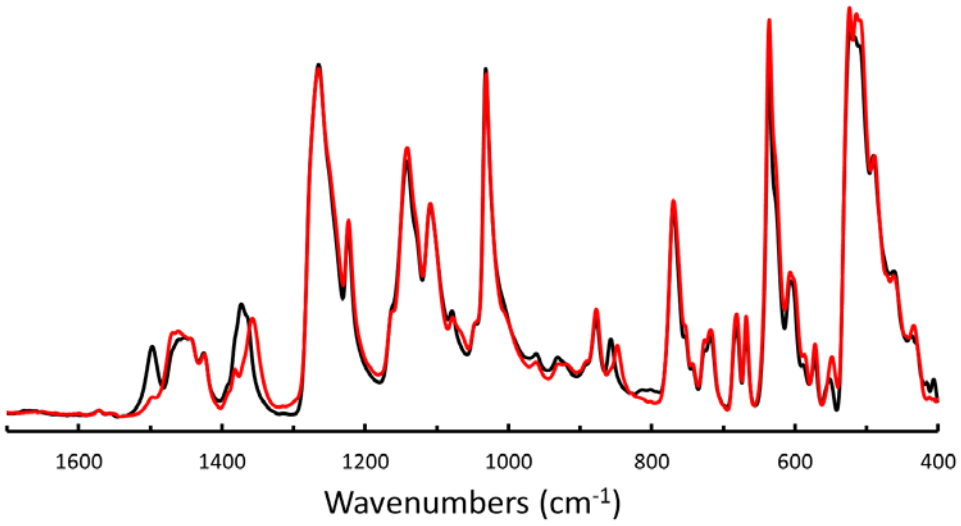

Figure A1.15. Overlaid IR absorption spectra of solid **4.6** (Black), and **^{15}N-4.6** (Red).

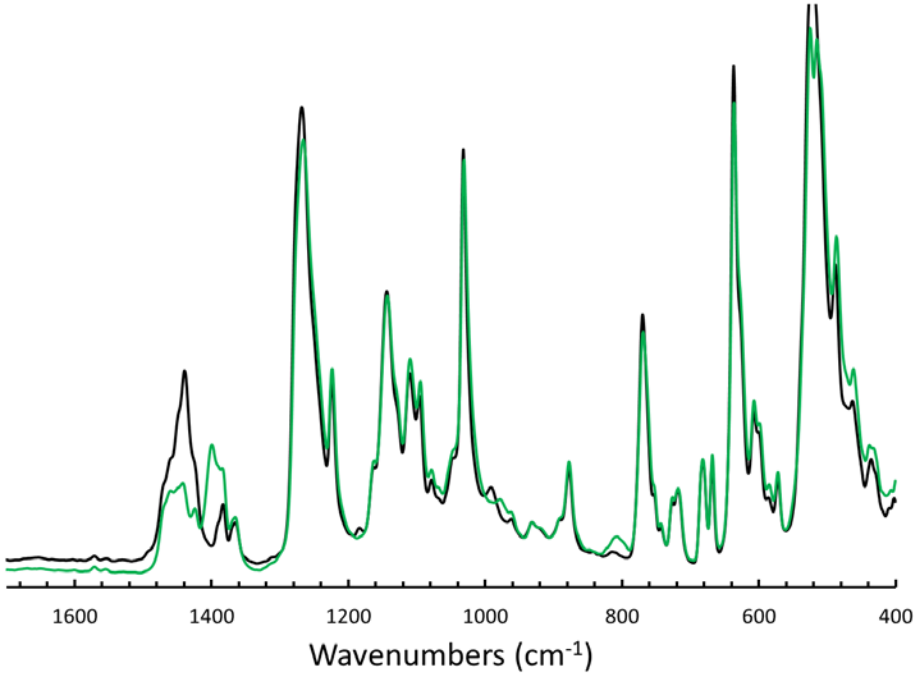

Figure A1.16. Overlaid IR absorption spectra of solid **4.6-d$_6$** (Black) and **^{15}N-4.6-d$_6$** (Green).

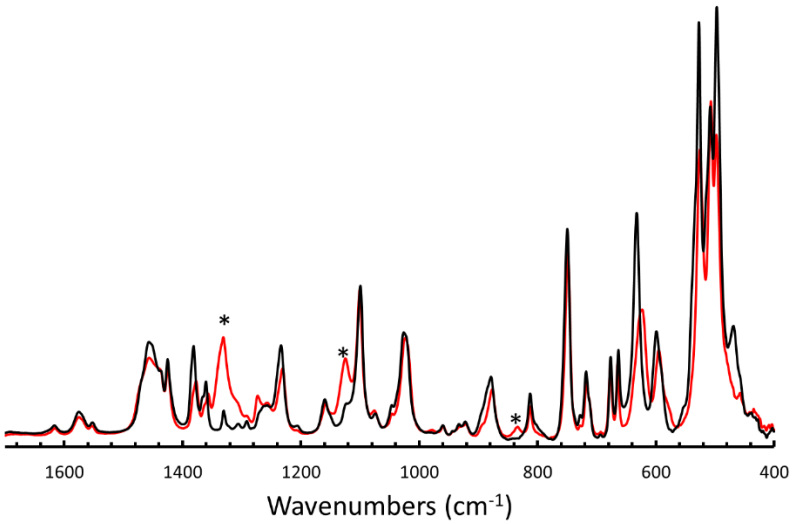

Figure A1.17. Overlaid IR absorption spectra of freshly-isolated **4.8** (Red) and following thermolysis at 60 ºC in C_6D_6 for 1 hour (black).

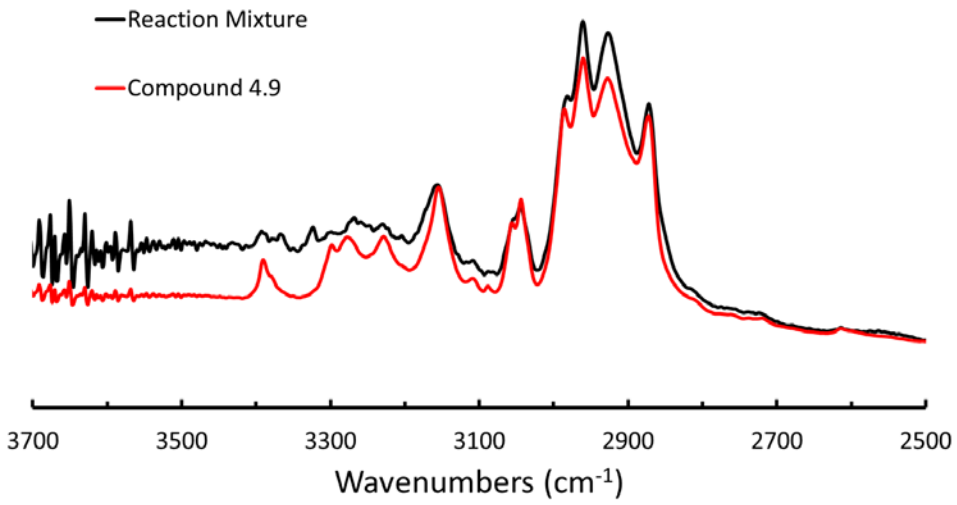

Figure A1.18. Overlaid KBr-IR absorption spectra of ground, crystalline **4.9** (Red) and the solid material obtained by the reaction of **4.5'** with Cp^*_2Co in THF followed by warming to r.t and evaporation of solvent *in vacuo* (Black).

UV-Visible Spectra

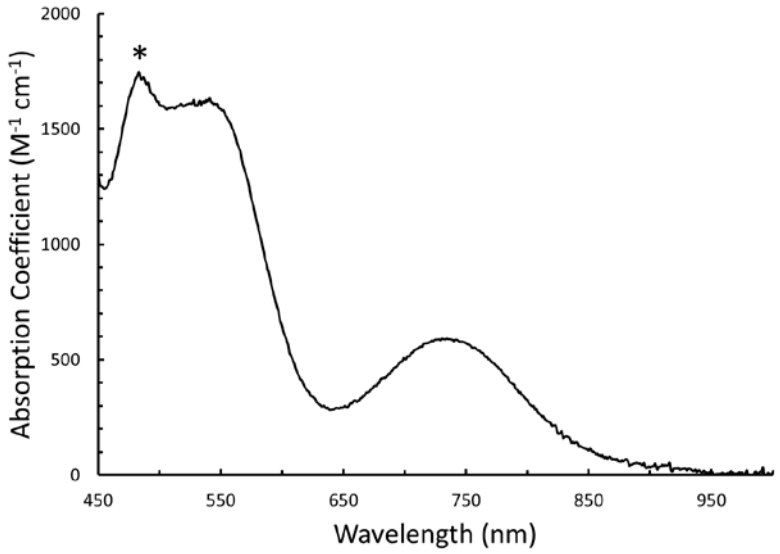

Figure A1.19. UV/visible spectra of **4.5'** in THF at 193 K. The asterisk denotes an absorbance derived from a small impurity (~4%) of [SiP$^{iPr}_3$]Fe(OTf) generated upon dissolution of **4.5'**. The density increase of THF at cryogenic temperatures was not accounted for.

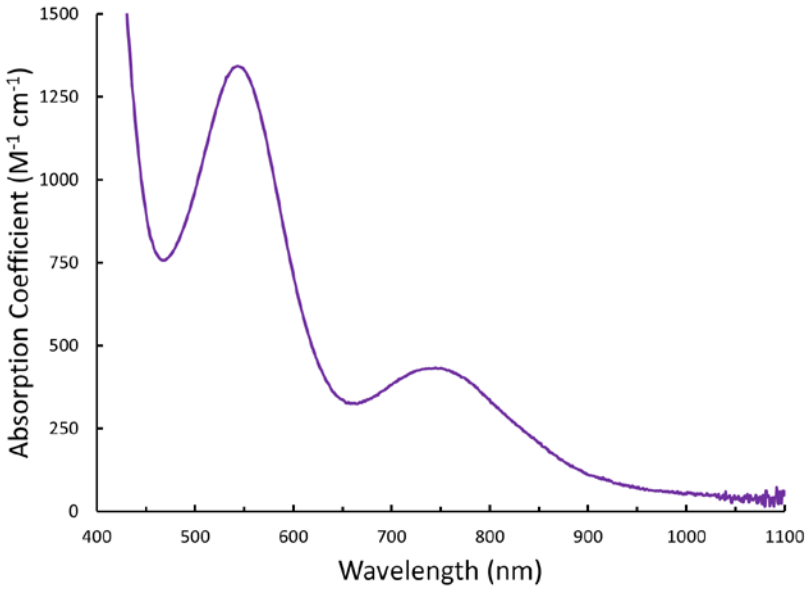

Figure A1.20. UV/visible spectra of **4.6** in THF at 298 K.

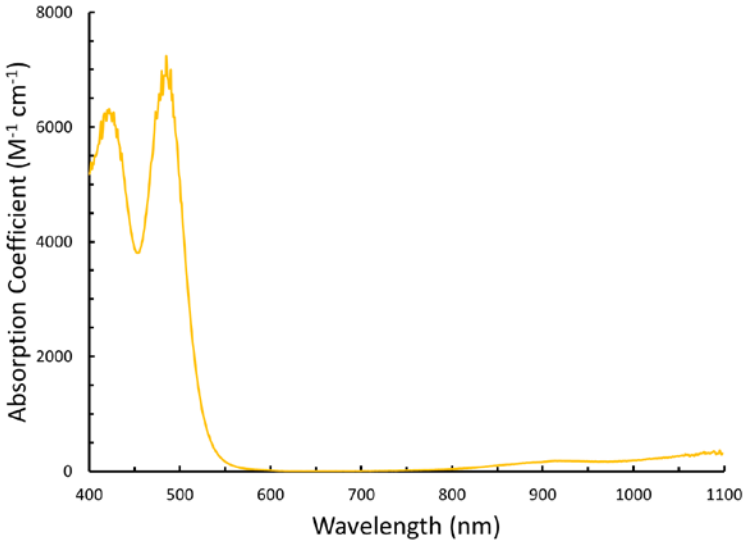

Figure A1.21. UV/visible spectra of [SiP$^{iPr}_3$]Fe(OTf) in THF at 298 K.

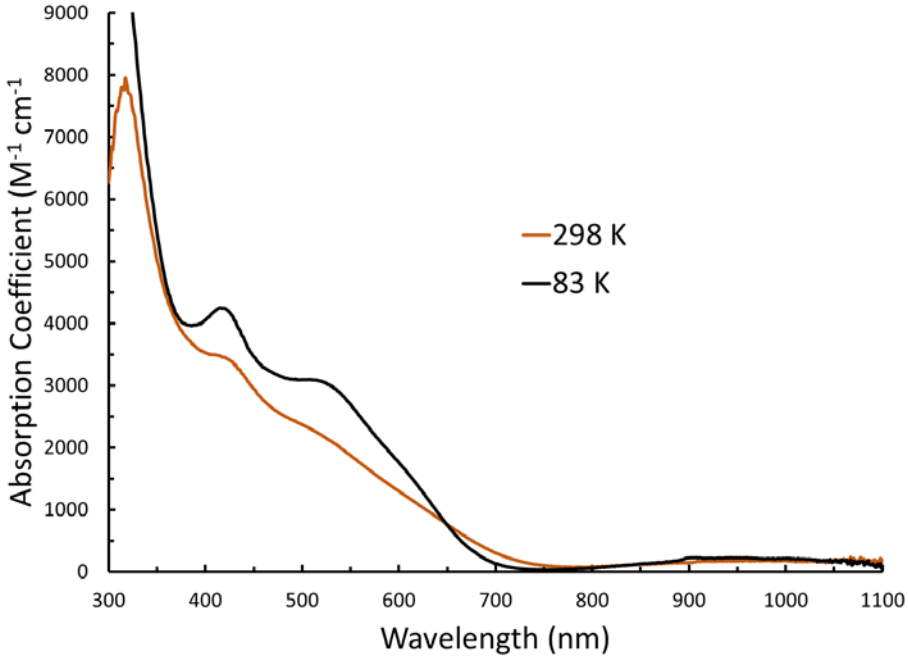

Figure A1.22. UV/visible spectra of **4.8** in 2-MeTHF at 298 and 83 K.

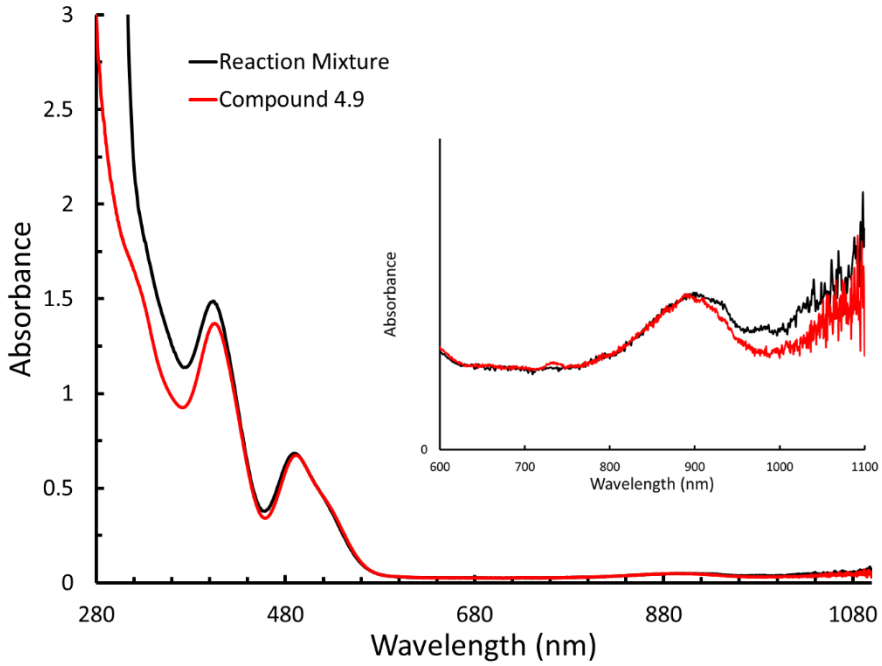

Figure A1.23. Overlaid UV-visible spectra of **4.9** (Red) and the solid material obtained by the reaction of **4.5'** with Cp^*_2Co in THF followed by warming to r.t and evaporation of solvent *in vacuo*. Compound **4.2** was subsequently removed by extensive washes with pentane and the resulting orange solid was dissolved in THF and the resulting spectra are shown in Black.

^{57}Fe Mössbauer Spectra

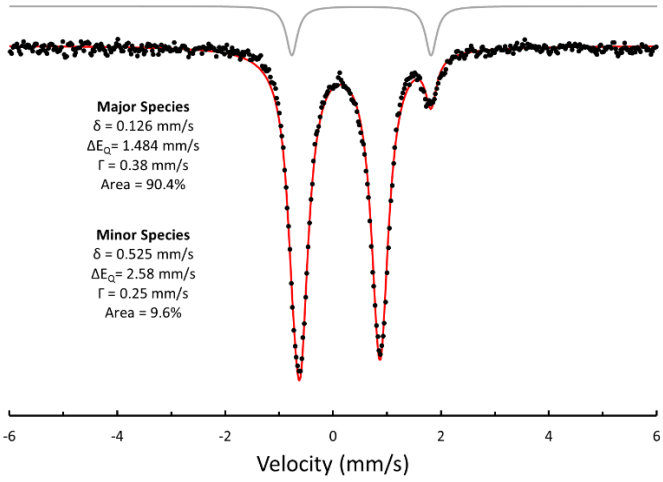

Figure A1.24. 80 K zero-field ^{57}Fe Mössbauer spectrum of **4.5** in a frozen 2-MeTHF glass generated *in situ*. The spectrum was obtained by combining a 2-MeTHF solution of **^{57}Fe-4.1** (~5 mM) with a 2-MeTHF solution of $\{H(Et_2O)_2\}\{BAr^F{}_{24}\}$ (~25 mM) at -135 °C. The minor species is compound **4.3**.

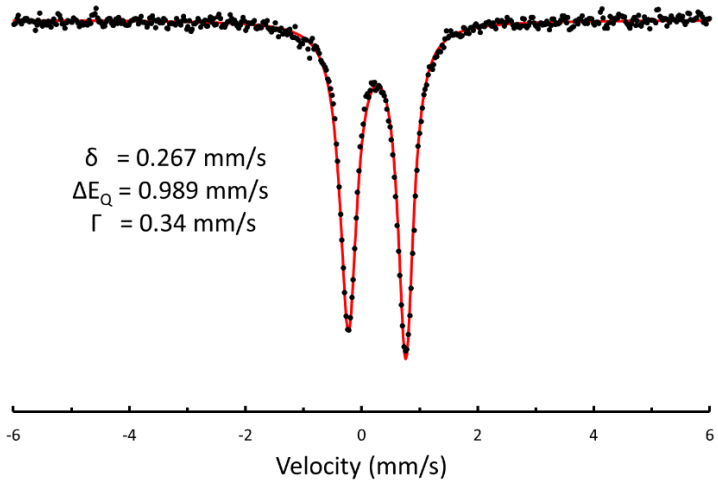

Figure A1.25. 80 K Zero-field ^{57}Fe Mössbauer spectrum of **^{57}Fe-4.1** (~5 mM) in a frozen 2-MeTHF glass.

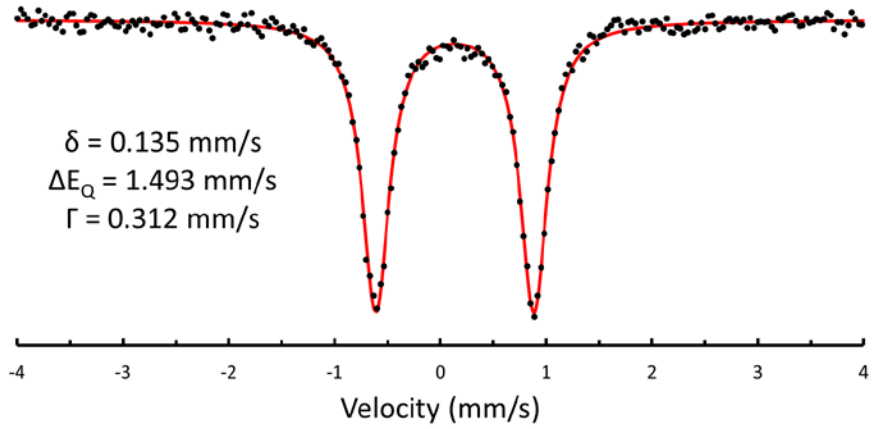

Figure A1.26. 80 K Zero-field ^{57}Fe Mössbauer spectrum of solid **4.6**.

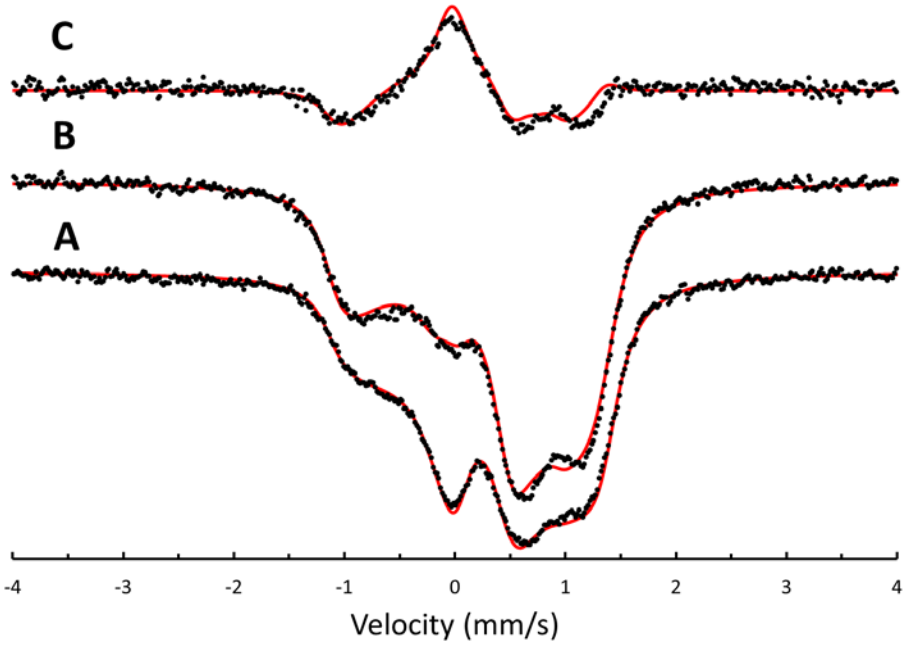

Figure A1.27. 5 K ^{57}Fe Mössbauer spectra of a frozen 2-MeTHF solution of 5 mM **4.2** in the presence of a 50 mT magnetic field oriented (A) perpendicular and (B) parallel to the propagation of the γ-beam. The difference spectrum (C) was obtained by subtracting the features of (A) from those of (B). Refer to Table A1.1 for the resulting fit parameters.

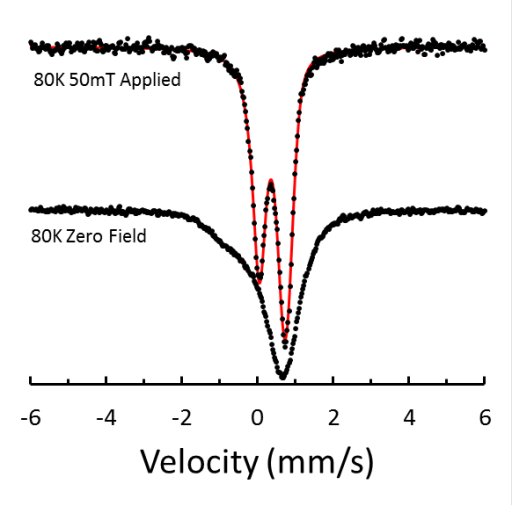

Figure A1.28. 80 K ^{57}Fe Mössbauer spectra of a frozen 2-MeTHF solution of 5 mM **4.2** in the presence (top) or absence (bottom) of a 50 mT magnetic field applied parallel to the propagation of the γ-beam.

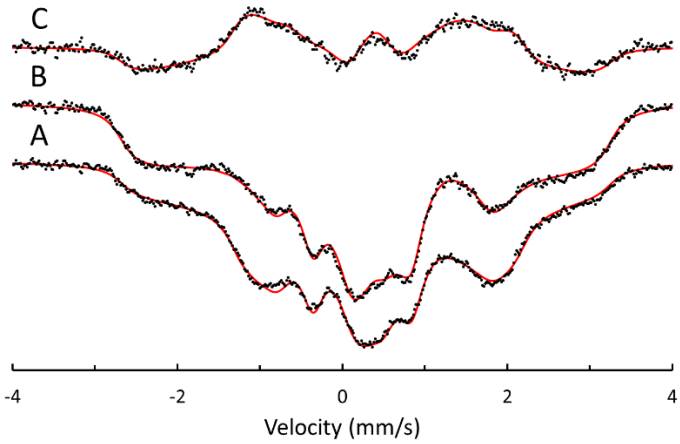

Figure A1.29. Raw 5 K ^{57}Fe Mössbauer spectra of a frozen 2-MeTHF solution of 5 mM **4.8** in the presence of a 50 mT magnetic field oriented (A) perpendicular and (B) parallel to the propagation of the γ-beam. The difference spectrum (C) was obtained by subtracting the features of (A) from those of (B). The solid red lines represent best fits to the data by the simultaneous simulation of data in (A) and (B). Fit parameters for **4.8** are listed in Table A1.1.

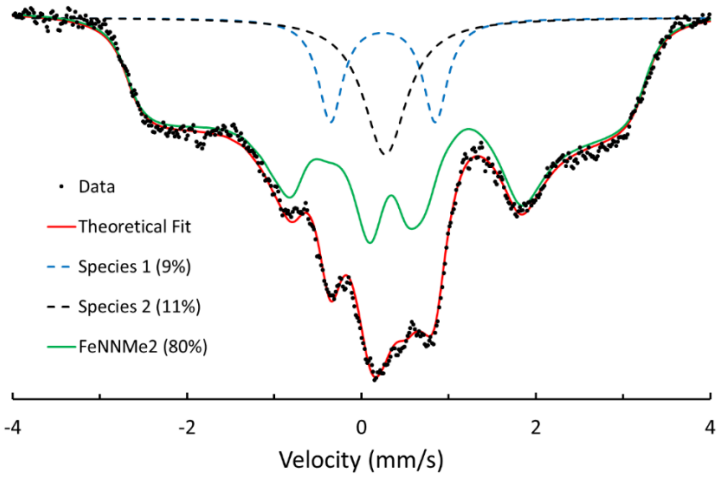

Figure A1.30. Spectral decomposition of the 5 K ^{57}Fe Mössbauer spectra of a frozen 2-MeTHF solution of 5 mM **4.8** in the presence a 50 mT magnetic field applied parallel to the propagation of the gamma beam. Species 1 is characterized by a $\Delta E_Q = 1.20$ and $\delta =$ 0.24 mm/s. Species 2 is characterized by a $\Delta E_Q = 0.2$ and $\delta = 0.28$ mm/s.

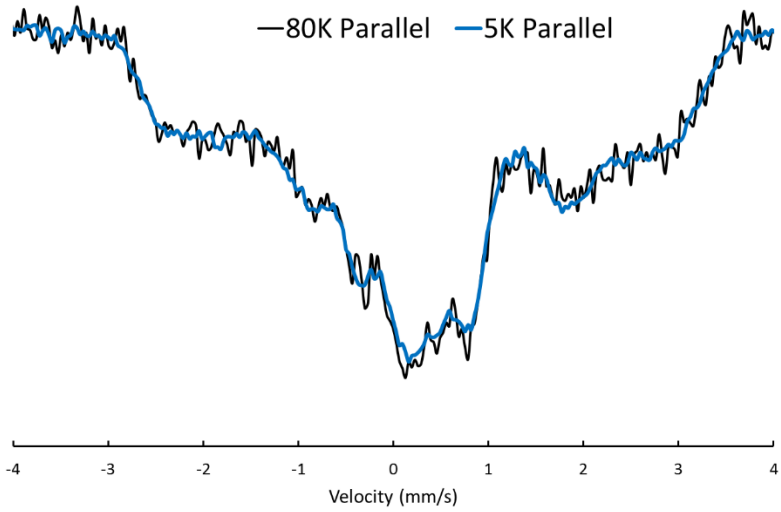

Figure A1.31. ^{57}Fe Mössbauer spectra of a frozen 2-MeTHF solution of **4.8** in the presence of a 50 mT magnetic field applied parallel to the propagation of the gamma beam collected at 80 K (Black) and 5 K (Blue).

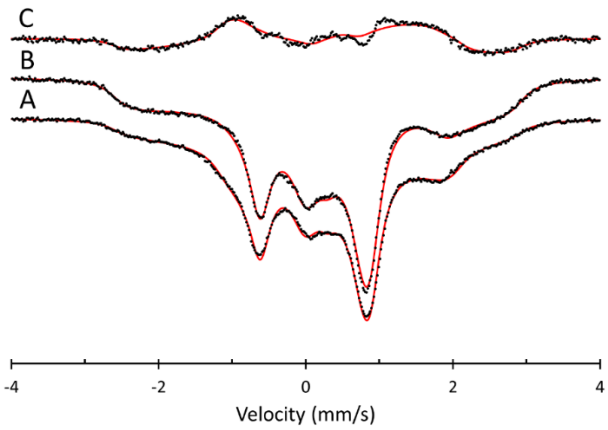

Figure A1.32. Raw 80 K ^{57}Fe Mössbauer spectra of a frozen 2-MeTHF solution of 5 mM **4.7** in the presence of a 50 mT magnetic field oriented (A) perpendicular and (B) parallel to the propagation of the γ-beam. The difference spectrum (C) was obtained by subtracting the features of (A) from those of (B). The solid red line represent best fits to the data by the simultaneous simulation of data in (A) and (B). Fit parameters for **4.7** are listed in Table A1.1.

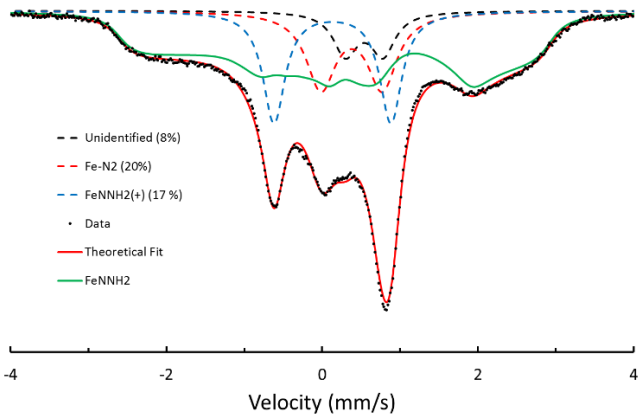

Figure A1.33. Spectral decomposition of the 80 K ^{57}Fe Mössbauer spectra of a frozen 2-MeTHF solution of 5 mM **4.7** in the presence a 50 mT magnetic field applied parallel to the propagation of the gamma beam. Unreacted **4.5'** constitutes 17% of the spectrum. **4.2**

constitutes 20% of the spectrum. An unidentified impurity constitutes 8% of the spectrum ($\Delta E_Q = 0.49$ and $\delta = 0.54$ mm/s) and the remainder is ascribed to **4.7** (55%, green).

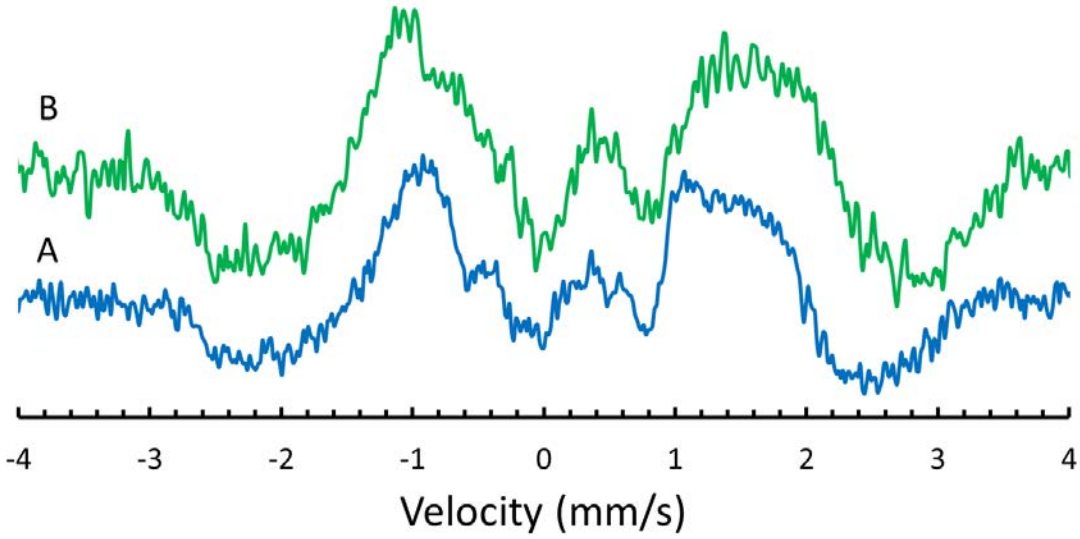

Figure A1.34. Comparison of the ^{57}Fe Mossbauer difference spectra for **4.7** (A, bottom) and **4.8** (B, top) taken from Figures A1.32 and A1.29.

	4.7	**4.8**	**4.2**
g_x	2.070	2.080	2.400
g_y	2.027	2.030	2.000
g_z	2.004	2.000	2.000
ΔE_Q (mm/s)	0.856	0.898	0.674
δ (mm/s)	0.31	0.36	0.374
η	0.303	0.612	-1
$^{Fe}A_x$ (T)	33.1	35.9	14.8
$^{Fe}A_y$ (T)	7.4	8.8	4.8
$^{Fe}A_z$ (T)	14.6	12.8	0.3

Table A1.1. Best fit parameters derived from simulation of the magnetically-perturbed ^{57}Fe Mössbauer spectra of **4.7**, **4.8** and **4.2**. The g values were obtained by EPR spectroscopy (see below).

Supplemental Mossbauer Discussion

The magnetically-perturbed ^{57}Fe Mössbauer spectra of **4.7** and **4.8** shown in Figure 4.6 of Chapter 4 were obtained by subtraction of quadrupole doublet impurities from the raw data, and this procedure deserves some additional discussion. The raw experimental data for **4.7** (Figure A1.32) and **4.8** (Figure A1.29) are shown above. In order to observe the features ascribable to slow electronic relaxation, investigations of **4.8** were initially conducted at 5 K, as is typical for such studies, and the spectra of **4.8**, shown in Figure 4.6, are derived from these studies. At this temperature, the simultaneous fitting of spectra (A) and (B) in Figure A1.29 suggested the presence of two quadrupole doublet impurities amounting to 20% of the [Fe] content (Figure A1.30). The identity of these impurities is unknown, but **4.8** is known to decompose in solution, and these impurities may be the products of that decomposition.

Later studies (Figure A1.31) informed by EPR measurements (Figure A1.35) indicated that **4.8** displayed unusually slow relaxation properties. As such, ^{57}Fe Mössbauer data collected at 80 K displayed unquenched magnetic splitting: they are identical to that collected at 5 K. Collection of data at 80 K in these studies offers a number of advantages, most notably that rapidly-relaxing, EPR-active contaminants appear as quadrupole doublets, simplifying the interpretation of data. **4.2** is a ubiquitous impurity found in preparations of **4.7**, as evidenced by EPR studies (Figure A1.36), and relaxes rapidly, rendering the 80 K Mossbauer spectrum of this complex to appear as a quadrupole doublet (Figure A1.27 and A1.28).

As EPR spectroscopy indicates that **4.7** and **4.8** have similar electronic structures, we assumed that **4.7** would display similar relaxation properties. Therefore the ^{57}Fe Mössbauer spectra of **4.7** was collected at 80 K, (Figure A1.32). The spectra shown display features spread out over a similar range to that of **4.8** and are indicative of slow magnetic relaxation. While samples containing **4.7** and **4.8** are contaminated with quadrupole-doublet impurities, these features associated with these impurities are not influenced by the orientation of the applied magnetic field, and thus the difference spectra (Figure A1.34) of these samples uniquely highlight the features ascribed to slowly-relaxing Fe species. Obviously, these difference spectra are remarkable similar and reflect the presence of similar, slowly-relaxing EPR-active species in these preparations, namely **4.7** and **4.8.**

Using the difference spectra as a guide, along with the known parameters of **4.5'** and **4.2** at 80 K, the simulation of the sample containing **4.7** is straightforward (Figure A1.33). Furthermore, since both **4.7** and **4.8** display features spread over a wide range that extends past those of the impurities (Figure A1.30 and A1.33), initial fits focused on properly simulating the outer portions of the spectra. Taken together, the ^{57}Fe Mössbauer studies conclusively indicate that an Fe-containing complex (**4.7**) that displays nearly identical parameters and physical properties to **4.8** (Table A1.1) is obtained upon chemical reduction of **4.5'**. This statement is bolstered by the EPR studies below.

EPR Spectra

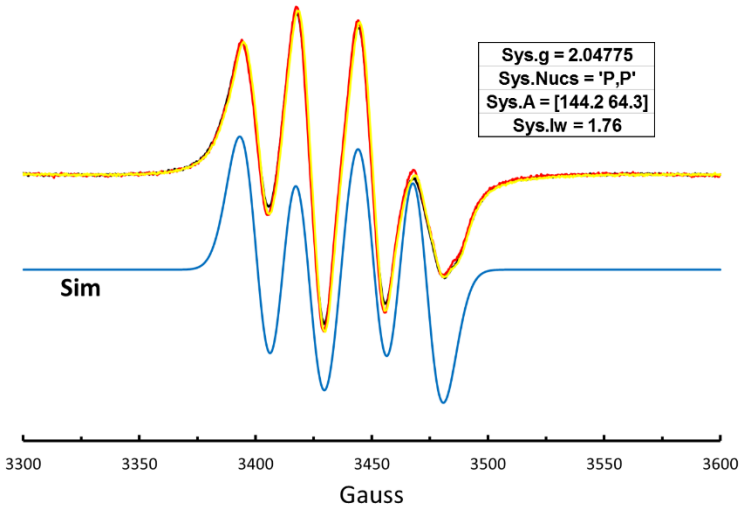

Figure A1.35. Overlaid 298 K X-band EPR spectra of **4.6** (black), **4.6-d$_6$** (red), and **^{15}N-4.6** (yellow). The blue trace is derived from the simulation parameters listed in the table.

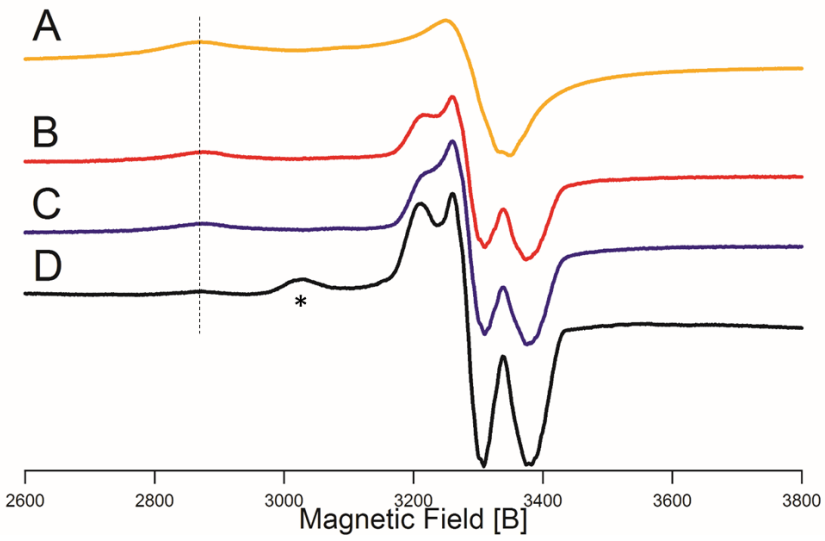

Figure A1.36. Raw EPR spectra of (A) **4.2**, (B) the reaction mixture obtained by stoichiometric addition of HOTf to **4.1**, (C) the reaction mixture obtained by stoichiometric addition of NEt_3 to **4.5'**, and (D) the reaction mixture obtained by addition of stoichiometric Cp^*_2Co to **4.5'**. The asterisk denotes a Cp^*_2Co-derived impurity.

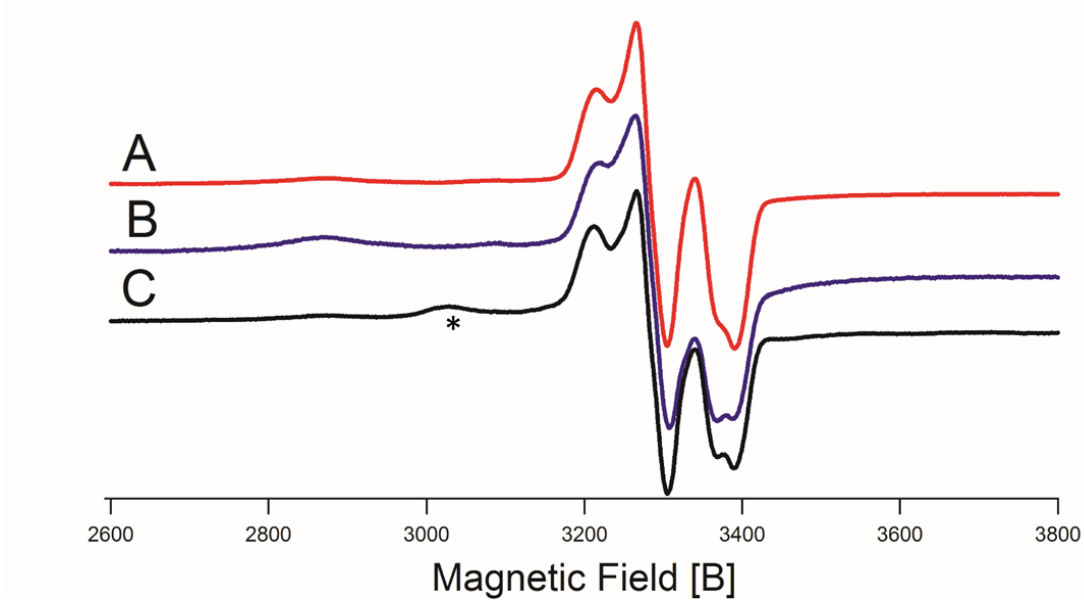

Figure A1.37. Raw EPR spectra of (A) the reaction mixture obtained by stoichiometric addition of DOTf to **4.1**, (B) the reaction mixture obtained by stoichiometric addition of NEt_3 to **4.5'-*d*$_2$**, and (C) the reaction mixture obtained by addition of stoichiometric Cp^*_2Co to **4.5'-*d*$_2$**. The asterisk denotes a Cp^*_2Co-derived impurity.

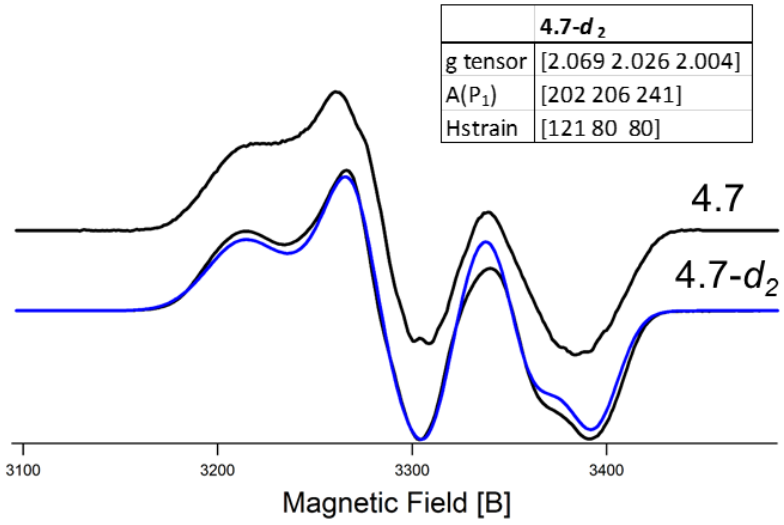

Figure A1.38. EPR spectra of **4.7** and **4.7-*d*$_2$** (black traces) and the best-fit simulation of **4.7-*d*$_2$** (blue trace). (Inset) Simulation parameters corresponding to the blue trace.

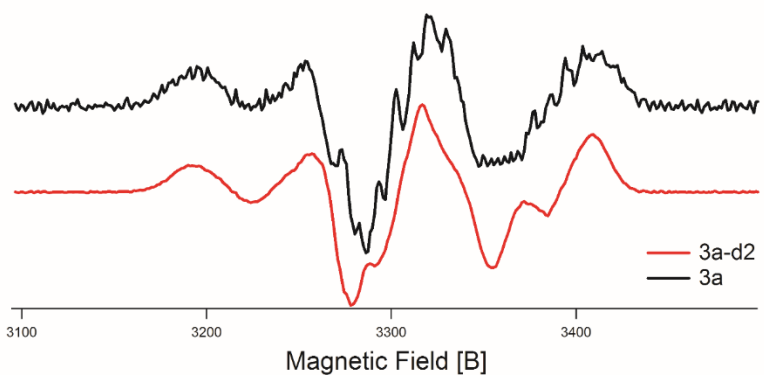

Figure A1.39. 2nd derivative of the EPR absorption envelope of **4.7** (top, black) and **4.7-*d*$_2$** (bottom, red) collected at 77 K in a 2-MeTHF glass. The sharp features in the spectra of **4.7** display a relatively consistent spacing of ~25 MHz, placing a lower limit on the A(^{1}H) for one or more of the NNH_2 protons.

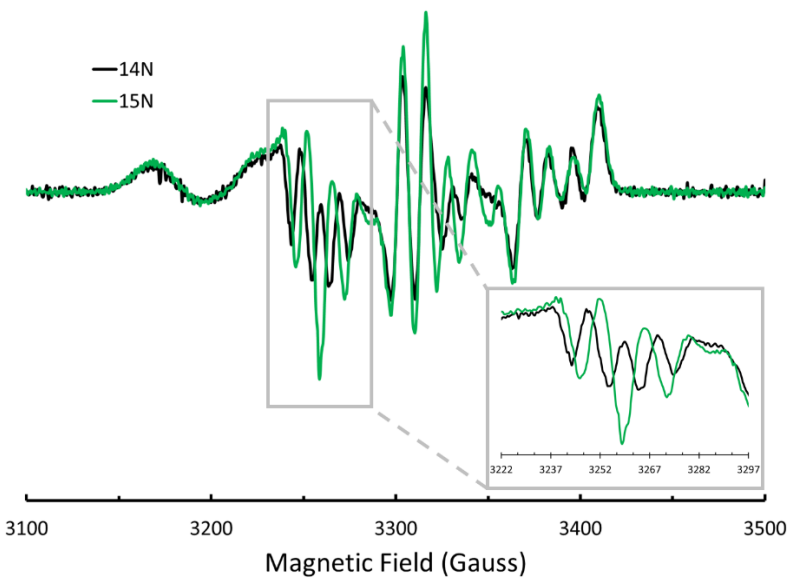

Figure A1.40. 2nd derivative of the EPR absorption envelope of **4.8** (black) and **^{15}N-4.8** (green) collected at 77 K in a 2-MeTHF glass. (Inset) region of greatest difference that highlights features arising from hyperfine coupling to one N-atom and one P-atom of similar magnitude. These features display spacings of 28 and 37 MHz for **4.8** and **^{15}N-4.8**,

respectively, providing a crude estimate of the magnitude of the hyperfine coupling constants for these nuclei.

Supplemental EPR Discussion

Compounds **4.7**, **4.8** and their isotopomers display rhombic EPR spectra centered around g = 2. These compounds display slow electronic relaxation, as evidenced by the ^{57}Fe Mössbauer studies and the fact that **4.8** displays an intense EPR signal at elevated temperatures. At 298 K, the invariance in the spectra shown in Figure A1.35 indicate large hyperfine coupling to two chemically-inequivalent ^{31}P nuclei. At 77 K, the small g-anisotropy and hyperfine coupling of this magnitude causes substantial overlap of the spectral features, hindering effective spectral simulations. Additional, weaker hyperfine coupling to a third ^{31}P nuclei as well as a single N atom is also observed. The nitrogen hyperfine coupling was conclusively assigned by comparison of the spectra of **4.8** and **^{15}N-4.8**. As shown in Figure 4.5 of Chapter 4, four distinct features are observed in the region around g_2 in **4.8**, whereas only three distinct features are seen in **^{15}N-4.8**. In figure A1.40, the 2nd derivative of the EPR absorption envelope of **^{15}N-4.8** and **4.8** are shown with an emphasis on the differing features.

For compound **4.7**, preparations employing Cp^*_2Co and **4.5'** are invariably contaminated with an additional impurity seen at 2950 Gauss that may arise from competing protonation of Cp^*_2Co (Cp^*_2Co is completely consumed in these reaction, by comparison to an authentic sample). This feature is not observed when **4.7** is prepared by the reaction of **4.5'** with NEt_3 or upon reaction of **4.1** with stoichiometric HOTf (Figure S36 and S37). Compound **4.2** is also observed in each spectra, but its contribution can be

effectively removed since this complex displays a feature at 2850 Gauss, which is well separated from those ascribable to **4.7**.

Compound **4.7** and **4.7-*d*$_2$** prepared by each route display significant differences. Overall, **4.7-*d*$_2$** exhibits smoother features, and is noticeably distinct from **4.7** at the highest magnetic fields. **4.7-*d*$_2$** can be effectively simulating with a simple model that includes large hyperfine coupling to a single ^{31}P nuclei (Figure S38). The broad nature of the lineshape required to simulate the spectrum indicates substantial hyperfine coupling to other nuclei (and possibly some amount of g-Strain). In **4.7**, some of this hyperfine coupling is partially resolved, as seen in Figure 3.38, but is more clearly seen in the 2nd derivative spectrum (Figure A1.39). While we have not yet been able to effectively simulate the spectrum of **4.7**, the difference in linewidths observed between **4.7** and **4.7-*d*$_2$** and the features present in the 2nd derivative spectra (A1.39) imply hyperfine coupling constants of approximately 25 MHz to one or more hydrogen atoms. In depth EPR and ENDOR studies on these complexes will be reported in due course.

XANES Spectra

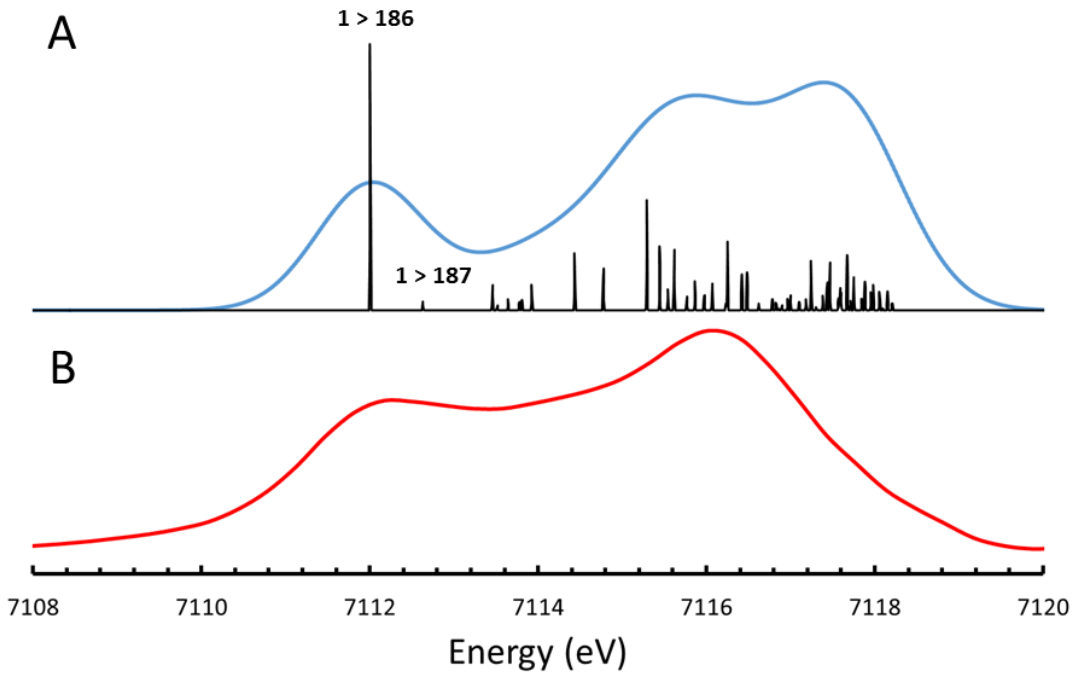

Figure A1.41. (A) TD-DFT-predicted XANES spectra for **4.5'**. (B) Experimental XANES spectra of **4.5'**. The unoccupied orbitals correspond to those shown in Figure A1.52.

X-Ray Diffraction Data

Compound	**4.1**	**4.5'**	**4.6**	**{Fe[NN(Me)H]}{OTf}**	**4.8**
chem formula	$C_{40}H_{63}FeKN_2OP_3Si$	$C_{46.5}H_{72}F_3FeN_2O_5P_3SSi$	$C_{39}H_{60}F_3FeN_2O_3P_3SSi$	$C_{46}H_{74}F_3FeN_2O_5P_3SSi$	$C_{38}H_{60}FeN_2P_3Si$
fw	803.87	1001.49	870.83	1000.98	721.73
cryst syst	Triclinic	Monoclinic	Orthorhombic	Monoclinic	Triclinic
Space group	P-1	C2/C	$Pna2_1$	$P2_1/C$	P-1
a [Å]	10.3640(4)	27.371(3)	20.9744(9)	17.1900(12)	10.3195(9)
b [Å]	10.9643(4)	12.5437(11)	14.6729(7)	17.7939(12)	10.8239(10)
c [Å]	18.9571(8)	31.967(3)	13.7649(8)	16.5123(11)	19.3470(17)
α [°]	88.362(2)	90	90	90	78.665(5)
β [°]	84.430(2)	108.726(3)	90	97.288(4)	78.078(5)
γ [°]	93.401(2)	90	90	90	62.522(4)
V [$Å^3$]	2129.47(14)	10394.4(18)	4236.2(4)	5009.9(6)	1863.1(3)
Z	2	8	4	4	2
D_{calcd} [g cm^{-1}]	1.254	1.284	1.365	1.325	1.286
F(000)	858	4264	1840	2120.5	774
μ [mm^{-1}]	5.287	0.5	0.599	0.518	0.595
temp [K]	100	100	100	100	100
wavelength [Å]	0.71073	0.71073	0.71073	0.71073	0.71073
measured reflns	56761	111272	51709	76833	94112
unique reflns	8672	10623	12545	10285	11387
data/restraints/param	8672/0/467	10623/0/599	12545/1/568	10285/0/583	11387/0/420
R(F) (I>2σ(I))	0.0606	0.0444	0.0359	0.0612	0.0269
wR(F^2) (all)	0.151	0.1236	0.0876	0.1556	0.071
GOOF	1.03	1.072	1.047	1.059	1.029

Table A1.2. X-ray diffraction table.

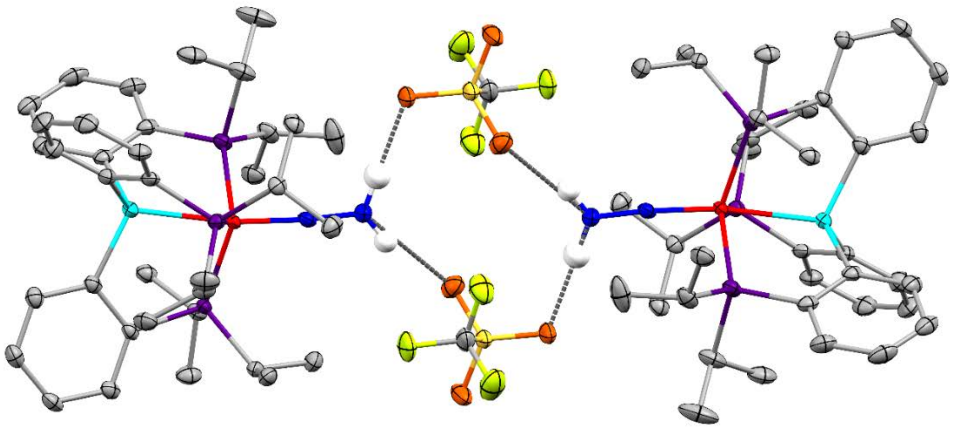

Figure A1.42. Expanded view of the XRD structure of **4.5'** illustrating the hydrogen bond network within the crystal lattice.

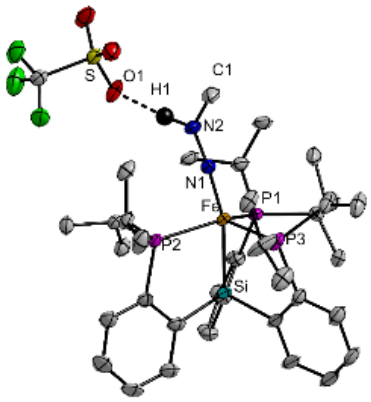

Figure A1.43. X-ray diffraction crystal structure of {[SiP$^{iPr}_3$]Fe[NN(H)Me]}{OTf}, derived from the sequential reaction of **4.1** with MeOTf and HOTf after stirring for 3 hr at -78 ^{o}C. Thermal ellipsoids are drawn at 50% probability. Hydrogen atoms (excepting the NH) and co-crystallized solvent molecules have been removed for clarity.

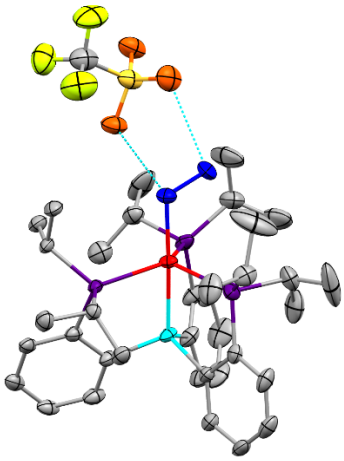

Figure A1.44. X-ray diffraction crystal structure of {[SiP$^{iPr}_3$]Fe(NH_2NH_2){OTf}, derived from the reaction of **4.5'** with Cp*$_2$Co at -110 ^{o}C in THF, followed by warming to rt. The resulting solution was filtered, concentrated *in vacuo* and layered with pentane to afford X-ray quality crystals. Thermal ellipsoids are drawn at 50% probability. The terminal N-atom is only 70% occupied, reflecting a 30% component of cocrystallized {[SiP$^{iPr}_3$]Fe(NH_3)}{OTf}.

Variable Temperature NMR Discussion

As discussed previously,[10] the chemical shift of nuclei experiencing temperature-dependent paramagnetism can be fit with equation A1.3 to estimate the singlet-triplet energy gap.

$$f(T) = \mathbf{A} + (\mathbf{B}*EXP(\mathbf{C}/(8.3145*T)))/((1 +3*EXP(\mathbf{C}/(8.3145*T)))*T) \qquad \textbf{Eqn A1.3}$$

Where **A**, **B** and **C** are fit constants and T is the temperature in Kelvin. **A** is the chemical shift (in ppm) of the diamagnetic ground state at 0 K, **B** is proportional to the hyperfine coupling constant, and **C** is the difference in energy between the ground and excited states in Joules. The justification for the use of this equation for the present case has been previously described.[10] The behavior of the ^{31}P, ^{1}H and ^{29}Si nuclei of **4.6** was independently fit to equation A1.3 and the resulting **C** parameters were used to estimate the singlet-triplet energy gap of **4.6**.

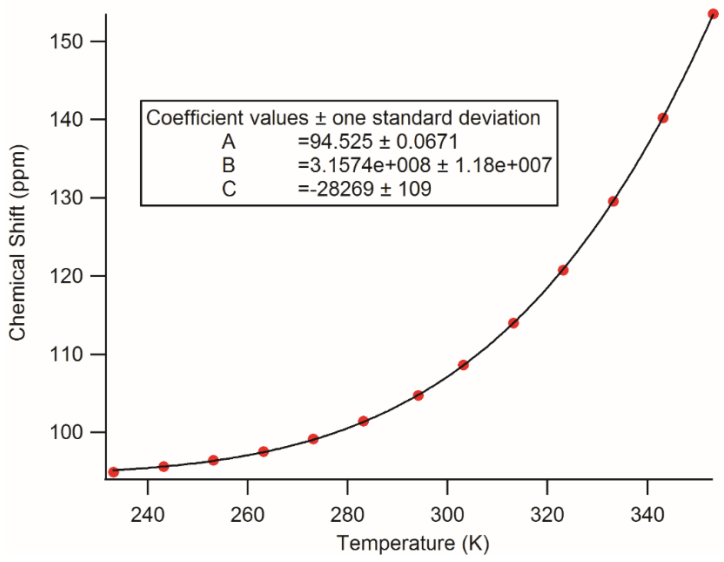

Figure A1.45. The temperature dependence of the ^{31}P{^{1}H} NMR chemical shift of **4.6** fit to equation A1.3. The resulting best fit parameters are listed in the legend.

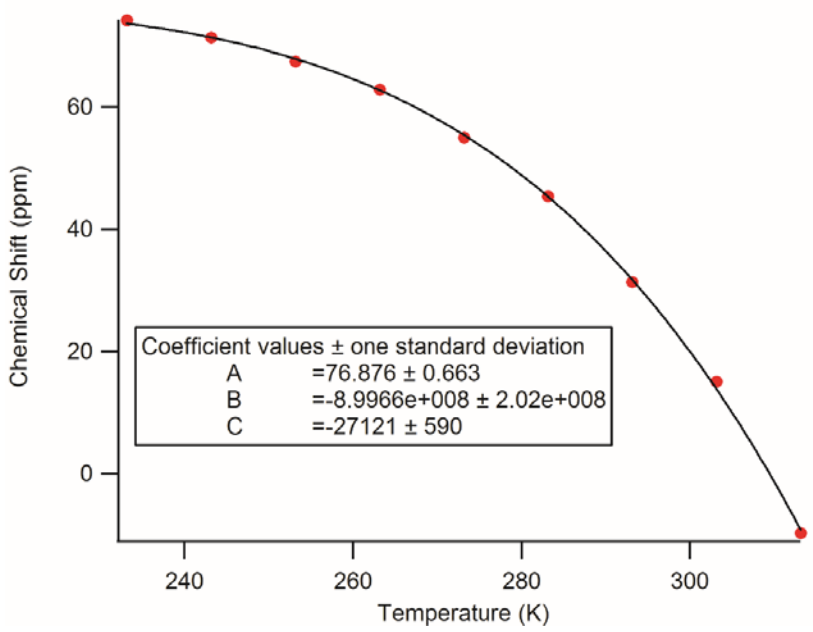

Figure A1.46. The temperature dependence of the $^{29}Si\{^{1}H\}$ NMR chemical shift of **4.6** fit to equation A1.3. The resulting best fit parameters are listed in the legend.

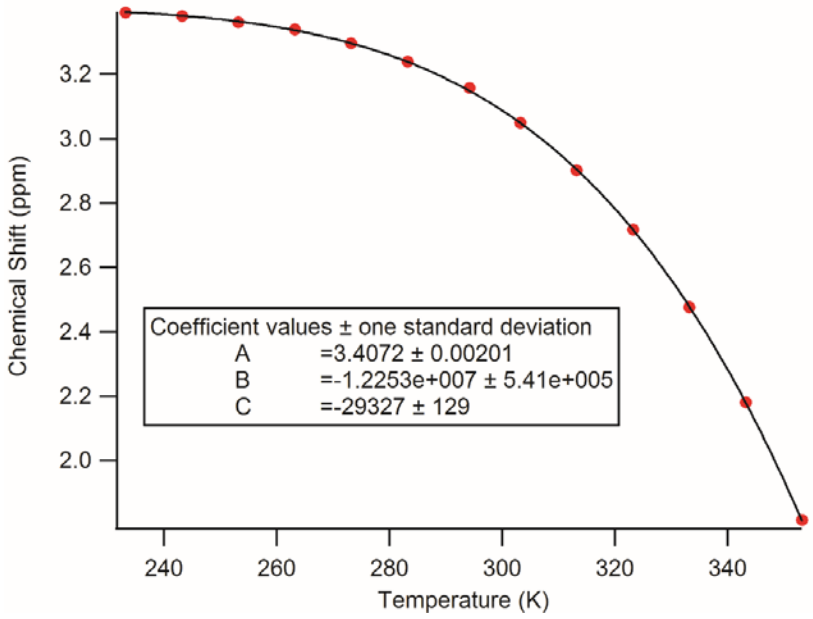

Figure A1.47 The temperature dependence of the ^{1}H NMR chemical shift of the FeNN(CH_3)$_2$ protons in **4.6** fit to equation A1.3. The resulting best fit parameters are listed in the legend.

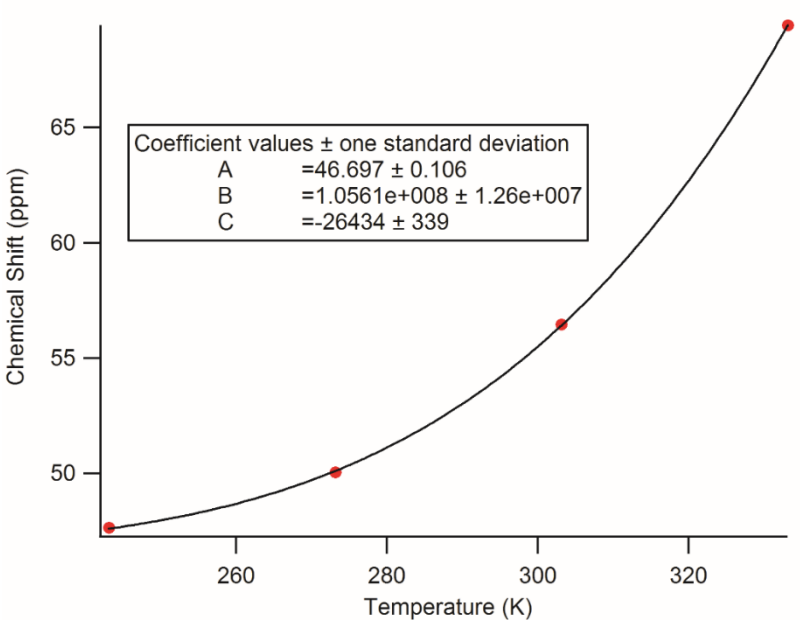

Figure A1.48. The temperature dependence of the ^{13}C NMR chemical shift of the FeNN(CH_3)$_2$ carbons in **4.6** fit to equation A1.3. The resulting best fit parameters are listed in the legend.

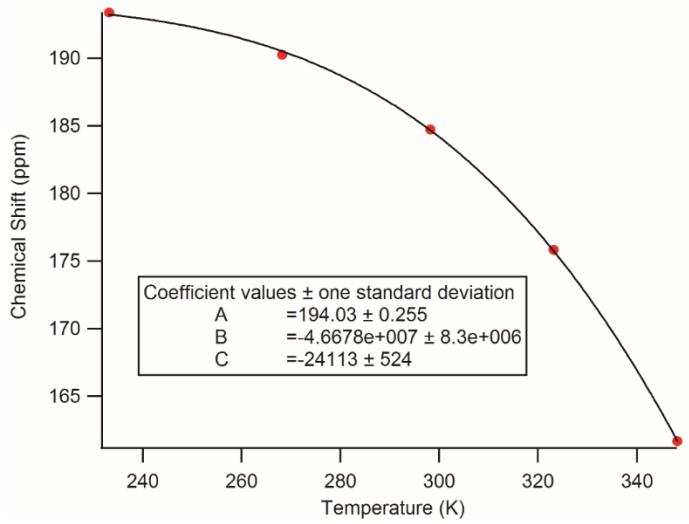

Figure A1.49. The temperature dependence of the ^{15}N NMR chemical shift of the beta nitrogen of **4.6** fit to equation A1.3. The resulting best fit parameters are listed in the legend.

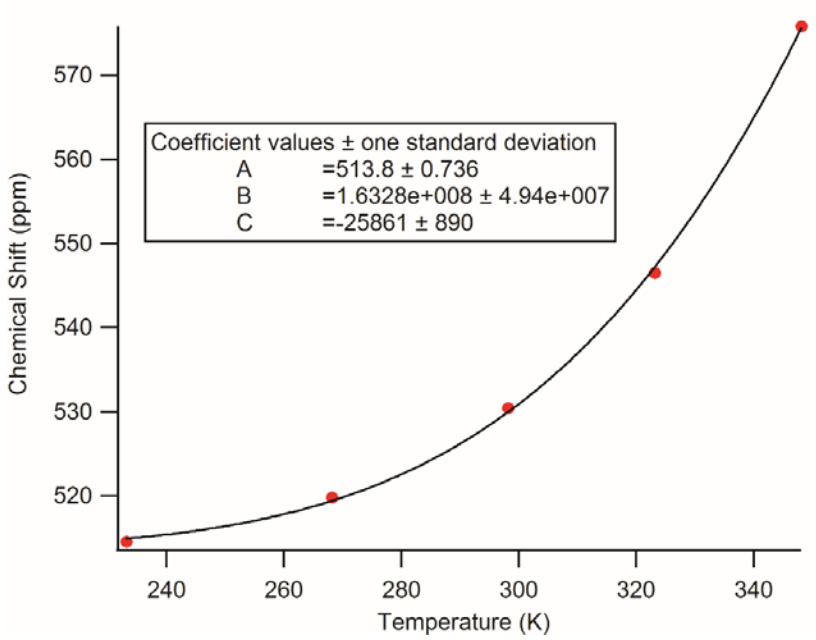

Figure A1.50. The temperature dependence of the ^{15}N NMR chemical shift of the alpha nitrogen of **4.6** fit to equation A1.3. The resulting best fit parameters are listed in the legend.

DFT Calculations

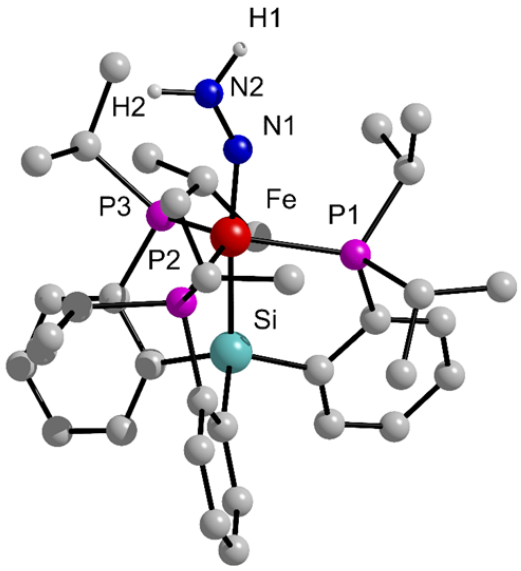

Figure A1.51. Gas-phase optimized geometry of **4.7**. Fe-N(1): 1.747 Å, N(1)-N(2): 1.294 Å, Fe-P(1): 2.335 Å, Fe-P(2): 2.276 Å, Fe-P(3): 2.276 Å, Fe-Si: 2.333 Å, Si-Fe-N(1): 175.3º, Fe-N(1)-N(2): 150.6º.

	7[a]	**8**[a]	**8**[b]
Fe-N[c]	1.7468	1.7705	1.773(1)
Fe-Si[c]	2.3333	2.3318	2.3021(5)
Fe-P1[c]	2.2762	2.2883	2.2700(3)
Fe-P2[c]	2.2762	2.2963	2.2989(4)
Fe-P3[c]	2.3349	2.3514	2.3182(4)
N-N[c]	1.2941	1.2828	1.276(2)
Si-Fe-N[d]	175.29	174.97	174.20(4)
Fe-N-N[d]	150.58	158.11	158.64(9)
P1-Fe-P2[d]	118.58	120.38	118.13(1)
P2-Fe-P3[d]	114.78	111.858	112.83(1)
P1-Fe-P3[d]	116.99	117.65	119.21(1)

Table A1.3. Comparison of pertinent bond metrics. [a]DFT-optimized geometry (gas-phase). [b]X-ray diffraction crystal structure (solid state).

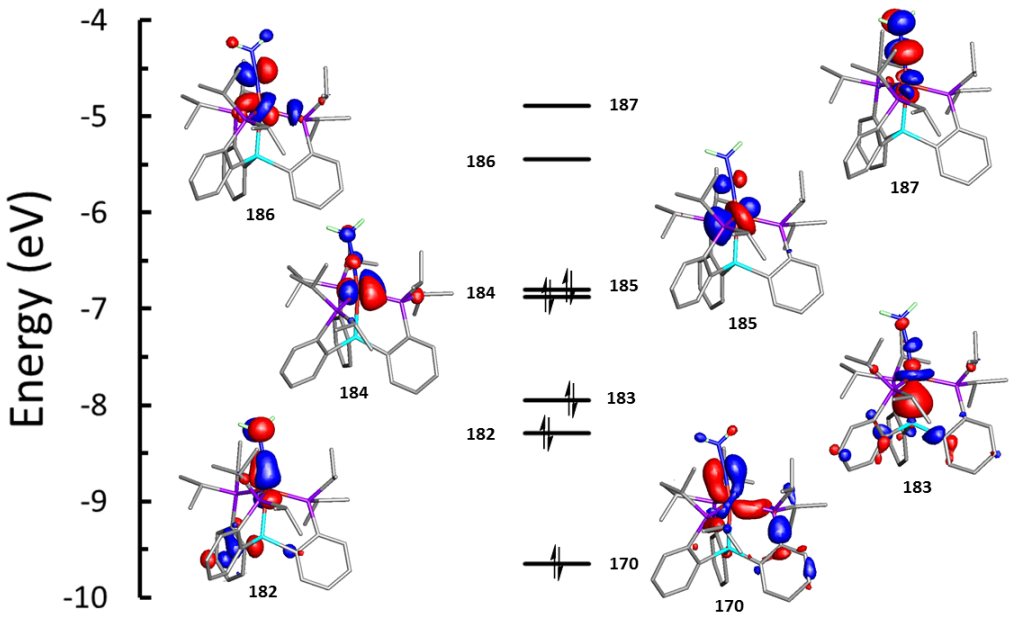

Figure A1.52. Frontier molecular orbitals of **4.5'**. Contour values set to 0.05 Å^3.

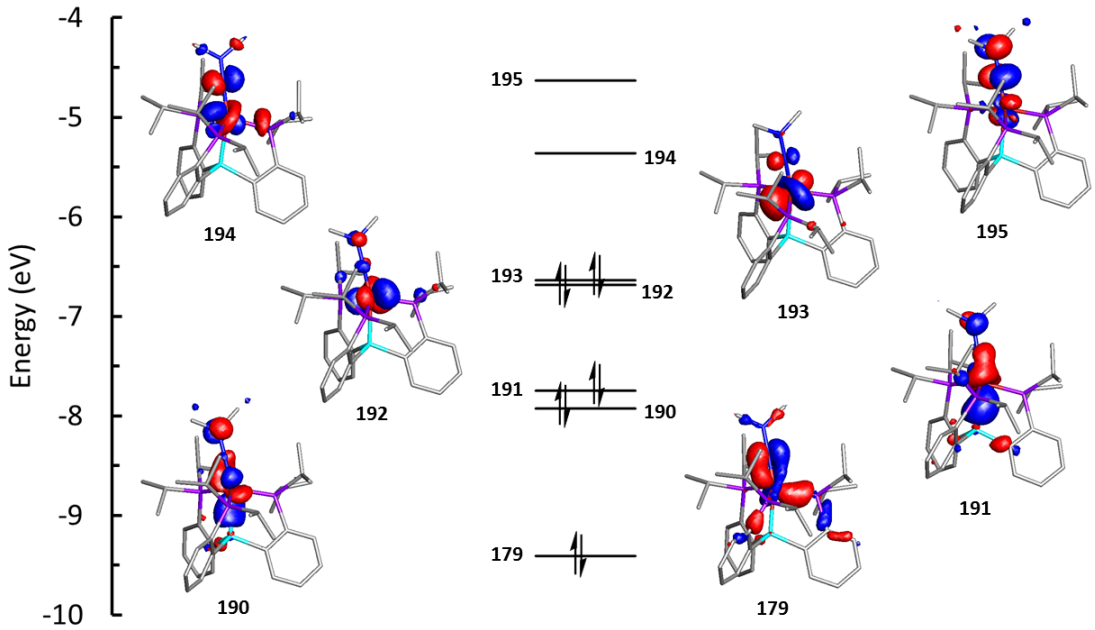

Figure A1.53. Frontier molecular orbitals of **4.6**. Contour values set to 0.05 Å^3.

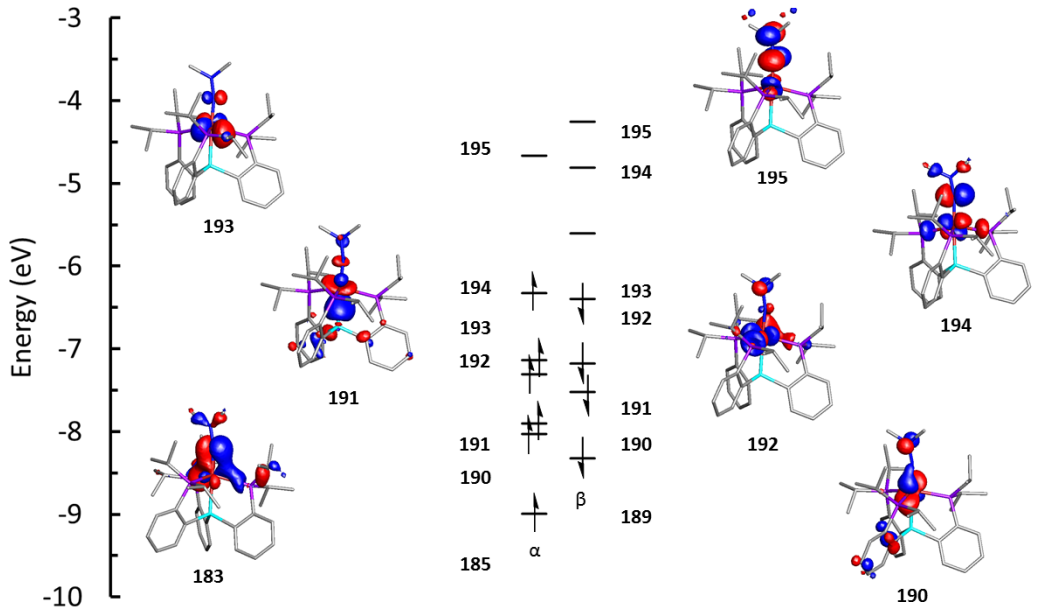

Figure A1.54. Frontier molecular orbitals of **4.6 (S = 1)**. Contour values set to 0.05 Å^3.

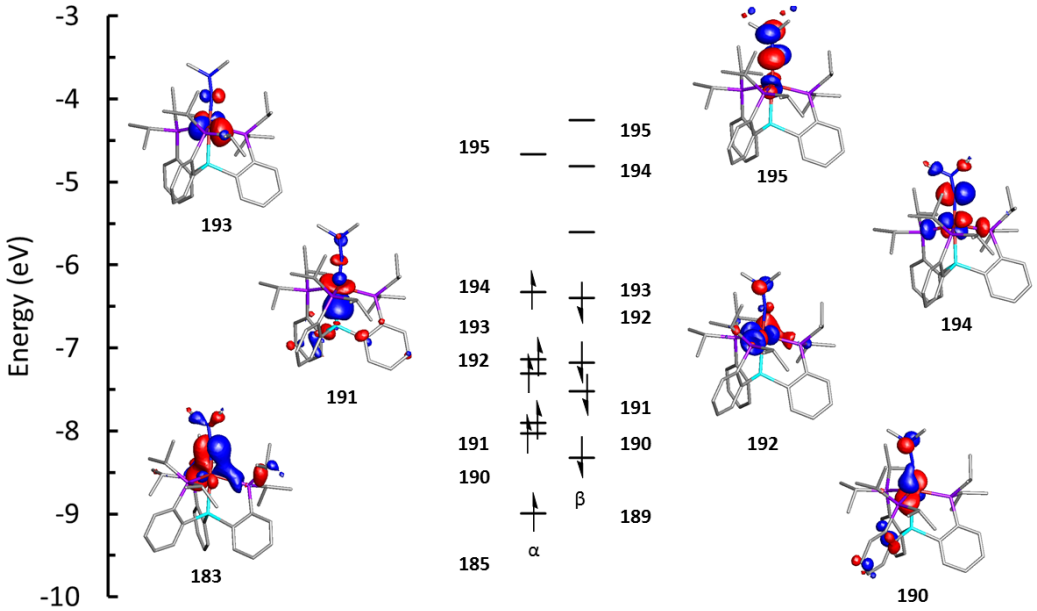

Figure A1.55. Frontier molecular orbitals of **4.8**. Orbitals shown correspond to the α manifold. Contour values set to 0.05 Å^3.

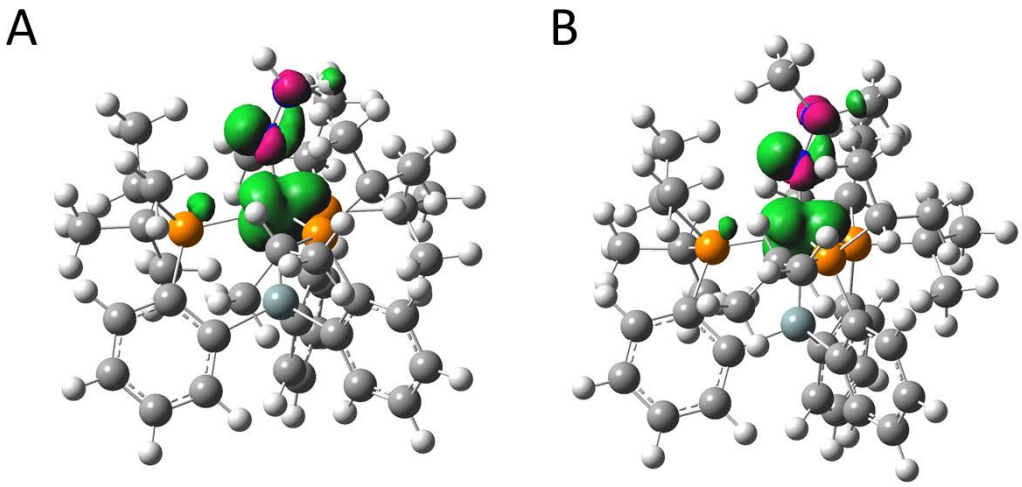

Figure A1.56. Spin density plots of **4.7** (A) and **4.8** (B) with contour values set to 0.03 $Å^3$.

Cited References.

1. Lee, Y.; Mankad, N. P.; Peters, J. C. *Nat. Chem.* **2010**, 2, 558-565.
2. Brookhart, M.; Grant, B.; Volpe, A. F. *Organometallics* **1992**, *11*, 3920.
3. Berto, T. C.; Hoffman, M. B.; Murata, Y.; Landenberger, K. B.; Alp, E. E.; Zhao, J. Y.; Lehnert, N. *J. Am. Chem. Soc.* **2011**, *133*, 16714.
4. Evans, D. F. *J. Chem. Soc.* **1959**, 2003.
5. Stoll, S.; Schweiger, A. *J. Magn. Reson.* **2006**, *178*, 42.
6. Münck, E. *Aspects of ^{57}Fe Mössbauer Spectroscopy*; University Science Books: Sausalito, CA, 2000.
7. https://home.comcast.net/~sam_webb/sixpack.html
8. http://bruceravel.github.io/demeter/
9. Gaussian 09, Revision B.01, Frisch, M. J.; Trucks, G. W.; Schlegel, H. B.; Scuseria, G. E.; Robb, M. A.; Cheeseman, J. R.; Scalmani, G.; Barone, V.; Mennucci, B.; Petersson, G. A.; Nakatsuji, H.; Caricato, M.; Li, X.; Hratchian, H. P.; Izmaylov, A. F.; Bloino, J.; Zheng, G.; Sonnenberg, J. L.; Hada, M.; Ehara, M.; Toyota, K.; Fukuda, R.; Hasegawa, J.; Ishida, M.; Nakajima, T.; Honda, Y.; Kitao, O.; Nakai, H.; Vreven, T.; Montgomery, J. A., Jr.; Peralta, J. E.; Ogliaro, F.; Bearpark, M.; Heyd, J. J.; Brothers, E.; Kudin, K. N.; Staroverov, V. N.; Kobayashi, R.; Normand, J.; Raghavachari, K.; Rendell, A.; Burant, J. C.; Iyengar, S. S.; Tomasi, J.; Cossi, M.; Rega, N.; Millam, J. M.; Klene, M.; Knox, J. E.; Cross, J. B.; Bakken, V.; Adamo, C.; Jaramillo, J.; Gomperts, R.; Stratmann, R. E.; Yazyev, O.; Austin, A. J.; Cammi, R.; Pomelli, C.; Ochterski, J. W.; Martin, R. L.; Morokuma, K.; Zakrzewski, V. G.; Voth, G. A.; Salvador, P.; Dannenberg, J. J.; Dapprich, S.; Daniels, A. D.; Farkas,

Ö.; Foresman, J. B.; Ortiz, J. V.; Cioslowski, J.; Fox, D. J. Gaussian, Inc., Wallingford CT, 2009.

10. Neese, F. *Wiley Interdiscip. Rev.-Comput. Mol. Sci.* **2012**, 2, 73.

11. Pfirrmann, S.; Limberg, C.; Herwig, C.; Knispel, C.; Braun, B.; *et al*. *J. Am. Chem. Soc.* **2010**, 132, 13684-13691

Appendix 2. Supplementary Information for Chapter 5

Experimental Part

General Considerations. All manipulations were carried out using standard Schlenk or glovebox techniques under an N_2 atmosphere. Unless otherwise noted, solvents were deoxygenated and dried by thoroughly sparging with N_2 gas followed by passage through an activated alumina column in the solvent purification system by SG Water, USA LLC. Non-halogenated solvents were tested with a standard purple solution of sodium benzophenone ketyl in tetrahydrofuran in order to confirm effective oxygen and moisture removal. All reagents were purchased from commercial vendors and used without further purification unless otherwise stated. $[SiP^{iPr}_3]Fe(Cl)$,[1] $\{H(OEt_2)_2\}\{BAr^F_{24}\}$,[2] $\{Cp_2Fe\}\{BAr^F_{24}\}$,[3] KC_8,[4] and anhydrous $^{57}FeCl_2$[5] were synthesized following literature procedures. ^{57}Fe-enriched **5.1** was obtained via $[SiP^{iPr}_3]^{57}Fe(Cl)$ by replacing $FeCl_2$ with $^{57}FeCl_2$.[1] The anilinium salts were obtained with slight modifications of the reported procedure.[6] Deuterated solvents were purchased from Cambridge Isotope Laboratories, Inc., degassed and stored over activated 3 Å molecular sieves prior to use. Elemental analyses were performed by Midwest Microlab, LLC, Indianapolis, IN. ^{1}H, ^{13}C and ^{29}Si chemical shifts are reported in ppm relative to tetramethylsilane, using residual solvent resonances as internal standards. ^{31}P chemical shifts are reported in ppm relative to 85% aqueous H_3PO_4. ^{15}N chemical shifts are reported in ppm relative to liquid NH_3 at 0 ppm. Solution phase magnetic measurements were performed by the method of Evans.[7] Solid IR measurements were obtained on a Bruker Alpha spectrometer equipped with a diamond ATR probe or as KBr pellets using a Bio-Rad Excalibur FTS 3000 spectrometer.

EPR Spectroscopy. X-band EPR spectra were obtained on a Bruker EMX spectrometer on 2-5 mM solutions prepared as frozen glasses in 2-MeTHF. Samples were collected at powers ranging from 20 μW to 15 mW and modulation amplitudes of 1 – 5 Gauss. Spectra were simulated using the EasySpin[8] suite of programs with Matlab 2013.

Optical Spectroscopy. Measurements were taken on a Cary 50 UV-Visible spectrophotometer using a 1-cm quartz cell connected to a round-bottom flask and sealed with a Teflon stopcock or a rubber septa. Variable temperature measurements were collected with a Unisoku CoolSpek cryostat mounted within the Cary spectrophotometer. Spectra of **5.5** were obtained by charging the cuvette with solid **5.5** and a flea stir bar, followed by evacuation of the headspace and sealing the Teflon stopcock. The adjacent compartment was charged with THF and sealed after application of mild vacuum. The cuvette was then mounted within the Unisoku cryostat and chilled to the desired temperature. Stirring was commenced and the stopcock separating the two compartments was opened and allowing the THF to transfer *in vacuo* and dissolve **5.5** at the desired temperature.

X-Ray Crystallography. XRD studies were carried out at the Beckman Institute Crystallography Facility on a Brüker Kappa Apex II diffractometer (Mo Kα radiation). Structures were solved using SHELXS or SHELXT and refined against F^2 on all data by full-matrix least squares with SHELXL. The crystals were mounted on a glass fiber under Paratone N oil.

Electrochemistry. Electrochemical measurements were carried out in a thick-walled one-component electrochemical cell fitted with a Teflon stopcock and tungsten leads protruding from the top of apparatus. A CD instruments 600B electrochemical analyzer

was used for data collection. A freshly-polished glassy carbon electrode was used as the working electrode and platinum wire was used as the auxiliary electrode. Solutions (THF) of electrolyte (0.1 M tetra-*n*-butylammonium hexafluorophosphate) contained ferrocene (1 mM), to serve as an internal reference, and analyte (1 mM). All reported potentials are referenced to the ferrocene/ferrocenium couple, Cp_2Fe^+/Cp_2Fe.

^{57}Fe Mössbauer Spectroscopy. Spectra were recorded on a spectrometer from SEE Co (Edina, MN) operating in the constant acceleration mode in a transmission geometry. The sample was kept in an SVT-400 cryostat from Janis (Wilmington, MA). The quoted isomer shifts are relative to the centroid of the spectrum of a metallic foil of α-Fe at room temperature. Solid samples were prepared by grinding polycrystalline material into a fine powder and then mounted in a Delrin cup fitted with a screw-cap as a boron nitride pellet. Solution samples were transferred to a sample cup chilled to 77K inside of the glovebox. Upon freezing of the solution, the cup was quickly removed from the glovebox and immersed in liquid N_2 until being mounted in the cryostat. Data analysis was performed using the program WMOSS (www.wmoss.org) and quadrupole doublets were fit to Lorentzian lineshapes.

Features undergoing slow electronic relaxation in the magnetically-perturbed Mossbauer data were fit in the $S = 1/2$ representation. The Hamiltonian in this representation is given by,

$$\mathcal{H} = \beta\vec{S} \cdot \mathbf{g} \cdot \vec{B} + \vec{S} \cdot \mathbf{A} \cdot \vec{I} + \mathcal{H}_Q \qquad \textbf{Eqn A2.1}$$

$$\mathcal{H}_Q = \left(\frac{eQV_{zz}}{12}\right)\left[3I_z^2 - \frac{15}{4} + \eta\left(I_x^2 - I_y^2\right)\right] \qquad \textbf{Eqn A2.2}$$

Where **g** is the g tensor obtained by EPR simulation, **A** is the ^{57}Fe hyperfine tensor, H_Q is the nuclear quadrupole interaction of the $I = 3/2$ excited state, and $\eta = (V_{xx} - V_{yy}) / V_{zz}$ is the asymmetry parameter.[9]

Fe K-edge X-ray Absorption Spectra. Samples were prepared by grinding polycrystalline material into a fine powder and then mounted in a Delrin cup. XAS data were collected in fluorescence mode at ~20K with a 30-element germanium detector (SSRL, BL 4-1) using a Si(220) $\Phi = 90^o$ double monochromator with a 9.5 keV cutoff for harmonic rejection. Photoreduction of the samples was not observed on subsequent scans (exposure time ~20 min per scan). Data averaging, background removal and curve fitting were performed with the SIXPACK[10] and Demeter[11] suites of programs. Edge energies were calibrated using α-Fe metal foil (7111.3 eV).

DFT Calculations. Geometry optimizations, single-point calculations and frequency calculations were performed using the Gaussian 09 (Rev B.01) suite of programs with the BP86 functional, the 6-31G(d) basis set for C and H atoms, and the def2TZVPP basis set for Fe, P, Si, N and CN-derived C atoms.[12] Frequency calculations were performed on optimized geometries to ensure true minima.

Determination of pKa values of the CNH ligand in 4'. The pKa(FeCN-H) value for **5.4'** was estimated in THF using optical methods. The initial conversion of **5.1** to **5.4'** was probed with a series of anilinium, pyridinium and ammoniums salts that display pKa values of 4.5-13.7 in THF.[13] Compound **5.1** was not protonated by [$HNEt_3$][OTf] (pKa: 13.7) or [LutH][OTf] (pKa: 9.5) but the stoichiometric addition of chlorinated anilinium salts caused the formation of mixtures of **5.1** and **5.4'**. Spectrophotometric titrations were then performed with [2-Cl-$PhNH_3$][OTf] (pKa = 6.0 in THF) or [2,5-Cl_2-$PhNH_3$][OTf]

(pKa = 4.5 in THF) and **1**. In a typical experiment, a 1 mM solution of **5.1** in THF (3 mL) and a magnetic stir bar were charged into a cuvette fitted with a septum in the glovebox. The cuvette was placed within a Unisoku Cryostat mounted within the spectrophotometer and set to a temperature of 25 ^{o}C. A 0.1 M THF solution of [2-Cl-PhNH$_3$][OTf] was added in aliquots of 10 μL via a gastight Hamilton syringe. The contents of the cuvette were vigorously stirred and UV-visible absorbance spectra were periodically collected. The pKa(FeCN-H) was determined by monitoring the absorbance changes at 532, 927 and 819 nm after the addition of each aliquot of acid and comparing these values to those of pure **5.1** and **5.4'**. The average pKa(FeCN-H) value estimated from these experiments was 5.6(1).

Determination of pKa values of the CN(H)Me ligand in 6-OTf. The pKa(FeCN(Me)-H) value for **5.9'** was estimated in THF using optical methods similar to those described above. Compound **5.8** was not protonated by [HNEt$_3$][OTf] (pKa: 13.7) or [LutH][OTf] (pKa: 9.5) but the addition of chlorinated anilinium salts caused the formation of mixtures of **5.8, 5.9'**, **5.10'**, and **5.11**. As described in the text, this mixture results from rapid electron and proton transfer between the various Fe-containing components (equations S3 and S4) and complicates the determination of the pKa(FeCN(Me)-H) by single wavelength analysis. *[A-H][OTf]* denotes an arbitrary anilinium salt and *A* represents the corresponding aniline.

$$[A-H][OTf] + \mathbf{5.8} \overset{K_1}{\Leftrightarrow} A + \mathbf{5.9'} \qquad \textbf{Eqn A2.3}$$

$$\mathbf{5.8} + \mathbf{5.9'} \overset{K_2}{\Leftrightarrow} \mathbf{5.6'} + \mathbf{5.11} \qquad \textbf{Eqn A2.4}$$

To determine the relative concentrations of **5.8, 5.9'**, **5.10'** and **5.11** produced upon addition of acid to **5.8**, the resulting spectral traces were simulated as a weighted sum of pure spectra. Since complex **5.11** cannot be prepared in pure form and therefore its UV-visible spectrum is unknown, the spectrum of **5.6** was used to model the spectral features of **5.11**. Complex **5.6** and **5.11** are likely to display similar UV-visible features as their multinuclear NMR parameters are very similar, and their 1-electron oxidized complexes, **5.9** and **5.7**, display nearly identical UV-visible, ^{57}Fe Mossbauer and EPR features. As shown below (Figure A2.33-35), the spectral traces are well-simulated by a weighted sum of the spectra of **5.8, 5.9'**, **6**, and **5.10'**, and the relative concentrations of these compounds were used to evaluate the equilibrium concentrations of species in Eqn A2.3.

Spectrophotometric titrations were performed with [$PhNH_3$][OTf] (pKa = 8.0 in THF), [4-Cl-$PhNH_3$][OTf] (pKa = 7.0 in THF) or [2-Cl-$PhNH_3$][OTf] (pKa = 6.0 in THF) and **5.8**. In a typical experiment, a 1 mM solution of **5.8** in THF (3 mL) and a magnetic stir bar were charged into a cuvette fitted with a septum in the glovebox. The cuvette was placed within a Unisoku Cryostat mounted within the spectrophotometer and set to a temperature of 25 ^{o}C. A 0.3 M THF solution of [2-Cl-$PhNH_3$][OTf] was added via a gastight Hamilton syringe to produce final concentrations of 1 mM, 3 mM and 10 mM [2-Cl-$PhNH_3$][OTf]. The contents of the cuvette were vigorously stirred and UV-visible absorbance spectra were periodically collected. The pKa(FeCN(Me)-H) was determined by simulating the resulting spectral traces to a weighted sum of **5.8, 5.9'**, **5.10'**, and **5.6**. The average pKa(FeCN(Me)-H) value estimated from these experiments was 7.1(3).

Typical NH_3 Generation Protocol from 1. A 50 mL Schlenk tube was charged with solid **5.1** (2 mg, 0.0029 mmol), Cp^*_2Co (19 mg, 0.057 mmol), [2,5-Cl_2-$PhNH_3$][OTf] (19

mg, 0.06 mmol) and a magnetic stir bar. The flask was chilled to -78 ^{o}C, Et_2O (4 mL) was added and stirring was commenced. The tube was sealed with a Teflon stopcock and the mixture was stirred at -78 ^{o}C overnight and then slowly warmed to rt.

Typical $HNMe_2$ and NMe_3 Generation Protocol from 5.6. Compound **5.6** (5 mg, 0.007 mmol) was dissolved in Et_2O (2 mL) in a 50 mL Schlenk tube equipped with a stir bar. This suspension was vigorously stirred and cooled to -78 °C in a cold well inside of the glove box. A similarly cooled solution of HOTf, (6 μL, 0.068 mmol) in Et_2O (2 mL) was added to the suspension in one portion with rapid stirring. Solid KC_8 (11.2 mg, 0.083 mmol) was suspended in cold Et_2O (0.75 mL) and added in one portion to the rapidly stirred solution in the Schlenk tube which was then tightly sealed. The reaction was allowed to stir for 1 hour at -78 °C before being warmed to room temperature and stirred for 15 minutes.

Volatile Nitrogen Collection and Analysis. A Schlenk tube was charged with HCl (3 mL of a 2.0 M solution in Et_2O, 6 mmol). Reaction mixtures were vacuum transferred into this collection flask. Residual solid in the reaction vessel was treated with a solution of [Na][O-*t*-Bu] (40 mg, 0.4 mmol) in THF (2 mL) and sealed. The resulting suspension was allowed to stir for 10 minutes before all volatiles were again vacuum transferred into the collection flask. After completion of the vacuum transfer, the flask was sealed and warmed to room temperature. Solvent was removed i*n vacuo* and $[NH_4][Cl]$ quantified by the Indophenol method[14] or dissolved in DMSO-d_6 containing mesitylene as an internal standard and analyzed by NMR spectroscopy. $[NH_4][Cl]$, $[H_2NMe_2][Cl]$ and $[HNMe_3][Cl]$ were identified by ^{1}H, ^{15}N, and ^{13}C NMR spectroscopy and compared to authentic samples. $[H_3NMe][Cl]$ was not observed.

Typical CH_4 Generation Protocol from 5.1. A 20 mL scintillation vial was charged with solid **5.1** (2 mg, 0.002 mmol), Cp^*_2Co (19 mg, 0.057 mmol), [2,5-Cl_2-$PhNH_3$][OTf] (19 mg, 0.06 mmol) and a magnetic stir bar. The flask was chilled to -78 ^oC, Et_2O (4 mL) was added and stirring was commenced. The tube was sealed with a gastight threaded cap fitted with a rubber septa and the mixture was stirred at -78 ^oC overnight and then slowly warmed to rt.

Typical CH_4 Generation Protocol from 5.6. Compound **5.6** (2 mg, 0.003 mmol) was dissolved in Et_2O (3 mL) in a 20 mL scintillation vial equipped with a stir bar. This suspension was vigorously stirred and cooled to -78 °C in a cold well inside of the glove box. A similarly cooled solution of HOTf, (3 μL, 0.034 mmol) in Et_2O (2 mL) was added to the suspension in one portion with rapid stirring. Solid KC_8 (4 mg, 0.030 mmol) was suspended in cold Et_2O (0.75 mL) and added in one portion to the rapidly stirred solution which was then tightly sealed with a gastight threaded cap fitted with a rubber septa. The reaction was allowed to stir for 1 hour at -78 °C before being warmed to room temperature and stirred for 15 minutes.

Volatile Carbon and Hydrogen Analysis. The headspace of reaction flasks were analyzed by gas chromatography to quantify CH_4 production from **5.1** and **5.6** using an SRI Instruments gas chromatograph equipped with a flame ionization detector. Mass spectral analysis of the headspace was analyzed using electron ionization methods. H_2 evolution was determined by gas chromatography with an Agilent 7890A (HP-PLOT U, 30 m, 0.32 mm i.d., 30 ^oC isothermal, 1 mL/min flow rate, N_2 carrier gas) using a thermal conductivity detector.

Synthetic Procedures

[SiP$^{iPr}_3$]Fe(CN) (5.1). A 50 mL Schlenk tube was charged with [SiP$^{iPr}_3$]Fe(Cl) (200 mg, 287 μmol), NaCN (200 mg, 4.1 mmol), THF (10 mL) and MeOH (10 mL). The flask was sealed with a Teflon stopcock and heated to reflux overnight causing a color change from yellow to wine red. The mixture was cooled to room temperature and solvent was removed *in vacuo*. The resulting pink residue was extracted with benzene (2 x 20 mL) and lyophilized. The solid was washed with pentane (3 x 5 mL) furnishing 172 mg of **5.1** as a red solid (87 % yield). Single crystals of **5.1** suitable for X-ray diffraction were obtained by layering a concentrated benzene solution of **5.1** with pentane at room temperature and allowed to stand overnight. ^{1}H NMR (300 MHz, C_6D_6, 298 K, ppm): 5.76, 2.75, 2.07, -1.75. μ_{eff} (C_6D_6, 298 K, 300 MHz): 2.6 μ_B. UV-Visible (THF, 298 K, nm {cm^{-1} M^{-1}}): 918 {175}, 528 {566}, 358 {3262}. IR (KBr, 298 K, cm^{-1}): 2076. Anal: calc. for $C_{37}H_{54}FeNP_3Si$: C 64.44, H 7.89, N 2.03; found: C 64.75, H 8.09, N 1.54.

[SiP$^{iPr}_3$]Fe(C^{15}N) (^{15}N-5.1). Prepared in an analogous fashion to **5.1** but employing ^{15}N-enriched KCN. IR (KBr, 298 K, cm^{-1}): 2045.

[SiP$^{iPr}_3$]Fe(^{13}CN) (^{13}C-5.1). Prepared in an analogous fashion to **5.1** but employing ^{13}C-enriched KCN. IR (KBr, 298 K, cm^{-1}): 2031.

{[SiP$^{iPr}_3$]Fe(CN)}{BAr$^F_{24}$} (5.2). To a stirring solution of **5.1** (33 mg, 48 μmol) in THF (5 mL) was added a solution of {Cp_2Fe}{BAr$^F_{24}$} (50 mg, 48 μmol) in THF (5 mL) causing a color change to forest green. After stirring at room temperature for 1 hour the mixture was filtered through glass filter paper and evaporated to dryness *in vacuo*. The residue was washed with pentane (2 x 5 mL) and Et_2O (1 mL) to remove Cp_2Fe. The remaining dark-green solid was dissolved in THF (3 mL), layered with pentane (10 mL)

and allowed to stand at -30 ºC for 3 days. Single crystals of **5.2** suitable for X-ray diffraction deposit during this time. The crystals were washed with pentane (2 x 5 mL) and dried *in vacuo* to afford 53 mg of **5.2** (72 % yield). ^{1}H NMR (300 MHz, 9:1 C_6D_6: THF-d_8, 298 K, ppm): 15.63, 12.23, 8.26, 7.62, 6.08, 3.82, -12.26. μ_{eff} (9:1 C_6D_6: THF-d^8, 298 K, 300 MHz): 3.6 μ_B. UV-Visible (THF, 298 K, nm {$cm^{-1}\,M^{-1}$}): 1031 {180}, 852 {50}, 693 {180}, 587 {400}, 435 {800}. IR (KBr, 298 K, cm^{-1}): 1944. Anal: calc. for $C_{69}H_{66}BF_{24}FeNP_3Si$: C 53.37, H 4.28, N 0.90; found: C 53.44, H 4.34, N 1.00.

{[SiP$^{iPr}_3$]Fe(CN)}{BAr$^F_{24}$} (^{13}C-5.2). IR (KBr, 298 K, cm^{-1}): 1902.

{Na(12-crown-4)$_2$}{[SiP$^{iPr}_3$]Fe(CN)} (5.3). To a stirred solution of **5.1** (20 mg, 0.029 mmol) in THF (5 mL) was added Na(Hg) (5 mg Na, 0.217 mmol, 2 g Hg), and 12-crown-4 (20 mg, 0.113 mmol) and stirring was continued for 1 hr. The resulting brown solution was filtered through a glass filter paper to remove Hg, and concentrated *in vacuo* to 1 mL. The solution was filtered again and then layered with pentane (5 mL). Overnight, 24 mg of crystals of **5.3** suitable for X-ray diffraction deposit that were washed with pentane (2 x 2 mL) (77 % yield). ^{1}H NMR (300 MHz, THF-d_8, 298 K, ppm): 15.2, 6.9, 6.4, 3.7, 1.6. μ_{eff} (THF-d_8, 298 K, 300 MHz): 2.0 μ_B. UV-Visible (THF, 298 K, nm {$cm^{-1}\,M^{-1}$}): 502 {2600}, 385 {5700}. IR (KBr, 298 K, cm^{-1}): 2014. Anal: calc. for $C_{37}H_{54}FeNP_3Si$: C 59.77, H 8.14, N 1.32; found: C 60.01, H 7.97, N 1.28.

{Na(12-crown-4)$_2$}{[SiP$^{iPr}_3$]Fe(^{13}CN)} (^{13}C-5.3). IR (KBr, 298 K, cm^{-1}): 1972.

{[SiP$^{iPr}_3$]Fe(CNH)}{BAr$^F_{24}$} (5.4). To a stirring suspension of **5.1** (48 mg, 70 μmol) in Et_2O (5 mL) was added a solution of {H(OEt$_2$)$_2$}{BAr$^F_{24}$} (70 mg , 69 μmol) in Et_2O (5 mL) causing a color change to deep blue. After stirring at room temperature for 1 hour the mixture was filtered through glass filter paper and concentrated to ~ 3 mL *in vacuo*.

The solution was layered with pentane (10 mL) and allowed to stand at -30 ^{o}C for 3 days. Single crystals of **5.4** suitable for X-ray diffraction deposit during this time. The crystals were washed with toluene (2 x 5 mL) and pentane (2 x 5 mL) and dried with a gentle stream of N_2 to afford 95 mg of **5.4** (85 % yield). ^{1}H NMR (300 MHz, 9:1 C_6D_6: THF-d^8, 298 K, ppm): 15.66, 10.28, 9.36, 8.28, 7.66, 5.77, 3.16, -2.68, -4.83, -13.19, -36.51. μ_{eff} (9:1 C_6D_6: THF-d_8, 298 K, 300 MHz): 2.6 μ_B. UV-Visible (THF, 298 K, nm {cm^{-1} M^{-1}}): 804 {220}, 602 {257}. IR (KBr, 298 K, cm^{-1}): 2029, 2700 (FWHM ~700 cm^{-1}). Anal: calc. for $C_{69}H_{67}BF_{24}FeNP_3Si$•($C_7H_8$): C 55.46, H 4.59, N 0.85; found: C 55.43, H 4.96, N 1.01.

{[SiP$^{iPr}_3$]Fe(CNH$_2$)}{OTf} (5.5). In the glovebox, complex **5.3** (43 mg, 40 μmol) was dissolved in 2-MeTHF (2 mL) in a 20-mL scintillation vial and frozen in a coldwell chilled externally with liquid nitrogen. A second scintillation vial was charged with HOTf (15 mg, 100 μmol) and 2-MeTHF (1 mL) and similarly frozen in the cold well. The acid solution was briefly thawed and layered on top of the frozen Fe-containing solution followed by refreezing the solutions. To combine the two layers, the vial was elevated off of the floor of the coldwell with forceps, and a pre-chilled spatula was used to mechanically stir the two layers until homogenous. The resulting solution was layered with pre-chilled pentane (15 mL) and mechanical stirring was continued at cryogenic (< -100 ^{o}C) temperatures until a finely-dispersed pink solid had formed. This solid was separated via gravity filtration through a medium frit at -30 ^{o}C and subsequently washed with additional chilled pentane (2 x 20 mL). The solid was finally washed with room temperature toluene (2 x 5 mL) and pentane (2 x 5 mL), furnishing 25 mg of **5.5** as a purple solid (74 % yield) after drying *in vacuo*. Single crystals of **5.5** suitable for X-ray

diffraction were obtained by layering a concentrated THF solution of **5.5** with pentane at -35 ^{o} C and allowed to stand for 16 hours. UV-Visible (THF, 193 K, nm): 929, 640, 525, 394. IR (Solid, 298 K, cm^{-1}): 3232, 3031,1615.

[SiP$^{iPr}_3$]Fe(CND$_2$) (5.5-*d$_2$*). Prepared in an analogous fashion to **5.5** but employing HOTf-*d$_1$*. IR (Solid, 298 K, cm^{-1}): 2408, 2247, 1525, 1500.

[SiP$^{iPr}_3$]Fe(CNMe$_2$) (5.6). A 20 mL scintillation vial was charged with **5.1** (115 mg, 166 μmol), 1,2-dimethoxyethane (5 mL), Na(Hg) (10.4 mg Na, 452 μmol, 2.0 g Hg) and a magnetic stir bar. The vial was sealed and stirred vigorously at room temperature for 1 hour causing a color change to dark amber. The solution was cooled to -60 ^{o}C and MeOTf (16.8 μL, 190 μmol) was added via syringe and the mixture was slowly warmed to rt with stirring. The solution was stirred for an additional hour at rt causing a color change to deep purple. The solution was cooled to -60 ^{o}C and MeOTf (16.8 μL, 190 μmol) was added via syringe and the mixture was slowly warmed to rt with stirring. The dark amber solution was stirred for an additional hour at rt before being concentrated to dryness *in vacuo*. The brown residue was extracted with pentane (3 x 10 mL), filtered through Celite and concentrated to dryness *in vacuo*. The resulting brown solid was washed with pentane (2 mL) and dried *in vacuo* furnishing 102 mg of **5.6** (82 % yield). Single crystals of **5.6** suitable for X-ray diffraction were obtained by slow evaporation of a concentrated Et_2O solution of **5.6**. ^{1}H NMR (500 MHz, toluene-*d$_8$*, 298 K, ppm): 8.20 (3H, d, 7.0 Hz), 7.35 (3H, d, 7.6 Hz), 7.21 (3H, t, 7.0 Hz), 7.06 (3H, t, 7.5 Hz), 2.83 (6H, s), 2.31 (6H, hept, 5.9 Hz), 1.03 (18H, bs), 0.72 (18H, bs). ^{13}C NMR (125.7 MHz, toluene-*d$_8$*, 293 K, ppm): 279.6 (Fe=*C*=NMe_2). ^{31}P{^{1}H} NMR (202.4 MHz, toluene-*d$_8$*, 298 K, ppm): 103.6 (bs). UV-Visible (THF, 298 K, nm {$cm^{-1}\,M^{-1}$}): 595 {470}, 417 {5500}. IR (KBr, 298 K,

cm^{-1}): 1154, 1383, 1520. Anal: calc. for $C_{39}H_{60}FeNP_3Si$: C 65.08, H 8.40, N 1.95; *found: C, H, N.*

[SiP$^{iPr}_3$]Fe(^{13}CNMe$_2$) (^{13}C-5.6). IR (KBr, 298 K, cm^{-1}): 1142, 1375, 1506.

[SiP$^{iPr}_3$]Fe(C^{15}NMe$_2$) (^{15}N-5.6). IR (Solid, 298 K, cm^{-1}): 1152, 1375, 1505. $^{15}N\{^1H\}$ NMR (500 MHz, C_6D_6, 293 K, ppm): 129.1 (s).

{[SiP$^{iPr}_3$]Fe(CNMe$_2$)}{BAr$^F_{24}$} (5.7). A 20 mL scintillation vial was charged with **5.6** (10 mg, 13.9 μmol), Et_2O (5 mL) and a magnetic stir bar and stirred vigorously at room temperature. A solution of {Cp_2Fe}{BAr^F_{24}} (14.5 mg , 13.8 μmol) in Et_2O (5 mL) was added in one portion causing a color change to lavender over 1 hour. The solution was stirred at rt for 1 hour and then concentrated *in vacuo* to ~ 1 mL. This solution was layered with pentane (5 mL) and stored at -30 ^oC overnight causing the deposition of crystals suitable for X-ray diffraction. The mother liquor was decanted and the crystals were washed with benzene (2 mL) and pentane (2 mL) affording 21 mg of **5.7** (95 % yield). ^1H NMR (300 MHz, CD_3CN, 298 K, ppm): 13.45, 12.76, 7.66, 7.37, 6.73, 5.39, -0.34, -0.62, -2.40. μ_{eff} (CD_3CN, 298 K, 300 MHz): 2.1 μ_B. UV-Visible (THF, 298 K, nm {$cm^{-1}\,M^{-1}$}): 979 {170}, 658 {80}, 543 {320}, 326 {3950}. IR (KBr, 298 K, cm^{-1}): 1559, 1395. Anal: calc. for $C_{71}H_{72}BF_{24}FeNP_3Si\bullet(C_6H_6)$: C 55.68, H 4.73, N 0.84; found: C 55.24, H 4.44, N 1.08.

{[SiP$^{iPr}_3$]Fe(^{13}CNMe$_2$)}{BAr$^F_{24}$} (^{13}C-5.7). IR (KBr, 298 K, cm^{-1}): 1540, 1391.

{[SiP$^{iPr}_3$]Fe(CNMe)}{OTf} (5.10'). To a stirring suspension of **5.1** (67 mg, 97 μmol) in benzene (5 mL) was added neat MeOTf (50 μL, 442 μmol) via syringe causing the precipitation of a fine blue solid. After stirring at room temperature for 1 hour the solids

were collected on a fine sintered glass frit and washed with additional benzene (2 x 5 mL) and Et_2O (2 x 5 mL) furnishing 80 mg of **5.10'** (97 % yield). Single crystals of **5.10'** suitable for X-ray diffraction were obtained by layering a concentrated THF solution of **5.10'** with pentane. ^1H NMR (300 MHz, CD_3CN, 298 K, ppm): 86.26, 18.65, 10.60, 9.01, 5.91, 3.08, 2.42, -4.48. μ_{eff} (CD_3CN, 298 K, 300 MHz): 2.7 μ_B. UV-Visible (THF, 298 K, nm {$cm^{-1}\,M^{-1}$}): 800 {370}, 600 {340}, 331 {5470}. IR (KBr, 298 K, cm^{-1}): 2128. Anal: calc. for $C_{39}H_{57}F_3FeNO_3P_3SSi$: C 54.86, H 6.73, N 1.64; found: C 54.87, H 6.77, N 1.71.

{[SiP$^{iPr}_3$]Fe(^{13}CNMe)}{OTf} (^{13}C-5.10'). IR (KBr, 298 K, cm^{-1}): 2092.

[SiP$^{iPr}_3$]Fe(CNMe) (5.8). A 20 mL scintillation vial was charged with **5.10'** (80 mg, 94 μmol), Et_2O (5 mL), Na(Hg) (4.5 mg Na, 196 μmol, 1.5 g Hg) and a magnetic stir bar. The vial was sealed and stirred vigorously at room temperature overnight. The resulting red solution was filtered through Celite and concentrated to dryness *in vacuo*. The resulting residue was washed with pentane (2 x 2 mL) and dried *in vacuo* furnishing 58 mg of **5.8** (88 % yield). Single crystals of **5.8** suitable for X-ray diffraction were obtained by slow evaporation of a concentrated Et_2O solution of **5.8**. ^1H NMR (300 MHz, C_6D_6, 298 K, ppm): 18.09, 10.37, 6.78, 4.47, 1.57. μ_{eff} (C_6D_6, 298 K, 300 MHz): 1.6 μ_B. UV-Visible (THF, 298 K, nm {$cm^{-1}\,M^{-1}$}): ~1200 {250}, 415 {3300}. IR (KBr, 298 K, cm^{-1}): 1970, 1912. Anal: calc. for $C_{38}H_{57}FeNP_3Si$: C 64.76, H 8.15, N 1.99; found: C 64.43, H 8.26, N 1.64.

[SiP$^{iPr}_3$]Fe(^{13}CNMe) (^{13}C-5.8). IR (KBr, 298 K, cm^{-1}): 1943, 1883.

{[SiP$^{iPr}_3$]Fe[CN(Me)H]}{BAr$^F_{24}$} (5.9). To a stirring solution of **5.8** (20 mg, 28 μmol) in Et_2O (5 mL) chilled to -78 ^oC was added a solution of {$H(OEt_2)_2$}{BAr^F_{24}} (30 mg , 30 μmol) in Et_2O (2 mL) causing a color change to lavender. After stirring at -78 ^oC for 1

hour, the mixture was concentrated to ~ 2 mL *in vacuo* and filtered through a glass filter paper. The solution was layered with pentane (10 mL) and allowed to stand at -30 ^{o}C for 2 days. Single crystals of **5.9** suitable for X-ray diffraction deposit during this time in addition to small amounts of **5.10**. The crystals were washed with toluene (2 x 5 mL) and pentane (2 x 5 mL) and dried *in vacuo* to afford 40 mg of **5.9** (<91 % yield). Complex **5.9** decomposes in solution and the solid state at room temperature to **5.10** and therefore combustion analysis was not obtained. ^{1}H NMR (500 MHz, 1:1 CD_3CN:THF-d^8, 233 K, ppm): 20.9, 14.5, 7.7, 7.6, 7.5, 6.6, 4.8, -2.6, -7.9, -16.1. UV-Visible (THF, 298 K, nm {cm^{-1} M^{-1}}): 933 {200}, 672 {70}, 534 {310}. IR (KBr, 298 K, cm^{-1}): 3337, 1536.

{[SiP$^{iPr}_3$]Fe(CNMe(D))}{BAr$^{F}_{24}$} (5.9-*d*$_1$). IR (Solid, 298 K, cm^{-1}): 2478, 1526.

{[SiP$^{iPr}_3$]Fe(^{13}CNMe(H))}{BAr$^{F}_{24}$} (^{13}C-5.9). IR (KBr, 298 K, cm^{-1}): 3337, 1518.

***In situ* Generation of mixtures that contain [SiP$^{iPr}_3$]Fe(CNMe(H)) (5.11).** A J-Young NMR tube was charged with a solution containing **^{13}C-5.8** (7.7 mg, 11 μmol) and **^{15}N-5.8** (7.7 mg, 11 μmol) in THF-d_8 (400 μL) and cooled to -78 ^{o}C. A pre-chilled solution of {H(OEt_2)$_2$}{BAr$^{F}_{24}$} (11 mg , 11 μmol) in THF-d_8 (200 μL) was rapidly transferred into the NMR tube causing an immediate darkening of the solution. The tube was sealed and rapidly transferred to the NMR probe pre-chilled to -78 ^{o}C. ^{13}C{^{1}H} NMR (125.7 MHz, THF-d_8, 193 K, ppm): 279.7 (Fe=*C*=N(H)Me, major isomer) 282.7 (Fe=*C*=N(H)Me, minor isomer). ^{15}N{^{1}H} NMR (50.6 MHz, THF-d_8, 193 K, ppm): 135.2 (d, $^{1}J_{NH}$: 94 Hz). ^{31}P{^{1}H} NMR (202.4 MHz, THF-d_8, 298 K, ppm): 98.6 (bs).

NMR Spectra

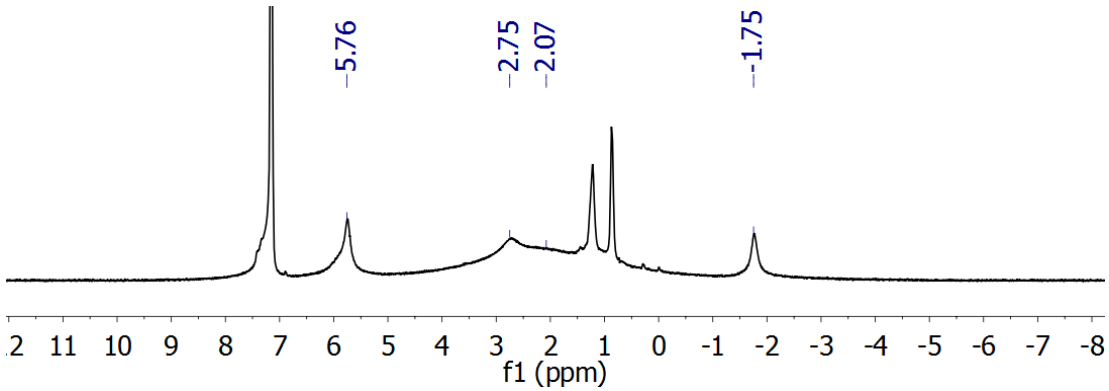

Figure A2.1. ^{1}H NMR spectrum (300 MHz, 293K) of **5.1** recorded in C_6D_6.

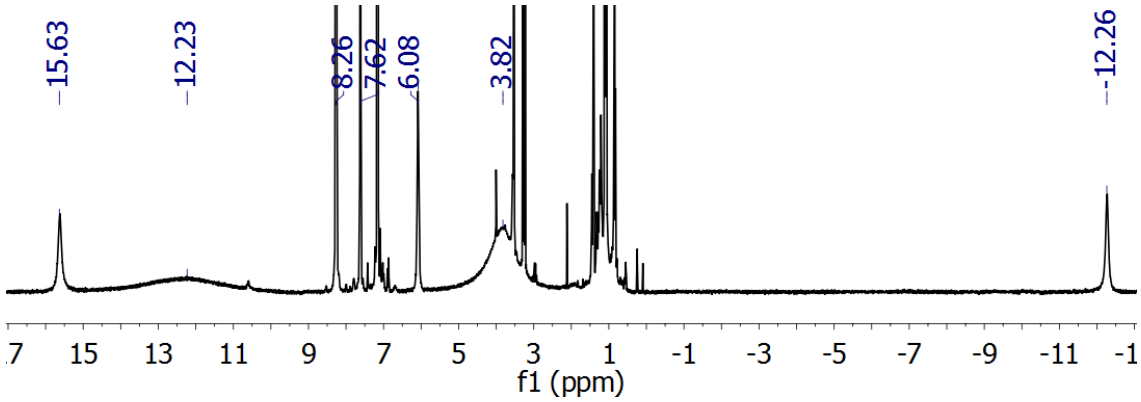

Figure A2.2. ^{1}H NMR spectrum (300 MHz, 293K) of **5.2** recorded in 9:1 C_6D_6: THF-d_8.

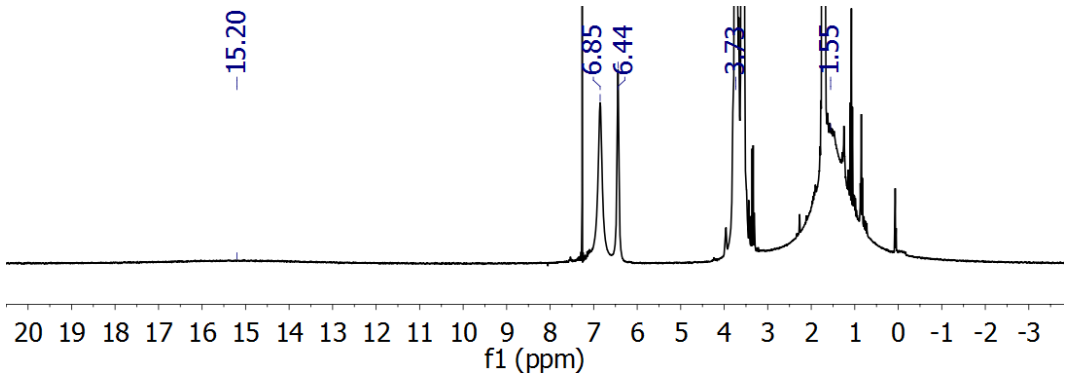

Figure A2.3. ^{1}H NMR spectrum (300 MHz, 293K) of **5.3** recorded in THF-d_8.

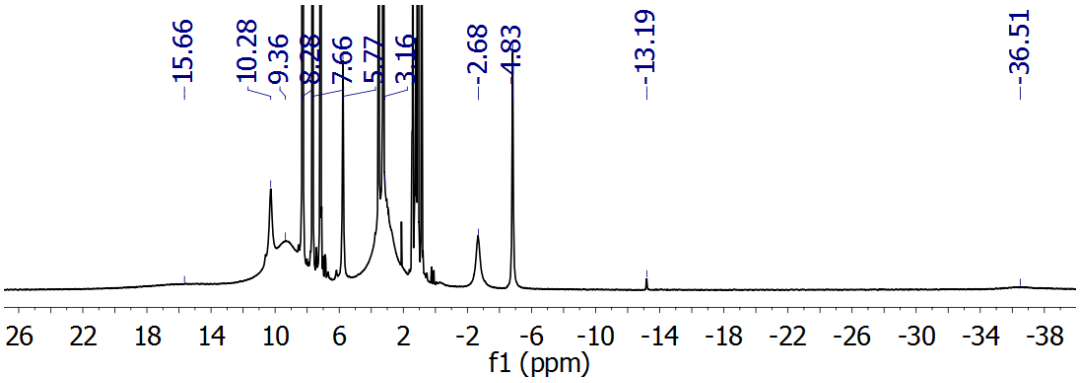

Figure A2.4. ^{1}H NMR spectrum (300 MHz, 293 K) of **5.4** recorded in 9:1 C_6D_6: THF-d_8.

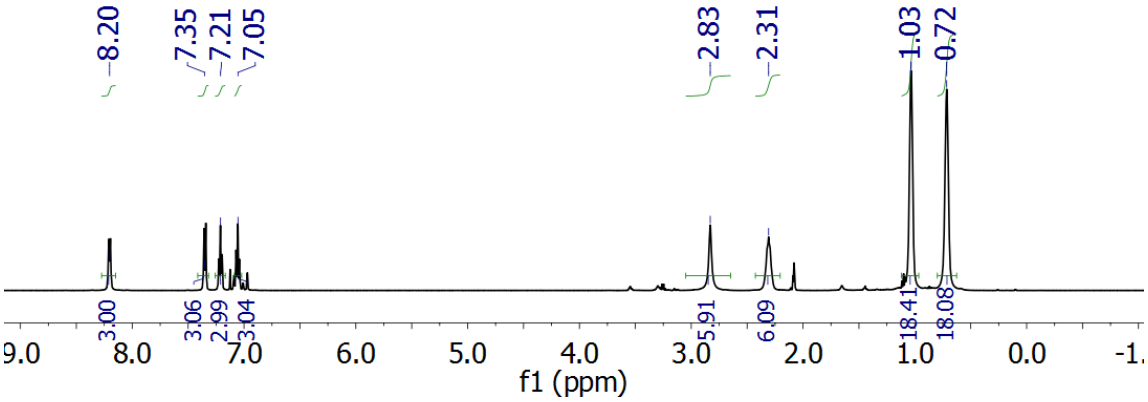

Figure A2.5. ^{1}H NMR spectrum (500 MHz, 293K) of **5.6** recorded in C_6D_6.

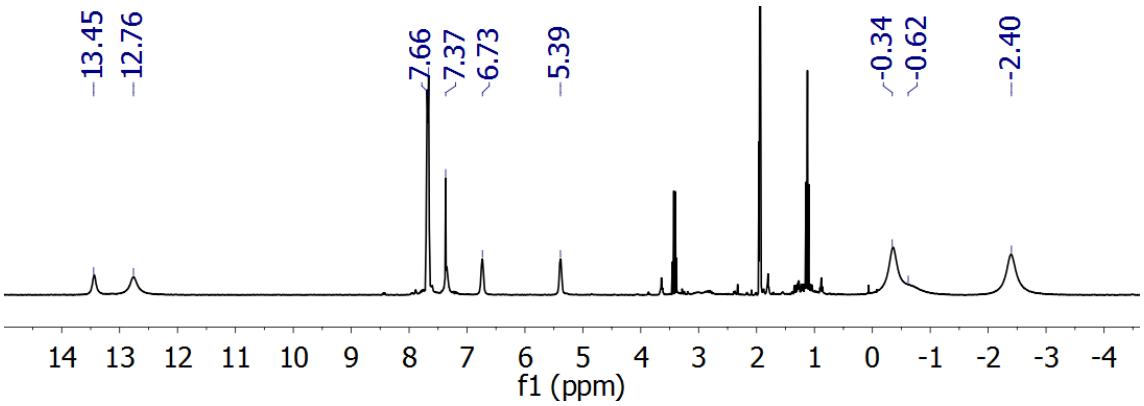

Figure A2.6. ^{1}H NMR spectrum (300 MHz, 293K) of **5.7** recorded in CD_3CN.

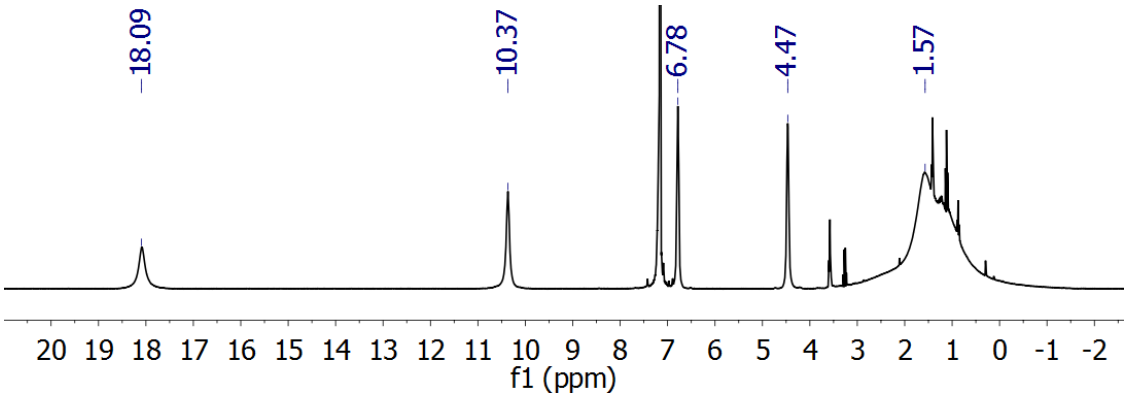

Figure A2.7. ^{1}H NMR spectrum (300 MHz, 293K) of **5.8** recorded in C_6D_6.

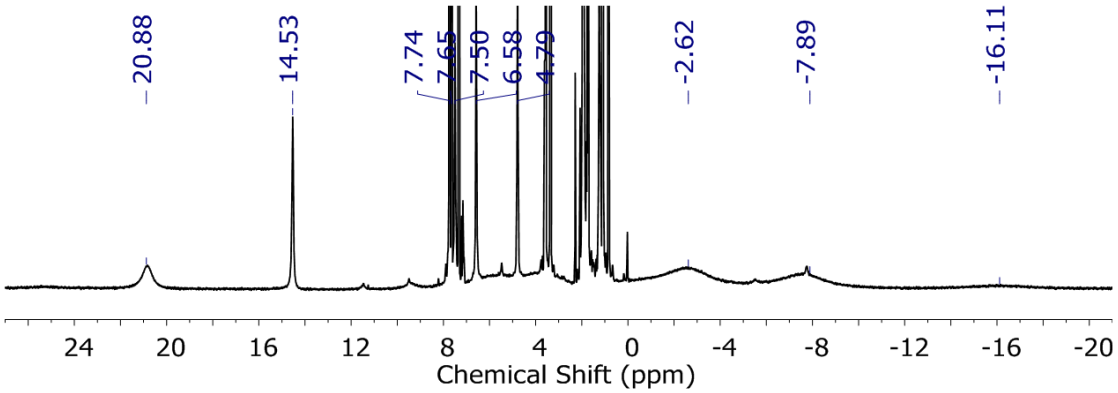

Figure A2.8. ^{1}H NMR spectrum (500 MHz, 233K) of **5.9** recorded in 1:1 THF-*d*$_8$:CD_3CN. The small paramagnetically-shifted peaks scattered throughout the spectrum are derived from **5.10**, which is the product of the decomposition of **5.9**.

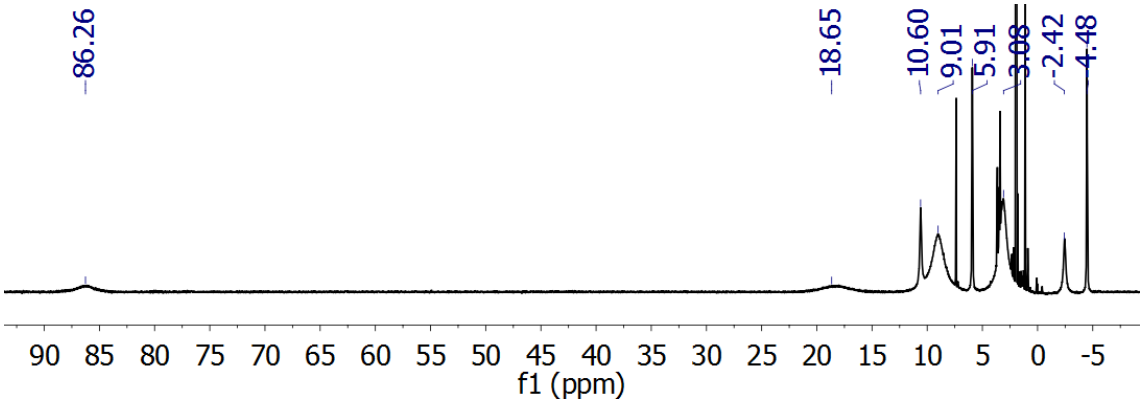

Figure A2.9. ^{1}H NMR spectrum (300 MHz, 293K) of **5.10'** recorded in CD_3CN.

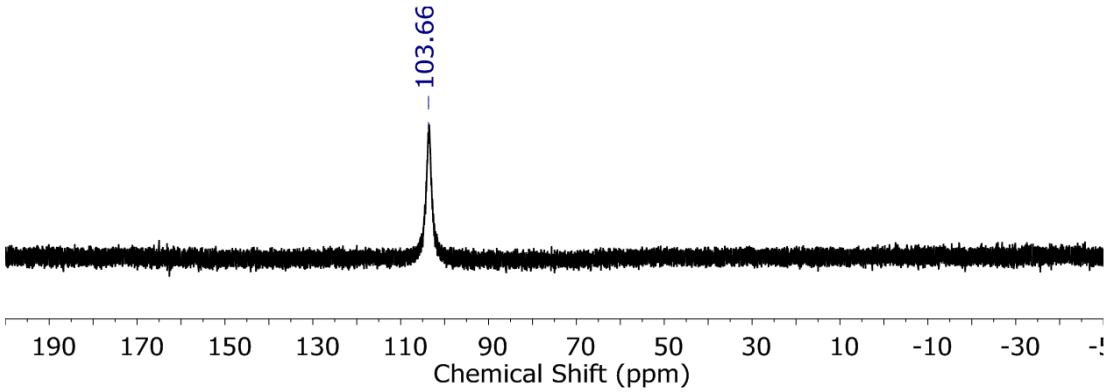

Figure A2.10. ^{31}P NMR spectrum (500 MHz, 298K) of **5.6** recorded in toluene-d_8.

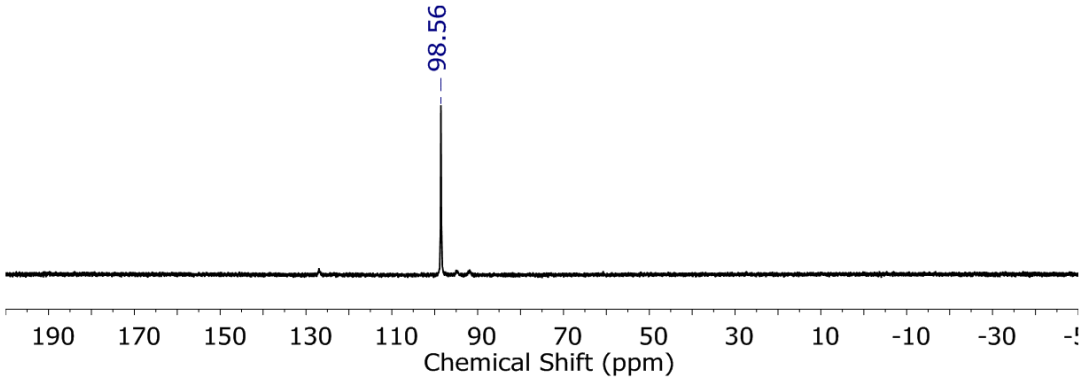

Figure A2.11. ^{31}P NMR spectrum (500 MHz, 193K) of **5.11** recorded in THF-d_8.

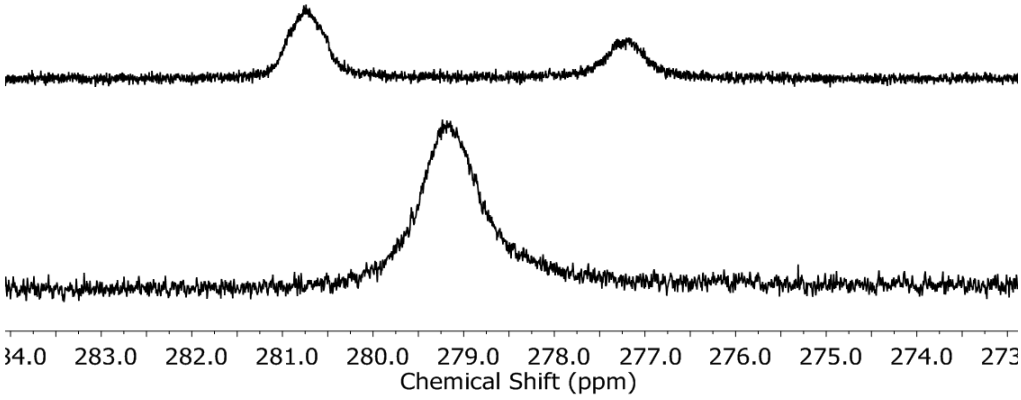

Figure A2.12. ^{13}C NMR spectrum (500 MHz) of **^{13}C-5.6** recorded in toluene-d_8 at 298 K (bottom) and 193 K (top).

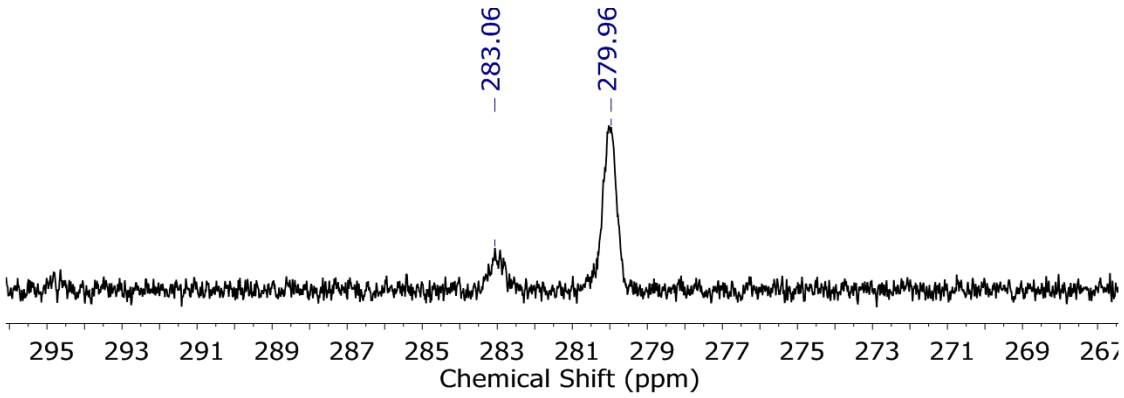

Figure A2.13. ^{13}C NMR spectrum (500 MHz, 193K) of **5.11** recorded in THF-d_8.

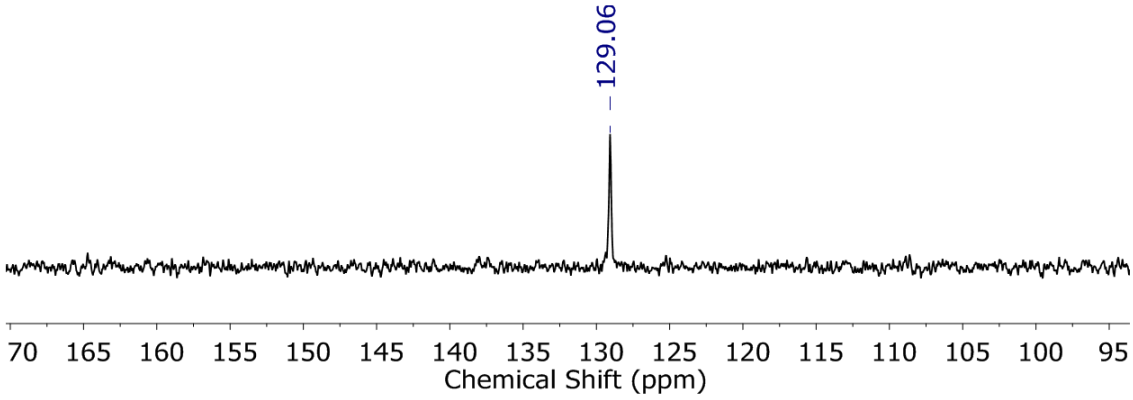

Figure A2.14. $^{15}N\{^{1}H\}$ NMR spectrum (500 MHz, 298K) of **5.6** recorded in C_6D_6.

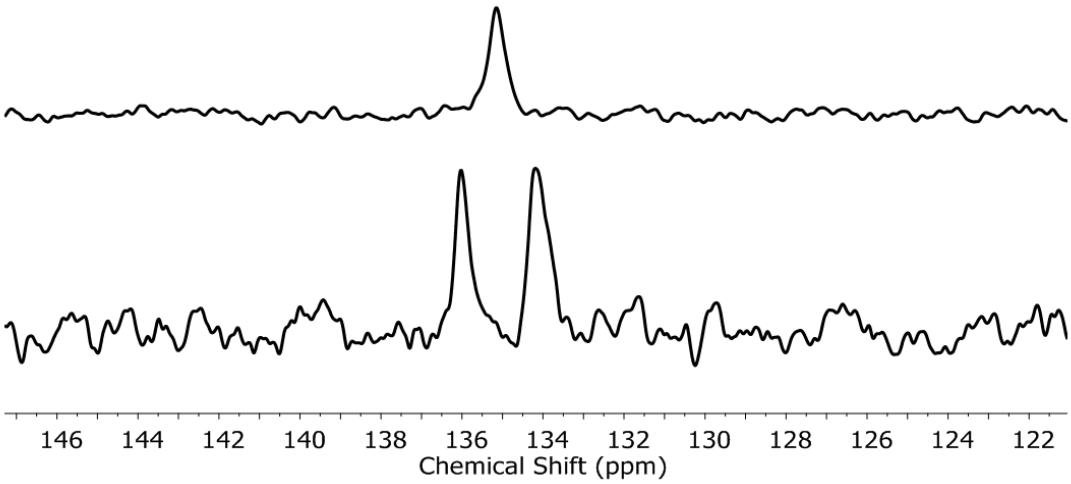

Figure A2.15. $^{15}N\{^{1}H\}$ (Top) and ^{15}N (bottom) NMR spectra (500 MHz, 193K) of **5.11** recorded in THF-d_8.

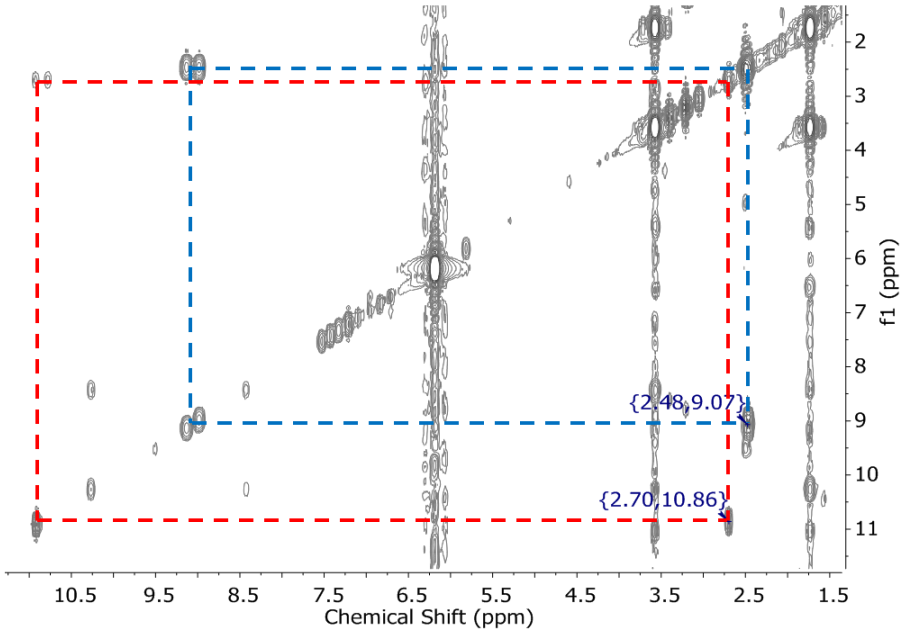

Figure A2.16. ^{1}H COSY (500 MHz, 293K) of the reaction volatiles derived the reduction of ^{15}**N-5.6** recorded in DMSO-d_6. The red dashed line highlights crosspeaks associated with [HNMe$_3$][Cl] and the blue dashed line highlights crosspeaks associated with [H$_2$NMe$_2$][Cl].

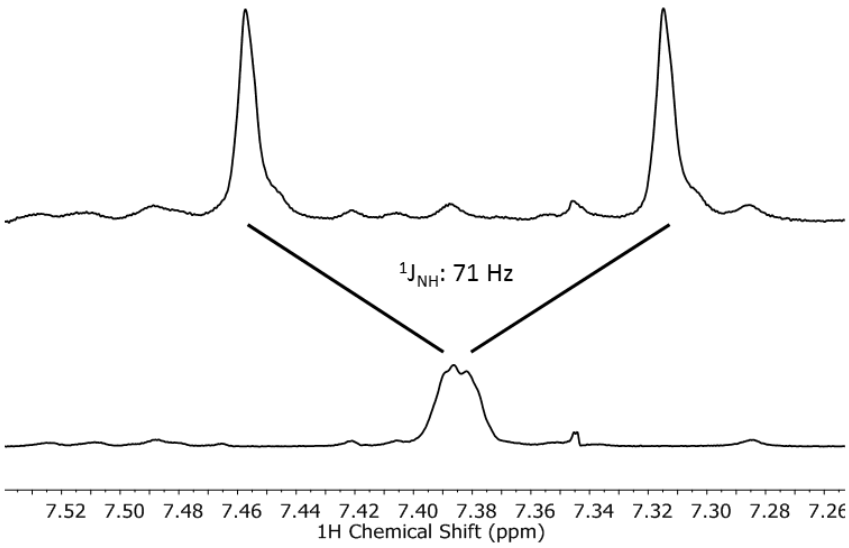

Figure A2.17. ^{1}H NMR (top) and {^{15}N}^{1}H NMR (bottom) (500 MHz, 293K) of the reaction volatiles derived the reduction of ^{15}**N-5.1** recorded in DMSO-d_6.

IR Spectra

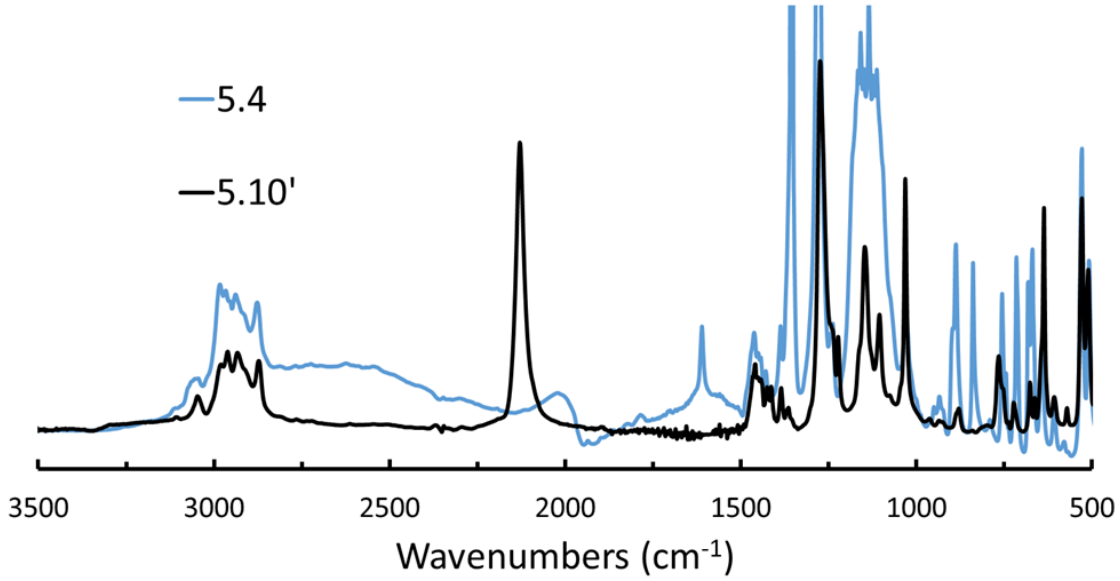

Figure A2.18. Overlaid KBr-IR absorption spectra of solid **5.4** (Blue), and **5.10'** (Black).

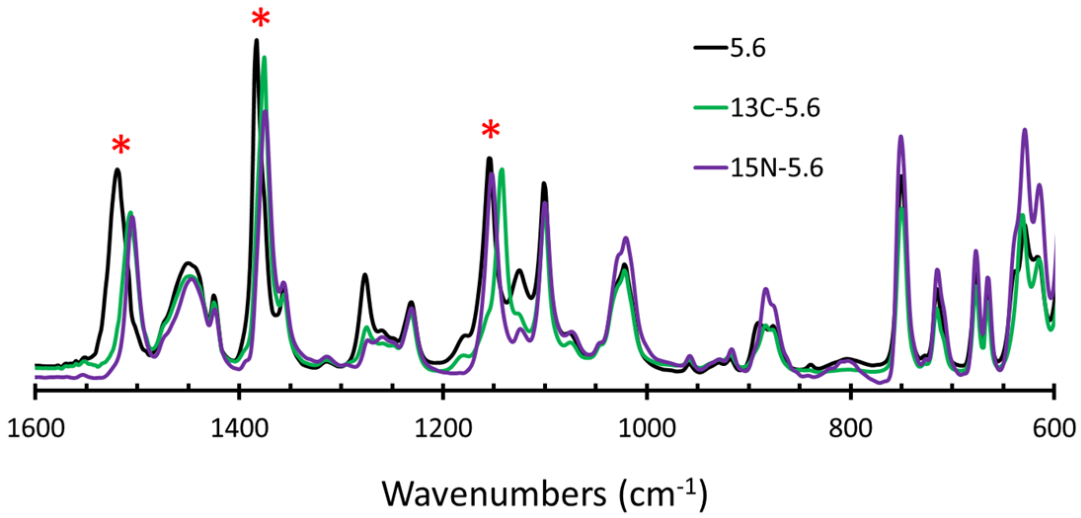

Figure A2.19. Overlaid IR absorption spectra of solid **5.6** (Black), **^{13}C-5.6** (Green), and **^{15}N-5.6** (Purple) with asterisks marking regions of notable difference.

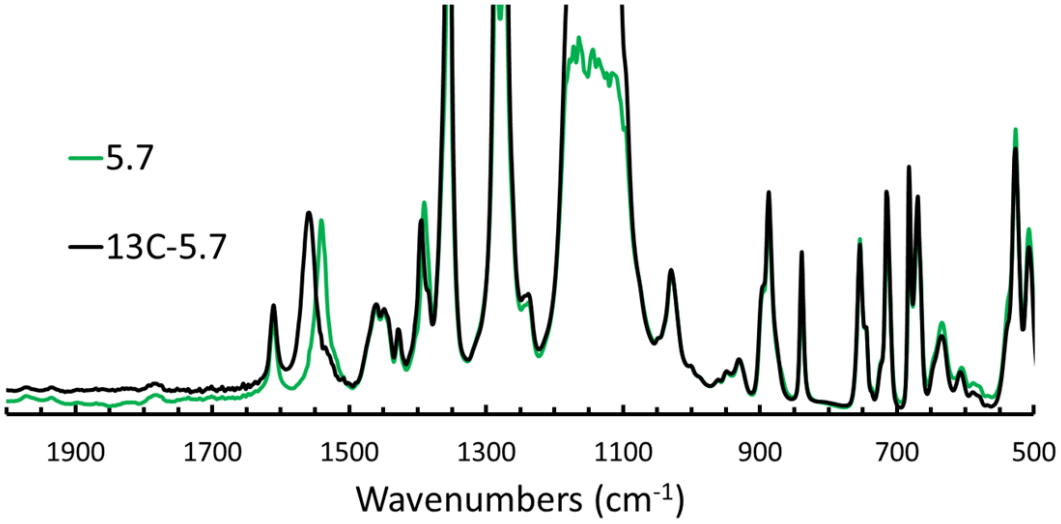

Figure A2.20. Overlaid IR absorption spectra of solid **5.7** (Green) and **^{13}C-5.7** (Black).

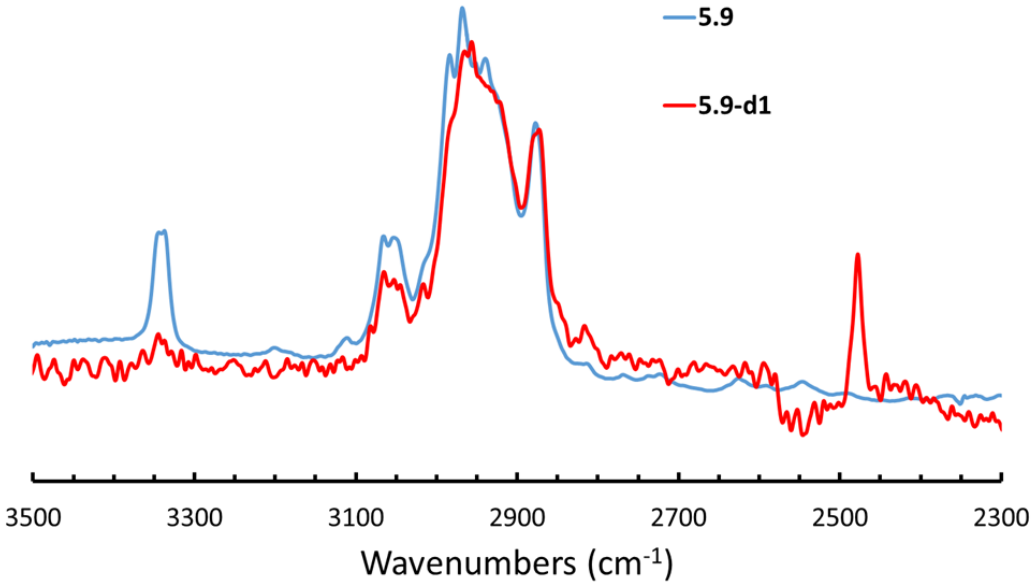

Figure A2.21. Overlaid IR absorption spectra of solid **5.9** (Blue) and **5.9-*d*$_1$** (Red).

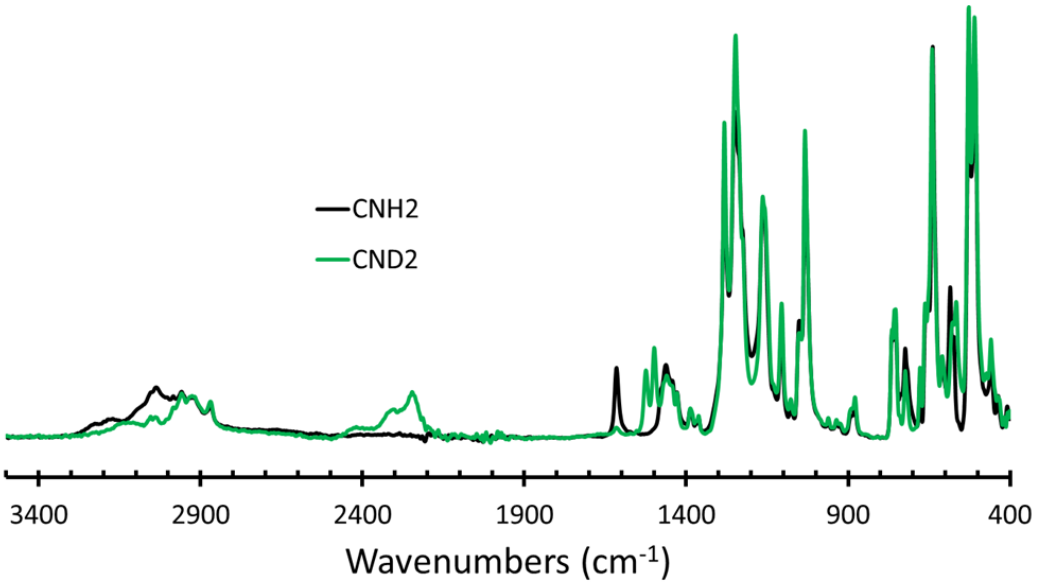

Figure A2.22. Overlaid IR absorption spectra of solid **5.5** (Black), and **5.5-*d*$_2$** (Green).

UV-Visible Spectra

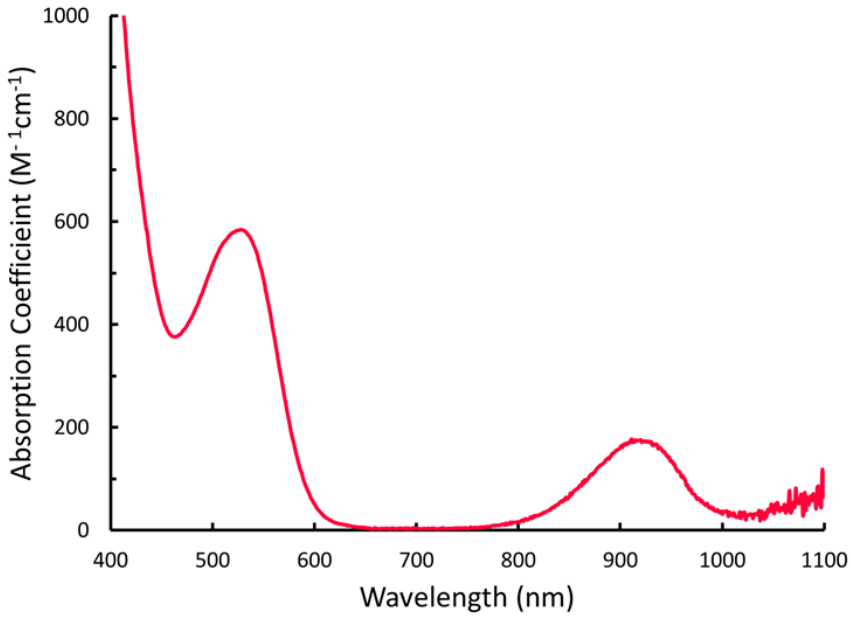

Figure A2.23. UV/visible spectrum of **5.1** in THF at 298 K.

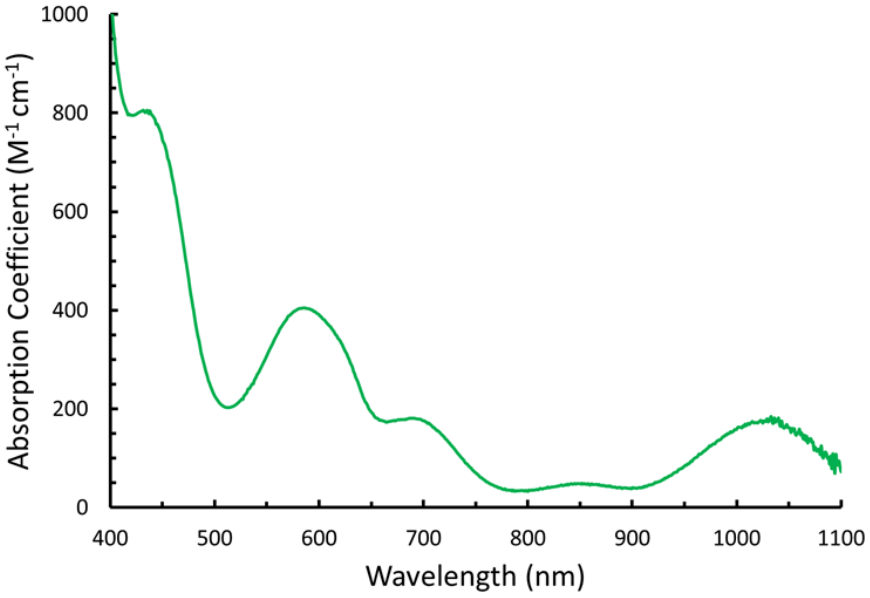

Figure A2.24. UV/visible spectra of **5.2** in THF at 298 K.

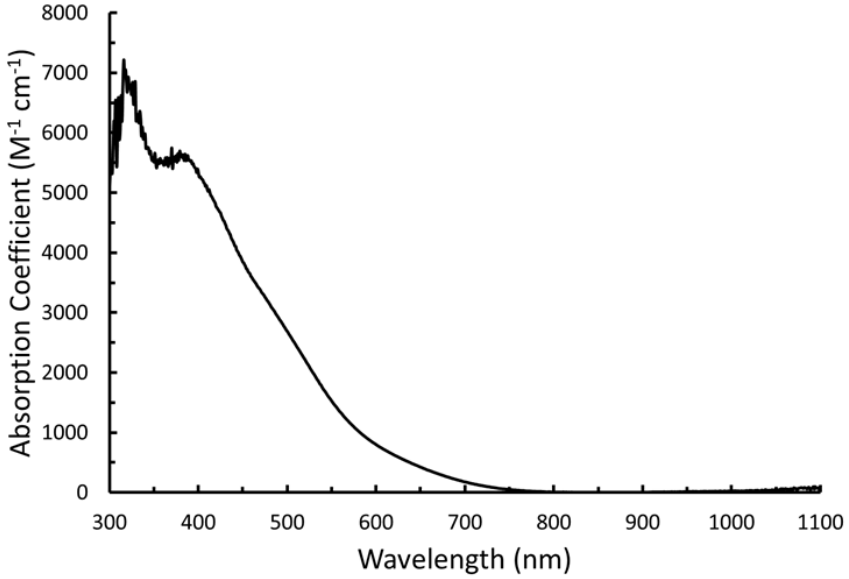

Figure A2.25. UV/visible spectra of **5.3** in THF at 298 K.

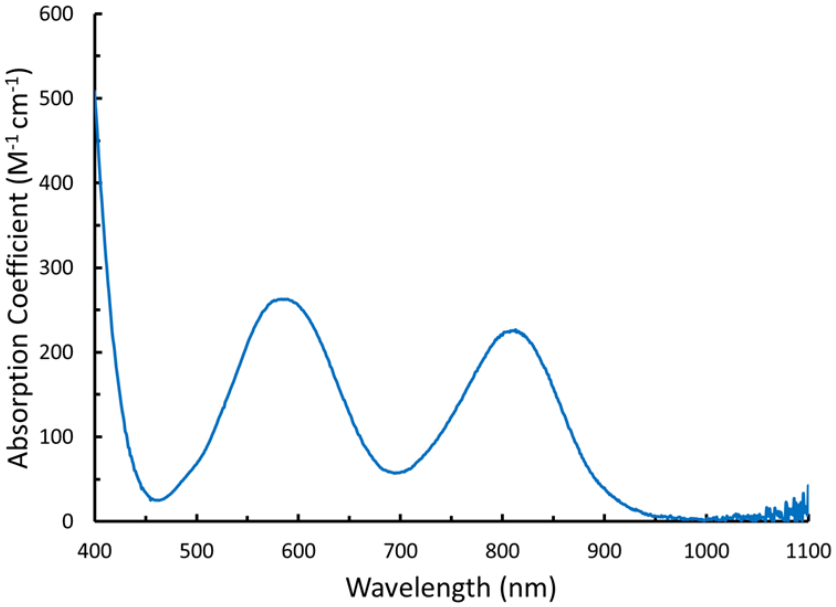

Figure A2.26. UV/visible spectra of **5.4** in THF at 298 K.

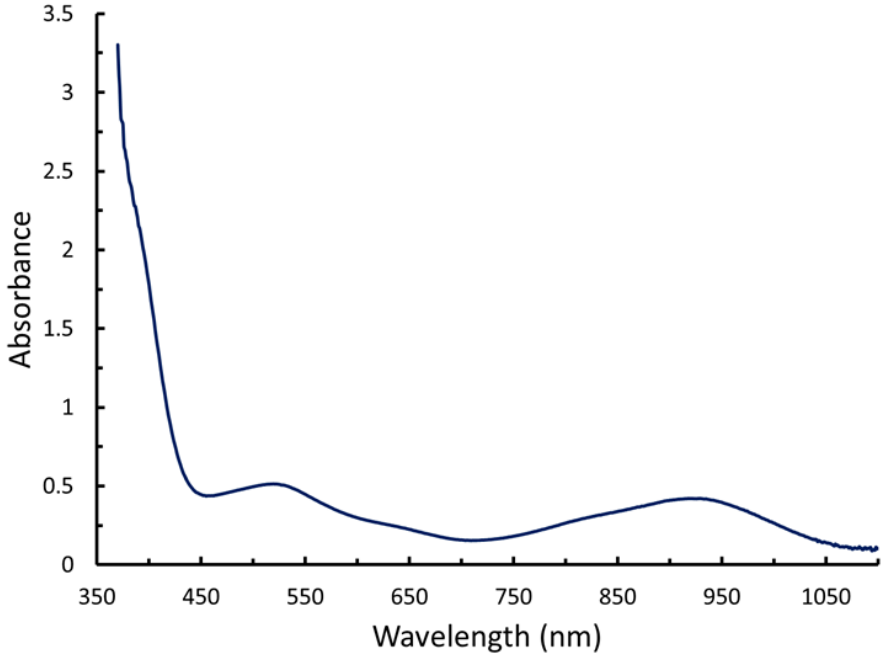

Figure A2.27. UV/visible spectra of **5.5** in THF at 223 K.

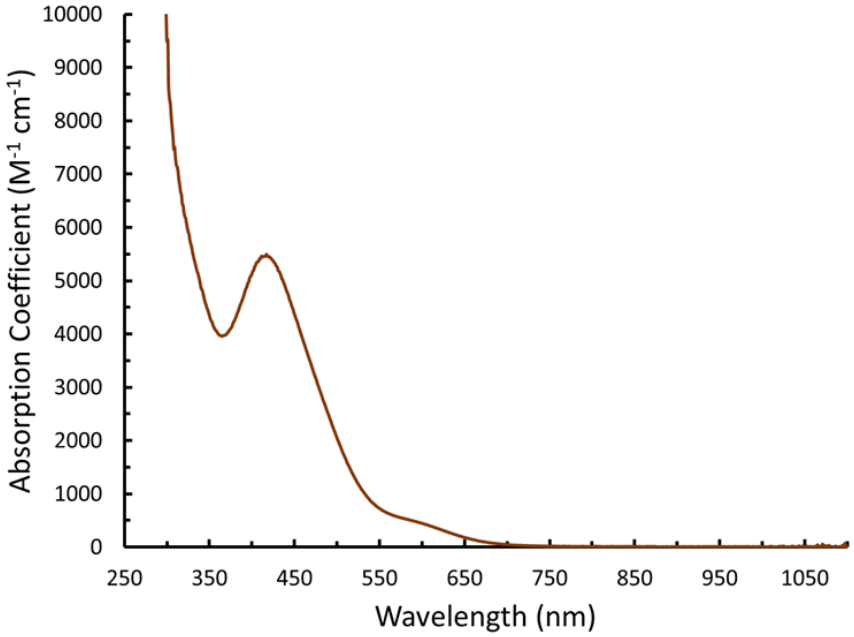

Figure A2.28. UV/visible spectra of **5.6** in THF at 298 K.

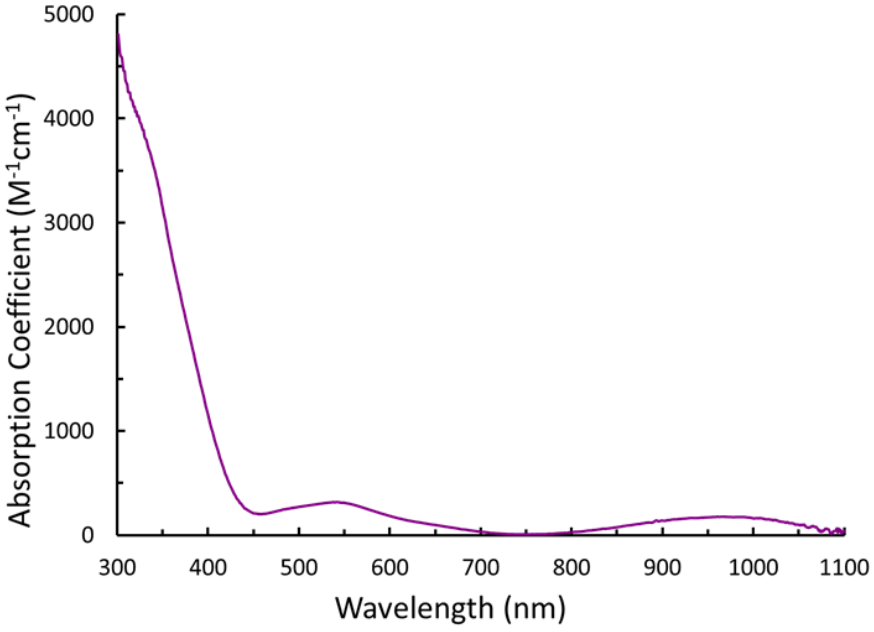

Figure A2.29. UV/visible spectra of **5.7** in THF at 298 K.

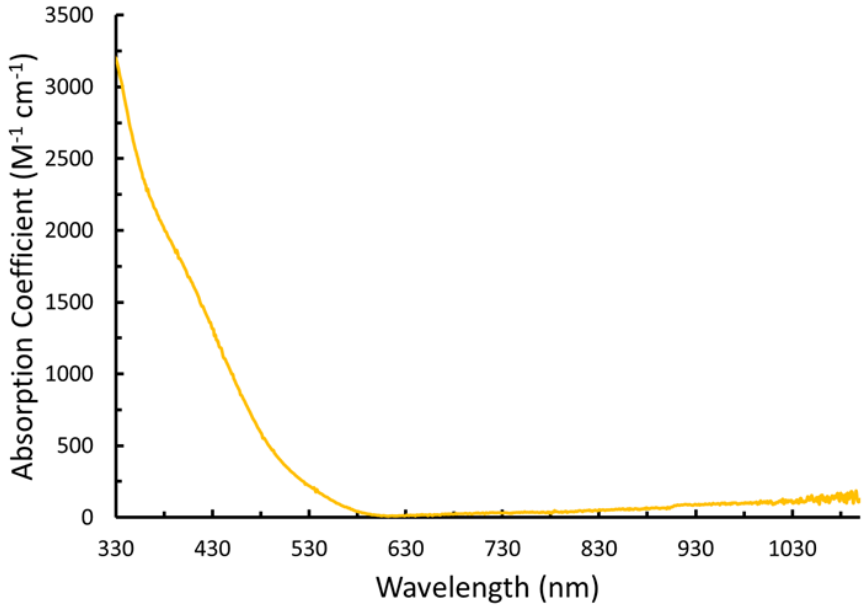

Figure A2.30. UV/visible spectra of **5.8** in THF at 298 K.

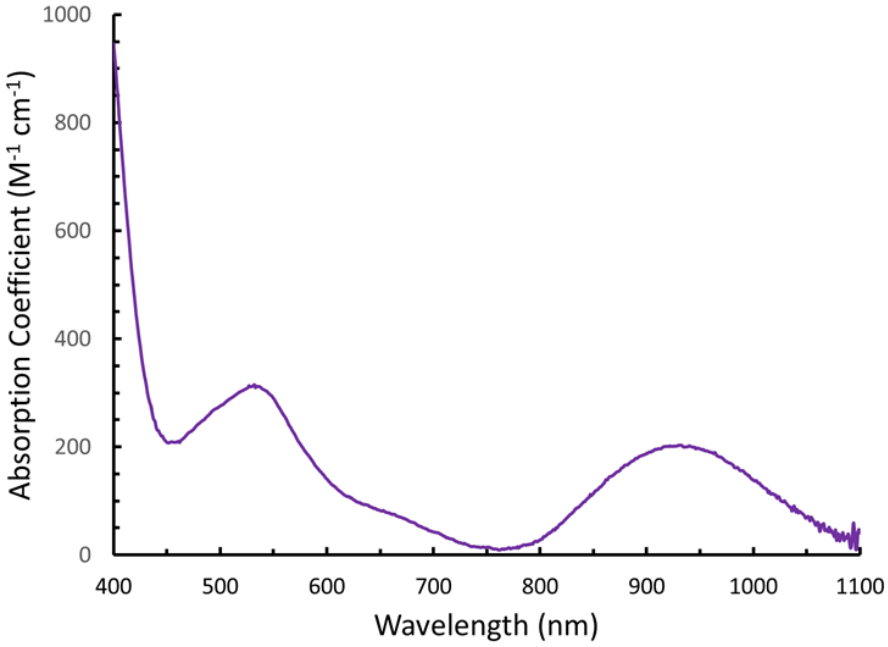

Figure A2.31. UV/visible spectra of **5.9** in THF at 298 K.

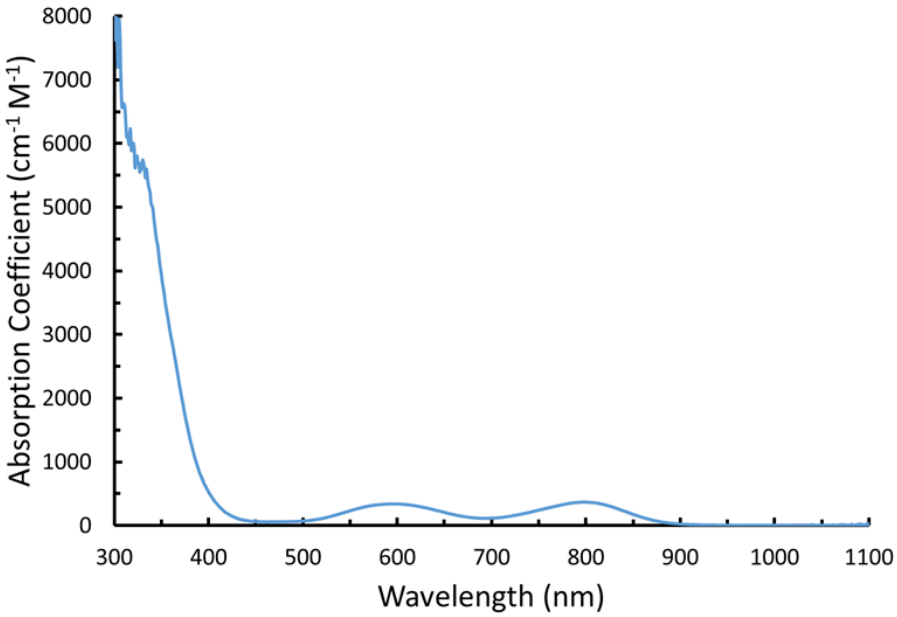

Figure A2.32. UV/visible spectra of **5.10'** in THF at 298 K.

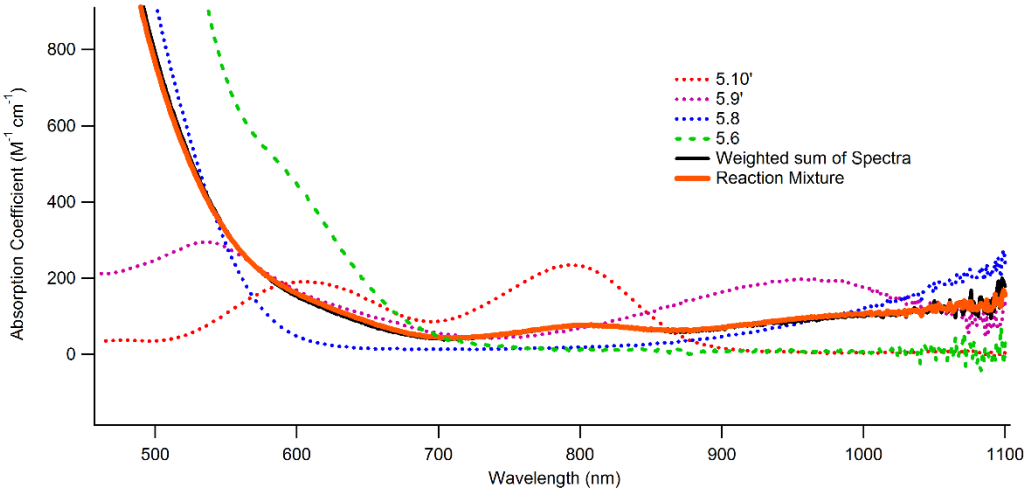

Figure A2.33. Comparison of the UV/visible spectra obtained by combining **5.8** with 3 equivalents of [4-Cl-PhNH$_3$][OTf] (Orange) and the weighted sum of spectra of compounds **5.6, 5.8**, **5.9'**, and **5.10'** in THF at 298 K (molar ratio of 0.12 : 0.48 : 0.27 : 0.20). Subsequent analysis furnishes a pKa of 6.7 for **5.9'** in this particular experiment.

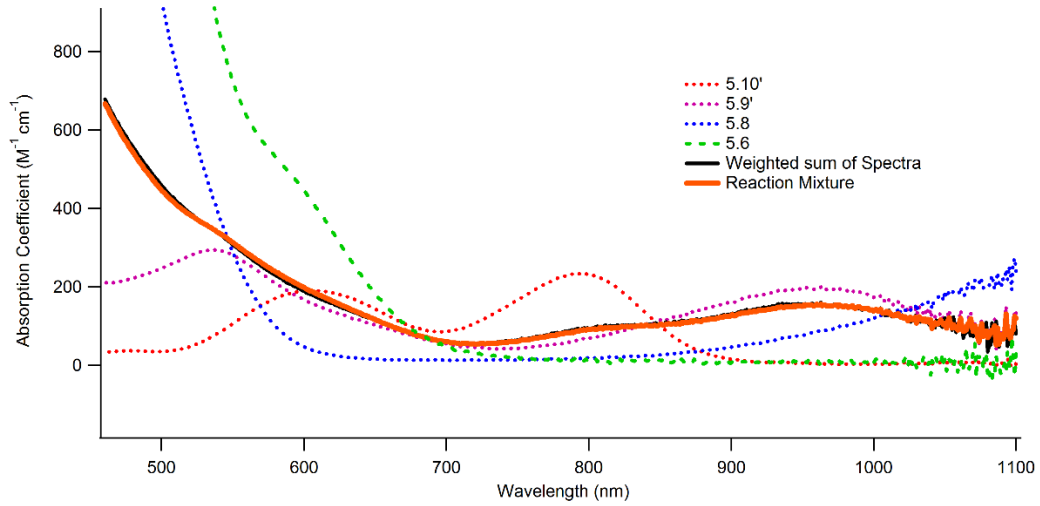

Figure A2.34. Comparison of the UV/visible spectra obtained by combining **5.8** with 3 equivalents of [2-Cl-PhNH$_3$][OTf] (Orange) and the weighted sum of spectra of compounds **5.6, 5.8**, **5.9'**, and **5.10'** in THF at 298 K (molar ratio of 0.09 : 0.08 : 0.74 : 0.16). Subsequent analysis furnishes a pKa of 6.8 for **5.9'** in this particular experiment.

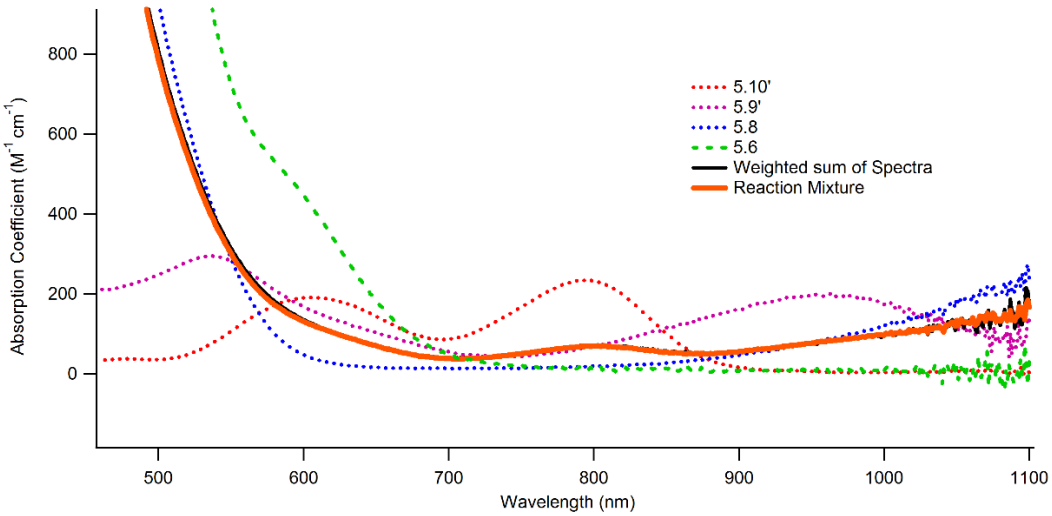

Figure A2.35. Comparison of the UV/visible spectra obtained by combining **5.8** with 10 equivalents of [PhNH$_3$][OTf] (Orange) and the weighted sum of spectra of compounds **5.6, 5.8**, **5.9'**, and **5.10'** in THF at 298 K (molar ratio of 0.09 : 0.60 : 0.145 : 0.20). Subsequent analysis furnishes a pKa of 7.3 for **5.9'** in this particular experiment.

^{57}Fe Mössbauer Spectra

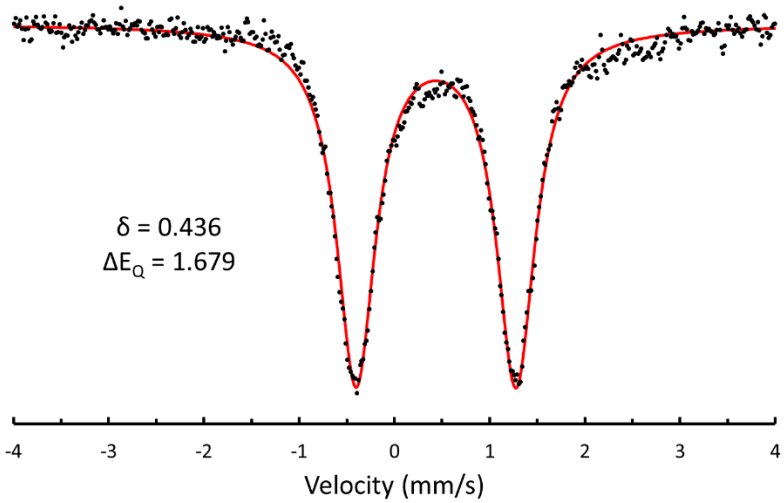

Figure A2.36. 80 K Zero-field ^{57}Fe Mössbauer spectrum of solid **5.1**.

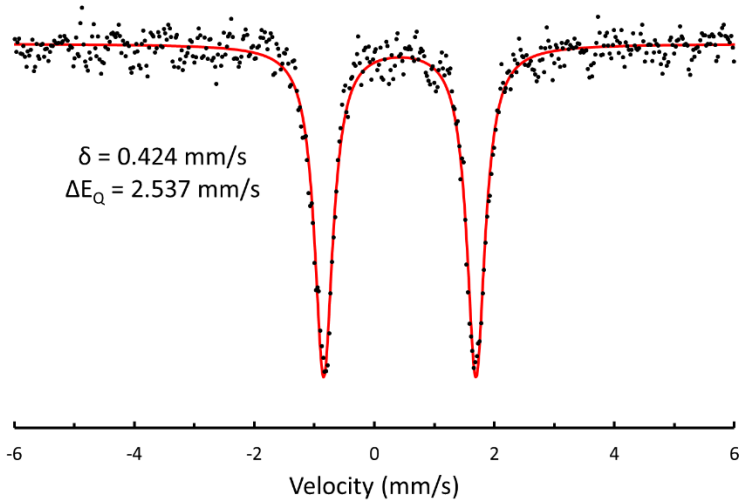

Figure A2.37. 80 K Zero-field ^{57}Fe Mössbauer spectrum of **^{57}Fe-5.2** as a 2 mM solution in frozen 2-MeTHF.

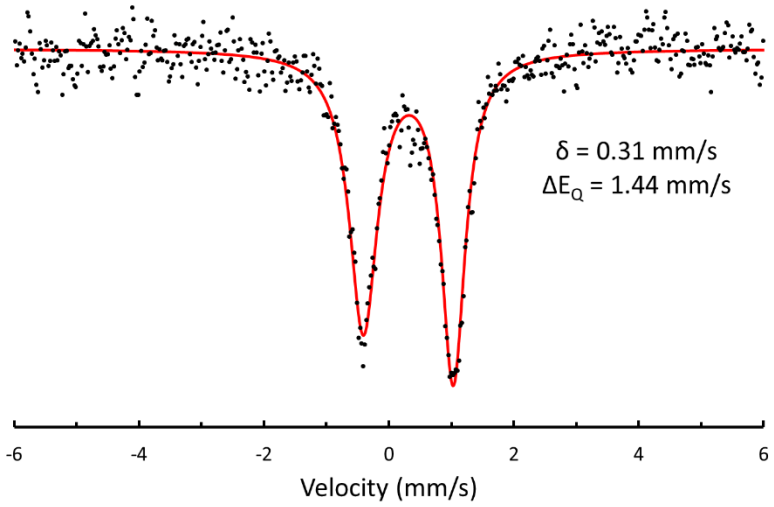

Figure A2.38. 80 K Zero-field ^{57}Fe Mössbauer spectrum of **^{57}Fe-5.3** as a 2 mM solution in frozen 2-MeTHF.

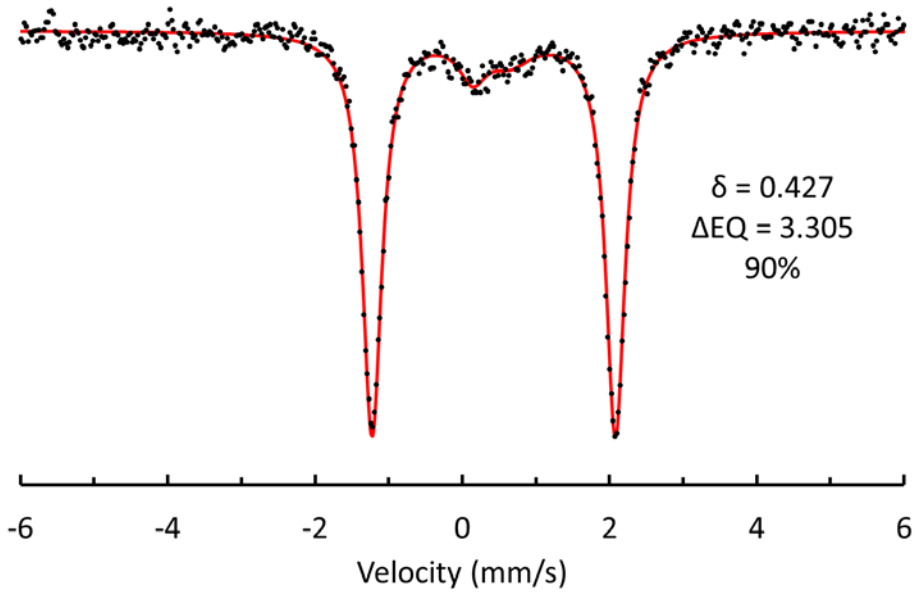

Figure A2.39. 80 K Zero-field ^{57}Fe Mössbauer spectrum of solid **5.4**. The unknown contaminating species has a $\delta = 0.40$ and a $\Delta E_Q = 0.52$ mm/s.

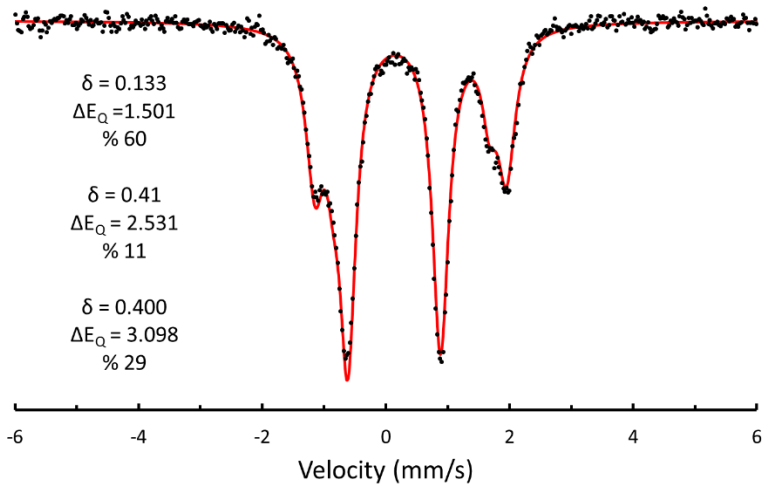

Figure A2.40. 80 K Zero-field ^{57}Fe Mössbauer spectrum of **^{57}Fe-5.5** (major species) as a 2 mM solution in frozen 2-MeTHF. The two minor species display parameters similar to that of **5.4** and are likely generated upon dissolution of **5.5**.

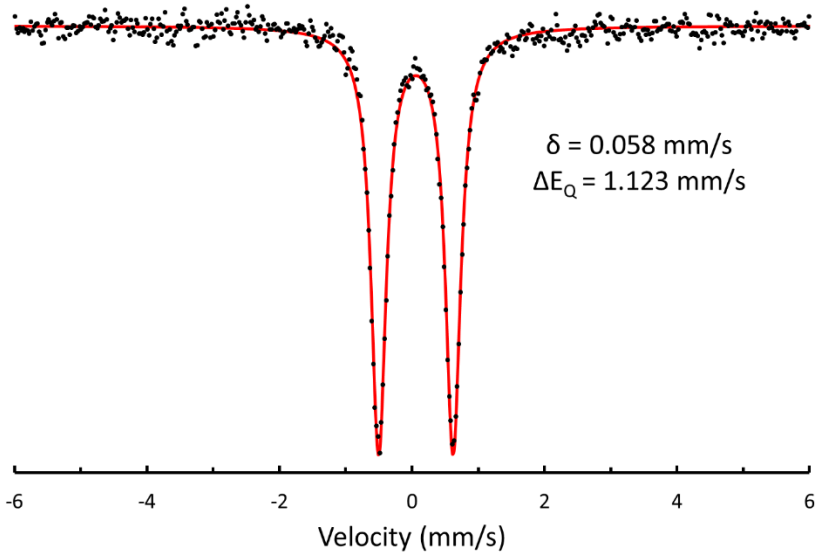

Figure A2.41. 80 K Zero-field ^{57}Fe Mössbauer spectrum of solid **5.6**.

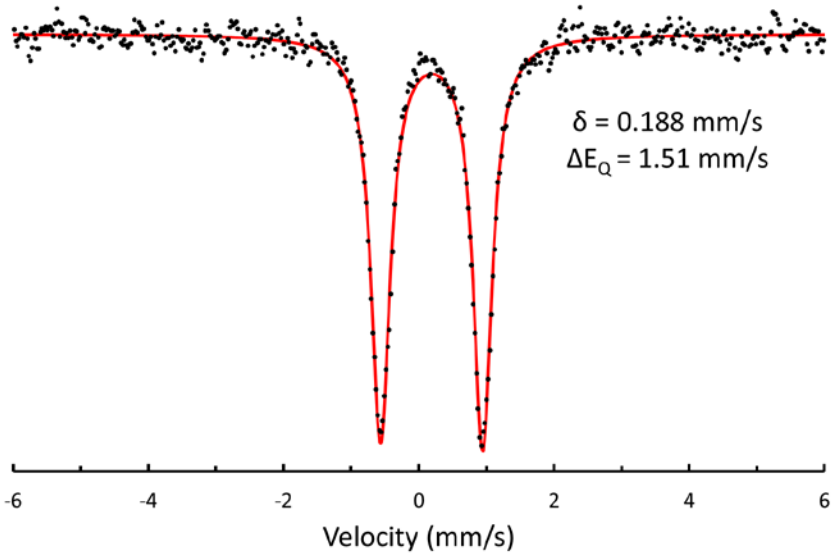

Figure A2.42. 80 K Zero-field ^{57}Fe Mössbauer spectrum of solid **5.7**.

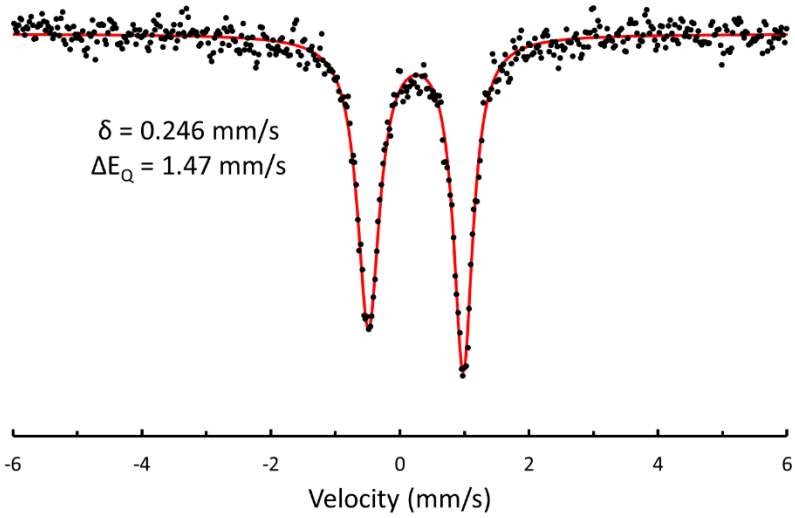

Figure A2.43. 80 K Zero-field ^{57}Fe Mössbauer spectrum of **^{57}Fe-5.8** as a 2 mM solution in frozen 2-MeTHF. The asymmetry in the features is a result of the onset of slow electronic relaxation.

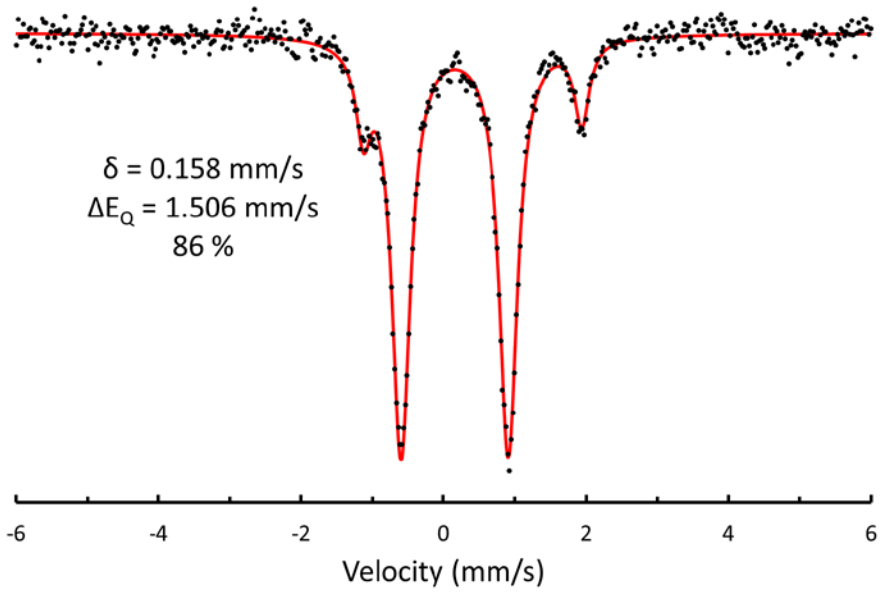

Figure A2.44. 80 K Zero-field ^{57}Fe Mössbauer spectrum of **^{57}Fe-5.9** as a 2 mM solution in frozen 2-MeTHF. The minor species displays parameters similar to that of **5.10** and are likely generated upon dissolution of **5.9**.

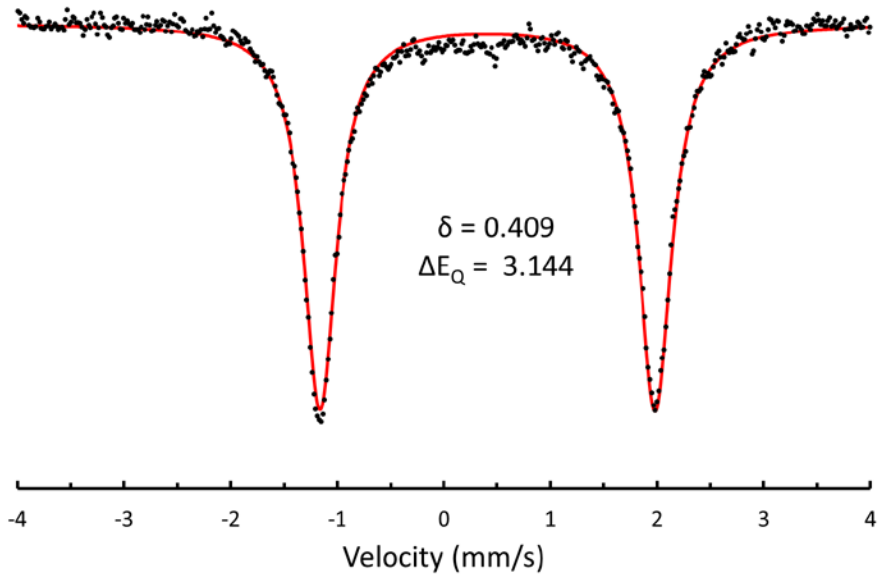

Figure A2.45. 80 K Zero-field ^{57}Fe Mössbauer spectrum of solid **5.10'**.

EPR Spectra

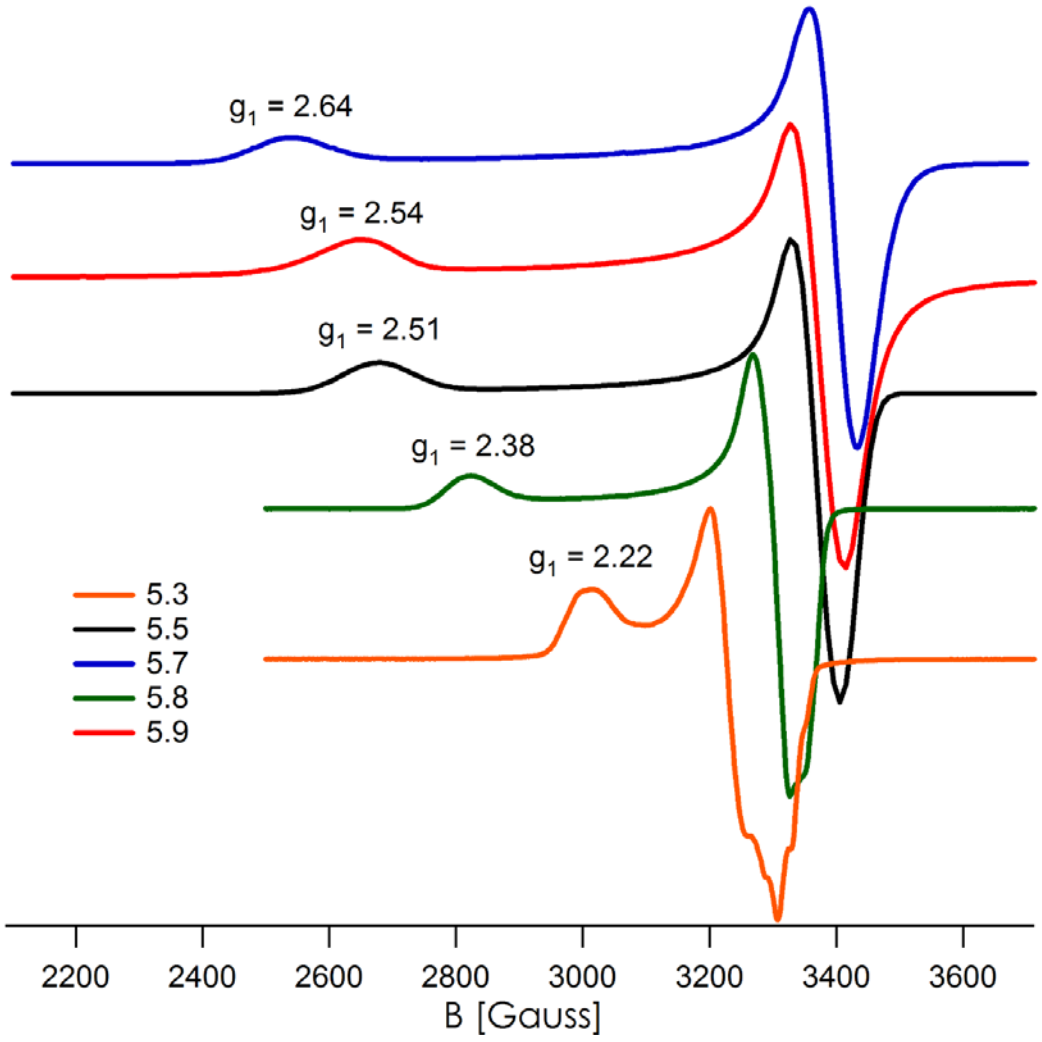

Figure A2.46. X-Band EPR spectra of the listed compounds collected at 20 K as 5 mM solutions in 2-MeTHF at a power of 1.8 mW.

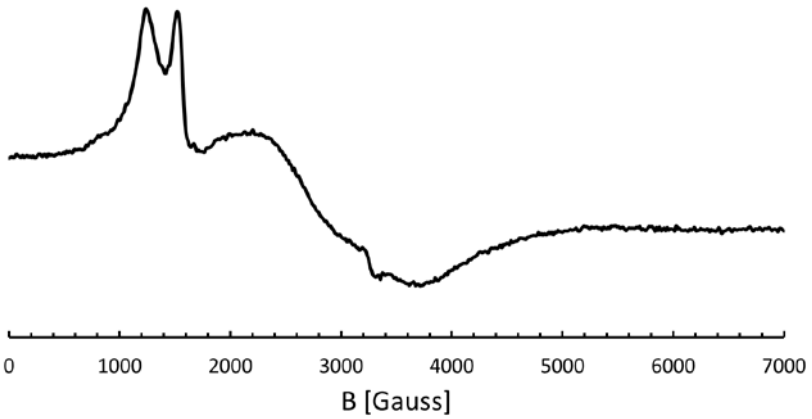

Figure A2.47. X-Band EPR spectra of compound **5.2** collected at 10 K as a 5 mM solutions in 2-MeTHF at a power of 1.8 mW.

XANES Spectra

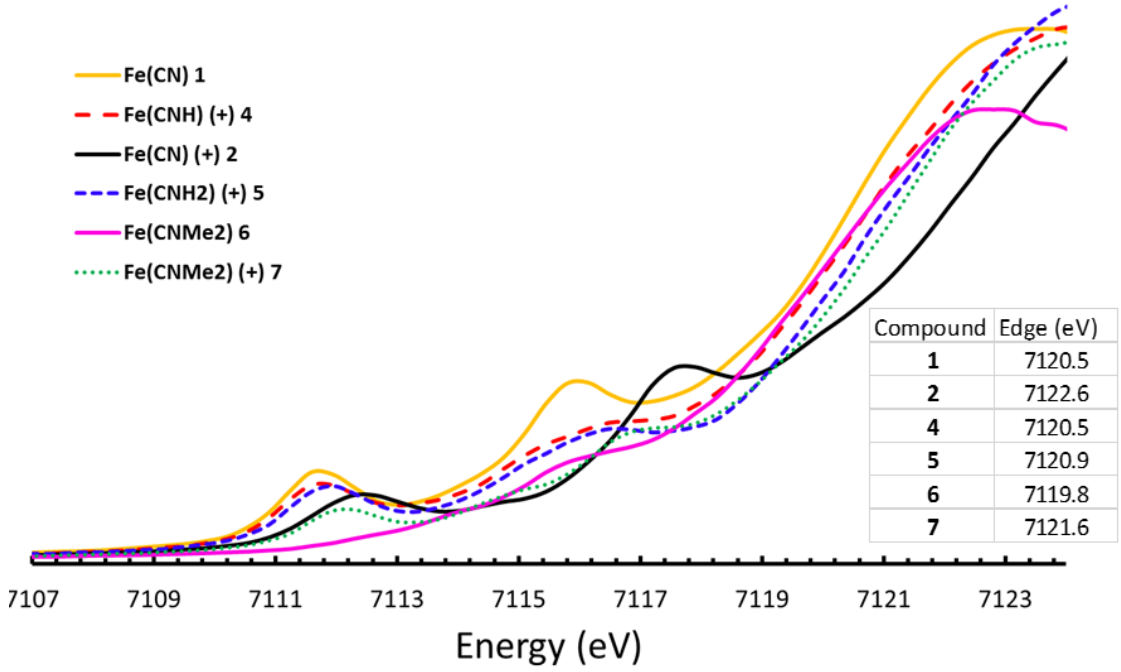

Compound	Edge (eV)
1	7120.5
2	7122.6
4	7120.5
5	7120.9
6	7119.8
7	7121.6

Figure A2.48. Fe K-edge XANES spectra of the listed compounds with the edge energies listed in the table.

X-Ray Diffraction Data

Compound	**1**	**2**	**3**	**4**	**5**	**6**	**7**	**8**	**9**	**10**
chem formula	$C_{43}H_{60}FeNP_3Si$	$C_{71}H_{71}BF_{24}FeNOP_3Si$	$C_{59}H_{90}FeNNaO_{10}P_3Si$	$C_{76}H_{85}BF_{24}FeNOP_3Si$	$C_{42}H_{64}F_3FeNO_4P_3SSi$	$C_{39}H_{60}FeNP_3Si$	$C_{71}H_{72}BF_{24}FeNP_3Si$	$C_{38}H_{57}FeNP_3Si$	$C_{70}H_{60}BF_{24}FeNP_3Si$	$C_{39}H_{57}F_3FeNO_3P_3SSi$
fw	768.15	1597.95	1173.16	1672.11	912.85	719.73	1582.96	704.7	1558.85	853.77
cryst syst	Monoclinic	Triclinic	Monoclinic	Triclinic	Monoclinic	Triclinic	Monoclinic	Triclinic	Triclinic	Monoclinic
Space group	$P2_1/C$	P-1	C_2/C	P-1	$P2_1/C$	P-1	$P2_1/C$	P-1	P-1	$P2_1/C$
a [Å]	12.7654(6)	12.6721(16)	46.808(2)	15.0167(11)	24.4156(7)	10.7372(9)	12.8247(5)	10.530(2)	12.9953(9)	15.0339(9)
b [Å]	15.4011(7)	16.407(2)	10.8136(6)	16.9753(12)	17.3909(5)	10.8095(10)	15.0774(6)	10.877(2)	14.3232(10)	12.9751(7)
c [Å]	20.6031(9)	19.169(2)	29.9223(19)	17.8198(13)	21.7555(6)	18.6713(16)	37.9194(16)	18.902(4)	20.0060(13)	21.9518(13)
α [°]	90	106.503(5)	90	108.035(3)	90	83.158(5)	90	74.62(3)	88.513(2)	90
β [°]	92.160(2)	99.988(5)	125.839(3)	110.461(3)	103.284(1)	87.492(5)	97.108(2)	88.11(3)	73.783(2)	93.558(4)
γ [°]	90	100.240(5)	90	95.579(3)	90	61.186(4)	90	61.95(3)	87.956(3)	90
V [$Å^3$]	4047.7(3)	3653.1(8)	12277.9(12)	3937.7(5)	8990.4(4)	1885.0(3)	7275.9(5)	1831.4(6)	3572.9(4)	4273.8(4)
Z	4	2	8	2	8	2	4	2	2	4
D_{calcd} [g cm^{-1}]	1.261	1.453	1.269	1.41	1.349	1.268	1.445	1.278	1.449	1.327
F(000)	1641	1636	5016	1724	3864	772	3244	754	1586	1800
μ [mm^{-1}]	0.554	0.393	0.406	0.368	0.569	0.587	0.393	0.603	0.399	0.591
measured reflns	217872	126663	311138	169724	160393	142801	221384	173013	78341	17400
unique reflns	23286	23927	22177	19528	22352	18076	27783	18512	15815	8508
data/restraints/param	23286/0/463	23927/72/997	22177/0/828	19528/0/1037	22352/12/1329	18076/0/420	27783/18/980	18512/0/410	15815/0/933	8508/0/483
R(F) (I>2σ(I))	0.03	0.0472	0.054	0.0502	0.059	0.036	0.0463	0.0533	0.049	0.0364
wR(F^2) (all)	0.0785	0.1276	0.1351	0.1365	0.1658	0.0846	0.1247	0.1142	0.1169	0.0861
GOOF	1.009	1.031	1.153	1.026	1.096	1.043	1.071	1.099	1.027	1.14

Table A2.1 X-ray Diffraction Table

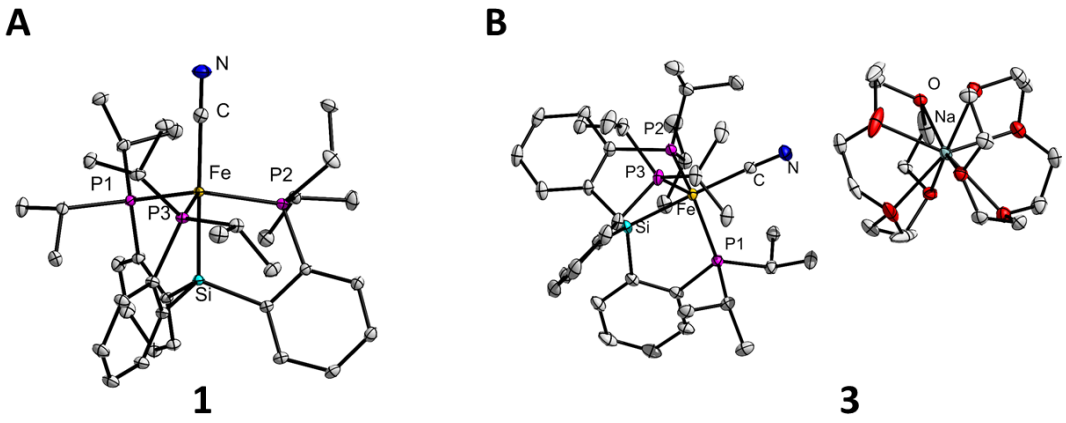

Figure A2.49. X-ray structure of compound **5.1** and **5.3** with thermal ellipsoids drawn at 50%. Cocrystallized solvent and disorder in the cation of **5.3** has been omitted for clarity.

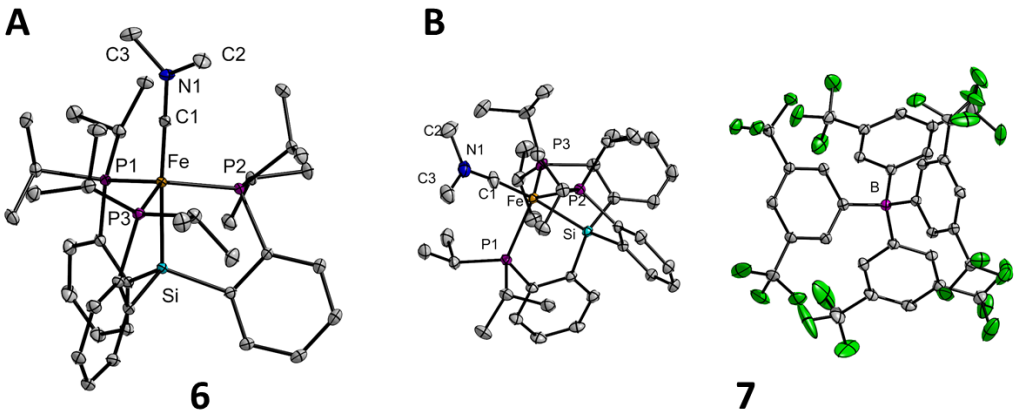

Figure A2.50. X-ray structure of compound **5.6** and **5.7** with thermal ellipsoids drawn at 50%.

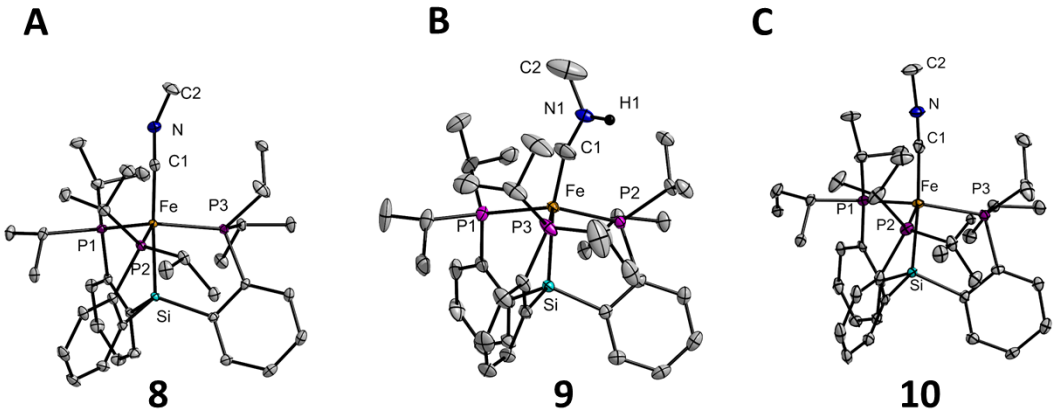

Figure A2.51. X-ray structure of compound **5.8**, **5.9** and **5.10'** with thermal ellipsoids drawn at 50%. Disordered portions of the aminocarbyne ligand in **5.9** and the anions of **5.9** and **5.10'** have been omitted for clarity.

Electrochemistry

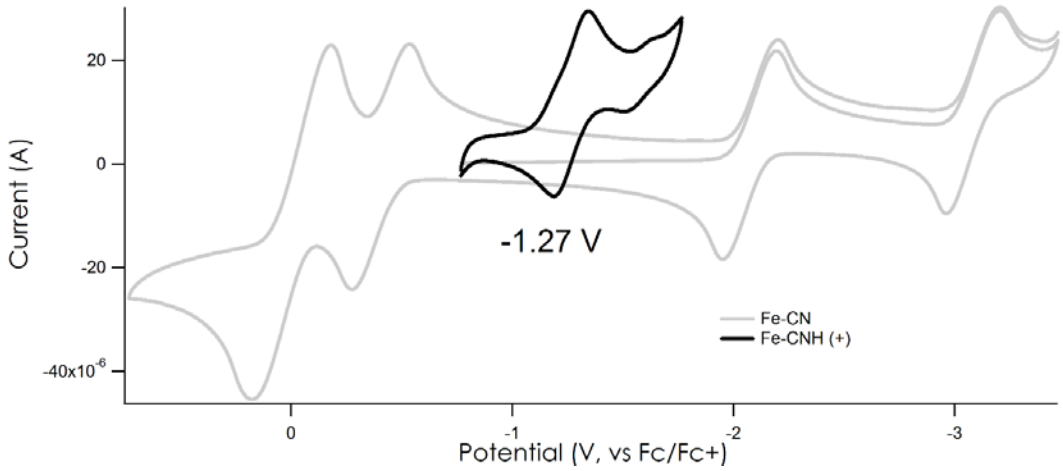

Figure A2.52. Overlaid cyclic voltammograms obtained on 1 mM solutions of **5.1** (gray) and **5.4** (black) collected in 0.1 M [TBA][PF_6] at 100 mV/s. The feature at -1.27 V corresponds to a reduction event of **5.4**.

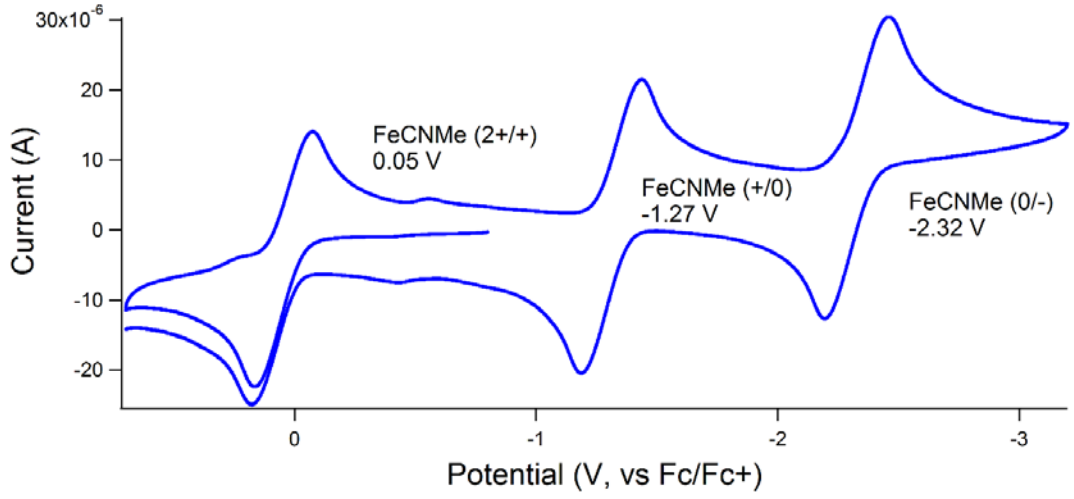

Figure A2.53. Cyclic voltammogram obtained on a 1 mM solutions of **5.10'** collected in 0.1 M [TBA][PF_6] at 100 mV/s. The feature at -1.27 V corresponds to a reduction event of **5.10'**.

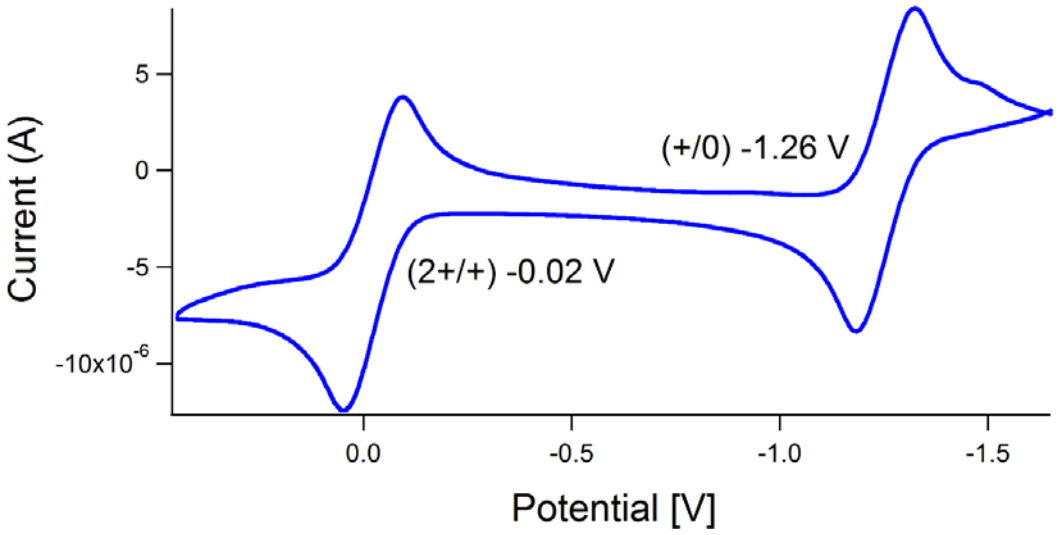

Figure A2.54. Cyclic voltammogram obtained on a 1 mM solutions of **5.6** collected in 0.1 M [TBA][PF_6] at 20 mV/s. The feature at -1.26 V corresponds to an oxidation event of **5.6**.

Cited References.

1. Lee, Y.; Mankad, N. P.; Peters, J. C. *Nat. Chem.* **2010**, 2, 558-565.
2. Brookhart, M.; Grant, B.; Volpe, A. F. *Organometallics* **1992**, *11*, 3920.
3. Chavez, I.; Alvarez-Carena, A.; Molins, E.; Roig, A.; Maniukiewics, W.; Arancibia, A.; Arancibia, V.; Brand, H.; Manriquez, J. M. *J. Organomet. Chem.* **2000**, 601, 126.
4. Weitz, I. S. & Rabinovitz, M. *J. Chem. Soc. Perkin Trans.* **1993**. 1, 117–120.
5. Berto, T. C.; Hoffman, M. B.; Murata, Y.; Landenberger, K. B.; Alp, E. E.; Zhao, J. Y.; Lehnert, N. *J. Am. Chem. Soc.* **2011**, *133*, 16714.
6. Anderson, L. L.; Arnold, J.; Bergman, R. G. *J. Amer. Chem. Soc.* **2005**. 127, 14542-14543.
7. Evans, D. F. *J. Chem. Soc.* **1959**, 2003.
8. Stoll, S.; Schweiger, A. *J. Magn. Reson.* **2006**, *178*, 42.
9. Münck, E. *Aspects of ^{57}Fe Mössbauer Spectroscopy*; University Science Books: Sausalito, CA, 2000.
10. https://home.comcast.net/~sam_webb/sixpack.html
11. http://bruceravel.github.io/demeter/
12. Gaussian 09, Revision B.01, Frisch, M. J.; Trucks, G. W.; Schlegel, H. B.; Scuseria, G. E.; Robb, M. A.; Cheeseman, J. R.; Scalmani, G.; Barone, V.; Mennucci, B.; Petersson, G. A.; Nakatsuji, H.; Caricato, M.; Li, X.; Hratchian, H. P.; Izmaylov, A. F.; Bloino, J.; Zheng, G.; Sonnenberg, J. L.; Hada, M.; Ehara, M.; Toyota, K.; Fukuda, R.; Hasegawa, J.; Ishida, M.; Nakajima, T.; Honda, Y.; Kitao, O.; Nakai, H.; Vreven, T.; Montgomery, J. A., Jr.; Peralta, J. E.; Ogliaro, F.;

Bearpark, M.; Heyd, J. J.; Brothers, E.; Kudin, K. N.; Staroverov, V. N.; Kobayashi, R.; Normand, J.; Raghavachari, K.; Rendell, A.; Burant, J. C.; Iyengar, S. S.; Tomasi, J.; Cossi, M.; Rega, N.; Millam, J. M.; Klene, M.; Knox, J. E.; Cross, J. B.; Bakken, V.; Adamo, C.; Jaramillo, J.; Gomperts, R.; Stratmann, R. E.; Yazyev, O.; Austin, A. J.; Cammi, R.; Pomelli, C.; Ochterski, J. W.; Martin, R. L.; Morokuma, K.; Zakrzewski, V. G.; Voth, G. A.; Salvador, P.; Dannenberg, J. J.; Dapprich, S.; Daniels, A. D.; Farkas, Ö.; Foresman, J. B.; Ortiz, J. V.; Cioslowski, J.; Fox, D. J. Gaussian, Inc., Wallingford CT, 2009.

13. Garrido, G.; Rosés, M.; Ràfols, C.; Bosch, E. *J. Solution Chem.* **2008**. 37, 689-700.

14. Weatherburn, M. W. *Anal. Chem.* **1967**. 39, 971.